Development of Some Novel Nano-composites for Energy Harvesting Applications

Thesis Submitted

To Jadavpur University

For the Degree of

Doctor of Philosophy (Science)

By

Suvankar Mondal

Department of Physics

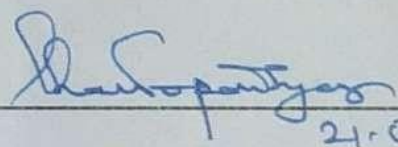Jadavpur University

Jadavpur, Kolkata-700032

India

2023

Prof. (Dr.) Kalyan Kumar Chattopadhyay

The Head

Department of Physics

Jadavpur University

Jadavpur, Kolkata-700032, India

Email: kalyan_chattopadhyay@yahoo.com

CERTIFICATE FROM THE SUPERVISOR

This is to certify that the thesis entitled *"Development of some novel nanocomposites for energy harvesting applications"* submitted by *Mr. Suvankar Mondal*, who got his name registered on *13/11/2019* for the award of *Ph.D. (Science) degree of Jadavpur University* is based upon his work under the supervision of *Prof. Kalyan Kumar Chattopadhyay* and that neither his thesis nor any part of the thesis has been submitted for any degree/diploma or any other academic award anywhere before.

21.02.23

Prof. Kalyan Kumar Chattopadhyay

(Signature of the Supervisor, date with office seal)

Professor
Dept. of Physics
Jadavpur University
Kolkata-700032, India

DECLARATION

I *Suvankar Mondal* registered on *13/11/2019* do hereby declare that this thesis entitled "*Development of Some Novel Nanocomposites for Energy Harvesting Applications*" contains a literature survey and original research work done by the undersigned candidate as part of doctoral studies.

All information in this thesis has been obtained and presented in accordance with existing academic rules and ethical conduct. I declare that, as required by these rules and conduct, I havefully cited and referred all materials and results that are not original to this work.

Also, it has not been submitted for any degree or examination in any other university. I further declare that all the resources I have used or quoted have been indicated and acknowledged by complete references.

Suvankar Mondal

- -

Signature of Candidate: Date: 21.02.2023

[Suvankar Mondal]

Dedicated to my beloved parents......

A sincere gratitude to……

All the enthusiastic minds who are working towards a vision of serving human kind through continuous striving for knowledge and wisdom with an indomitable willpower against the various adversities and obstacles in life.

CONTENTS

CONTENTS

CONTENTS

CONTENTS

CONTENTS

ACKNOWLEDGEMENTS

parents. One very close person's name is consciously omitted in this acknowledgment page as our association is beyond this sort of writing. Last of all, my thanks go to all my well- wishers, my brother, sister, friends and teachers, whom I shall always keep in mind to remember throughout my life.

February 2023

Department of Physics
Jadavpur University
Kolkata –32, India   **(Suvankar Mondal)**

LIST OF PUBLICATIONS

1. **S. Mondal,** T. Paul, S. Maiti, B. K. Das, and K. K. Chattopadhyay. *Human Motion Interactive Mechanical Energy Harvester Based on All Inorganic Perovskite-PVDF.* **Nano Energy**, *74* (2020) 104870.

2. **S. Mondal,** S. Maiti, T. Paul, A. Sahoo, S. Bhattacharjee, N. S. Das, and K. K. Chattopadhyay. *All-Inorganic Halide Perovskite Tuned Robust Mechanical-Energy Harvester: Self-Driven Posture Monitor and Power Source for Portable Electronics.* **Appl. Mater. Today**, *26* (2022) 101385.

3. **S. Mondal,** S. Thakur, S. Maiti, S. Bhattacharjee, and K. K. Chattopadhyay. *Self-Charging Piezo-Supercapacitor: One-Step Mechanical Energy Conversion and Storage.* **ACS Appl. Mater. Interfaces** 15(6) (2023) 8446–8461.

4. **S. Mondal,** S. Das, S. Maiti, N. Besra, T. Paul, and K. K. Chattopadhyay. *Hybrid Piezoelectric Nanogenerator Based on PVDF Film and Vertically Aligned Zno Nanorods for Energy Harvesting Applications.* **Int. J. Nanotechnol**, 18(5-8) (2021) 669-678.

5. S. Bhattacharjee, **S. Mondal,** A. Banerjee, and K. K. Chattopadhyay. *Dielectric and Piezoelectric Augmentation in Self-Poled Magnetic Fe_3O_4/Poly (Vinylidene Fluoride) Composite Nanogenerators.* **Mater. Res. Express**, *7*(4) (2020) 044001.

6. S. Bhattacharjee, N. Mazumder, **S. Mondal,** K. Panigrahi, A. Banerjee, D. Das, S. Sarkar, D. Roy, and K. K. Chattopadhyay. *Size-Modulation of Functionalized Fe_3O_4: Nanoscopic Customization to Devise Resolute Piezoelectric Nanocomposites.* **Dalton Trans**, *49*(23) (2020) 7872-7890.

7. T. Paul, S. Maiti, U. Mukherjee, **S. Mondal,** A. Sahoo, and K. K. Chattopadhyay. *Cube Shaped FAPbBr$_3$ for Piezoelectric Energy Harvesting Devices.* **Materials Letters**, *301* (2021) 130264.

PAPERS PRESENTED AT INTERNATIONAL AND NATIONAL CONFERENCES

1. **ICONSEA-2018, 4-6 October, Jawaharlal Nehru Technology University, Hyderabad.** Presenting a poster on "**Self-Poled Piezoelectric Nanogenerator Based on PVDF and Zno Nanocomposite for Energy Harvesting**".

2. **NCRDNN-2019, 29-31 January, Jadavpur University, School of Materials Science & Nanotechnology, Kolkata.** Presenting a poster on "**Piezoelectric Nanogenerator Based on Room Temperature Grown Zno Nanorods and PVDF for Energy Harvesting**".

3. **ICNAN-2019, 29th November-1st December, Centre for Nanotechnology Research, Vellore Institute of Technology, Chennai.** Presenting poster on "**Development of Building Deformation and Bridge Safety Sensor Based on PVDF-CsPbCl$_3$**".

4. **AMT-2020, 26-28 August, Department of physics, School of applied science, Kalinga Institute of Industrial Technology, Bhubaneswar.** Presenting poster on "**All-Inorganic Halide Perovskite Tuned Robust Mechanical-Energy Harvester: Self-Driven Posture Monitor and Power Source for Portable Electronics**".

5. **FMT-2020, 13-14 October, Department of physics, School of applied science, Kalinga Institute of Industrial Technology, Bhubaneswar.** Presenting poster on "**Human Motion Interactive Mechanical Energy Harvester Based on All Inorganic Perovskite-PVDF**".

LIST OF FIGURES

Figure 3.11: Digital photograph of TEM.

Figure 4.1: Schematic illustration of room temperature synthesis of all-inorganic perovskite $CsPbX_3$ (X =Cl, Br, I) rods.

Figure 4.2: Schematic illustration of PVDF composites preparation.

Figure 4.3: Schematic presentation of PNG device and working principle.

Figure 5.1: (a) XRD (b) reflectance spectra (c) FESEM (d) EDX spectra of $CsPbBr_3$.

Figure 5.2: (a) FTIR spectra in the range $1600-400$ cm^{-1} and (c) $3050-2960$ cm^{-1}. (d) RAMAN spectra of PVDF and composite films. (b) Dependency of electroactive (β) phase on perovskite wt. %.

Figure 5.3: Core level XPS spectra of (a) Cs (b) Pb (c) Br of $CsPbBr_3$ and (d) C (e) F of PVDF.

Figure 5.4: (a) XRD and (b) UV-Vis spectrum for $CsPbBr_3$, PVDF and PCS 5. (c) FESEM image PCS 5. (d) The dielectric loss of PVDF and PCS 5 (e) PL spectra and image of the PCS 5.

Figure 5.5: (a) Side view of PVDF chain (b) Side view of orthorhombic $CsPbBr_3$ (c) Top view of $CsPbBr_3$-PVDF. Total density of state of (TDOS) (d) $CsPbBr_3$ (e) PVDF (f) $CsPbBr_3$-PVDF and (g) variation of electrostatic potential with distance from surface for $CsPbBr_3$-PVDF composite.

Figure 5.6: (a) Output voltage (b) current of all the PNGs. (c) output power variation with wt. % $CsPbBr_3$. (d) variation in output voltage and current (e) variation of output power with load resistance for PNG 5 (f) equivalent diagram and glowing of 10 LED bulbs with constant hammering. Output voltage (g) forward connection (h) reverse connection. (i) Rectified DC output voltage of PNG 5.

Figure 5.7: Voltage response of PNG 5 (a) as a function of time for different applied pressures (b) at different applied pressure (c) due to arm bending. (d) Due to finger pressing. (e) The digital image demonstrates the response of PNG 5 due to the drum beats of a toy. (f) The output

voltage of PNG 5 under the impact of drum beats. Inset shows the press and release of (c) arm and (d) finger.

Figure 5.8: Output voltage of PNG 5 film (a) under the finger tapping (b) under the toe pressing (c) due to air blower pressure (d) due to table fan air pressure (f) due to mobile vibration. (e) Digital image of the piezo-response under mobile vibration.

Figure 5.9: (a) I-V characteristics of the detector under dark and light conditions (b) change in output current and (c) output voltage under dark and light conditions, with the same periodic stress.

Figure 5.10: Output voltage recorded over time for continuous 15000 cycles (a) on the first day (b) after 2 months (c) after 4 months. (d) Glowing of 12 LEDs designed according to our university name "JU".

Figure 6.1: (a) XRD profile, (b) rietveld refinement, (c) crystal structure, (d) FESEM, and (e) TEM image of $CsPbCl_3$.

Figure 6.2: (a) FTIR spectra of all synthesized films, (b) Variation in β phase concentration and (c) r_{dc} and $\overline{v}$ values with different wt. % perovskite loading, (d) Raman spectra of all films; (e) XRD profile of PVDF and PPF 3 within the range $2\theta = 16\text{-}23°$; (f) crystallinity variation of different phases in PVDF and hybrids.

Figure 6.3: (a) EDX scan; XPS spectra of (b) Cs 3d, (c) Pb 4f, (d) Cl 2p, (e) C 1s and (f) F 1s of PPF 3.

Figure 6.4: (a) P-E loop of PVDF and all the hybrid films (inset shows variation in remanent and saturation polarisation as a function of perovskite loading) (b) variation of ε_r with frequency (c) variation of dielectric loss with frequency (d) variation in conductivity of PVDF and hybrid films with frequency. The inset shows variation in ε_r and d_{33} values with respect to perovskite loading.

Figure 6.5: (a) Output voltage (b) current from RNG and PNG due to hand hammering; (c) charging comparison of RNG and PNG 3. (d) Output voltage and current and (e) instantaneous power across load resistance. Output voltage generated from PNGs due to (f) finger tapping and (g) leg pressing. (h) Output current in forward and reverse connection and (i) output voltage in forward and reverse connection (inset shows zoom in the profile of a single peak).

Figure 6.6: (a) Output voltage due to half banding and complete bending recorded by a digital oscilloscope. (b) Open circuit voltage (c) short circuit current due to bending at various angles (insets show zoom in view). (d) Output voltage and current (e) effective stress (f) effective strain (g) output power with respect to bending angle. (h) Output voltage and current vs resistance at 5^0 bendings; (i) Resistance vs power variation of PNG 3 at different bending angles.

Figure 6.7: Output voltage across the fabricated sensor at different bending postures.

Figure 6.8: Output voltages for (a) slow pressing-slow releasing, (b) slow pressing-fast releasing, (c) fast pressing-slow releasing and (d) fast pressing-fast releasing. Output voltages due to (e) jogging, running and walking.

Figure 6.9: (a) Schematic of the capacitor charging process and different capacitor charging, (b) power up a calculator, (c) fitting of PNG 3 inside the shoe, total circuit connection for mobile charging.

Figure 6.10: (a) Output voltage and (b) current of PNG 3 for first 10000 cycles (c) fatigue test output voltage for consecutive 5 months. (e) Digital image showing the glowing LED array and university acronym "JU".

Figure 7.1: (a, b) FESEM morphology of CCNO (inset: X-ray diffraction pattern of CCNO); (c) TEM and (d) HRTEM images of CCNO nanoform.

Figure 7.2: (a-b) FESEM image of CCNO grown on CC at different magnifications.

Figure 7.3: Core level XPS spectra of (a) Cu 2p, (b) Co 2p, (c) Ni 2p, (e) F 1s and (f) C 1s of PNCU 1 and (d) F 1s of PVDF.

Figure 7.4: (a) FTIR spectra of all films; (b) Variation of d_{33} and F_{EA} with CCNO content in the sample; (c, d) FESEM image of the PNCU 1 film at two different magnifications; (e) XRD pattern of CCNO, PVDF and PNCU 1 films. Deconvoluted XRD region (16°-30°) of (f) PVDF; and (g) PNCU 1 showing different phase proportions; (h) Raman spectra of all composite films and neat PVDF film.

Figure 7.5: Local piezoelectric behavior PNCU 1 material. (a, b) Topography image of the film; (c) PFM amplitude (butterfly loop); (d) PFM phase image; (e) 3D surface morphology; (f) phase hysteresis loop of PNCU 1.

Figure 7.6: Dispersions within the frequency range 100 Hz to 10 MHz of (a) dielectric constant; (b) dielectric loss tangent and (c) ac conductivity (inset: magnified view of conductivity variation for the range 0.6-10 MHz) of all synthesized composite films along with neat PVDF film; (d) comparison of dielectric constant and dielectric loss with CCNO loading in the PVDF matrix at 100 Hz.

Figure 7.7: P-E curves for all synthesized films under a maximum applied field of (a) 0.6 MV m^{-1}; (b) 0.8 MV m^{-1}; (c) 1.0 MV m^{-1}; and (d) 1.2 MV m^{-1} (the enlarged view is presented in the inset).

Figure 7.8: (a) Variation of saturation polarisation of the composite films at different applied fields. (b) Change of saturation polarization and coercive field as a function of the piezoelectric coefficient (d_{33}). Electric polarisation vs Electric field hysteresis loop (P-E Loop) of (c) PVDF and (d) PNCU 1 at electric field 1.2 MV m^{-1}. (e) Energy density and (f) energy loss as a function of applied field for different samples.

Figure 7.9: (a) Open-circuit voltage with the enlarged view of voltage (right side); and (b) short circuit current with the enlarged view on the right side for different nanogenerators (RNG,

PNG 0.25, PNG 0.5, PNG 1 and PNG 2); (c) Variation of maximum open-circuit voltage and short circuit current as a function of filler loading in PVDF matrix; (d) Charge transfer with time for all nanogenerators under hammering.

Figure 7.10: (a) Variation of the voltage, current and (b) power with the load resistance (R_L) and the inset shows the schematic circuit diagram; (c) Output voltage and (f) current measured in forward and reverse connection; (d) Rectified DC output voltage and (e) zoom view of rectified DC voltage of PNG 1; (g) Charging performance of 1 µF capacitor with different imparting frequency from 1-8 Hz; (h) The measured output voltage across the various commercial capacitors of 1, 2.2, 4.7, and 10 µF as charged by PNG 1 at 8 Hz; (i) Simulation results of PNG 1 using the COMSOL Multiphysics programming software.

Figure 7.11: (a) Measured output voltage of PNG 1 under different pressure; (b) Sensitivity of fabricated PNG 1 in the pressure range 0-2.2 kPa; (c) Output voltage under different pressing frequency form 1-7 Hz; (d) variation of output voltage as a function of tapping frequency. The open-circuit voltage generated under (e) bending; (f) twisting by the finger; (g) finger tapping; and (h) leg pressing on PNG 1 (insets show corresponding captured images); (i) Captured image in the dark of commercial LEDs glowing in a 'JU' pattern.

Figure 7.12: (a-d) Long cycle stability test of PNG 1 over 12 months (30,000 cycles) with an enlarged view in the inset; (e) consistency of peak voltage at different times under long cycle tests; (f) digital photograph showing the ability of PNG 1 to drive 89 LEDs.

Figure 7.13: (a) CV profile at different scan rates; (b) GCD profiles at different applied current ranges; (c) specific device capacitance at different scan rates. (d) Capacitance retention performance after 10,000 cycles (inset: last 10 charging-discharging cycles) of the CCNO electrodes.

Figure 7.14: (a) Variation calculated power density with energy density (Ragone plot) of the fabricated device. (b) The specific areal capacitances vs current density plot.

PREFACE

A piezoelectric nanogenerator is a device that converts low-frequency mechanical vibration into electrical energy through piezoelectric, pyroelectric and triboelectric effects. Many researchers deploy PVDF as a piezoelectric material in a piezoelectric nanogenerator. PVDF and its co-polymers are the most suitable candidates due to their excellent energy storage ability, high piezoelectric coefficient, desirable flexibility, and capability to transform into different elaborate shapes. Generally, PVDF exhibits five polymorphs based on different chain conformations *viz.*, α, β, γ, δ, and ε phases. Among these, α and δ phase shows trans-gauche-trans-gauche (TGTG) configuration, and β phase exhibits all-trans (TTTT) configuration and γ phase shows T^3GT^3G configuration. α and δ phases show no spontaneous polarization which makes them non-polar, while due to the parallel dipolar configuration, both of β and γ phases are polar. A monomer unit —$(CH_2$—$CF_2)$— is repeated in the PVDF matrix (for β phase) to form a nonconjugated linear fluorinated hydrocarbon with a high vacuum dipole moment (7×10^{-30} C m), pointing roughly from the negatively charged fluorine atom to the positively charged hydrogen atom. However, with larger spontaneous polarization β phase predominantly manifests the piezoelectric effect. But in a normal PVDF matrix, β phase content is nominal, so it is needed to enhance the associated β phase fraction. Hence, our primary objective is to enhance the electroactive phase content of the PVDF matrix as much as possible. Different groups have elaborated versatile and novel approaches to transform the nonpolar phase into an electroactive phase; such as mechanical stretching, electrical polling under high field, thermal annealing, filler incorporation in PVDF matrix, etc. Among these, filler incorporation is a more convenient process for multifunctional applications that hardly affects the flexibility of the film.

The research described in this Ph.D. thesis explains how to synthesize PVDF composite materials and how to use them in multipurpose piezoelectric nanogenerators. The thesis begins with an overview of PVDF composites (**chapter 1**) that provides a brief description of their structure, numerous physical characteristics, and several optoelectronic factors that significantly influence their uses. The literature overview of PVDF-based piezoelectric nanogenerators and their applications, as well as several ground-breaking reports, are discussed in **chapter 2**. **Chapter 3** describes the precise synthesis processes for the PVDF composite and the precise device construction process. **Chapter 4** discusses the fundamental operating principles and a broad overview of the crucial characterization tools that are utilised during the entire course of the study.

Chapter 5 also provides an introduction to A novel piezoelectric sensor fabricated by a composite with room temperature processed all-inorganic cesium lead bromide ($CsPbBr_3$) perovskite rod and polyvinylidene fluoride (PVDF) nanofiber. $CsPbBr_3$ enables nucleation of the electroactive β phase in PVDF >90% and makes it suitable for piezoelectric energy harvesting. Piezoelectric energy generation from the devices has been investigated under several simple human movements like hammering by hand, finger touch, toe pressing, bending by arm, and so on. Optimized composite (5 wt. % $CsPbBr_3$ containing PVDF film) based PNG delivered an output power of 4 mW with a high open-circuit voltage of 120 V and short-circuit current of 35 μA. In addition, the photosensitivity of the composite is demonstrated under light, which promises its potential as a photodetector. Considering the photoresponse and electroactive features, a new class of self-powered photoactive piezoelectric energy harvesters has also been fabricated.

Chapter 6 introduces cesium lead chloride ($CsPbCl_3$)-embedded β-phase comprising polyvinylidene fluoride (PVDF) hybrid films turn into a suitable functional material for piezoelectric-based mechanical energy harvesters. Incorporation of $CsPbCl_3$ in the PVDF

matrix enables high crystallinity and nucleation of electroactive β-phase ~86% in the PVDF with piezoelectric coefficient d_{33} of 49 pm/V, much higher as compared to pristine PVDF. The fabricated PNG delivered an instantaneous output voltage of 168 V and a peak-to-peak output current of 2 μA. The high sensitivity of the flexible PNGs enables us to measure even a slight deformation due to bending by 2°. Considering its good flexibility and high electrical output performance, optimized PNG was utilized for the fabrication of a wearable self-powered posture sensor to monitor the regular movement of our spine. Walking-based wearable PNGs are also devised for powering up normal android mobile phone batteries.

Chapter 7 introduces a self-charging flexible supercapacitor is successfully realized that can harvest sporadic mechanical energy, convert it to electrical energy, and simultaneously store power. Initially, chemically processed multi-metallic oxide, namely copper cobalt nickel oxide ($CuCoNiO_4$) is amalgamated within the PVDF framework in different wt% to realize high-performance PNGs. The combination of $CuCoNiO_4$ as filler creates a notable electroactive phase inside the PVDF matrix, and the composite realised by combining 1wt% $CuCoNiO_4$ with PVDF exhibits the highest electroactive phase (>86%). Under periodic hammering (~100 kPa), PNGs fabricated with this optimized composite film deliver an instantaneous voltage of ~67.9 V and a current of ~4.15 μA. Furthermore, PNG is ingeniously integrated into a supercapacitor to construct PSCFS, using PNCU as a separator and $CuCoNiO_4$ nanowires on carbon cloth as the positive and negative electrodes. The self-charging behavior of the rectifier-free storage device was established under bending deformation. This work offers a high-performance, self-powered device that can be used to replace bulky batteries in everyday electronic devices by harnessing mechanical energy and converting mechanical energy from its environment into electrical energy.

Energy harvesting from mechanical strain using piezoelectric materials has attracted considerable attention from researchers for their direct utilization in cutting-edge smart

devices. In **chapter 8**, a piezoelectric nanogenerator based on polyvinylidene fluoride (PVDF) and aligned zinc oxide (ZnO) nanorods is fabricated for mechanical energy harvesting. ZnO nanorods array over zinc foil was realized via facile wet chemical method at ambient conditions. ZnO- PVDF hybrid structure was prepared by stacking PVDF on ZnO nanorods. The synergistic piezoelectric effect of PVDF and ZnO nanorods delivered high output characteristics under applied pressure. As fabricated device showed an open-circuit voltage of ~21.5 V and instantaneous power of ~135.45 μW at an applied pressure of 4.5 MPa. Generated output power was more than sufficient to glow commercial green LEDs.

Finally, in **chapter 9**, a summary of the major findings of this thesis and scopes for future work are discussed.

February 2023

<div align="right">

Suvankar Mondal

Department of Physics

Jadavpur University

Kolkata –700032, India

</div>

CHAPTER 1

Introduction

1.1. The background and motivation: Energy demands in the present and future

O   ver the decades, the energy demand has gradually increased owing to rapid developments in technology, the industrial revolution, and a growing civilization. Moreover, we need more energy to get sufficient industrial products to maintain our lifestyle. EIA expects the global energy demand will grow up to 48% in the nearer 20 years [1]. Figure 1.1 shows the enhancement of energy demands year over year. Nowadays, we are mostly dependent on energy from fossils fuels to meet our energy needs, which has several disadvantages. First of all, the resource of fossil fuels reducing rapidly which limits their use in the distant future. Secondly, such a type of source emits a huge amount of CO_2, which directly causes air pollution and global warming, and it is predicted that this amount will increase in the upcoming future.
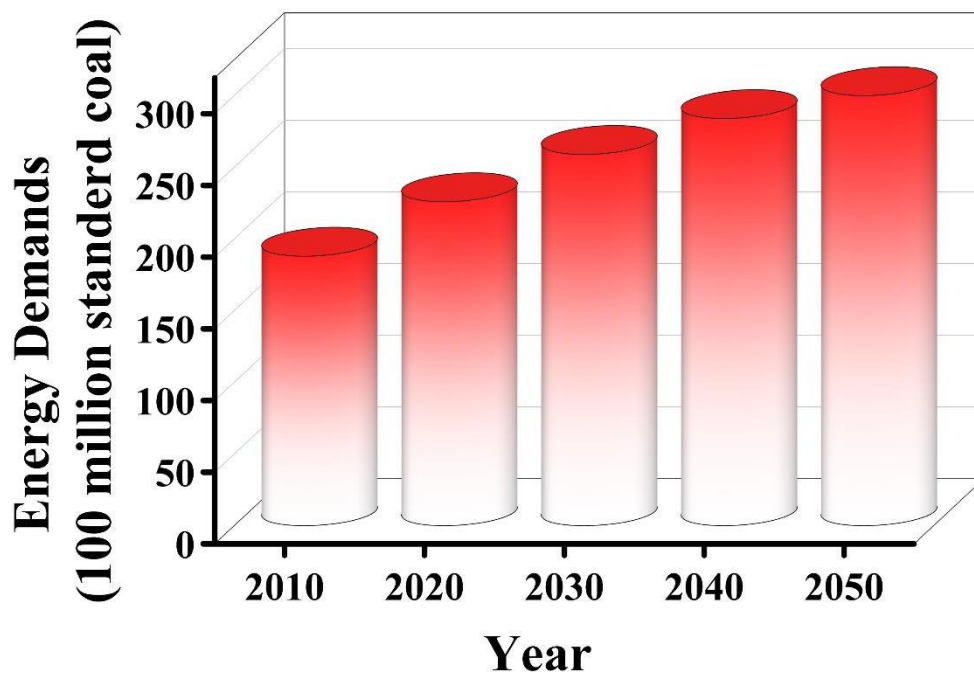
Figure 1.1: Enhancement of energy demands year over year.

Global warming raises the environmental temperature of the earth which increases the seawater layer. Also, global change in climate causes the prevalence of various deadly diseases. In the previous 30 years, the average earth's temperature increased by 0.2°C per decade, as illustrated
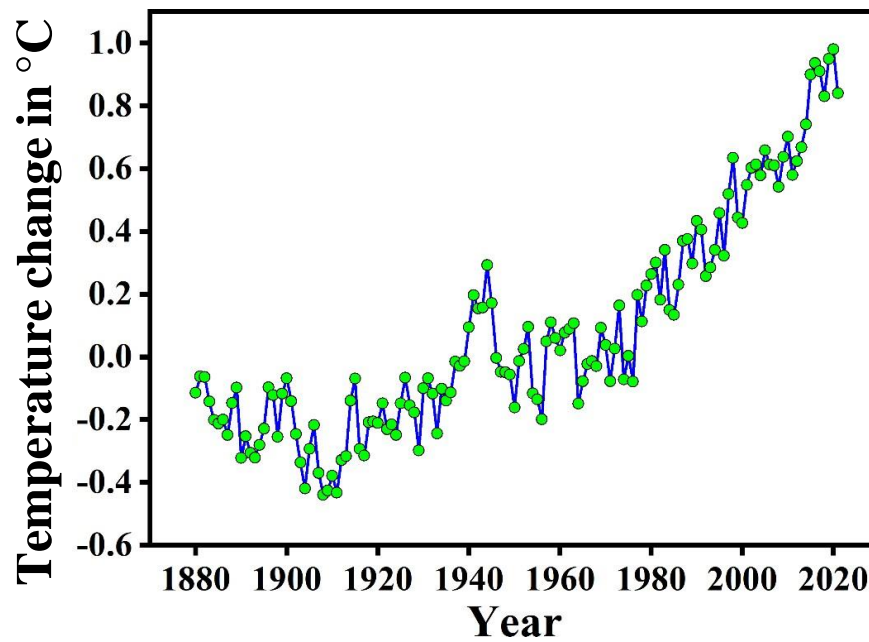
Figure 1.2: *Global temperature change year over year.*

in figure 1.2 [2]. Due to such kind of issue, if we cannot find out a replacement for fossil fuel energy, the existence of civilization will be in crisis. In these circumstances, researchers/scientists are doing lots of work to find a complement to traditional energy [3-5]. Formally, we are predominantly dependent on fossil fuel energy, but there are so many overwhelming renewable energy sources that can meet our demands. Solar energy, hydro energy, geothermal energy, wind energy, bioenergy, thermal energy, biomechanical energy, etc. are the most probable and efficient energy sources to harvest in the future. Among them, mechanical energy harvesting is one of the best alternatives to resolve the upcoming problem. There is a large amount of mechanical energy in our environment and if we harness a small fraction of it, which may be sufficient. The nanogenerator is such a type of device that can extract various mechanical stimuli in our surroundings and convert them to electrical energy [6-9].

According to the U.S energy information administration reports in 2011, the energy demands will increase by almost 53% during the period 2011-2035 [10]. Moreover, only fossil fuels cannot meet these huge energy demands. Once, it causes pollution and global warming, which

harms human life. In this context and it is required to develop more sustainable and renewable energy sources. But such type of source is non-renewable and gradually decreases, which will run out shortly. Thereafter, the development of renewable sources becomes an important assignment [11-13].

1.1.1. Non-sustainable energy

Cole, petroleum and natural gas are the key sources of non-renewable energy that meet almost 77% of total energy demand. Continued consuming coal is heightening the climate change issue, as there are so many secondary products like CO_2 and various toxic gases that have been released, which cause air pollution and the greenhouse effect. Again, on another side, billions of years have taken to the formation of these sources. Henceforth, the generation of energy
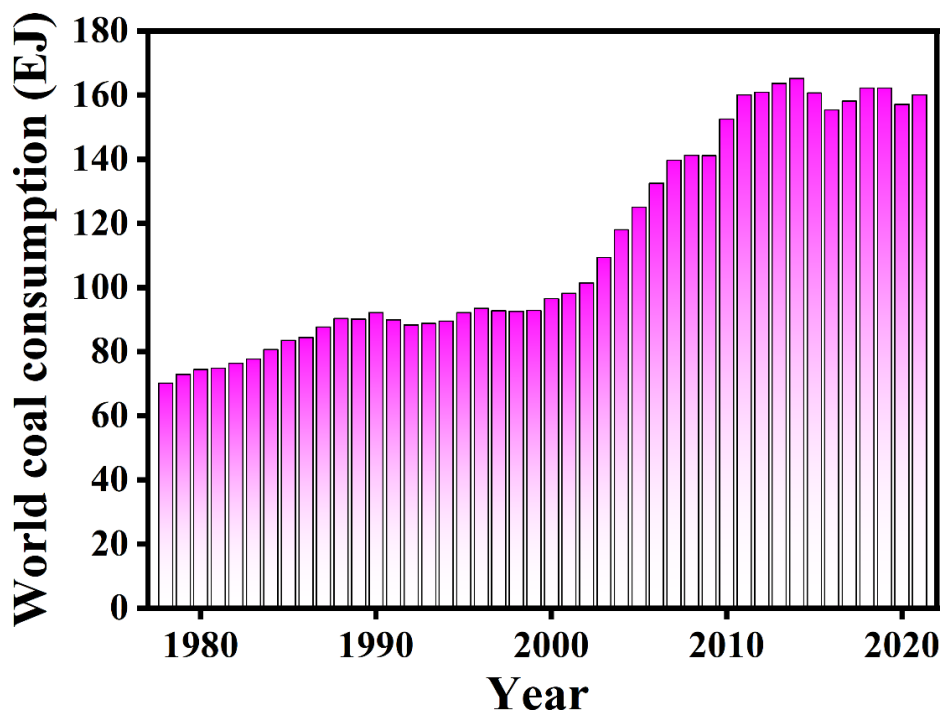
Figure 1.3: *World coal consumption, 1978-2021.*

while maintaining the environment is a big challenge. Figure 1.3 presents the year-wise consumption of coal in the time range 1975-2021. Over the decade, petroleum and natural gas will become the primary sources of energy in the transport sector. But for our future security,

it is necessary to find a renewable energy source that could be an alternative to petroleum and gas.

1.1.2. Sustainable Energy

Renewable energy means energy that cannot be run out or an endless energy source that will not be over, such as the sun, wind, hydro, geothermal, etc. These are sources of energy that may be appropriate substitutes for the largely used unsustainable sources like coal, petroleum, etc. Global electricity generation has grown from 20% to 28% in the past decade (2011-2021) and renewable energy contributes more than 20% of it. Moreover, the use of fossil fuels is reduced from 68% to 62%, as well as the use of nuclear energy, which decreased from 12% to 10%. There are several types of renewable energy sources viz. solar, wind, biomass, hydropower, geothermal energy, etc. Figure 1.4 shows the energy generated from the different
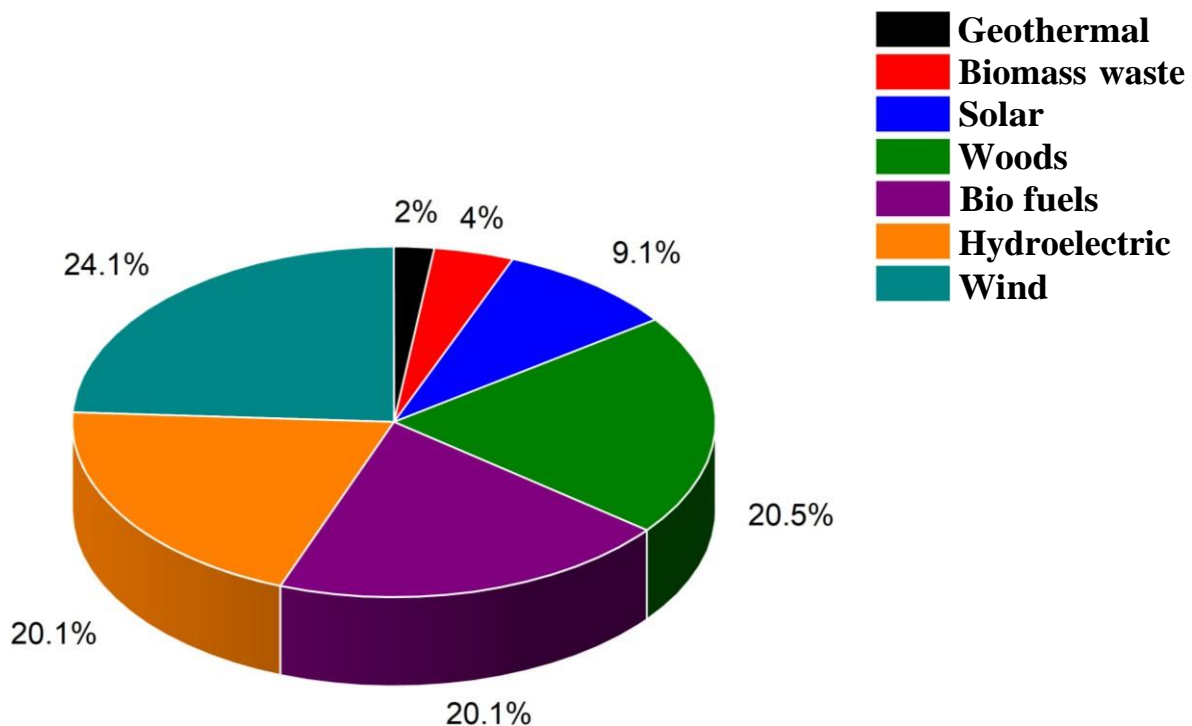
Figure 1.4: *Energy from various renewable sources.*

renewable sources. In recent times, solar photovoltaics and wind energy have become the largest renewable energy sources, producing most of the energy among all renewable sources. While electrical power generation from sunlight and wind blow is increased from 2% to 10%

which is impressive. But all of the aforementioned sources have lower efficiency and cost effects. Mechanical energy harvesting using piezoelectric transduction is one of the best ways to overcome the upcoming challenge. Piezoelectric nanogenerators can able to convert mechanical energy/vibrational energy into electrical energy which has received great attention over the last few decades. The key motivation of this technology is to power up smart, portable electronic gadgets by acquiring energy from our surroundings. These may be useful alternatives to the bulky battery, which solves several disadvantages like periodic replacement, maintenance cost, chemical waste, etc. of conventional batteries. According to the report, the efficiency of the piezoelectric nanogenerator is as high as 66% [14].

1.2. Energy Harvesting (EH)

A lot of wasted energy is present around us in the form of heat and harnessing such energy and storing by using different devices is known as energy harvesting. There are many kinds of devices like solar cells, thermoelectric generators, piezoelectric nanogenerators and so on that can capture waste energy from the surroundings and convert it into electrical power [15-17]. Solar energy comes to the earth in various forms as solar photovoltaic, solar heat, solar heating, solar thermal, and photo-catalysis and such energy can be converted into electrical power through the solar cell. Also, the heat energy can be harvested by using a thermoelectric or pyroelectric generator. However, mechanical energy harvesting by using recently invented piezoelectric nanogenerators may be another alternative to electrical energy. Extraction of wind and water energy harvesting using turbines and windmills has been already well explored. Notwithstanding, small-scale waste energy extraction is a significant approach that can power up the wireless, self-powered device. Such type of piezoelectric device captures the ambient energy and supply to the electronic device for a longer period. Piezoelectric materials can function in different kinds of ways like piezoelectric, piezo-resistive, piezo-supercapacitor, piezo-catalysis and so on which explain briefly in the next chapter.

Chapter 1

1.3. The Piezoelectric Effect

Some materials possess a specific structural conformation that causes the development of electrical potential in response to mechanical stimuli applied to them; these such materials are known as piezoelectric materials. In piezoelectric materials, the molecular dipole has been formed when the actual structure of the materials is deformed. Basically, the positive and negative charge centers of the unit cells of the materials have been shifted under mechanical strain that causes an external electric field [18]. Reversibility is the unique feature of piezoelectric materials. The direct piezoelectric effect exhibits an electric response under mechanical stress, while the reverse piezoelectric effect shows mechanical deformation under an applied electric field. Many applications have been demonstrated by using the direct and indirect piezoelectric effects. The piezoelectric Nanogenerator is feasible in different sensors, powered-up small electronics, IoT technology, etc. Several industrial and scientific instruments like AFM, STM, etc. are established based on the piezoelectric effect [19]. Piezoelectric materials are used in some daily-used appliances such as cigarette lighters [20].

1.3.1. Brief History of Piezoelectricity

The word "Piezoelectric" originated from the Greek word "piezein" which means "to press tightly". It is an electrochemical interaction between mechanical domains to electrical domains. In 1880, Pierre and Jacques Curie brothers were first ever exposed to the direct piezoelectric effect [21]. At first, they revealed the direct piezoelectric behaviour of Quartz and Rochelle salt crystal and at that time, the inverse piezoelectric effect was unexplored. The inverse piezoelectric effect was realised mathematically by Lippmann in 1881 and in same year, Curie established the inverse piezoelectric effect experimentally [22]. The Curie brothers also show the piezoelectric effect of tourmaline, quartz, topaz, cane sugar, and Rochelle salt crystals. In 1910 Woldemar Voigt published a book on the theoretical study of the elastic behaviour of crystals, where he described the characteristics of piezoelectric crystals using tensor analysis

[23]. During World War I, France's scientist Paul Langevelt and his co-researchers invented sonar using quartz crystal in 1917, which is the first practical implication of the piezoelectric property of materials [24]. Over the next few years, researchers and scientists established a number of piezoelectric materials and some new applications have been demonstrated. During World War II, worldwide some groups of researchers are developing a few piezoelectric materials like barium titanate and lead zirconate titanate materials which possess higher piezoelectric constants than natural ones. The aforementioned materials have some specific characteristics property that is efficient for practical device application. In 2006, Professor Z. L. Wang first introduced the concept of self-powering consequently the invention of piezoelectric nanogenerators (PENGs) by utilizing the piezoelectric effect of nanowires [25]. This study becomes a milestone for self-powered device applications. Mechanical energy extraction from our living environment and converting electrical energy be a worthy approach to meet our energy needs.

1.3.2. Theory of Piezoelectric Nanogenerators from Maxwell's Equations

In In order to explain the behaviour of the piezoelectric nanogenerator theoretically, the fundamental Maxwell equation in electromagnetism [26],

Gauss's theorem:

$$\nabla . \boldsymbol{E} = \frac{\rho_f}{g_0} \tag{1.1}$$

Gauss's law for magnetism:

$$\nabla . \mathbf{B} = 0 \tag{1.2}$$

Faraday's law:

$$\nabla \times \boldsymbol{E} = \frac{\partial \boldsymbol{B}}{\partial t} \tag{1.3}$$

Chapter 1

Ampere's circuital law with Maxwell's correction [27]:

$$\nabla \times \boldsymbol{B} = \mu_0 \left(\boldsymbol{J}_f + \epsilon_0 \frac{\partial \boldsymbol{E}}{\partial t} \right) \tag{1.4}$$

Where E is the applied electric field; B is the magnetic field; ρ_f denotes the free electric charge density; J_f refers to the free electric current density.

The displacement field, D is given by,

$$\boldsymbol{D} = \epsilon_0 \boldsymbol{E} + \boldsymbol{P} \tag{1.5}$$

Where $\boldsymbol{P}$ is the polarisation field.

Also in an isotropic medium, $\boldsymbol{D} = \epsilon \boldsymbol{E}$

ϵ denotes the permittivity of the medium.

The second term of equation (1.4) is known as displacement current which arises due to the change of electric field with time.

The displacement current is given by [28],

$$\boldsymbol{J}_D = \epsilon_0 \frac{\partial \boldsymbol{E}}{\partial t} \tag{1.6}$$

In 2006, professor Z. L. Wang introduce an extra term, Ps in equation (1.5); Ps is the polarization caused by the electrostatic surface charge due to mechanical response on the medium which is different from polarization (P) of the medium under the external electric field [29].

So equation (1.5) becomes, $\boldsymbol{D} = \epsilon_0 \boldsymbol{E} + \boldsymbol{P} + \boldsymbol{P}_s$ $\tag{1.7}$

If the force is applied along the z-axis then polarisation occurred along the z-axis. So we can write, $\boldsymbol{P}_s = \boldsymbol{P}_z = \sigma_p(z)$.

Thereafter, the displacement current density due to stress-induced polarisation, $\boldsymbol{P}_z$.

$$J_P = \frac{\partial P_Z}{\partial t} = \frac{\partial \sigma_p(z)}{\partial t} \tag{1.8}$$

The equation (1.8) means that the current arises owing to a change of stress-induced polarisation with time.

Also, the magnitude of the open-circuit voltage of the piezoelectric nanogenerator has been demonstrated in the equation below;

$$V_{OC} = \frac{Z\sigma_P}{g} \tag{1.9}$$

Z is the thickness of the piezoelectric materials.

1.3.3. Working Principle of Piezoelectric Nanogenerator

The piezoelectricity of solid materials highly depends on the polarizability of the molecular dipoles or ions in crystal lattice sites with asymmetrically distributed charge environments. The net dipole moment of the crystal can be evaluated by vectorially summing up the dipole moments per volume of the unit cell [30]. The dipoles are close to one another and are likely to be lined up in Weiss domains that are commonly oriented randomly. The orientation of the dipole will change when mechanical pressure is applied and tends to line up along the direction depending on the direction of stress [31]. The piezoelectric nanogenerator has been fabricated by sandwiching the piezoelectric material between two electrodes. In normal conditions, the material is in a balanced condition, i.e., the net dipole moment is zero. When the piezoelectric nanogenerator has been subjected to mechanical stress then the atomic dipoles form or orient themselves along the direction of the mechanical force. The orientation of the dipole possesses an internal electric field inside the piezoelectric materials. This field induces the opposite charge on both electrodes and a potential difference has been created. Due to the potential difference, an electric current is flowing through the external circuit. Wherein after the release, the electric field in the piezoelectric materials is disappeared as a result a current flows in the

reverse direction. Overall, an AC flows in a complete pressing and releasing cycle. The

Working mechanism of the piezoelectric nanogenerator has been demonstrated in figure 1.5.

The stress-induced polarisation of piezoelectric materials is mainly dependent on the

piezoelectric coefficients of the materials, which will discuss in the next section.
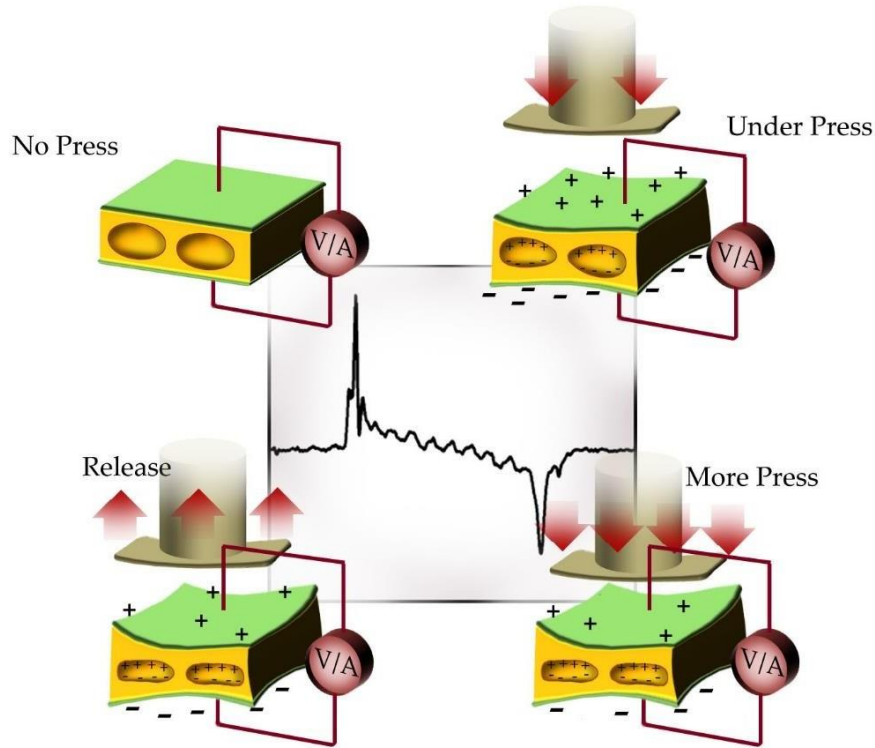
Figure 1.5: Working principle of piezoelectric nanogenerator.

1.4.   Piezoelectric Materials

Piezoelectric materials are a special type of material that develops a charge on their surface under

mechanical stress. Piezoelectric materials possess a non-centrosymmetric crystal structure that can

produce a surface charge when exposed to dimension change under mechanical stress, obviously due

to dislocation between the positive and negative charge centers of the materials [32]. There are several

kinds of known piezoelectric materials; among them, are naturally created and some are manmade.

Basically, man-made piezoelectrics like piezo-ceramics, piezo-perovskite, etc. show more strong

piezoelectric character than natural ones. The piezoelectric nature of the materials can be demonstrated

mainly by the piezoelectric coefficients, d_{33} and d_{31}. In d_{33} mode, the potential developed in materials

along the direction of applied strain while in d_{31} mode the potential developed along the perpendicular

to the applied strain. Generally, the d_{33} value is greater than that of the d_{31} value [33].

1.4.1. Naturally Occurring Piezoelectric Materials

Natural single-crystal Quartz is one of the first discovered natural piezoelectric materials. Also, several naturally developed piezoelectric crystals such as Cane sugar, Tourmaline, Rochelle salt, Topaz, etc. are already well established [34]. Moreover, some biological materials like bone, DNA, Enamel, Dentin, and many more materials show the piezoelectric effect [35].

- **Quartz:** Quartz crystal is the continuous framework of SiO_2 which exhibits the piezoelectric property with a piezoelectric coefficient (d_{33}) of ~3 pC/N. This time, a very popular application of quartz is in a crystal oscillator. Moreover, quartz is also used in quartz clocks and many other applications.

- **Sugarcane:** Sugar Cane is a bio-composite, which composed of strontium titanate ($SrTiO_3$).

- **Rochelle salt:** The chemical name of Rochelle salt is known as Potassium sodium tartrate tetrahydrate, which is a double salt of tartaric acid. Sir David Brewster first time shows the piezoelectric effects in Rochelle salts in 1824. Various electronic appliances like speakers, microphones, etc. were invented depending on the piezoelectric effect of Rochelle salt.

- **Topaz:** The general chemical formula of Topaz is $Al_2SiO_4(F,OH)_2$ which exhibits an orthorhombic crystal structure with a Pbnm space group.

- **Bio-piezoelectric materials:** Bone has piezoelectric properties because of the highly oriented and patterned structure of collagen, which can respond to mechanical stress. Also, elements that exist in our teeth like enamel, dentin, etc. behave as piezoelectric material. Due to the presence of hydroxyapatite in enamel and dentin, these materials can show the piezoelectric effect. The piezoelectricity of hydroxyapatite in enamel is lower than that of dentin. The d_{33} value of dentin is approximately 0.003 pC/N.

1.4.2. Ceramic and perovskite piezoelectric materials

Piezo ceramics are a special kind of piezoelectric material that exhibits ferroelectric characteristics with a polycrystalline framework (perovskite, tetragonal/rhombohedral crystals). These types of materials show simple cubic structural symmetry when the temperature is above the Curie temperature. Because

of the cubic symmetry, the centers of positive and negative charges have coincided, i.e., no dipoles have appeared in this condition. But below the Curie temperature, the cubic structure has not been maintained as a result, the charge centers no longer coincide, resulting in arising electric dipoles. After that, Weiss domains are formed through the realignment of the neighbouring dipoles. Moreover, the piezo ceramics show the piezoelectric nature below the Curie temperature. There are several piezo ceramics, such as zinc oxide (ZnO), lead zirconate titanate (PZT), barium titanate ($BaTiO_3$), lead titanate ($PbTiO_3$), potassium niobate ($KNbO_3$), lithium niobate ($LiNbO_3$), lithium titanate ($LiTaO_3$), sodium tungstate (Na_2WO_3), etc. well established in this field.

- **Zinc Oxide (ZnO):** ZnO was one of the most popular piezoelectric materials in the early days in this field. Hexagonal wurtzite and cubic zincblende structures are the main two forms of ZnO. The wurtzite structure is more stable than others in ambient conditions. Both structures have no inversion symmetry, which makes them piezoelectric. ZnO shows the ability to create self-powered systems. The hexagonal crystal structure has been demonstrated in figure 1.6. The d_{33} value of ZnO is 3.62 ± 0.5 pC/N. The lattice constants of hexagonal ZnO are a = 3.25 Å and c = 5.2 Å and the c/a ratio is closely 1.60 which is very near to the ideal value of 1.633.
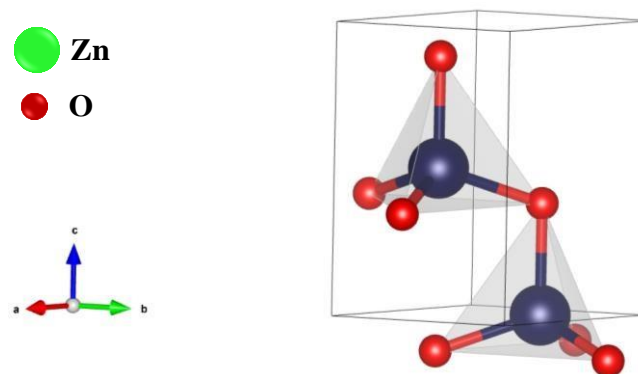
Figure 1.6: Crystal structure ZnO.

- **Lead Zirconate Titanate (PZT):** PZT is the most widely used inorganic perovskite piezoelectric compound that is used in electrochemical applications. The chemical name of PZT is Lead Zirconate Titanate, and the chemical formula is written as $Pb[Zr_xTi_{1-x}]O_3$ ($0 \leq x \leq 1$). Under the mechanical stimuli, The PZT compound creates an electric field due to the piezoelectric effect. Among the other piezoelectric materials, PZT shows a superior piezoelectric effect with greater sensitivity and a high piezoelectric coefficient (d_{33}) of ~245 pN/C. It is used in many devices in our

daily life such as ultrasonic transducers and piezoelectric nanogenerators are also used in different scientific instruments like STM, PFM, and so on. Figure 1.7 shows the crystal structure of the PZT.
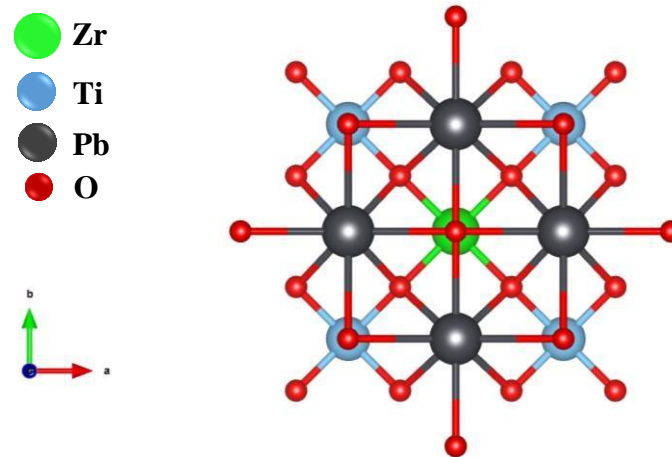
Figure 1.7: Crystal structure PZT.

- **Barium Titanate ($BaTiO_3$):** PZT carries a high piezoelectric coefficient but the presence of lead makes it toxic, which has a harmful effect on the environment. In this context, barium titanate was the first ever discovered polycrystalline ceramic material that exhibited piezoelectricity. Barium titanate possesses a cubic perovskite structure that crystallizes in the cubic $P\bar{m}3m$ space group as presented in figure 1.8. The piezoelectric coefficient of $BaTiO_3$ is approximately 500 pC/N.
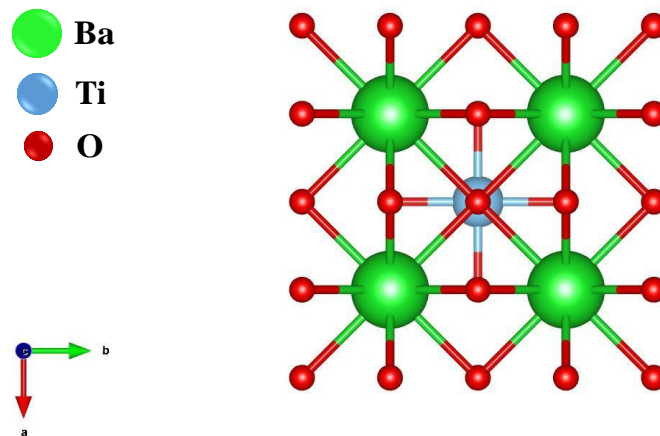
Figure 1.8: Crystal structure $BaTiO_3$.

- **Lead Titanate ($PbTiO_3$):** Lead titanate ($PbTiO_3$) is a lead-based inorganic perovskite compound. Technologically, it is a piezoelectric material that shows a d_{33} value of 110 pC/N. $PbTiO_3$ is an end member of the PZT system. The structural information of the Lead titanate is described in figure 1.9.
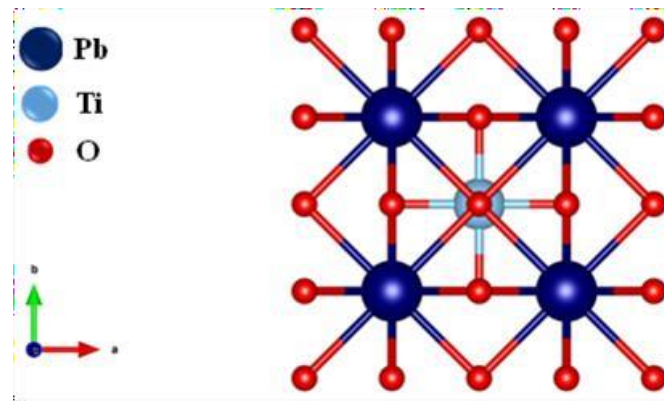
Figure 1.9: Crystal structure PbTiO₃.

- **Potassium Niobate (KNbO₃):** Potassium niobate (KNbO₃) is an inorganic lead-free perovskite compound that shows a piezoelectric effect. KNbO₃ belongs to the Amm2 space group in the orthorhombic system, as presented in figure 1.10.
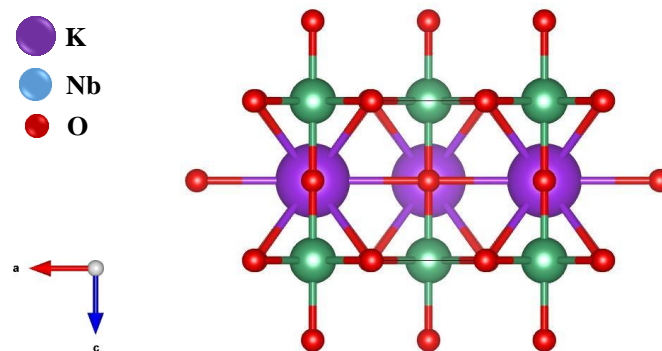
Figure 1.10: Crystal structure KNbO₃.

- **Lithium Niobate (LiNbO₃):** Lithium niobate is a man-made salt of niobium, lithium. Lithium niobate belongs to the trigonal R3c space group in the trigonal crystal system, as presented in figure 1.11. Inversion symmetry doesn't exist in this structure which makes it piezoelectric.
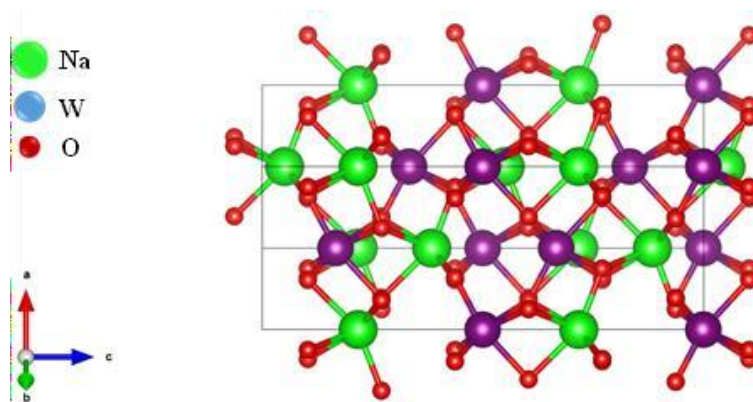
Figure 1.11: Crystal structure LiNbO₃.

- **Sodium Tungstate (Na₂WO₄):** Sodium tungstate is an inorganic compound that shows the piezoelectric effect. Na_2WO_4 crystallizes in the cubic $F\overline{d}3m$ space group and the crystal structure is presented in figure 1.12.
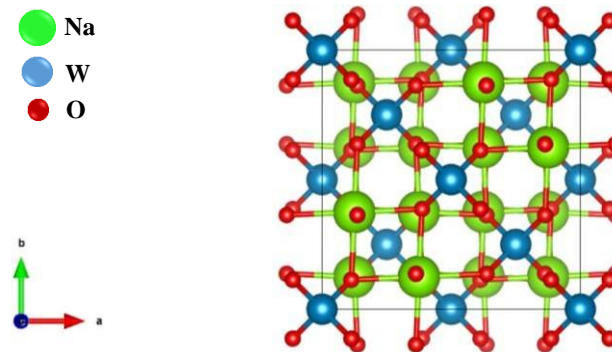
Figure 1.12: Crystal structure Na₂WO₄.

1.4.3. Piezoelectric Polymers

Over the decades, polymeric piezoelectric materials have become a promising research interest for their flexibility, durability, lightweight and excellent potential in the application of energy storage units. In comparison, perovskite piezo ceramics are brittle which limits their application area. The piezoelectricity in the polymer structure arises from the molecular dipoles present in the polymer chain and under mechanical stress, the molecular dipoles reorient themselves along the direction of stress. The piezo-polymers possess a moderate piezoelectric coefficient value of 20-30 pC/N [36]. However, the higher piezoelectric stress constants (g_{31}) of the piezoelectric polymers make them better in sensor application than other piezoelectric materials [37]. Also, polymers typically have a much higher dielectric breakdown and higher working electric field strengths, so they can endure high working electric fields than piezo-ceramics. Some piezo-polymers like poly (vinylidene fluoride) PVDF, PVDF-TrFE, PVDF-TFE, PVDF-HFP, poly (L-lactic acid) PLLA, polyimide, Liquid-crystalline, polyureas, etc. are meanwhile well established in this field. For a semi-crystalline polymer to be piezoelectric, it must have a polar crystalline phase. In a semi-crystalline polymer, crystallites exist within the amorphous region. The mechanical properties of the polymer are determined by the glass transition temperature

that depends on the amorphous region, whereas the melting temperature (i.e., the maximum used temperature) has been dependent on the crystalline region of the polymer. The preparation method of such polymers has a significant role in the degree of crystallinity of the polymer. A number of different phases exist in most of the semi-crystalline polymers, among them some of which may be shown polar character. In this context, it is necessary to transform the non-polar phase into a polar one. Thereafter, there are several processes such as mechanical stretching, thermal annealing, electric poling, electrospinning, filler insertion, etc. are the conventional method for phase transformation [37-41].

1.4.3.1.   Polyvinylidene Fluoride (PVDF)

The piezoelectricity in PVDF was first observed in 1969, and after that, the interest in these materials has been growing rapidly [42]. A thin film of PVDF polymer possesses a very high piezoelectric coefficient (d_{33}) of 6-7 pCN^{-1} that is almost ten times greater than any other polymer [43]. The electromechanical response of the PVDF polymer has arisen mainly due to the orientation of the hydrogen and fluorine atoms in the polymer chain. Moreover, the pristine PVDF exhibits a relative dielectric permittivity of about 17 much higher than most piezo-polymers. The aforesaid property of this polymer makes it interesting for device implementation using PVDF owing to the signal-to-noise ratio being very low for the materials with higher dielectric materials. The glass transition temperature of amorphous PVDF is -35ºC which is well below the room temperature and the material shows a quite flexible character at room temperature. Depending on the synthesis procedure the PVDF, amount of crystallinity can be enhanced up to 90%. PVDF typically possesses four crystal phases' viz. α, β, γ and δ. The α phase is thermally stable and exhibits the TGTG conformation of the polymer chain that makes it nonpolar. The β-PVDF shows piezoelectric nature due to its all-trans (TTTT) chain conformation. The γ phase shows a quite polar character due to its semi-crystalline chain

conformation [44]. In β phase, a polar monomer unit (—CH$_2$—CF$_2$—) perpendicular to the chain axis is repeated in the PVDF matrix to form a linear fluorinated hydrocarbon which possesses a high dipole moment of 7×10^{-30} C m [45]. Pristine PVDF is mostly composed of α phases and after the poling, the molecular dipoles are rotated to form a crystalline structure. Nowadays, some researchers and scientists have established the polarization stability of PVDF and its copolymers that are related to Colombian interactions between the surface charge of some filler materials and oriented molecular dipoles in the crystals. Due to occurring such type of interaction the molecular dipoles are trapped as a result the orientation of the dipoles is locked which stabilizes crystalline phases. Moreover, PVDF and its copolymers are the established piezo-polymers and their electromechanical properties have been studied widely.

1.5. Measurement of Some Electromechanical Coefficients

Firstly, the piezoelectric constitutive relationships to describe the piezoelectric behaviour of the materials from thermodynamic principles have been derived. A tensor notation has been manifested to recognize the coupling among the different parameters through the electrical and mechanical coefficients. Moreover, the subscript "1" denotes the direction of applied stress while "2" denotes the polarisation direction (which is perpendicular to the plane of the film). Thereafter "2" describe the direction orthogonal to both "1" and "3". The subscripts "4", "5" and "6" is the direction of the shear plane which are perpendicular to the "1", "2" and "3" respectively [46].

The piezoelectric constitutive equations can be written in the form of Einstein indicial notation [47, 48],

$$\sigma_{ij} = C_{ijmn}{}^{E}\, e_{mn} - e_{ijm}\, E_m \tag{1.1}$$

$$D_j = e_{imn}\, \varepsilon_{mn} + \kappa_{im}{}^{\varepsilon}\, E_m \tag{1.2}$$

Chapter 1

Where the independent variables electric field and elastic strain are denoted as E_m, and ε_{mn} respectively. The dependent variables, electric displacement is written as D_j, and stress is written as σ_{ij}. C_{ijmn}, κ_{im}, and e_{ijm} are the elastic moduli, the dielectric constant and the piezoelectric stress coefficient respectively. The superscript notation E, ε, and σ indicate the measurement in constant electric, strain, and stress fields, respectively and the subscript i, j, m, and n represent the spatial indices. Equation (1.1) describes the direct piezoelectric effect whereas equation (1.2) describes the reverse piezoelectric effect. Moreover, the electric field (E_i), polarization (P_i) and displacement vectors (D_i) are related by the relation below.

$$D_i = \varepsilon_0 E_i + P_i \tag{1.3}$$

Also, equations (1.1) & (1.2) can be written in the forms,

$$\varepsilon_{ij} = S_{ijmn}{}^E \varepsilon_{mn} + d_{mij} E_m \tag{1.4}$$

$$D_j = d_{imn} \sigma_{mn} + \kappa_{im}{}^\sigma E_m \tag{1.5}$$

Where, S_{ijmn}, and d_{mij} represent the compliance moduli and piezoelectric strain coefficient respectively.

1.5.1. Dielectric Coefficient (κ_{ij})

The dielectric coefficient κ_{ij} conveys the electric displacement along the direction of i-axis due to the applied electric field along the j-axis. In this context, it should be noted that, if the field is applied in the j-axis then the electric displacement has occurred only in that direction for maximum piezoelectric materials. The relative dielectric constant is described as the ratio of the permittivity of the material to the electric permittivity of free space.

1.5.2. Piezoelectric Strain Coefficient (d_{ij})

Herein, "i" represents the polarization direction (3 or z direction) and "j" (1 or x-direction) direction represents the direction of applied stress. Moreover, the 1-direction is mutually perpendicular to the 3-direction (polarization direction). In general, the mechanical stress applied to the piezoelectric materials is either along the 3-direction or 1-direction but polarization has occurred along the thickness of the film i.e. 3-direction. Based on this mechanism, piezoelectric nanogenerators are working in two operating modes viz. 31 modes (bender mode) and 33 modes (axial mode). A schematic representation of the operation of a piezoelectric nanogenerator in two different modes is displayed in figure 1.5. It should be noted that the value of piezoelectric constant d_{31} is negative (that is a serious departure of PVDF from other piezoelectric materials) which is due to the generation of negative strain along the 1-direction under the application of a positive electric field [49, 50].

1.5.3. Piezoelectric Voltage Coefficient (g_{ij})

The piezoelectric strain coefficient d_{ij} is the important figure of merit of the performance of the device while the piezoelectric voltage coefficient, g_{ij} correlates to the output voltage and sensitivity of the piezoelectric materials. The g_{ij} signifies that the piezo potential developed along the i-axis when the piezoelectric materials are given pressure along the j-axis [51]. If the applied force F is in the 1-direction and the resultant voltage difference is along the 3-direction, then it is written as;

$$V = g_{31}F/d \qquad (1.6)$$

Where d denotes the thickness of the piezoelectric materials.

1.5.4. Piezoelectric Coupling Coefficient (k_{ij})

The efficiency of the piezoelectric materials has been realized by the piezoelectric coupling coefficient. Besides, the piezoelectric coupling coefficient (k_{ij}) described the mechanical-to-

electrical energy conversion ability of the piezoelectric materials. The subscript "i" index denotes the electrodes are perpendicular to the i-direction and mechanical stress is applied in the j-direction. For instance, if the piezoelectric material is mechanical stretching along 1-direction and development piezo-potential in 3-direction, then the ratio between transformed mechanical energy to the electrical energy is $(k_{13})^2$

$$k_{13} = [W_{Elec}/W_{mech}]^{1/2}. \tag{1.7}$$

Also, the piezoelectric coupling coefficient can be written in terms of other piezoelectric coefficients:

$$(k_{ij})^2 = Yg_{ij}d_{ij} \tag{1.8}$$

, where Y represents the young modulus of the piezoelectric materials.

1.6. Aim and Structure of the Thesis

The main aim of the thesis is to investigate the effect of filler inserted in the PVDF matrix and characterize the properties of nanocomposites and explore the performance of piezoelectric nanogenerators using the synthesized composites. This thesis reports on the multifunctional use of the PVDF composite and piezoelectric nanogenerator in energy harvesting applications. Piezoelectric materials are a class of materials that produce electric current under mechanical stimuli. In 1880, French scientists Jacques and Pierre Curie established the piezoelectric property of materials for the first time. All crystalline materials belong to one of the 32 possible crystallographic point groups and among them, 20 point groups possess a non-centrosymmetric structure which shows piezoelectric nature. The structure of several piezoelectric materials was explained in this chapter previously. Also, the chain conformation of α, β and γ phases of PVDF have been explained in chapter 1. Moreover, pristine PVDF is mainly composed of a nonpolar α phase. In this regard, it is important to transform the chain conformation and convert

it into β-PVDF. There are some methods to enhance the electroactive phase of PVDF polymer. Filler insertion into the PVDF matrix is an effective method to enhance the crystallinity of the PVDF matrix. The formation of PVDF-based nanocomposite and its applications have been explained in chapter 2.

Self-powered and flexible piezoelectric nanogenerators (PNGs) have become an easily accessible and sustainable energy alternative owing to facile assembly and conformal structure. Perovskite-embedded PVDF matrix-based nanogenerators have been considered efficient technologies for energy harvesting applications. Chapter 5 also provides a PVDF composite-based piezoelectric nanogenerator and explores the output performance of the device under different periodic forces and different biomechanical movements. Firstly, the different amounts of $CsPbBr_3$ are inserted in the PVDF matrix to prepare the nanocomposite. After that, the crystallinity of all composites has been studied to select a superior composite. The optimum composite exhibits a high dielectric constant and electroactive phase, which is confirmed by FTIR and XRD spectroscopy. The optimum device, demonstrated by using the best composite performed better among the other devices. In addition, the composites exhibited a strong photoactive character and the optimum device was working as a photodetector. However, most of the self-powered devices based on this PVDF have several advantages for their high flexibility, durability and non-reactive nature. Chapter 6 introduces a self-powered posture sensor based on $CsPbCl_3$/PVDF composite. The superior $CsPbCl_3$/PVDF composite was synthesized by controlling the $CsPbCl_3$ Nano-cube in the PVDF matrix. Afterthat, the electrical properties of the polymer composites has been studied. Therefore, the performance of the device under different bending states of the piezoelectric nanogenerator has been tested. Flexible electronic devices have several advantages, such as foldability and flexibility better than conventional consolidated counterparts. The self-powered piezo-supercapacitor is a promising technology for the next generation of smart portable storage devices. Chapter 7

introduces the self-charging supercapacitor based on CuCoNiO$_4$/PVDF piezo-separator. The self-charging behaviour of the device under different bending was examined and recorded. Moreover, chapter 8 introduces a hybrid piezoelectric nanogenerator based on the combined piezoelectric effects of ZnO and PVDF. The output performance of the hybrid nanogenerator has been examined under different pressures.

1.7.   References

[1] P. Moodley, and C. Trois, Sustainable biofuels, Academic Press, (2021), 21-42.

[2] J. Hansen, M. Sato, R. Ruedy, K. Lo, D.W. Lea, M. Medina-Elizade, Proceedings of the National Academy of Sciences, (2006) 103(39), 14288-14293.

[3] A. V. Herzog, T. E. Lipman, D. M. Kammen, Forerunner Volume-'Perspectives and overview of life support systems and sustainable development, (2001) 76.

[4] C. Y. Lee, M. K. Lee, S. Yoo, Energy, 128 (2017) 284-290.

[5] R. Hafezi, M. Alipour, Affordable and clean energy, Springer (2021), 1085-1099.

[6] C. Wu, A. C. Wang, W. Ding, H. Guo, Z. L. Wang, Advanced Energy Materials, 9 (2019) 1802906.

[7] S. Niu, Y. S. Zhou, S. Wang, Y. Liu, L. Lin, Y. Bando, Z.L. Wang, Nano Energy, 8 (2014) 150-156.

[8] S. Y. Chung, S. Kim, J. H. Lee, K. Kim, S.W. Kim, C. Y. Kang, S. J. Yoon, Y. S. Kim, Advanced Materials, 24 (2012) 6022-6027.

[9] Y.-F. Lin, J. Song, Y. Ding, S.-Y. Lu, Z.L. Wang, Applied Physics Letters, 92(2) (2008) 022105.

[10] Y. Matsuo, A. Yanagisawa, Y. Yamashita, Energy Strategy Reviews, 2(1) (2013) 79-91.

[11] M. Majid, Energy, 10(1) (2020) 1-36.

[12] W. Li, Y. Duan, J. Rabaey, IEEE Transactions on Biomedical Circuits and Systems, 13(2) (2019) 435-443.

[13] S. K. Jain, G. D. Agrawal, R. Misra, P. Verma, S. Rathore, D. K. Jamuwa, Journal of Solar Energy Engineering, 141(6) (2019) 061008.

[14] S. K. Karan, S. Maiti, O. Kwon, S. Paria, A. Maitra, S. K. Si, Y. Kim, J. K. Kim, B. B. Khatua, Nano Energy, 49 (2018) 655-666.

[15] W. He, G. Zhang, X. Zhang, J. Ji, G. Li, X. Zhao, Applied Energy, 143 (2015) 1-25.

[16] H. Jouhara, A. Żabnieńska-Góra, N. Khordehgah, Q. Doraghi, L. Ahmad, L. Norman, B. Axcell, L. Wrobel, S. Dai, International Journal of Thermofluids, 9 (2021) 100063.

[17] R. Zhu, W. Zhang, R. Yang, Science of Advanced Materials, 4 (2012) 798-804.

[18] L. Kou, C. Tang, Y. Zhang, T. Heine, C. Chen, T. Frauenheim, The journal of physical chemistry letters, 3 (2012) 2934-2941.

[19] B. Bhushan, O. Marti, Nanotribology and Nanomechanics, (2017), 33-93.

[20] R. Bhavsar, N. Y. Vaidya, P. Ganguly, A. Humphreys, A. Robisson, H. Tu, N. Wicks, G.H. McKinley, F. Pauchet, Oilfield review, 20 (2008) 32-41.

[21] G.G. Guilbault, J.M. Jordan, E. Scheide, Analytical Chemistry, (1988) 1-28.

[22] S. Katzir, Springer, (2006) 15-64.

[23] J. Tichý, J. Erhart, E. Kittinger, J. Prívratská, Springer Science & Business Media, 2010.

[24] S. Katzir, Notes and Records of the Royal Society, 66(2), 141-157.

[25] Z. L. Wang, Advanced Functional Materials, 18(22) (2008) 3553-3567.

[26] Z. L. Wang, Materials Today, 20(2) (2017) 74-82.

[27] J. C. Maxwell, Edinburgh, D. P. Magazine, Science, 21 (1861) 161-175.

[28] Z. L. Wang, Materials Today, 20 (2017) 74-82.

[29] Z. L. Wang, Nano Energy, 68 (2020) 104272.

[30] M. J. Birkholz, Archives of environmental contamination and toxicology, 96 (1995) 333-340.

[31] M. Broadhurst, G. Davis, Ferroelectrics, 60(1) (1984) 3-13.

[32] N. Sharma, R. Maranganti, M. Sharma, Solids, 55 (2007) 2328-2350.

[33] F. Xu, F. Chu, Trolier-McKinstry, Journal of applied physics, 86(1) (1999) 588-594.

[34] S. S. Pradhan, R. Ramadurai, IIT HYDERABAD, 2021.

[35] V. S. Bystrov, I. K. Bdikin, A. Heredia, R. C. Pullar, E. D. Mishina, A. S. Sigov, A. L. Kholkin, Piezoelectric nanomaterials for biomedical applications, (2012) 187-211.

[36] W. Heywang, K. Lubitz, W. Wersing, Springer Science & Business Media, (2008) Vol. 114.

[37] H. Li, Z.D. Deng, T. J. Carlson, Sensor Letters, 10 (2012) 679-697.

[38] P. Xu, W. Fu, Y. Hu, Y. Ding, Technology, 158 (2018) 1-8.

[39] C. Lee, Tarbutton, Structures, 23 (2014) 095044.

[40] E. S. Cozza, O. Monticelli, E. Marsano, Polymer International, 62(1), (2013) 41-48.

[41] M. Tayyab, J. Wang, J. Wang, M. Maksutoglu, H. Yu, G. Sun, F. Yildiz, M. Eginligil, W. Huang, 77 (2020) 105178.

[42] E. Fukada, ferroelectrics, f. control, 47 (2000) 1277-1290.

[43] I. Chinya, A. Sasmal, S. Sen, Compounds, 815 (2020) 152312.

[44] S. Mondal, T. Paul, S. Maiti, B. K. Das, K. K. Chattopadhyay, Nano Energy, 74 (2020) 104870.

[45] S. Mondal, S. Thakur, S. Maiti, S. Bhattacharjee, and K. K. Chattopadhyay, ACS Appl. Mater. Interfaces (2023).

[46] S. R. Moheimani, A. J. Fleming, London: Springer, (2006) Vol. 1.

[47] T. R. Meeker, 1996. Publication and proposed revision of ANSI/IEEE standard 176-1987. IEEE Transactions on Ultrasonics Ferroelectrics and Frequency Control, 43(5), 717-772.

[48] C. C. Fuller, S. J. Elliott, P. A. Nelson, Academic press, 1996.

[49] I. Katsouras, K. Asadi, M. Li, T. B. Van Driel, K. S. Kjaer, D. Zhao, T. Lenz, Y. Gu, P. W. Blom, D. J. Damjanovic, Nature materials, 15(1) (2016) 78-84.

[50] M. Han, Y. C. Chan, W. Liu, S. Zhang, H. Zhang, The 8th annual IEEE international conference on nano/micro engineered and molecular systems, IEEE, 2013, 440-443.

[51] S. R. Moheimani, A. Fleming, London: Springer, 2006, 9-35.

CHAPTER 2

Literature Review

2.1. A Brief Discussion on Piezoelectric Nanogenerator

Nowadays, piezoelectric nanogenerators are emerging as the most promising self-powered technique due to their mechanical-to-electrical energy conversion ability [1-5]. At a very first, a piezoelectric nanogenerator (PENG) was proposed by Z. L. Wang in 2006. He invented a piezoelectric nanogenerator based on vertically aligned ZnO nanowires (NWs) [6]. An electric signal was developed when an AFM tip swept across a vertically grown ZnO NWs which mainly originated from the coupling between the semiconducting and piezoelectric properties of the ZnO NW. Immediately, after this work, extensive research work on piezoelectricity has taken place and related applications have manifested serious advancement [7-11]. In the beginning, the 1-D nanostructure of ZnO like nanorods, nanowires, nanotubes, and nanobelts was a very important semiconductor material due to their inherent physical and chemical properties [12-14]. In 2007, Z. L. Wang et al. approaches an innovative idea in small-scale mechanical energy harvesting performance of piezoelectric nanogenerators based on ZnO nanowire arrays [15]. The nanowire-based nanogenerator is performed under an ultrasonic wave, which produces an output signal. The discovery of piezoceramic $BaTiO_3$ was admirably liable for evolution in the piezoelectric field. It is noteworthy that the piezoceramics are very attractive due to their unique structure of the unit cells and high piezoelectric coefficient [16, 17]. In 2007, Min-Feng Yu et al. revealed the direct piezoelectric effect of single crystal $BaTiO_3$ nanostructure under low-frequency mechanical stress [18]. He found that the measured output voltage is directly proportional to the strain rate applied and the necessary circuit diagram has been manifested for a piezoelectric nanowire-based sensor under low-frequency operation. To enhance the application area of the perovskite-based nanogenerator it is required to design the device in a flexible substrate. For this purpose, Keon Jae Lee et al. and their co-workers have developed a flexible piezoelectric nanogenerator by depositing a thin film (300 nm) of $BaTiO_3$ by rf sputtering in the flexible substrate [19]. After that, a lot of perovskite piezo-ceramics such

as PZT, $ZnSnO_3$, $KNbO_3$, $LiNbO_3$, $PbTiO_3$, etc., are well established in this field [20-23]. Among the all discovered ceramics materials, PZT attracts the most attention due to the large piezoelectric coefficient value.

Moreover, several compositions of PZT-based piezo-ceramics have been studied and the d_{33} value varies from 300 to 1000 pC/N [24-26]. Yong Shi et al. report a piezoelectric nanogenerator based on PZT nanofiber with a length and diameter of approximately 500 nm and 60 µm [20]. In order to inhibit the PZT nanofibers from being spoiled, the PZT nanofibers were molded with a PDMS polymer that helped to extend the lifetime of the nanogenerator. The device possesses an output voltage and power under periodic mechanical stimuli of 1.63 V and 0.03 µW, respectively. Z. L. Wang et al. also demonstrate PZT nanowire arrays through the chemical epitaxial growth method [27]. The nanogenerators are constructed with a single PZT nanowires array, which produces an output voltage of nearly 0.7 V whereas the observed current density of 4 µA cm^{-2} and the power density of 2.8 mW cm^{-3}. The feasibility of such nanogenerators has been revealed in mobile powering and even daily used electronic gadgets. However, the presence of toxic lead raised concerns over the application of PZT. Again, Z. L. Wang et al. report, high-performance piezoelectric nanogenerators based on randomly oriented lead-free $KNbO_3$ nanorods of length 1 µm. The $KNbO_3$ possesses a piezoelectric coefficient of 55 pm V^{-1}. In this work, the frequency-dependent dielectric constant and dielectric loss of flexible $KNbO_3$/PDMS composite reveals 3.2 and 0.006 respectively in the frequency range of 102–105 Hz [28]. Moreover, several piezo polymers like PVDF attract much attention in this field owing to their flexibility, non-reactive nature, and high piezoelectric coefficient [29-33]. Therefore, the performance of piezoelectric nanogenerators is being investigated and the applications of the devices are advanced in different electronic devices [34-37].

2.1.1. Polymer-based Piezoelectric Nanogenerator

Piezoelectricity in Polyvinylidene difluoride or polyvinylidene fluoride (PVDF) polymer was first observed as early as 1969 [38]. This experiment reveals the piezoelectric coefficient of poled PVDF thin films is 6-7 pC/N, which is much larger than other piezoelectric polymers. Generally, piezoelectric polymers exhibit a lower piezoelectric strain constant (d_{31}) than piezoelectric ceramics, however, their piezoelectric stress constants (g_{31}) value is much higher than that of piezoelectric ceramic materials [39, 40]. Piezo-polymer material, PVDF possesses high breakdown strength, low elastic stiffness, non-reactive nature, higher operating field and flexibility, making it feasible in sensor and biomedical applications. PVDF is typically a semi-crystalline polymer that has a glass transition temperature (T_g) of −35 °C [41]. Typically, in a PVDF matrix, hydrogen and fluorine units are alternately attached to the carbon chain to form a repetitive unit cell structure ($-CH_2-CF_2-$). Depending on the chain conformation linkages, PVDF displayed four different crystalline polymorphs, namely α, β, γ and δ [42-45]. Henceforth, the four phases have different orientations in molecular chain conformation [46, 47]. Normally, the PVDF matrix is mostly composed of monoclinic α-PVDF [48-50]. The α phase presents trans-gauche-trans-gauche (TGTG) chain conformation that makes it non-polar. The inherent properties of the β−PVDF arise from the all-trans (TTTT) chain conformation that exhibits spontaneous polarization. The orthorhombic β-PVDF is an ongoing pursuit due to its outstanding ferroelectric and piezoelectric properties [51, 52]. The dipole moment per unit cell of β the phase of PVDF polymer is 7×10^{-30} C m, which is much better than other phases [53-55]. This is the most desired phase, which could be extensively utilised in energy storage applications, sensors, biomedical applications, IoT technology, etc. Another important phase is γ which shows the semi-crystalline nature because of its T^3GT^3G conformation. Figure 2 presents the structure of the PVDF chain of all phases. In recent years, PVDF and its co-polymer becomes a prospective polymer for their high ferroelectric property, flexibility, nontoxicity, long-term stability, non-reactivity, etc. Scientists and researchers are

● F   ● C   ○ H

(a)

(b)

(c)
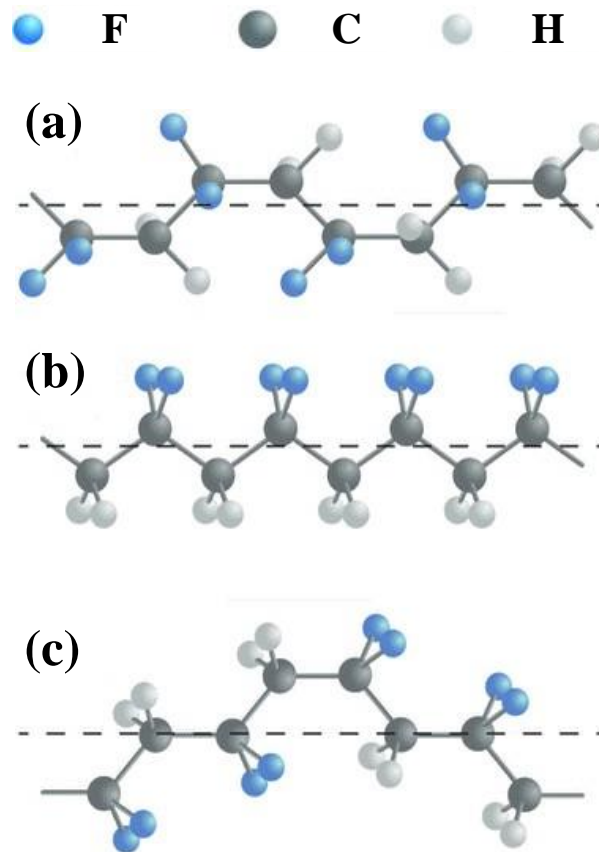
Figure 2: (a) α, (b) β and (c) γ phase structure of PVDF polymer.

introduced several approaches to enhance the electroactive β phase. In 2009, Lin et al. demonstrated a direct-write piezoelectric nanogenerator based on PVDF using electrospinning [56]. This experiment achieved a constant and repeated output voltage of 8.5 mV. Also, an output power of 7.2 pW is generated when an external strain of 0.092% is applied to a single electrospun PVDF nanofiber. After a few years, a systematic experiment has been performed by McAlpine et al to show the performance of a PVDF-based piezoelectric nanogenerator [57]. They demonstrate a wearable and implantable device that could harvest mechanical energy from the human body. Thereafter, a lot of research has been done in this field and the output performance of the PVDF-based nanogenerators has been improved year by year. The most recent, the performance of a PVDF/BiCl$_3$/ZnO nanocomposite-based nanogenerator has been investigated by Yuhei Yeung et al [58]. They found that the longitudinal piezoelectric coefficient (d$_{33}$) of the composite is up to 3.8 pC/N and composite-based PENG delivered an

open-circuit voltage (V_{OC}) of 12 V. Also, some copolymers of PVDF such as PVDF-TrFE, PVDF-TFE, and PVDF-HFP are shown a piezoelectric effect [2, 59, 60]. Copolymers can adopt an all-trans crystalline phase structure directly, which is similar to the β phase of PVDF [61, 62]. Addressing this opportunity, Wu et al develop a flexible piezoelectric nanogenerator using spin-coated PVDF-TrFE thin film [63]. The proposed piezoelectric nanogenerator displayed an open-circuit voltage of about 7 V and a short-circuit current of 58 nA with a current density of 0.56 $\mu A/cm^2$. In 2014, Schmeißer et al reported the performance of a silver nanoparticle doped poly (vinylidene fluoride–hexafluoropropylene) based piezoelectric nanogenerator through the electrospinning technique [64]. The yield of the electroactive phase is increased by the insertion of silver nanoparticles in the PVDF-HFP matrix. It was found that the PNG device possesses a maximum output voltage of 3 V along with a current density of 0.9 $\mu A/cm^2$ is achieved. Recently, another experiment was performed by Kwi-II Park et al to show the enhanced piezoelectric performance of the BCTZ-incorporated PVDF (TrFE) nanofiber [65]. The generated output performance (the output voltage and current 36.5 V and 1.09 μA, respectively) was significantly high compared to the previously reported work.

Except for PVDF and its copolymer, some other polymers like polypropylene, polystyrene, poly (methyl methacrylate), polyvinyl acetate and odd-number nylons such as Nylon-11 have quite piezoelectric properties [66-70]. In 2016, Sepúlveda et al introduced polypropylene as an active piezoelectric material in a flexible, efficient, and biocompatible piezoelectric nanogenerator device [71]. They were involved finite element method (FEM) to explain mechanical to electrical energy conversion mechanism in PPFE films. They realised a self-powered flexible/foldable keyboard. Asadi et al and his co-workers show the piezoelectricity in a nylon-11 fiber [72]. It is found that the demonstrated device has the potential to energy scavenging from low-frequency mechanical vibrations.

2.2. Synthesis of PVDF Films

PVDF film can be synthesized, followed by processes like melt casting, spin coating, film casting, and solution casting. Polar solvents like dimethyl formamide (DMF), dimethyl sulfoxide (DMSO), N-methyl pyrrolidone (NMP), or dimethylacetamide (DMAc) and more volatile butanone are employed for solution-based processing. In 2006, Prevedouros et al and his coworkers used the ionic form of Fluoro surfactant perfluorononanoic acid for aqueous emulsion polymerization [73]. Most of the researchers and scientists are using DMF (or DMSO) and acetone in a 3:2 ratio to dissolve the PVDF pallets or powder and the solution is stirred at 60°C for 2 hours. Thereafter, the solution is dropped cast onto a glass slide and kept in a vacuum oven to dry the film [42, 44].

2.3. Electroactive Phase Enhancement in PVDF Films

Normally, the prepared PVDF films are composed of a typically non-piezoelectric α phase. Thereafter, to achieve a piezoelectric β phase, there are several methods such as the electro-spinning technique, mechanical stretching, electric-poling process, etc. are approaches to gaining a piezoelectric response.

2.3.1. Electro-spinning Technique

In recent times, the electrospinning technique has becomes a popular method to prepare high-polar PVDF film [74, 75]. The electrospinning technique is an electric field-driven fabrication method that is controlled by an electrohydrodynamic phenomenon. In this process, electrospun PVDF nanofibers are realised from a polymer solution. In this typical process, a high electric field is established between the needle tip of the syringe and a specific collector by employing a certain voltage. When the syringe causes the solution to flow at a fixed rate and charges accumulate at the outer surface of the solution. At a time a specific point is reached where the

surface tension of the solution is lower than the electrostatic repulsion as a result of the liquid meniscus deforming into a conically shaped (known as a Taylor cone) and deposited on the collector. Baek et al demonstrated an electrospun nanofiber mat of CNT/PVDF composite by electrospinning method at 5kV in 2003 [76]. A 50-mL syringe with an 18-gauge needle is used to electrospun the polymer solution. Moreover, they used an aluminium sheet as a collector. In 2006, Sheng et al established the PVDF nanofiber mats of PVDF solutions taken in an 8:2 (v/v) ratio of DMF and acetone at a flow rate of 0.3-mL/h, 10~20 cm capillary-collector distance and 5 kV voltage [77]. They obtained fibrous PVDF membranes of a thickness of nearly 46 μm. over the decade, many other researchers have employed this method to get high polar PVDF nanofiber.

2.3.2. Mechanical Stretching

Mechanical stretching is also one of the best approaches to improving the piezoelectric property and dielectric properties of the PVDF matrix. Mainly, stretching causes the non-polar phase to change into a highly polar crystalline phase, and the amount of this phase depends on how much stretching is done. The improvement of the piezoelectric phase fraction of PVDF composite through mechanical stretching has been demonstrated by Nayak et al [78]. This work reports that due to stretching ratio 2 the maximum β-phase content reaches about 86 % and the dielectric constant is also improved by 28.5% has been achieved in such composite polymers. In 2010, Mendez et al reported the ferroelectric switching behaviour and piezoelectric response of Poly (vinylidene fluoride, or PVDF) by drawing at stretching ratios ranging from 1 to 5 and temperatures ranging from 80 to 140°C [79]. They examined that the temperature and stretching ratio have a significant impact on the phase transition from non-ferroelectric to ferroelectric. Several research teams have successfully used mechanical stretching to investigate the PVDF matrix's phase improvement.

2.3.3. Electric-poling Process

The most reasonable and widespread technique to polarise the nanocomposite is electrical poling. Atomic dipoles align themselves along the field direction and materials change into polar forms when an electric field is applied across the piezoelectric material. In 1989, Miranda et al and his co-workers investigated the polling effect on Poly (vinylidene fluoride, or PVDF) [80]. They reported that the thermal diffusivity and the dielectric constant both displayed a monotonically increasing behaviour with the poling field.

2.3.4. Incorporation of Filler Materials

Filler incorporation in the polymer matrix is the best, most conventional, and cost-effective way to enhance the electroactive phase fraction of the PVDF matrix. Conventionally, this polling process is known as the "self-polling" method. Usually, when any nanomaterials are inserted inside the PVDF matrix as a filler then the surface charge of the filler interacts with the dipole of the PVDF chain as a result, the dipoles are oriented along a specific direction. Many researchers have employed filler inclusion techniques over the years. In 2015, Mondal et al demonstrate the Cerium Complex-PVDF Composite based self-poled piezoelectric nanogenerator [81]. This work achieved a 99% electroactive phase through the simple filler insertion method. They show notable enhancement of the output voltage (~32 V) of a nanogenerator (NG) based on a PVDF composite film achieved under simple periodic human finger tapping, while a nanogenerator base on pristine PVDF does not show such kind of results. Another experiment has been done in 2021 by Gupta et al [37]. They report a portable polyvinylidene fluoride (PVDF)-carbon nanotube (CNT) composite-based flexible piezoelectric nanogenerator that is the first of its kind to transform mechanical energy into electricity. The as-prepared device displayed outstanding performances that confirm its potential application in self-powered IoT-based nano-systems.

2.3.5. Thermal Annealing

Thermal annealing is another technique that many researchers and scientists employ to fabricate thin, uniform ferroelectric PVDF films with ordered beta crystals. The subsequent rapid thermal treatment boosted the amount of crystals in the film, as demonstrated by Park et al [82]. The film was heated rapidly at a rate of 30°C/min until it reached a temperature below the melting point of PVDF, which caused residual DMF to evaporatively flow down the film's normal. A film that has undergone fast thermal annealing reveals a more than 90% crystal content.

2.4. Applications of PVDF-based Piezoelectric Nanogenerator

The invention of the piezoelectric nanogenerator (PENG) has received a lot of attention due to its ability to use piezoelectric nanomaterials to transform minute amounts of kinetic energy from the environment into electricity. The development of PENGs has seen significant advancements up to this point. Several commercial LEDs can be directly powered by the electricity produced by the PENG in real-time. Moreover, self-powered systems can be built to attain maintenance-free and sustainable functioning by combining PENGs with useful devices. Self-powered systems have each been proven for UV sensing, ion detection, blood pressure monitoring, etc. PENGs are used in the aforementioned applications, while their output must be improved; otherwise, high precision measurements or extra energy storage units should be given.

2.4.1. Piezo-phototronics/Photodetectors

Although classic polymer materials notably PVDF and its copolymer have been used to develop photodetectors based on the piezo-photronic effect for quite some time. It is a crucial exploration of simple, low-cost device architectures, and high-performance photodetectors

using low-temperature device assembly technologies are required. In 2010, Professor Zhong Lin Wang first introduced the core idea of piezo-phototronics in semiconductors with wurtzite structures such as ZnO, GaN, and InN which provides a creative approach to adjusting optoelectronic device performance [83]. Owing to the non-central symmetric crystal structure, carrier transport properties in electrical and optoelectronic devices can be affected by the generation of a piezo potential in the crystal under an external or internal strain. It has been identified that piezo-phototronics is the three-way coupling of piezoelectric polarisation, optical excitation, and semiconductor properties. It is an efficient method for tuning and controlling carrier processes, such as generation, transport, separation, and/or combination at the metal-semiconductor contact, which enhances the performance of optoelectronic devices. Recently, several research groups have studied the piezo-phototronics effects in PVDF nanocomposite that show a good on/off photocurrent ratio with low rise and decay times. In 2018, Mandal et al reported the outstanding performance of PVDF/Methylammonium lead iodide composite-based piezoelectric nanogenerator as an energy harvester and photodetector [84]. Under the illumination of non-monochromatic light, the photosensitive capabilities of the composite are demonstrated, which also suggests the potential of their use as photodetectors. The response time is a prime parameter for photodetectors for realizing the capability of a photodetector to follow fast-changing optical signals. The fact that the rising time and fading time are about 44 and 153 ms, respectively, suggests that the photo response is rapid. In a typical piezo-phototronic device, a heavily doped Si or ITO/polyethylene terephthalate (PET) substrate is used as a substrate, while PVDF composites act as an active layer, and a pre-patterned gold/aluminium/silver electrode makes up the photodetector. In fact, some performance figures of PVDF composite-based photodetectors are on par with or even superior to those of Si photodetectors.

2.4.2. Supercapacitors

Piezoelectric nanogenerator integrated with batteries or supercapacitors becomes an emerging technology that has attracted much attention due to energy generation and storage in a single-unit cell. For instance, Sun et al. demonstrate an ultralight and flexible, self-charging power unit using all electrospun paper-based triboelectric nanogenerators as energy harvesters and all electrospun paper-based supercapacitors as storage devices [85]. Wang et al. also described a paper-based flexible solid-state piezo supercapacitor biomimetic tactile sensor with an active PVDF separator that could be self-charged only by finger tapping and could display information of both the static and the dynamic pressure by electrical signal [86]. In recent times, a noble self-charging supercapacitor has been prepared using mesoporous PVDF-LiPF$_6$ composite film as piezo-electrolyte and separator both. The all-solid-state flexible supercapacitor can directly harvest and store the energy from human body motion since it is effectively charged up by mechanical deformation (Xue et al, 2017) [87]. A flexible solid-state piezo-supercapacitor has been constructed by sandwiching the gel electrolyte between positive and negative electrodes on flexible substrates. In contrast to conventional supercapacitors with liquid electrolytes, solid-state supercapacitors with gel-type electrolytes serve as both an electrolyte and a separator. Furthermore, unlike traditional supercapacitors, solid-state capacitors eliminate the possibility of electrolyte leakage as well as the short circuit of two electrodes. In this context, a simplified and low-cost method for fabricating a flexible self-charging supercapacitor power cell for portable applications is highly desired.

2.4.3. Sensors

Smart sensing devices with high reliability and self-powering capabilities will be essential in next-generation wearable applications. Piezoelectric nanogenerator (PNG) has been deemed as one of the most efficient methods of converting mechanical energies such as wind energy, human motion, vibrations, pulse, and heartbeat into electrical energy. In this context,

piezoelectric nanogenerators attract much attention in self-powering sensors. The electrical signal from PNG has also been used to demonstrate high-performance self-powered sensing systems such as biosensors, UV sensors, humidity sensors, pressure/speed sensors, gas sensors, etc. For the first time, Xue et al. reported a room temperature processed Au-MoSe$_2$ composite ammonia (NH$_3$) sensor powered by a novel flexible PNG based on 2D semiconductor MoS$_2$ flake [88]. In 2017, Li et al. is demonstrate a flexible PNG fabricated a wearable self-powered active sensor for respiration and healthcare monitoring [89]. A self-powered flexible humidity sensor based on PVA/MXene nanocomposite and monolayer molybdenum diselenide (MoSe$_2$) piezoelectric nanogenerator was reported by Yu et al [90]. Mandal et al and his co-researchers demonstrate a self-powered pressure mapping sensor by δ-PVDF. Following that, a self-powered piezoelectric nanogenerator-based sensor demonstrating its practical technological applicability [91].

2.4.4. Piezo-catalysis

Chemical dyes found in industrial wastes have become a growing threat as a result of rapid industrialization, polluting the water supply. Among the many dyes, methylene blue (MB), rhodamine B (RhB), and crystal violet (CV) are frequently used in the textile, paper, leather, and pharmaceutical sectors. These dyes are harmful to human health since they can cause kidney failure, breathing problems, and cancer. Because of their complex structures, these synthetic dyes are highly stable and non-biodegradable. Many strategies, including activated sludge, adsorption, coagulation, and ozonation, have been used to treat dye-containing effluents. Still, the methods are expensive, slow, or ineffective for completely degrading the dyes. For efficient and complete degradation, advanced oxidation processes (AOPs) such as electrocatalysis, photocatalysis, and piezo-catalysis have been developed. In contrast, the piezo-catalysis process produces electrons and holes on the surface of the piezo-catalyst for the

dye degradation process, making it a simple, cost-effective, and highly efficient strategy for environmental remediation. Tiwari et al examine the piezo-catalytic effect of freestanding PVDF/MoS$_2$ composite film which can use otherwise wasted mechanical energy to generate useful energy and purify water [92]. Several approaches have already been demonstrated in this field by utilising the piezoelectric properties of PVDF and its co-polymer. [93-95].

2.5. References

[1] J. Sun, H. Guo, J. Ribera, C. Wu, K. Tu, M. Binelli, G. Panzarasa, F. W. Schwarze, Z.L. Wang, I. Burgert, 14 (2020) 14665-14674.

[2] S. Badatya, A. Kumar, C. Sharma, A. K. Srivastava, J. P. Chaurasia, M. K. Gupta, 290 (2021) 129493.

[3] Y. Zhang, L. Zhou, X. Gao, C. Liu, H. Chen, H. Zheng, J. Gui, C. Sun, L. Yu, S. Guo, 89 (2021) 106319.

[4] D. Zhang, D. Wang, Z. Xu, X. Zhang, Y. Yang, J. Guo, B. Zhang, W. Zhao, 427 (2021) 213597.

[5] R. Z. Auliya, P.C. Ooi, R. Sadri, N. A. Talik, Z.Y. Yau, M. Haniff, B. T. Goh, C. F. Dee, N. Aslfattahi, S. Al-Bati, 11 (2021) 1-13.

[6] Y. Hu, Z. L. Wang, Nano Energy, 14 (2015) 3-14.

[7] Y. F. Lin, J. Song, Y. Ding, S. Y. Lu, Z. L. Wang, 92 (2008) 022105.

[8] J. Liu, P. Fei, J. Zhou, R. Tummala, Z. L. Wang, 92 (2008) 173105.

[9] C. Chang, V. H. Tran, J. Wang, Y. K. Fuh, L. Lin, 10 (2010) 726-731.

[10] S. N. Cha, J. S. Seo, S. M. Kim, H. J. Kim, Y. J. Park, S. W. Kim, J. Kim, 22 (2010) 4726-4730.

[11] S. Y. Chung, S. Kim, J. H. Lee, K. Kim, S. W. Kim, C. Y. Kang, S. J. Yoon, Y. S. Kim, 24 (2012) 6022-6027.

[12] Z. L. Wang, 32 (2007) 109-116.

[13] Y. Chen, C. Cheng, S. Liou, Y. Chen, 19 (2008) 485709.

[14] Z. L. Wang, 19 (2007) 889-892.

[15] X. Wang, J. Song, J. Liu, Z. L. Wang, 316 (2007) 102-105.

[16] R. J. S. R. Bogue, (2009).

[17] X. Song, X. He, H. Yang, Y. Qu, G. Qiu, 21 (2008) 295.

[18] Z. Wang, A. P. Suryavanshi, M. F. Yu, 89 (2006) 082903.

[19] K. I. Park, S. Xu, Y. Liu, G. T. Hwang, S.-J.L. Kang, Z. L. Wang, K. J. Lee, Nano Letters, 10 (2010) 4939-4943.

[20] X. Chen, S. Xu, N. Yao, Y. Shi, 10 (2010) 2133-2137.

[21] J. M. Wu, C. Xu, Y. Zhang, Z. L. Wang, 6 (2012) 4335-4340.

[22] R. Lewis, D. Allsopp, P. Shields, A. Šatka, S. Yu, V.Y. Topolov, C. Bowen, 429 (2012) 62-68.

[23] S. Xu, G. Poirier, N. Yao, 12 (2012) 2238-2242.

[24] S. Zhang, F. Li, F. Yu, X. Jiang, H. Y. Lee, J. Luo, T. R. Shrout, 55 (2018) 419-439.

[25] A. Behera, Piezoelectric materials, Advanced Materials, Springer, 2022, 43-76.

[26] B. Çeltikçi, Middle East Technical University, 2012.

[27] S. Xu, B. J. Hansen, Z. L. Wang, 1 (2010) 1-5.

[28] Y. Yang, J. H. Jung, B. K. Yun, F. Zhang, K. C. Pradel, W. Guo, Z. L. Wang, 24 (2012) 5357-5362.

[29] S. Cha, S. M. Kim, H. Kim, J. Ku, J. I. Sohn, Y.J. Park, B. G. Song, M. H. Jung, E. K. Lee, B.L. Choi, 11 (2011) 5142-5147.

[30] X. Wang, J. Shi, (2012) 135-172.

[31] J. Chang, L. Lin, 16th International Solid-State Sensors, Actuators and Microsystems Conference, IEEE, 2011, 747-750.

[32] M. Lee, C.Y. Chen, S. Wang, S. N. Cha, Y. J. Park, J. M. Kim, L.J. Chou, Z. L. Wang, 24 (2012) 1759-1764.

[33] R. Zhu, W. Zhang, R. Yang, 4 (2012) 798-804.

[34] L. Lu, W. Ding, J. Liu, B. J. N. E. Yang, 78 (2020) 105251.

[35] S. Sukumaran, S. Chatbouri, D. Rouxel, E. Tisserand, F. Thiebaud, T.J. Ben Zineb, Structures, 32 (2021) 746-780.

[36] S. Panda, S. Hajra, H. Jeong, B.K. Panigrahi, P. Pakawanit, D. Dubal, S. Hong, H.J. Kim, 102 (2022) 107682.

[37] S. Badatya, D.K. Bharti, N. Sathish, A.K. Srivastava, M.K. Gupta, 13 (2021) 27245-27254.

[38] H.J. Kawai, 8 (1969) 975.

[39] D. Berlincourt, C. Cmolik, H. Jaffe, 48 (1960) 220-229.

[40] H. Baerwald, 105 (1957) 480.

[41] J. Yang, P. Pan, L. Hua, B. Zhu, T. Dong, Y. Inoue, 43 (2010) 8610-8618.

[42] S. Mondal, T. Paul, S. Maiti, B.K. Das, K.K. Chattopadhyay, 74 (2020) 104870.

[43] L. Jin, X. Xiao, W. Deng, A. Nashalian, D. He, V. Raveendran, C. Yan, H. Su, X. Chu, T. Yang, W. Li, W. Yang, J. Chen, Nano Letters, 20 (2020) 6404-6411.

[44] S. Mondal, S. Maiti, T. Paul, A. Sahoo, S. Bhattacharjee, N.S. Das, K.K. Chattopadhyay, 26 (2022) 101385.

[45] A. Salimi, A. Yousefi, 22 (2003) 699-704.

[46] R. Gregorio, E.J. Ueno, 34 (1999) 4489-4500.

[47] K. Jurczuk, A. Galeski, M. Mackey, A. Hiltner, E. Baer, p. science, 293 (2015) 1289-1297.

[48] R. Wang, X. Zhou, W. Wang, Z. Liu, 417 (2021) 128060.

[49] C. Constantino, A. Job, R. Simoes, J. Giacometti, V. Zucolotto, O. Oliveira, G. Gozzi, D. Chinaglia, 12th International Symposium on Electrets, IEEE, 2005, 178-181.

[50] W. Yu, Z. Zhao, W. Zheng, B. Long, Q. Jiang, G. Li, X. Ji, Science, 49 (2009) 491-498.

[51] F. Algarni, V.E. Musteata, G. Falca, S. Chisca, N. Hadjichristidis, S.P. Nunes, 54 (2021) 10235-10250.

[52] N. María, J. Maiz, V. Rodionov, N. Hadjichristidis, A.J. Müller, 8 (2020) 13786-13797.

[53] R. Kepler, R.A. Anderson, 49 (1978) 1232-1235.

[54] C.-g. Duan, W.-N. Mei, W.-G. Yin, J. Liu, J. Hardy, S. Ducharme, P.A. Dowben, 69 (2004) 235106.

[55] N. Meng, X. Ren, X. Zhu, J. Wu, B. Yang, F. Gao, H. Zhang, Y. Liao, E. Bilotti, M. Reece, 8 (2020) 16436-16442.

[56] C. Chang, Y. K. Fuh, L. Lin, Actuators and Microsystems Conference, IEEE, 2009, 1485-1488.

[57] Y. Qi, M. C. McAlpine, E. Science, 3 (2010) 1275-1285.

[58] D. Zhang, X. Zhang, X. Li, H. Wang, X. Sang, G. Zhu, Y. J. Yeung, 166 (2022) 110956.

[59] T. Sharma, S. S. Je, B. Gill, J. X. Zhang, 177 (2012) 87-92.

[60] M. Mackey, L. Flandin, A. Hiltner, E. J. Baer, 49 (2011) 1750-1761.

[61] T. Furukawa, 18 (1989) 143-211.

[62] Q. Li, Q. Wang, Physics, 217 (2016) 1228-1244.

[63] Z. Pi, J. Zhang, C. Wen, Z. Zhang, D. Wu, 7 (2014) 33-41.

[64] D. Mandal, K. Henkel, D. Schmeißer, 16 (2014) 10403-10407.

[65] S. C. Park, C. Nam, C. Baek, M. K. Lee, G. J. Lee, K. Park, Engineering, (2022).

[66] X. Zhang, J. Hillenbrand, G.M. Sessler, 85 (2004) 1226-1228.

[67] M. Neshkova, R. Petrova, V. Petrov, 332 (1996) 93-103.

[68] Y. Tang, L. Chen, Z. Duan, K. Zhao, Z. Wu, 46 (2020) 6567-6574.

[69] K. Sinkó, K. Fél, J. Rohonczy, N. Hüsing, 10 (2001) 1078.

[70] B. Newman, P. Chen, K. Pae, J. Scheinbeim, 51 (1980) 5161-5164.

[71] W. Li, D. Torres, T. Wang, C. Wang, N. Sepúlveda, 30 (2016) 649-657.

[72] S. Anwar, M. Hassanpour Amiri, S. Jiang, M. M. Abolhasani, P. R. Rocha, K. Asadi, 31 (2021) 2004326.

[73] K. Prevedouros, I. T. Cousins, R. C. Buck, S. H. Korzeniowski, technology, 40 (2006) 32-44.

[74] E.S. Cozza, O. Monticelli, E. Marsano, P. Cebe, 62 (2013) 41-48.

[75] G. Kalimuldina, N. Turdakyn, I. Abay, A. Medeubayev, A. Nurpeissova, D. Adair, Z. Bakenov, 20 (2020) 5214.

[76] C. Seoul, Y. T. Kim, C. Baek, 41 (2003) 1572-1577.

[77] S. W. Choi, S.M. Jo, W. S. Lee, Y.R. Kim, 15 (2003) 2027-2032.

[78] S. Mishra, R. Sahoo, L. Unnikrishnan, A. Ramadoss, S. Mohanty, S. K. Nayak, 124 (2020) 110732.

[79] J. Gomes, J. S. Nunes, V. Sencadas, S. Lanceros-Méndez, Structures, 19 (2010) 065010.

[80] A. Franzan, N. Leite, L. Miranda, 50 (1990) 431-438.

[81] A. Sultana, P. Sadhukhan, M. M. Alam, S. Das, T. R. Middya, D. Mandal, interfaces, 10 (2018) 4121-4130.

[82] S. J. Kang, Y. J. Park, J. Sung, P. S. Jo, C. Park, K. J. Kim, B. O. Cho, 92 (2008) 012921.

[83] Z. L. Wang, Nano Today, 5 (2010) 540-552.

[84] A. Sultana, P. Sadhukhan, M. M. Alam, S. Das, T. R. Middya, D. Mandal, ACS Applied Materials & Interfaces, 10 (2018) 4121-4130.

[85] N. Sun, Z. Wen, F. Zhao, Y. Yang, H. Shao, C. Zhou, Q. Shen, K. Feng, M. Peng, Y. Li, X. Sun, Nano Energy, 38 (2017) 210-217.

[86] A. Ramadoss, B. Saravanakumar, S. W. Lee, Y.-S. Kim, S. J. Kim, Z. L. Wang, ACS Nano, 9 (2015) 4337-4345.

[87] H. He, Y. Fu, T. Zhao, X. Gao, L. Xing, Y. Zhang, X. Xue, Nano Energy, 39 (2017) 590-600.

[88] D. Zhang, Z. Yang, P. Li, M. Pang, Q. Xue, Nano Energy, 65 (2019) 103974.

[89] Z. Liu, S. Zhang, Y. M. Jin, H. Ouyang, Y. Zou, X. X. Wang, L. X. Xie, Z. Li, Semiconductor Science and Technology, 32 (2017) 064004.

[90] D. Wang, D. Zhang, P. Li, Z. Yang, Q. Mi, L. Yu, Nano-Micro Letters, 13 (2021) 57.

[91] V. Gupta, A. Babu, S. K. Ghosh, Z. Mallick, H. K. Mishra, D. Saini, D. Mandal, 119 (2021) 252902.

[92] B. Bagchi, N. A. Hoque, N. Janowicz, S. Das, M. K. Tiwari, 78 (2020) 105339.

[93] L. Wan, W. Tian, N. Li, D. Chen, Q. Xu, H. Li, J. He, J. Lu, 94 (2022) 106930.

[94] S.P. Muduli, S. Veeralingam, S. J. Badhulika, 48 (2022) 102934.

[95] M. Sharma, G. Singh, R. J. Vaish, 130 (2021) 085107.

CHAPTER 3

Instrumentations & Apparatus

3.1. Crystallographic Study

3.1.1. X-ray Diffractometer (XRD)

T he phase of the synthesized samples was evaluated using x-ray diffraction (XRD) on a D8 Advanced Bruker instrument, with the diffraction traces recorded in intensity vs. 2θ mode. For CuK_α (1.5406) radiation from a highly stabilized Bruker X-ray generator, a germanium (022) monochromator was used (K780). For first-order diffraction, the lattice spacing can be calculated using Bragg's equation:

$$2d \sin \theta = \lambda \qquad (3)$$

Where d is the inter-planar spacing, λ is the electron wavelength, and θ is the glancing angle. Figure 3.1 depicts a photograph of the instrument.

Figure 3.1: Photograph of XRD instrument.

3.2. Spectroscopic Techniques

3.2.1. UV–Vis–NIR Spectroscopy

Chapter 3

The ultraviolet-visible near-infrared (UV−Vis−NIR) spectrophotometer is the device used for the ultraviolet-visible spectrum. Utilizing radiant radiation from the far ultraviolet and near ultraviolet, visible, and near-infrared spectrums, the spectrophotometer offers a way for examining liquids, gases, and solids. Consequently, the specified electromagnetic radiation wavelengths were employed for ultraviolet (UV), visible light (Vis) and near-infrared (NIR) radiation. The UV-Vis instrument is operated by a beam of light directed through the sample, and the wavelength of the light that reaches the detector is then measured. The chemical structure is usefully shown by the wavelength, while the quantity, average quantity, or concentration of molecules is indicated by the intensity. The analysed data can be displayed using energy transmittance, absorptivity, or reflectivity in the wavelength range of 160 to 3500 millimeters. Figure 3.2 provides a digitised image of UV-Vis-NIR spectroscopy.

Figure 3.2: Digital photograph of UV-Vis-NIR spectroscopy.

3.2.2. Fourier Transform Infrared (FTIR) Spectroscopy

Electromagnetic radiation, which comprises all wavelengths between the visible and microwave region of the electromagnetic spectrum, includes infrared (IR) radiation. Additionally, the infrared region can be broken into three smaller regions known as the near-infrared (14000-4000 cm^{-1}), mid-infrared (4000-400 cm^{-1}) and far-infrared (400-20 cm^{-1}). Most molecules will change their intrinsic vibration level in the mid-infrared range, indicating that the spectrometer is capable of operating there. The infrared spectrum is obtained using the

following method: an interferometer is used to gather the interferogram of the sample signal, and the spectrum is then obtained. The absorption intensity varies with the quantity of molecules collected in all types of infrared spectrometers. In this investigation, the samples were analysed using IR spectroscopy using a Shimadzu-8400S IR Prestige spectrometer. Figure 3.3 displays the instrument's photograph.

Figure 3.3: Digital photograph of FTIR instrument.

3.2.3. Energy Dispersive X-ray (EDX)

This is a technique based on characteristic X-ray peaks produced when a high-energy electron beam interacts with the sample. Each element generates characteristic X-rays, which can be used to identify the presence of the element in the inspected area. The comparison of the relative intensity of the X-ray peaks can be used to determine the relative concentration of each element in the sample. Elements with atomic numbers less than the carbon number (Z = 6) are generally undetectable. The sample's composition is studied using an energy dispersive X-ray (HITACHI S4800 at 15 kV). The instrument is capable of detecting elements ranging from lithium (3) to uranium (92). It is linked to a scanning electron microscope with field emission (FESEM, Hitachi S-4800). Figure 3.10 depicts the photograph.

3.2.4. X-ray Photoelectron Spectroscopy (XPS)

Chapter 3

By using X-ray photoelectron spectroscopy, the chemical make-up of the nanostructure, the charge state of the dopants, and the purity of the sample was examined (XPS, Specs, Germany). The basic idea behind X-ray photoelectron spectroscopy is to expose a sample to an X-ray beam, which results in the sample emitting photoelectrons. Figure 3.4's illustration shows a schematic representation of this electron emission mechanism. $E_b = h\nu - E_k$, where $h\nu$ is the X-ray energy that may be calculated based on the number of electrons, relates the kinetic energy (E_k) and binding energy (E_b) of the emitted electrons. The most accurate method for classifying surface elements may be XPS since different elements have different binding energy sets. These slight changes in binding energy (chemical shifts) provide detailed information about the chemical state and short-range chemistry of the sample. A hemisphere energy analyser (HAS 3500) was used for sample analysis on SPECS, and the anode current was excited by photoelectrons using a monochromatic Mg K_α X-ray (1253.6 eV) or Al K_α X-ray (eV) light source operating at 10 kV and 17 mA. In the spectral mode, electrons are dispersed between the inner and outer hemispheres. The radius of 165 mm and the eight-channel detector ensures high spectral resolution and excellent sensitivity. Therefore, the kinetic energy distribution of the emitted photoelectrons can be measured, that is, the number of emitted photoelectrons varies with their kinetic energy, and the spectrum can be recorded. The photo of X-ray photoelectron spectroscopy is shown in figure 4.7. These minute variations in binding energy (chemical shifts) reveal specific details about the sample's short-range chemistry and chemical state. The anode current was stimulated by photoelectrons using a monochromatic Mg K_α X-ray (1253.6 eV) or Al K_α X-ray (eV) light source operating at 10 kV and 17 mA, and a hemispheric energy analyser (HAS 3500) was utilised for sample analysis on SPECS. The system's residual pressure is better than 10^{-9} mbar. Electrons are scattered between the inner

and outer hemispheres in the spectral mode. High spectral resolution and exceptional sensitivity are ensured by the 165 mm radius and eight-channel detector.
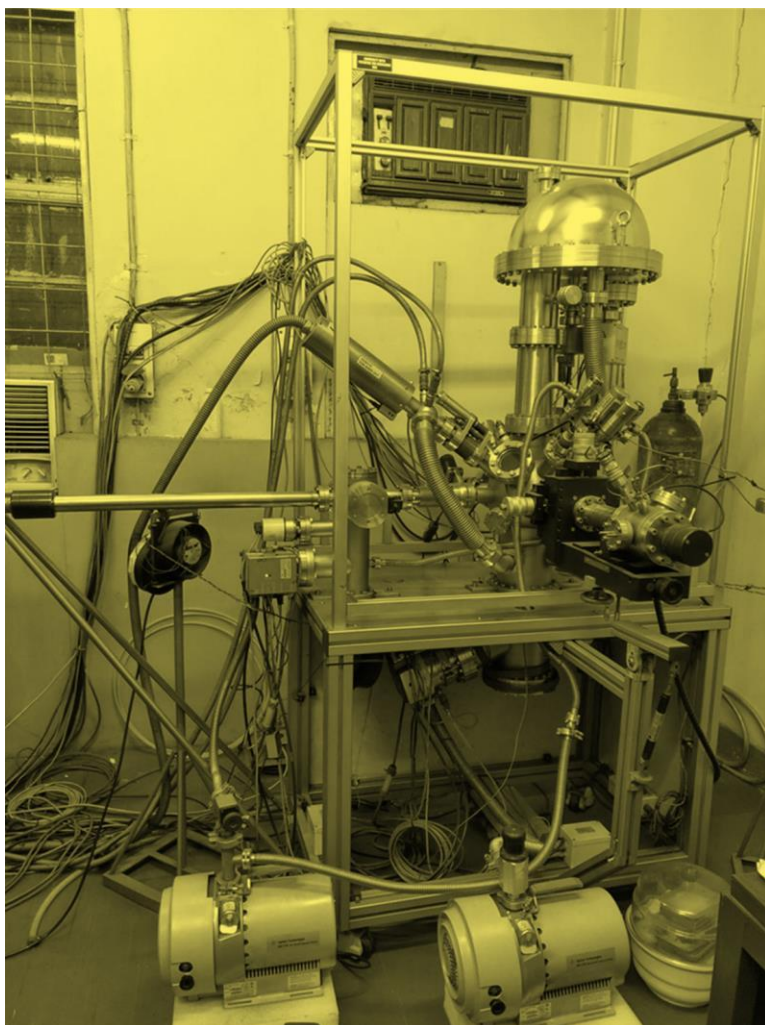
Figure 3.4: Digital photograph of XPS instrument.

3.2.5. Raman Spectroscopy

Raman spectroscopy is carried out using a Raman microscope, a laser-based microscopic instrument. Raman spectroscopy is frequently used in material science to analyse a sample's molecular composition by exposing it to a monochromatic laser beam. The Raman Effect, a scattering mechanism used in Raman spectroscopy, causes a small amount of scattered light to have a different frequency from the monochromatic incident radiation. It uses the interaction of vibrating molecules and inelastic scattering of incident radiation to detect molecular vibrations. A set of photons made up of radiation are dispersed when a laser beam strikes a

Figure 3.5: *Digital photograph of RAMAN microscope instrument.*

substance, but only one out of every 10^6–10^8 of these scattering events is in the Raman range.

All scattering interactions must conserve both momentum and energy simultaneously. When

incident photons interact with phonons in the sample crystal lattice indirectly to scatter photons

at a frequency that is just marginally different from the incident photons, is referred to as an

inelastic Raman scattering event. Stokes scattering is thought to occur when the frequency of

the scattered photon (incident energy) is lower than the frequency of the incident photon (less

energy). On the other hand, if the scattered photon has a higher frequency (more energy), it

will be referred to as non-Stokes scattering. Anti-Stokes scattering is how it is described. The

vibration frequency, which differs from the incident light and the measured frequency, is what

the Raman spectrometer measures. The Raman shift and anti-Stokes scattering of Stokes scattering are used to directly determine the vibrational energy of the molecules under investigation. Phonon interaction is not always required for Raman scattering to take place in an ordered lattice with allowed phonon modes since some molecular vibrations in amorphous materials can interact in a way that is comparable to phonon interaction. In this study, the sample's Raman spectrum was captured on an alpha 300RS confocal Raman microscope from WITec GmbH. Figure 3.5 displays an image of the Raman imaging setup. A Peltier-cooled back-illuminated CCD camera is coupled to a fiber-coupled UHTS 300 spectrometer, and the QE is greater than 90% when excited by visible light. It uses a laser radiation source with a 532nm wavelength and 40mW of power. The spectrum was recorded as the average of three scans throughout the course of the 25 s collection period. Witec Control 1.42 software was used to conduct the experiment on the computer interface, and Witec Project 1.90 software was used to complete the analysis.

3.3. Electrical Measurements

3.3.1. Electrometer, Multi-meter, Digital Storage Oscilloscope

Figure 3.6: *Digital photography of digital storage oscilloscope.*

The current-voltage characteristics and sample resistance are recorded using the Keithley Electrometers (671 and 6517A). The voltage and current ranges are 1000 V and 1 pA to 20 mA, respectively. Field emission currents ranging from 100 nA to 21 mA are measured using another Keithley electrometer (Model 6514). Several multi-meters were also used during the experiment (RISH MULTI 15 S, Agilent (model 3440-1A). Using a KEYSIGHT InfiniiVision DSOX2012A digital storage oscilloscope, the electroactive response of the as-fabricated piezoelectric nanogenerators is investigated. The voltage range of the oscilloscope is 0-400V, as presented in Figure 3.6.

3.3.2. Cyclic Voltammetry

The Autolab PGSTAT Multi Autolab/(M204) is used to measure the electrochemical properties of the as-prepared electrode. This instrument measures cyclic voltammetry (CV), galvanostatic charge-discharge (GCD), Nyquist, and Mott Schottky. In this instrument, three (3) and two (2)

Figure 3.7: Digital photography of cyclic-voltammetry setup.

electrode measurements were performed using Ag/AgCl as the reference electrode, Pt wire as the counter electrode, and as-synthesised nanomaterials in the flexible substrate as the working electrode with aqueous electrolyte in acidic/basic form as the required electrolyte. With a compliance voltage of 20 V, a bandwidth of 1 MHz, and a maximum current of 0.4A, this high-end, high-current multichannel galvanostat can perform multiple measurements at the same

time. The current ranges can be adjusted from 10 nA to 100 mA in 8 steps. Figure 3.7 depicts the instrument diagram.

3.3.3. Dielectric Measurement

Polarization occurs in all dielectric materials in the presence of an external electric field and/or mechanical strain. The piezoelectric deformation is proportional to the dielectric constant and varies linearly with polarisation. As a result, piezoelectric performance can be roughly estimated from the dielectric constant dispersion without the use of an external bias, as a higher deformation energy should be induced for a larger dielectric constant. An Agilent precision impedance analyser with an operating range of 40 Hz–110 MHz and 42 V maximum bias is used to record impedance spectra. Ag electrodes are deposited on both sides of the films to form a MIM geometry compatible with dielectric analysis. Figure 3.8 shows the digitally captured image of the dielectric property measurement instrument.

Figure 3.8: *Digital photography of dielectric property measurement instrument.*

3.3.4. P-E loop Measurement

One of the key measurements for ferroelectric materials is the natural polarization hysteresis loop. The P-E loop of synthetic films was measured using a Precision Premier II ferroelectric tester from Radiant Technologies, Inc. and a typical bipolar waveform. All measurements were taken at room temperature. With the input voltage and sample thickness, an approximation of

the electric field strength in the sample is obtained. Figure 3.9 shows the digitally captured image of the P-E loop measurement instrument.

Figure 3.9: *Digital photography of P-E loop measurement instrument.*

3.4. Microscopic Measurements

3.4.1. Field Emission Scanning Electron Microscope (FESEM)

Using a field emission scanning electron microscope (FESEM), which is similar to a transmission electron microscope (TEM) but has significant peculiarities, a thorough morphological analysis of a hybrid system based on ZnO and graphene was carried out. The energy-focused electron beam in FESEM is smaller than in TEM. In raster scan mode, it scans the sample's surface. The field emission cannon emits electrons with energies ranging from several hundred to 50 keV. Different deflection coils focus and accelerate the beam after it is generated by the gun. At last, the sample's surface is struck by the collimated beam, which then reacts with it. As a result, the sample emits electrons and photons. The energy exchange between the sample and the electron beam causes electromagnetic radiation to be emitted, secondary electrons to be emitted through inelastic scattering, high-energy electrons to be reflected through electromagnetic scattering, and all of these events can be detected by a
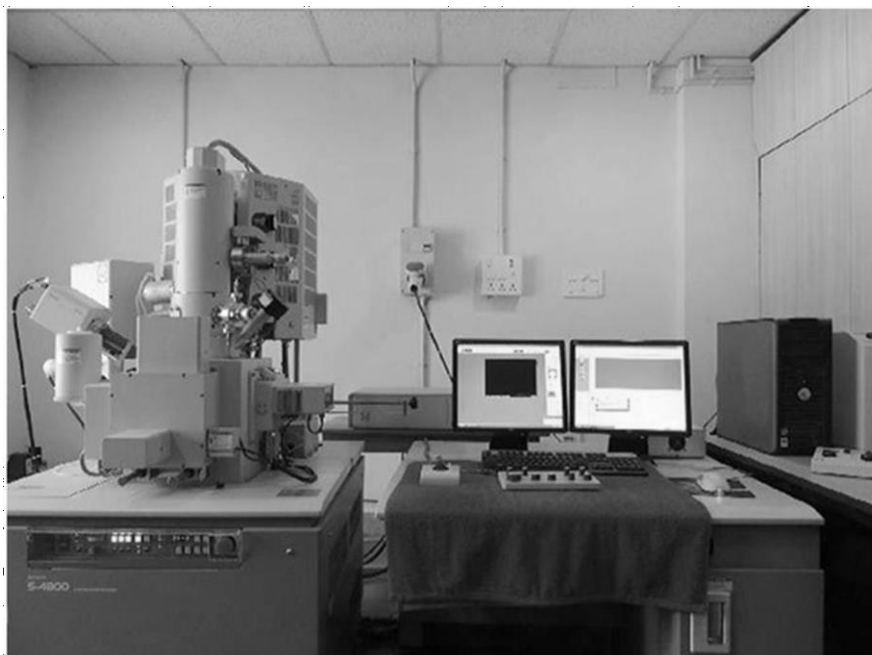
Figure 3.10: *Photograph of the FESEM unit with EDX attachment.*

particular detector and transformed into a signal containing sample information, Shape, content, and other features of the surface (such as electrical conductivity). The signals produced by FESEM include secondary electrons, backscattered electrons (BSE), light (cathodoluminescence), distinctive X-rays, sample currents, and transmitted electrons, among others. The sample under study must be conductive for conventional imaging in FESEM because it prevents the accumulation of static charges on the surface and is compatible with vacuum. Before imaging non-conductive samples, an ultra-thin gold/platinum coating is deposited on the sample using sputtering or evaporation technology. The FESEM (HITACHI S4800) instrument was used to detect surface morphology and film thickness throughout the thesis work. The magnification ranges from 30X to 300,000X, and the FESEM resolution is close to 5nm. The instrument has two image modes: secondary electron image (SEI) and backscattered electron image (BEI). The camera is a 35mm single-lens reflex (MP 35051, CSI 3) with a 50mm focal length. The resulting image could provide information about the film's uniformity and thickness. Figure 3.10 depicts a photograph of the SEM instrument.

3.4.2. Transmission Electron Microscope (TEM)

Chapter 3

A transmission electron microscope (TEM) is a characterization tool used to simultaneously study the crystal structure and microstructure of materials through diffraction and imaging techniques. Furthermore, the high-resolution transmission electron microscope (HRTEM) is another imaging mode of the transmission electron microscope (TEM), which can provide more accurate and precise images of the crystal structure of the sample at the atomic level. In a traditional TEM, a thin sample is exposed to an electron beam with a uniform current density. The electron gun generates electrons by spreading in multiple holes, and the lens illuminates the sample. In these lenses, the objective lens produces a diffraction pattern on the back focal plane, which can be described as the Fourier transform of the wave function at the object exit surface $\Psi(r)_n$. Thereafter, the collimated beam passes through the sample, and the image is focused on the phosphor screen. Finally, the image is digitally recorded by a CCD camera or direct exposure of the photographic emulsion and other technologies. The electron beam generated by the electron gun (usually removed with tungsten or LaB6) is accelerated by the electric field. The electron beam is usually much higher than the electron beam used in SEM, HRTEM (150-250) kV and (5-30 kV) in SEM. This way the beam can pass through the sample. The first image formed by the objective lens is enlarged by 25 times of the original image and is continuously enlarged by the subsequent lens to the final image, which is 106 times of the previous image. Each electron in the electron beam independently interacts with the sample. When the beam penetrates the sample, it is attracted by the positive atomic potential of the atomic nuclei and channels along the lattice atomic column. At the same time, the interaction between electron waves in different atomic columns causes Bragg diffraction. The accepted physical principles of electron scattering and electron microscope imaging help to more accurately simulate electron microscope images. Two imaging techniques are commonly used in TEM, bright field imaging and dark field imaging. In bright field imaging, an image is formed by passing only electrons without any diffraction, where the diffracted electrons are
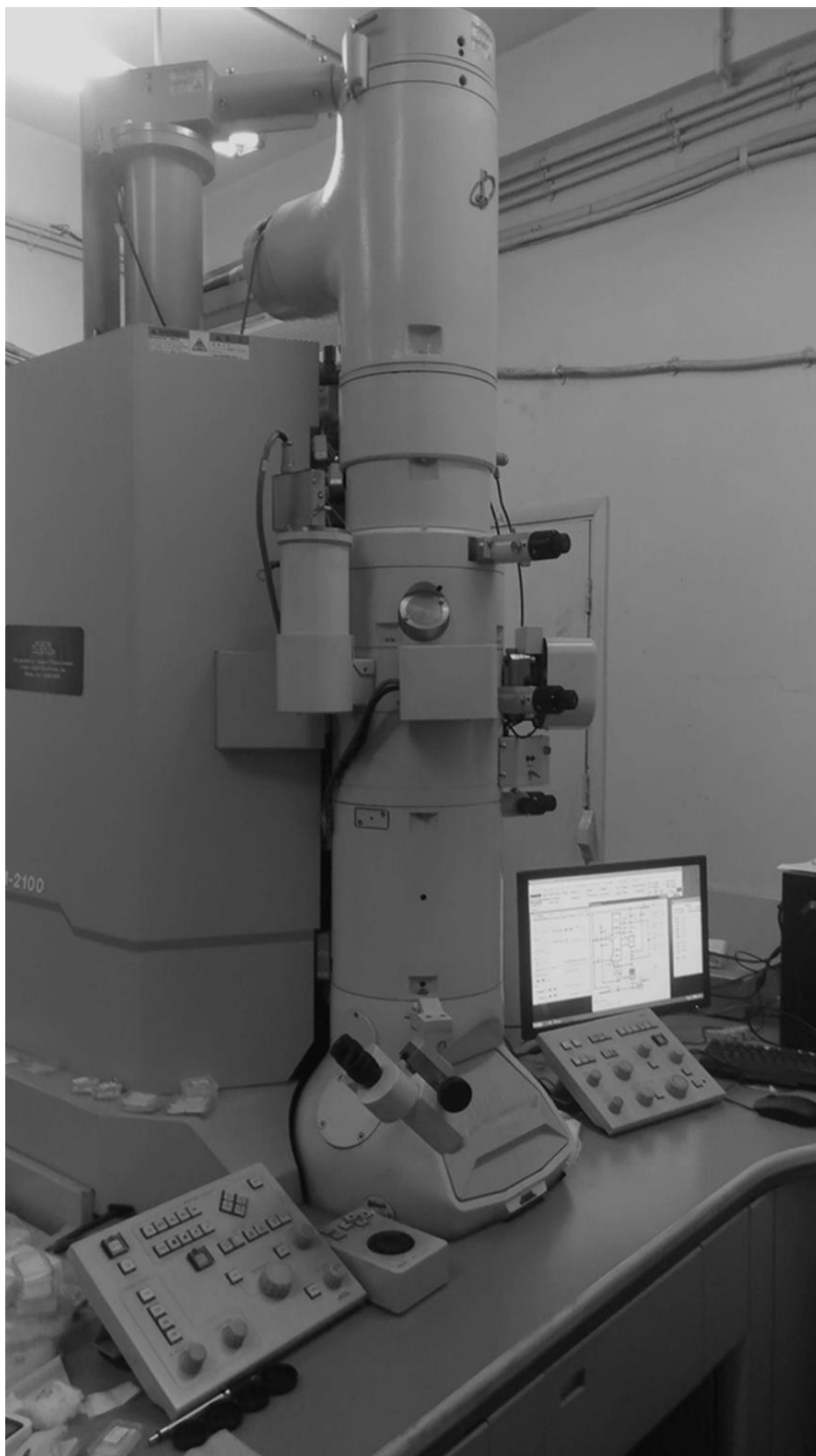
Figure 3.11: *Digital captured photograph of TEM.*

stopped by a diaphragm. On the other hand, in the dark field imaging mode, the diffracted beam

is used for imaging. In this work, a transmission electron microscope (JEOL-JEM-2100) was

used to study the crystal structure and microstructure of thin films deposited on various substrates. This model has three independent condensers, for any given probe size, and can generate high probe current, thereby enhancing analysis and diffraction capabilities. This model offers a variety of pumping options, including dry/turbo pumps for laboratory environments. Oil-based or rotary pumps are not allowed. The instrument has a guaranteed resolution of 0.1 nm however the attained during routine measurements is 8–10 Å. The magnification of this model can vary from 50X to 1,500,000X, and the acceleration voltage is 80-200 kV. The TEM sample was prepared by dropping the suspension of the sample onto a carbon-coated copper mesh and allowing the solvent to evaporate. The photo of HRTEM is shown in figure 3.11.

CHAPTER 4

Sample Preparation & Experimental Methods

4.1. Chemicals

Lead iodide (PbBr$_2$), cesium iodide (CsBr), Lead (ll) chloride (PbCl$_2$), and cesium chloride (CsCl), have been used from Sigma Aldrich prepare CsPbBr$_3$ and CsPbCl$_3$. Also, cobalt nitrate (Co(NO$_3$)$_2$, 6H$_2$O), urea (CO(NH$_2$)$_2$), nickel nitrate (Ni(NO$_3$)$_2$, 6H$_2$O), and ammonium fluoride (NH$_4$F) has been used to make CuCoNiO$_4$. Zinc nitrate hexahydrate (Zn(NO$_3$)$_2$. 6H$_2$O), potassium hydroxide (KOH), acetone, n, n-dimethylformamide (DMF) from Mark, India, deionized water (Millipore) to prepare ZnO nanorods. The raw materials are of chemical grade. For the synthesis of PVDF film, PVDF pellets (Mw $\approx$ 275000 g/mol by GPC Sigma Aldrich, USA), N, N-dimethylformamide (DMF) (Sigma Aldrich, USA), and acetone (Merck Life Science Private Limited, India). For electrolyte preparation, PVA from Loba Chemie and H$_3$PO$_4$ from Merck Life Science Private Limited, India.

4.2. Synthesis Procedures

4.2.1. Filler Preparation

4.2.1.1. CsPbBr$_3$ Synthesis

For the synthesis of CsPbBr$_3$, initially, a mixture was prepared by dissolving CsBr (0.259 mg) and PbBr$_2$ (0.461 mg) within DMF (2 ml). Simultaneously, an oil phase was also prepared by adding hexane with oleic acid and n-octylamine. Thereafter, the oil phase was added slowly with the aforesaid solution and stirred for 5 min. Tert-butanol was further added immediately to initialize the demulsification. Finally, the precipitates were dried overnight in a vacuum oven and collected [1, 2, 5].

4.2.1.2. CsPbCl$_3$ Synthesis

The synthesis of the CsPbCl$_3$ cubic structure is achieved via a simple solution casting method at room temperature. Firstly 0.2 mL dimethyl sulfoxide (DMSO) was taken in a beaker and 0.461 mg PbCl$_2$ was dissolved in the DMSO solvent and stirred for 5 minutes. Afterward, 0.259 mg CsCl was mixed with the above solution. Parallelly an oil phase solution was prepared by mixing 1mL of oleic acid and 0.5 mL of n-octylamine in 10 mL hexane. This oil phase solution was added slowly into the firstly prepared DMSO solution and stirred. Thereafter the final solution was centrifuged and precipitation was collected. This precipitation was further washed several times with hexane and dried in a vacuum at 70^{0}C overnight before it was further used [3, 6].
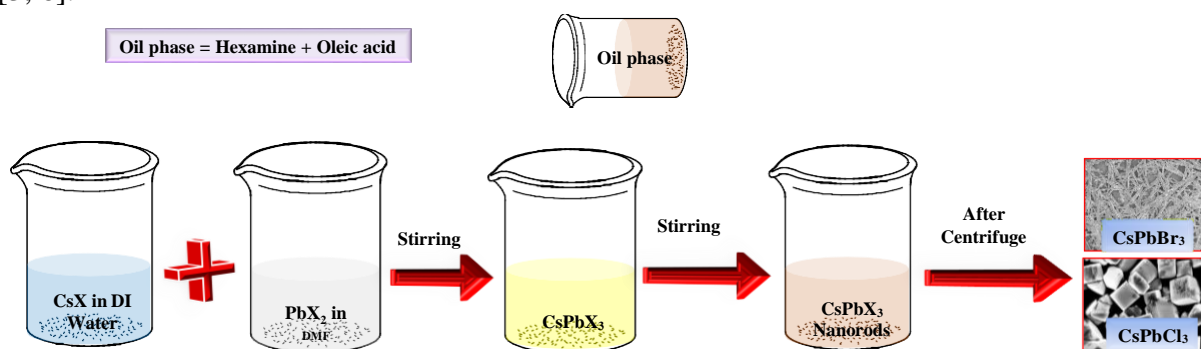
Figure 4.1: *Schematic illustration of room temperature synthesis of all-inorganic perovskite CsPbX$_3$ (X =Cl, Br, I) rods.*

4.2.1.3. CsCuNiO$_4$ Synthesis

For the synthesis of CuCoNiO$_4$ nanoparticles (abbreviated as CCNO), a simple hydrothermal method was used, followed by 350°C annealing. A typical synthesis technique involved mixing 1 mmol of cobalt nitrate hexahydrate (Co(NO$_3$)$_2$, 6H$_2$O), 1 mmol of copper nitrate hexahydrate (Cu(NO$_3$)$_2$·6H$_2$O), 1 mmol of nickel nitrate hexahydrate (Ni(NO$_3$)$_2$·6H$_2$O), 5 mmol of urea (CO(NH$_2$)$_2$), and 2 mmol of ammonium fluoride (NH$_4$F) with 80 mL of D. I. water and stirring for 20 minutes. The mixture was placed in a 100 ml Teflon-lined stainless-steel autoclave, where it was allowed to react for 6 hours at 150 °C in a standard laboratory oven. After the autoclave had cooled to ambient temperature, the product had been washed multiple times in

DI water and then dried at 60 °C overnight. In order to get rid of the hydroxide ions and other impurities, the samples were finally put in a furnace and heated to 350 °C for two hours [4, 7].

4.2.2. Synthesis of Polymer Composites

Pristine PVDF film and composite thin film were prepared via the single-step chemical method. For the synthesis of bare PVDF film, 20 mL solution of DMF and acetone was prepared in a 4:6 ratio and 1.5 g PVDF pallets were mixed with it. This mixture was stirred for 2 hours at 80˚C. Once, the solution becomes transparent, it was drop-casted on pre-cleaned glass slides. Thereafter, the as-coated glass slides were kept in a vacuum oven overnight at 85 ˚C. Finally, the coated slides were taken out of the oven and collected carefully from the glass slides. To prepare the composite film, all the experimental protocols remained the same except the extra addition of filler ($CsPbBr_3$, $CsPbCl_3$, $CuCoNiO_4$) with different wt% in the mixture solution of DMF, acetone and PVDF [5, 6, 7].
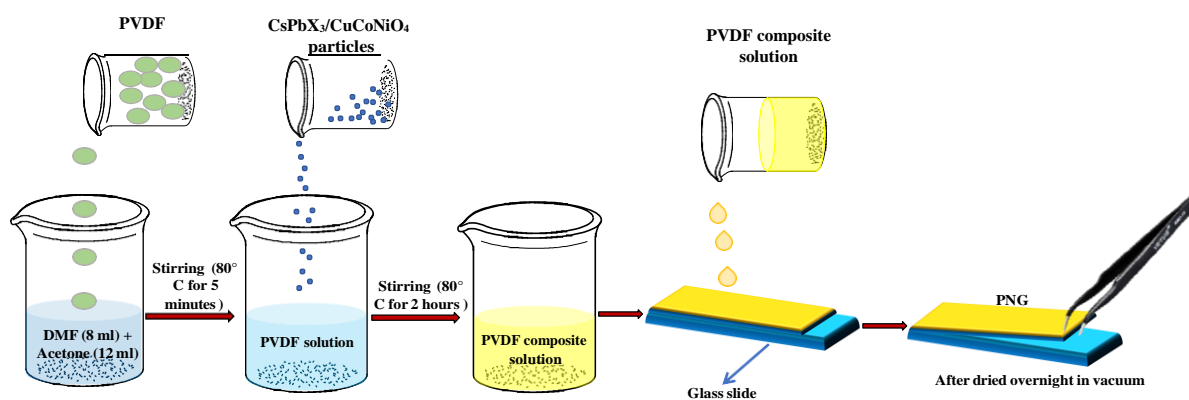
Figure 4.2: *Schematic illustration of PVDF composite preparation.*

4.2.3. Synthesis of ZnO Nanorods (NRs) on Zinc Foil

ZnO nanorods on zinc foil were synthesized via a chemical route. Two separate solutions of 10 mL with 5.7M KOH and 0.5M ($Zn(NO_3)_2 \cdot 6H_2O$) were taken in two beakers. These two solutions were mixed in a 30 mL borosilicate glass bottle. Therefore an analytically graded zinc foil (1 cm × 1 cm) was ultrasonically cleaned with ethanol and then one side of the zinc

foil was covered with Teflon while the other side was kept open. This foil was then placed inside the above-mentioned glass bottle with the open side of the foil facing down and making an angle of 45^0 with the bottom surface of the bottle then the system was left in this condition at ambient temperature for 1 h and after that, the zinc foil was withdrawn from the solution and washed by deionized water. Finally, the Teflon was uncovered and it was dried at room temperature [8].

4.3. Device Fabrication
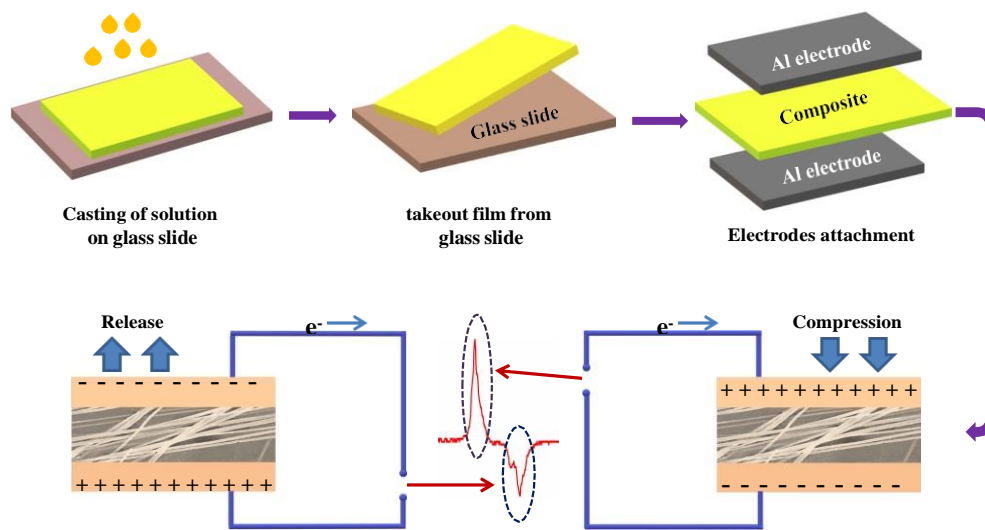
Figure 4.3: *Schematic presentation of PNG device and its working principle.*

To fabricate a piezoelectric nanogenerator (PNG), firstly a PET substrate and an aluminium (Al) sheet (bottom electrode) were glued together. As prepared films were then placed on the bottom Al electrode followed by another Al sheet (top electrode) attached to it. Two copper wires were then connected with top and bottom electrodes [5, 6, 7].

4.4. References

1. T. Paul, B. K. Chatterjee, S. Maiti, N. Besra, S. Thakur, S. Sarkar, K. Chanda, A. Das, P.K. Sarkar, K. Sardar and K. K. Chattopadhyay, AIP Conference Proceedings, 1953, 2018, 030085-030089.

2. T. Paul, B. K. Chatterjee, N. Besra, S. Thakur, S. Sarkar and K. K. Chattopadhyay, Materials Today: Proceedings 5, 2018, 2234-2240.

3. T. Paul, B. K. Chatterjee, S. Maiti, N. Besra, S. Thakur, S. Sarkar, K. Chanda, A. Das, P. K. Sarkar, K. Sardar, and K. K. Chattopadhyay, In AIP Conference Proceedings, 1953, 2018, 030085.

4. S. Thakur, S. Maiti, K. Sardar, N. Besra, P. Bairi, K. Panigrahi, K. Chanda, T. Paul, and K. K. Chattopadhyay, , Journal of Energy Storage, 35, 2021, 102249.

5. S. Mondal, T. Paul, S. Maiti, B.K. Das, and K.K. Chattopadhyay, Nano Energy, 74, 2020, 104870.

6. S. Mondal, S. Maiti, T. Paul, A. Sahoo, S. Bhattacharjee, N.S. Das, and K. K. Chattopadhyay,. Applied Materials Today, 26, 2022, 101385.

7. S. Mondal, S. Thakur, S. Maiti, S. Bhattacharjee, and K. K. Chattopadhyay, Self-Charging Piezo-Supercapacitor: One-Step Mechanical Energy Conversion and Storage. ACS Appl. Mater. Interfaces (2023).

8. S. Mondal, S. Das, S. Maiti, N. Besra, T. Paul, and K. K. Chattopadhyay. International Journal of Nanotechnology, 18(5-8), 2021, 669-678.

CHAPTER 5

Human Motion Interactive Mechanical Energy Harvester based on all Inorganic Perovskite-PVDF
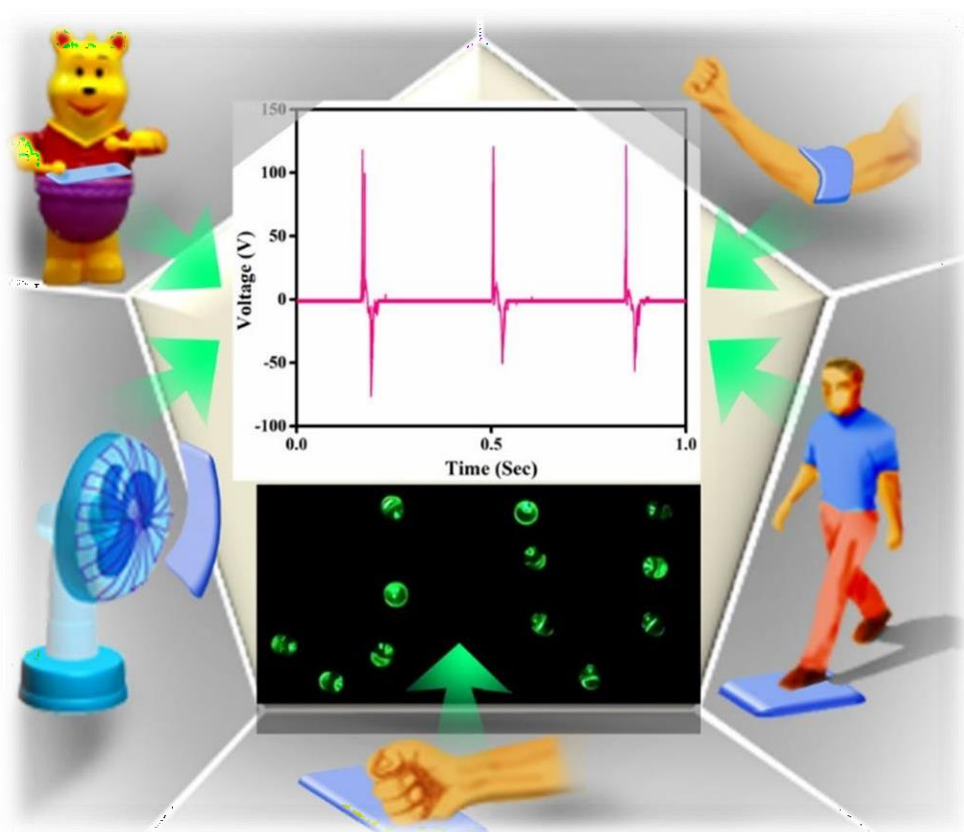
5.1. Introduction

Current setting of mass production of budgetary self-powered portable electronic system has inspired the development of suitable environment benign materials for proficient and renewable energy harvesting [1, 2]. Several kinds of energy sources like solar, mechanical, thermal, vibration, wind and sonic waves are available in our surroundings. Amongst them, solar and mechanical are the safest and most sustainable sources of energy because of their availability and noble hybridizing opportunities [3, 4]. These two energy sources work on completely different principles. Existing designs presented in the literature mostly harvest the above-mentioned resources i.e. either solar or mechanical energy separately [3]. Metal halide perovskites, both in organic and all inorganic forms have registered their usage potential in optoelectronic arena namely in solar energy harvesting owing to their excellent optoelectronic features. In particular, all inorganic cesium lead halides with empirical formula $CsPbX_3$ where X denotes different kinds of halides have garnered gigantic research attention in photovoltaics and photodetection. It possesses several intriguing features like high thermal stability, carrier mobility, absorption coefficient, etc. [5]. Despite these beneficial traits, its widespread usage applicability is still restricted due to its questionable stability [6]. Intrinsic ionic character makes the perovskites samples very sensitive towards the water and polar molecules. Gigantic amount of research effort is made to improve their stability towards water, functionality as well as on encapsulation for device lifetime enhancement [7, 8]. Besides shielding of inner perovskite material, functionality enhancement of the encapsulation layer via mechanical energy harvesting is very intriguing as it has a huge impact both on energy sectors and scientific communities. Nanogenerator is a device that converts low-frequency mechanical vibration into electrical energy through piezoelectric, pyroelectric and triboelectric effects. Numerous piezoelectric nanogenerators have been realized in recent times using various materials like inorganic oxides (ZnO, $ZnSnO_3$, $BaTiO_3$, PZT, etc.), nitride (GaN), polymer and co-polymers,

Chapter 5

etc. [9,10] However, versatile utilization of inorganic semiconductors for practical applications is restricted due to their several kinds of bottleneck in fabrication and growth like necessity of cost-intensive complex processing, high growth temperature, etc. [9,10] These materials also have specific deformations to very small range due to their brittle and rigid nature. Such poor flexibility and inherent brittleness limit their versatile utilization [9, 10]. Quite the opposite, the piezoelectric polymers and copolymers are lightweight, flexible and easy to realize. To harvest aforesaid multimode energies separately as well as simultaneously on availability, hybrid energy harvester may be devised by incorporating a photoactive material inside a polymer matrix. From large assortment of piezoelectric polymers and copolymers, poly (vinylidene fluoride) (PVDF) is considered as one of the most suitable ones for mechanical energy harvesting as it possesses high piezoelectric co-efficient and shows chemical resistivity, high thermal stability and bio-compatibility [11, 12]. It is also lightweight in nature. PVDF is a semi-crystalline polar polymer with high dielectric constant. It generally exhibits at least four polymorphs namely stable non-electroactive crystalline α (trans-gauche conformation TGTG), β (all trans planar TTTT conformation), γ (T^3GT^3G conformation), and δ (polar version of α) phase depending on their molecular chain conformations [11,13,14] Among these polymorphs, β phase is the most desirable one as it possesses the highest dipole moment unit volume with maximum ferroelectric hysteresis as compared to others which ensure superior piezo-, pyro- and ferro-electricity. Along with high β phase constitution, recent studies also advise that strain effect and charge collecting area have a massive impact on piezoelectricity and sensitivity enhancement of PVDF film [3]. Induction of β phase in PVDF is achieved via preferential orientation of $-CH_2-/-CF_2-$ dipoles in the direction normal to chain axis of PVDF. Several protocols such as mechanical stretching, high-temperature processing, electric poling, electro-spinning, hydrated salt addition etc. are adopted to make such orientation and thereby achieve β phase [3, 11, 15]. Compared to the abovementioned protocols, preparation of a hybrid

structure via assimilation of an external assisting agent in PVDF to get rid of unwanted structural deformations and added energy consumptions is much effective. Such external additives not only improve the β phase induction in PVDF matrix also makes hybrid system suitable for multifunctional applications [3]. Considering the current call for a single device with multifunctionality, introduction of optically active filler in PVDF is very fascinating as it makes the hybrid system more suitable for next generation foldable and wearable devices like laser emitters, solar cell, photosensor, etc. Perovskites are special kind of materials which not only presented optical eminence also explored piezoelectricity because of their prominent piezo- and ferro-electric response. Thus, a single device with the ability of mechanical energy harvesting as well as photodetection and their hybridization can be visualized via induction of electro active phase in PVDF and high optical absorption quality of perovskite material in a composite. Documented previous works suggest that the amalgamation of perovskites with PVDF is largely confined to organic-inorganic hybrid like formamidinium lead halide perovskite, methyl ammonium lead halides, etc. whereas the usage of all inorganic perovskite in this regard is not explored till now [3,16]. Here, a new sort of hybrid by incorporating all inorganic cesium lead bromide ($CsPbBr_3$) in PVDF at room temperature has been reported for the first time. $CsPbBr_3$ rods are realized via facile chemical approach at ambient and as prepared $CsPbBr_3$ is combined with PVDF via solution casting method. Optimized incorporation of $CsPbBr_3$ in PVDF matrix induces β phase >90%. PVDF encapsulation of $CsPbBr_3$ also ensures improved stability of perovskite from atmosphere. Photoactive mechanical energy harvester is realized with optimized $CsPbBr_3$-PVDF composite. Energy generation from the PNGs has been revealed under different kind of external stimuli. Operation stability of PNG even after 15,000 cycles and after 4 months showed no discernible changes in output behaviour. Self-powered photodetector with an ability of light detection showed significant change in output voltage and current under light. Functionality enhancement of the

composite based system is explained on the basis of electroactive phase content and the charge transfer in hybrid. To get detail insight of the charge transfer process, density functional theory (DFT) analysis was also performed.

5.2. Characterizations

Powder x-ray diffraction (XRD) patterns of the synthesized samples are recorded on a Bruker D8 diffractometer with Cu-K$_\alpha$ radiation of wavelength 1.5404 Å at room temperature. Field emission scanning electron microscope (FESEM) images are taken to determine the size and morphology of the as-synthesized samples by a HITACHI S4800 electron microscope. UV-Vis reflectance spectra of the samples are recorded by using a Jasco V670 spectrophotometer. Films were characterized using Fourier transform infrared spectroscopy (Shimadzu FTIR spectrometer, IR prestige). Different Raman modes of the samples were analyzed by a high-resolution Raman spectrometer (WITECH) by using an excitation of 532 nm laser source. Compositional analysis of CsPbBr$_3$ and PVDF-CsPbBr$_3$ composite were investigated by x-ray photoelectron spectroscopy (XPS) using a SPECS HSA-3500 hemispherical analyzer with a monochromatic Mg Kα x-ray source. Photoluminescence was recorded on Horiba Jobin Yvon Fluorolog-3 spectrophotometer and Edinburgh F980 instrument. All-time vs voltage measured by KEYSIGHT InfiNiiVision DSOX2012A digital storage oscilloscope. Current−voltage measurements were performed out using a Keithley 2602B dual channel source meter.

5.3. Results and Discussion

5.3.1. Structural, Morphological and Compositional Analysis of CsPbBr$_3$

XRD profile of the as synthesized CsPbBr$_3$, presented in Figure 5.1 a shows diffraction peaks at 2θ = 15.41˚, 21.82˚, 31.07˚, 34.65˚ and 38.02˚ corresponds to (100), (110), (200), (210) and (211) planes respectively. Such positioning of the peaks agrees well with literature and confirms orthorhombic phase formation of CsPbBr$_3$ [5, 19]. Band gap of synthesized CsPbBr$_3$
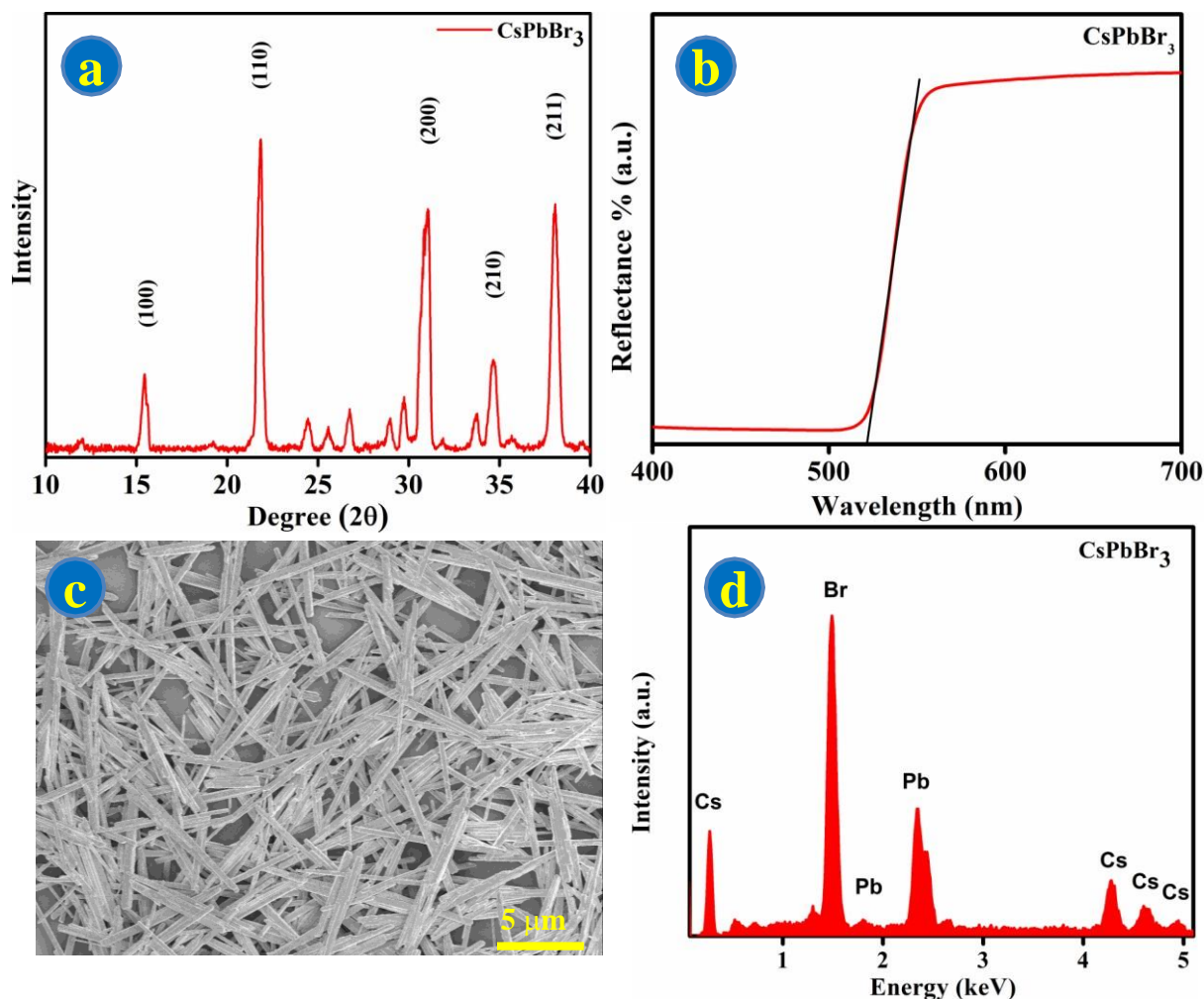
Figure 5.1: *(a) XRD, (b) reflectance spectra, (c) FESEM and (d) EDX spectra of CsPbBr₃.*

is assessed from UV-Vis analysis. Reflectance curve, *i.e.*, reflection (%) as a function of wavelength of CsPbBr$_3$ displayed in Figure 5.1 b shows sharp attenuation around 523 nm. Calculated band gap is found to be ~2.37 eV which also agrees well with the reports. [20] FESEM image of CsPbBr$_3$ shown in Figure 5.1 c depicts morphological uniformity of the synthesized products over large scale. One dimensional rod-like morphology with average diameter and length ~ 600 nm and 10-12 μm respectively is obvious from this image. EDX spectrum of CsPbBr$_3$ rods in Figure 5.1 d reveals the only presence of Cs, Pb and Br. Absence of any impurity related peaks in the EDX profile confirms pure phase formation. Atomic ratio of constituent elements of CsPbBr$_3$ is found to be in the stoichiometric ratio of 1:1:3 which match well with literature. [5]

5.3.2. FTIR Analysis

FTIR spectroscopy was carried out for all the samples to identify the crystalline phase presence and the results are shown in Figure 5.2 a. Characteristics vibrational band at 1150, 976, 796, 764, 613, 532 cm^{-1} are assigned to non-polar α phase of PVDF whereas semi-polar γ phase related characteristics band appeared at 1234, 812 cm^{-1}. [3, 15] Desired β phase vibrational band is peaked at ~1279 cm^{-1} [21, 22]. In general, bare PVDF constitutes low percentage of β phase which limits their usage in energy harvesting application. CsPbBr$_3$ rods acting as filler in PVDF matrix interact with α phase chain and convert into desired β phase. Absorption band intensity of the characteristic peak of α-phase (Fig. 2a) is much stronger for bare PVDF and intensity of these bands decreased gradually with the incorporation of CsPbBr$_3$ up to 5 wt. % of CsPbBr$_3$. While the intensity of the band at 1279 cm^{-1} related to β phase enhanced progressively with the increase of CsPbBr$_3$ content in composite film up to 5 wt. % of perovskites. Superposed band at ~840 cm^{-1} is assigned to ascertain the relative proportion of electroactive phase content samples [15]. Relative electroactive phase content (F_{EA}) for all the samples are assessed using the following equation:

$$F_{EA} = \frac{A_{840}}{\frac{K_{840}}{K_{764}}A_{764} + A_{840}} \times 100\% \tag{5}$$

Where A_{764} and A_{840} are the peak intensity at 764 and 840 cm^{-1} respectively. K_{764} and K_{840} are absorption coefficient corresponding to the aforesaid bands with values 6.1×10^4 and 7.7×10^4 cm^2/mol respectively. [15] Electroactive phase concentration in the samples increased with perovskite content increment up to 5wt. % and thereafter it decreased (Figure 5.2 b). Maximum is as low as 39%. Interaction between positive surface charge of CsPbBr$_3$ and –CH$_2$-CF$_2$–dipole in PVDF chain enhances the electroactive phase percentage in the composite. Due to percentage of F_{EA} is achieved for PCS 5 which is nearly 90% whereas the same for PVDF film low perovskite content in PCS 3 and PCS 4, such interaction is nominal which in turn limits
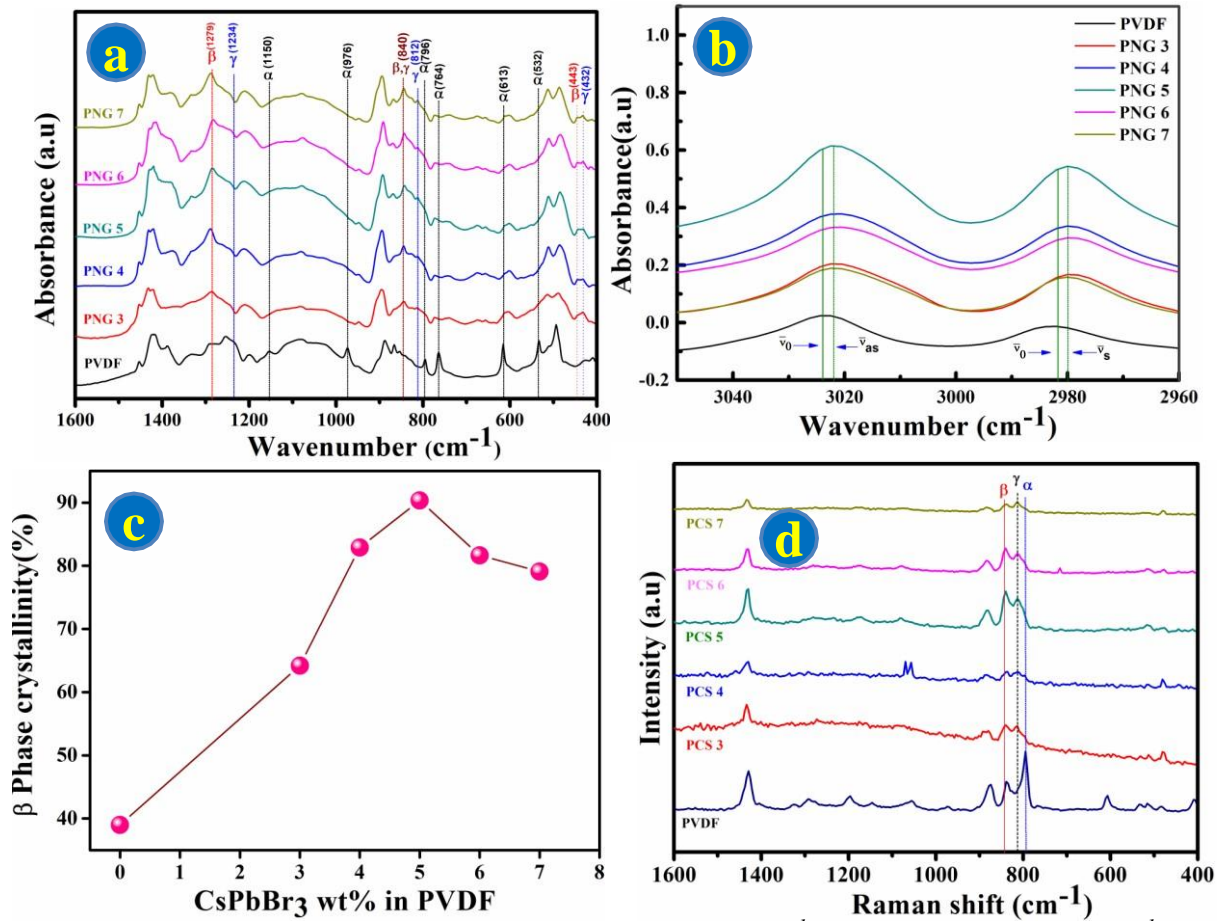
Figure 5.2: *(a) FTIR spectra in the range 1600−400 cm^{-1} and (c) 3050−2960 cm^{-1}, (d) RAMAN spectra of PVDF and composite films. (b) Dependency of electroactive (β) phase on perovskite wt. %.*

the conversion β phase from α phase. With moderately high loading of perovskite (PCS 5), filler distributed throughout the polymer matrix uniformly and more interaction is resulted. Filler concentration beyond 5 wt. %, created agglomeration of perovskite with in the polymer and surface charge interaction with the dipole is lowered. Interfacial interaction of $CsPbBr_3$ and PVDF dipole is obvious from the FTIR spectrum within the range 3050-2960 cm^{-1} in Figure 5.2c. Absorption peaks at ~2980 and ~3023 cm^{-1} related to the symmetric and asymmetric $-CH_2-$ bond stretching respectively have great meaning in analyzing the electroactive phase formation via interfacial interaction. [3] Shifting of these is only accounted due to the disruption of the vibrational bands. Both peaks are blue shifted for the composite films as compared PVDF only which suggests interaction between the perovskite and PVDF

dipole. Increase in interfacial interactions enhanced the effective mass of -CH_2- molecules which further lead to a decrease in vibrational frequency of the aforesaid. Such interaction acts a source of damping. [3] Damping constant is related with angular frequency of -CH_2 stretching vibration dipole under damped and undamped condition. Assessed values of damping constants are found to increase with the perovskite content in the film. It is noteworthy to mention here that F_{EA} and damping constant follow the similar kind of behavior with perovskite loading. Such analogous behavior suggests a direct relationship between β phase formation in PVDF matrix as a consequence of interaction of the diploes with $CsPbBr_3$ [23]. Figure 5.2d represents the Raman spectrum of all the synthesised samples. Vibrational band observed at ~800 cm^{-1} is due to CH_2 bond rocking, associated with the non-polar α phase. [24] Intensity of this peak gradually decreases in composite film. Intensity of Raman peak at ~838 cm^{-1} due to CH_2 rocking, CF_2 stretching and skeletal C–C stretching gradually increased up to 5 wt. % perovskite filling and decreases thereafter. This band denotes the presence of highly polarised β phase in samples. Another peak at ~811 cm^{-1} linked with quite polar γ phase appeared due to CH_2 out of plane wag. [24] Analysis of these peaks also suggested maximum β phase constitution in PCS 5 and corroborated with the FTIR results.

5.3.3. XPS Analysis

Chemical compositions of as well as oxidation states of the constituent elements of $CsPbBr_3$, PVDF and PCS 5 are further confirmed by x-ray photoelectron spectra (XPS). Referencing the C 1s peak positioned at 284.6 eV, all the spectra were charge corrected. XPS spectra of Cs and Pb of $CsPbBr_3$ sample presented in Figure 5.3a and 5.3b exhibited typical doublet features of both. Cs 3d$_{3/2}$ and 3d$_{5/2}$ peaks are observed at ~740.4 and ~726.36 eV while peaks for Pb 4f$_{5/2}$ and 4f$_{7/2}$ are appeared at ~145.46 and ~140.57 eV respectively. Asymmetric Gaussian curve related to Br is deconvoluted to two peaks at ~70.05 and 67.99 eV which correspond to Br 3d$_{3/2}$ and 3d$_{5/2}$ respectively (Figure 5.3c). Such positioning of these peaks suggests that all the
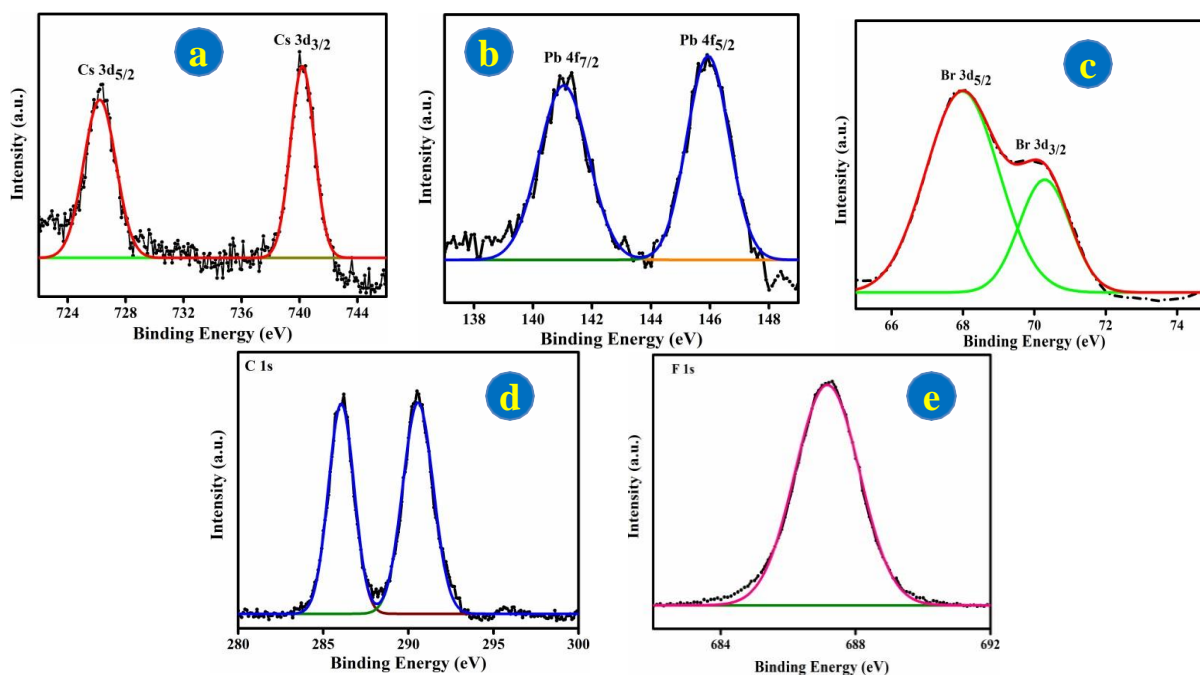
Figure 5.3: *Core level XPS spectra of (a) Cs (b) Pb (c) Br of CsPbBr₃ and (d) C (e) F of PVDF.*

constituent elements (Cs, Pb and Br) are in their normal oxidation state i.e. 1^+, 2^+ and 1^- states [25]. In pristine PVDF, the C1s peak exhibited two components at ~286.1 eV and ~290.5 eV corresponds to CH_2 and CF_2 bond respectively (Figure 5.3d). Fluorine 1s peak is symmetric and well fitted, with a single Gaussian curve that peaks at 687.2 eV (Figure 5.3e). For PCS 5, a C1s and F1s peak is found to be shifted towards higher binding energies whereas the characteristics peaks of $CsPbBr_3$ shift to lower binding energies. Shift in binding energies for PCS 5 with respect to base samples is obvious from the Figure 5.3a-e. Such kind of shifting in binding energies may be accredited to the internal electric field generation due to hybrid formation which affects the local binding energies of the base materials significantly [26].

5.3.4. XRD, UV-Vis and Morphological Analysis

XRD was carried out to explore the crystallinity and phase purity of pristine PVDF, $CsPbBr_3$ and PCS 5 and the result is illustrated in Figure 5.4a. Diffraction peaks at 17.6°, 18.2°, 19.7°, 27.4° and 38.7° are related to (100), (202), (110), (111) and (002) planes of the α-crystalline phase of PVDF. [3] On the other hand, intensity of the aforesaid peaks in PCS 5 is decreased and few new peaks appeared. Diffraction peak at 19.2° corresponds to (002) plane of γ
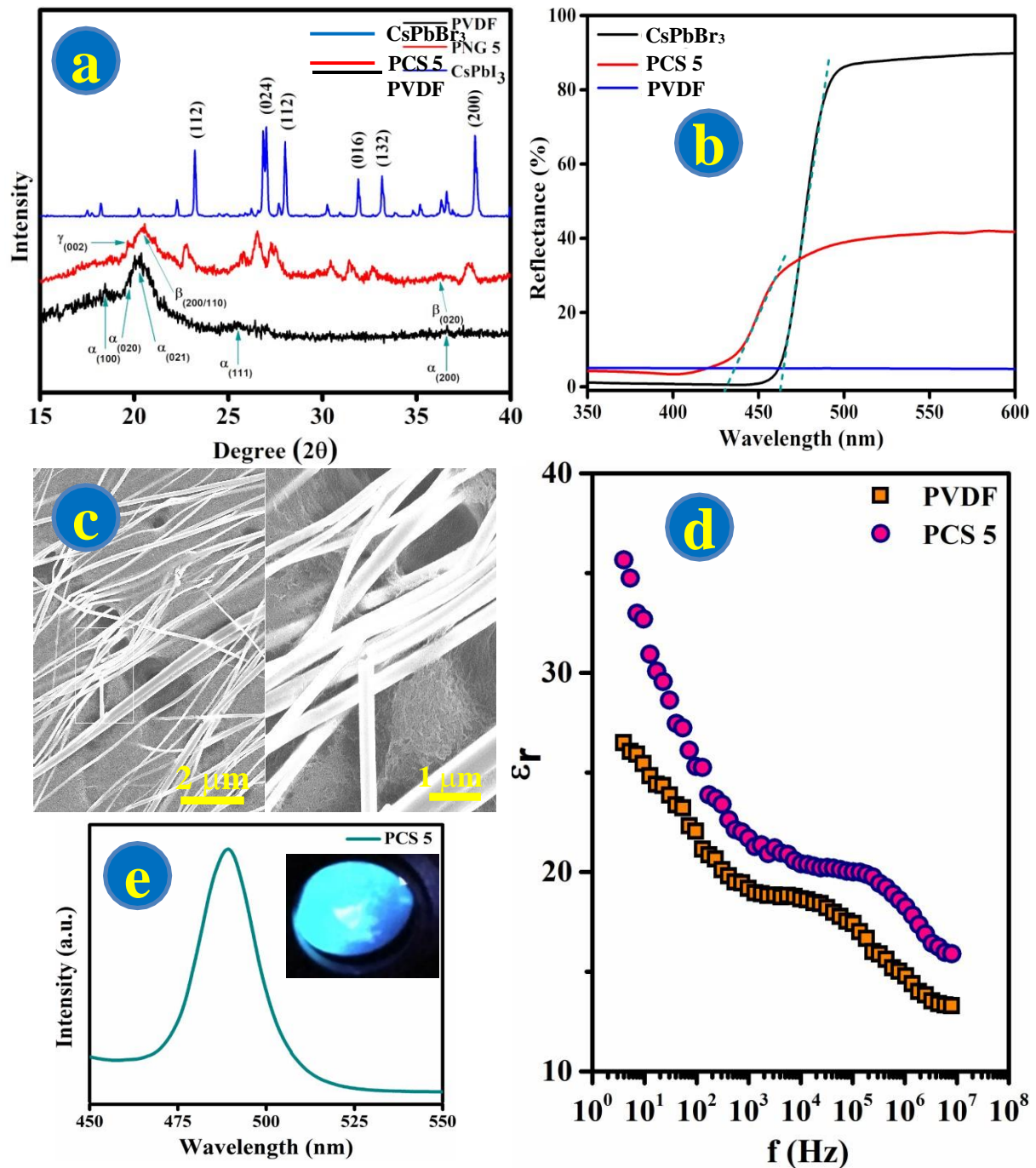
Figure 5.4: *(a) XRD and (b) UV-Vis spectrum for CsPbBr₃, PVDF and PCS 5. (c) FESEM image PCS 5. (d) Dielectric constant of PVDF and PCS 5. (e) PL spectra and image of the PCS 5.*

crystalline phase, a semi-electroactive phase. Peaks in XRD profile of PCS 5 at 20.8° and 37.1° are associated with the (110/200) and (020) plane of electro active β-phase [3]. Reflectance curve, *i.e.*, reflection (%) as a function of wavelength of CsPbBr₃, PVDF and composite displayed in Figure 5.4b. Surface morphology of PCS 5 sample shown in Figure 5.4c suggests

clean and smooth surfaces. No additional impurity particles or no visible cracks are observed which indicated that $CsPbBr_3$ perovskites mixed well within PVDF matrix. Piezoelectric coefficients (d) strongly depend on the dielectric property of material where the dependency is related by following: $d=\varepsilon P_r$, where ε and P_r denote dielectric permittivity and permanent polarization respectively. Figure 5.4d shows frequency response of dielectric constant (ε_r) of PVDF and PCS 5 at room temperature with in the frequency range 10 to 10^7 Hz. Dielectric permittivity of pristine PVDF is found to be 18.7 at 1 kHz. With the introduction of perovskite, dielectric constant increases over entire frequency range. Dielectric permittivity of PCS 5 is found to increase to 22.5 at 1 kHz. This behavior is analogous to the β phase content in the films, as observed from FTIR and XRD results. Careful observation suggests a gradual decrement in permittivity values with the increase in frequency. This is attributed to the dipolar contribution reduction at high frequency region [27]. Figure 5.4e shows photoluminescence spectra of the PCS 5 sample. Sharp photoluminescence peak centered at 488 nm corresponds to a band gap of 2.54 eV. This value is in well accordance with its UV-vis analysis. Photo-image of the PCS 5 sample under UV (365 nm) irradiation is shown in inset of Figure 5.4e. An intense cyan emission originating from band edge of the film is detected. Overall emission is bright enough to be observed by naked eye.

5.3.5. DFT Analysis

Theoretical studies using Vienna ab-initio simulation package (VASP) [28-31] with projector-augmented-wave (PAW) [32, 33] approach has been performed. The exchange-correlation factors were treated within generalized gradient approximation (GGA) using the Perdew–Burke–Ernzerhof (PBE) [34] functional. Γ centered k point meshes of (4×3×4) and (3×8×1) were implemented during the structural optimization and electronic property calculation of pristine $CsPbBr_3$ and PVDF respectively whereas a Γ centered k point mesh of (1×1×1) was used for the sufficiently large composite system. Plane wave basis set up to energy cut-off 600
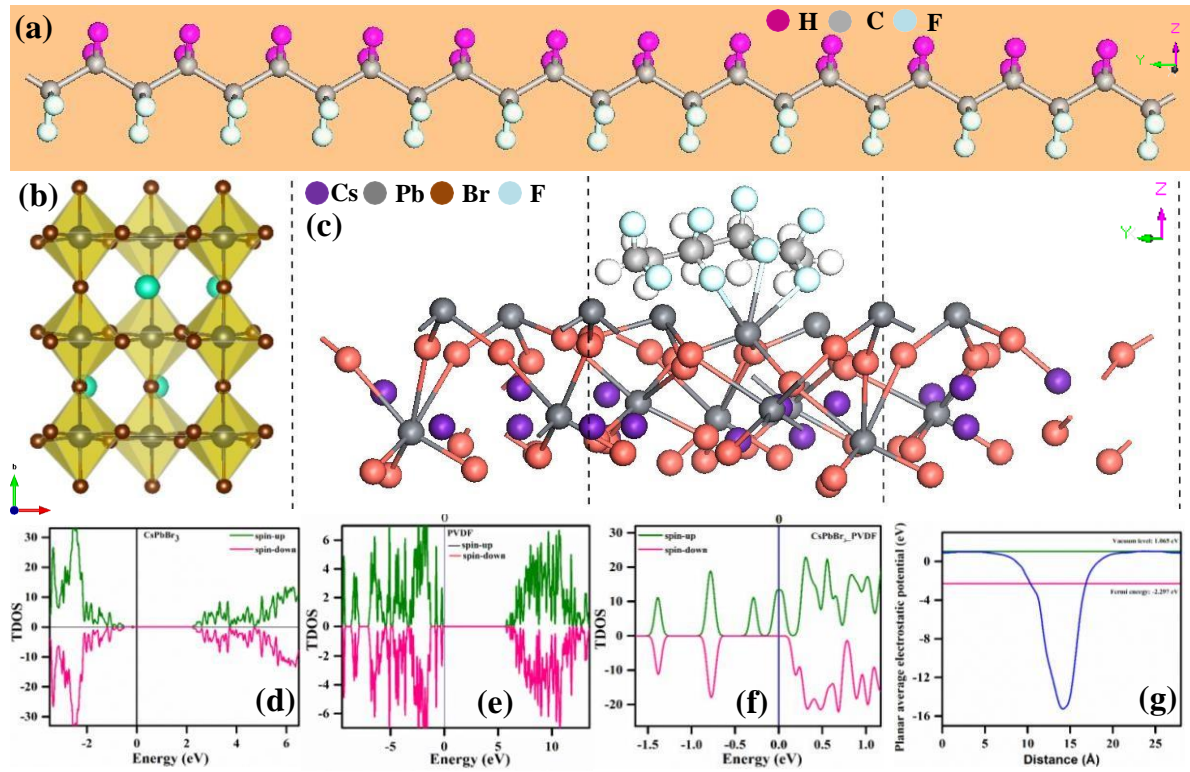
Figure 5.5: *(a) Side view of PVDF chain (b) Side view of orthorhombic CsPbBr$_3$ (c) Top view of CsPbBr$_3$-PVDF. Total density of state of (TDOS) (d) CsPbBr$_3$ (e) PVDF (f) CsPbBr$_3$-PVDF and (g) variation of electrostatic potential with distance from surface for CsPbBr$_3$-PVDF composite.*

eV was applied for all the calculation. The structural relaxation processes were allowed to continue until the total energies converged below 1×10^{-5} eV/atom. Dispersive force corrections were also taken into account via the PBE+D2 force field (Grimme's) method [35]. All the calculations were carried out in spin unrestricted manner. The optimized lattice parameters of orthorhombic pristine CsPbBr$_3$, as found from the first principles calculations are a = 8.244 Å, b = 11.735 Å and c = 8.198 Å. Keeping in line with experiments, it was considered the orthorhombic β phase of PVDF for the theoretical study and the optimized lattice parameters were found to be a = 8.336 Å, b = 4.910 Å and c = 2.583 Å. The optimized PVDF polymer chain and orthorhombic CsPbBr$_3$ perovskite structure is shown in Figure 5.5a and 5.5b respectively. After optimization, PVDF chain was found to be bonded with CsPbBr$_3$ surface via physisorption as shown in Figure 5.5c. From the Figure 5.5c it is confirmed that Pb (lead)

atom of CsPbBr₃ perovskite bonded with F (fluorine) atom of the PVDF chain. Pristine CsPbBr₃ was found to be a semiconductor with band gap value 2.34 eV (Figure 5.5d) whereas pristine PVDF was found to be an insulator with large band gap of value 5.53 eV (Figure 5.5e). For the composite system, PVDF chain has been placed on the Pb rich (110) plane of CsPbBr₃. The electronic properties of the composite system within the framework of GGA has been explored and it is found that the composite behaves as half-metal with zero band gaps for one type of spins (up-spin) and a band of value 0.71 eV for opposite type of spins (down-spin). The defect states near the Fermi level, resulting the metallic character of the composite systems for up-spins were mostly contributed by the Pb and Br atoms, which were close to PVDF chain after physisorption (interacting via weak Van-der-Waals force). TDOS of pristine and composite systems along with their optimized geometries are shown in Figure 5.5f. Also work function of the PVDF–CsPbBr₃ composite was calculated via DFT shown in Figure 5.5g. The value of the work function was calculated to be 3.36 eV.

5.3.6. Performance of Piezoelectric Nanogenerators

To study the piezoelectric response, several kinds of nanogenerators using PCS 3, PCS 4, PCS 5, PCS 6, and PCS 7 composite have been prepared and coined as PNG 3, PNG 4, PNG 5, PNG 6 and PNG 7 where PNG stands for piezoelectric Nanogenerator and the attached numeric with that denotes weight percentage of CsPbBr₃ in the composite. For facile comparison, another device using PVDF has been fabricated and henceforth designate as RNG (reference nanogenerator). Mechanical energy-harvesting features of all the devices were examined without any electrical poling treatment. Piezo response of all the nanogenerators was analyzed by applying repeated hammering with hand (with gloves) in a vertical direction with an amplitude of 100 MPa. Both current and voltage output are found to be higher for the PNGs as compared to the RNG (Figure 5.6a and 5.6b). RNG delivered an open circuit voltage (V_{oc}) 12 volts and short circuit current (I_{sc}) 480 nA. Among all PNGs, PNG 5 showed maximum output
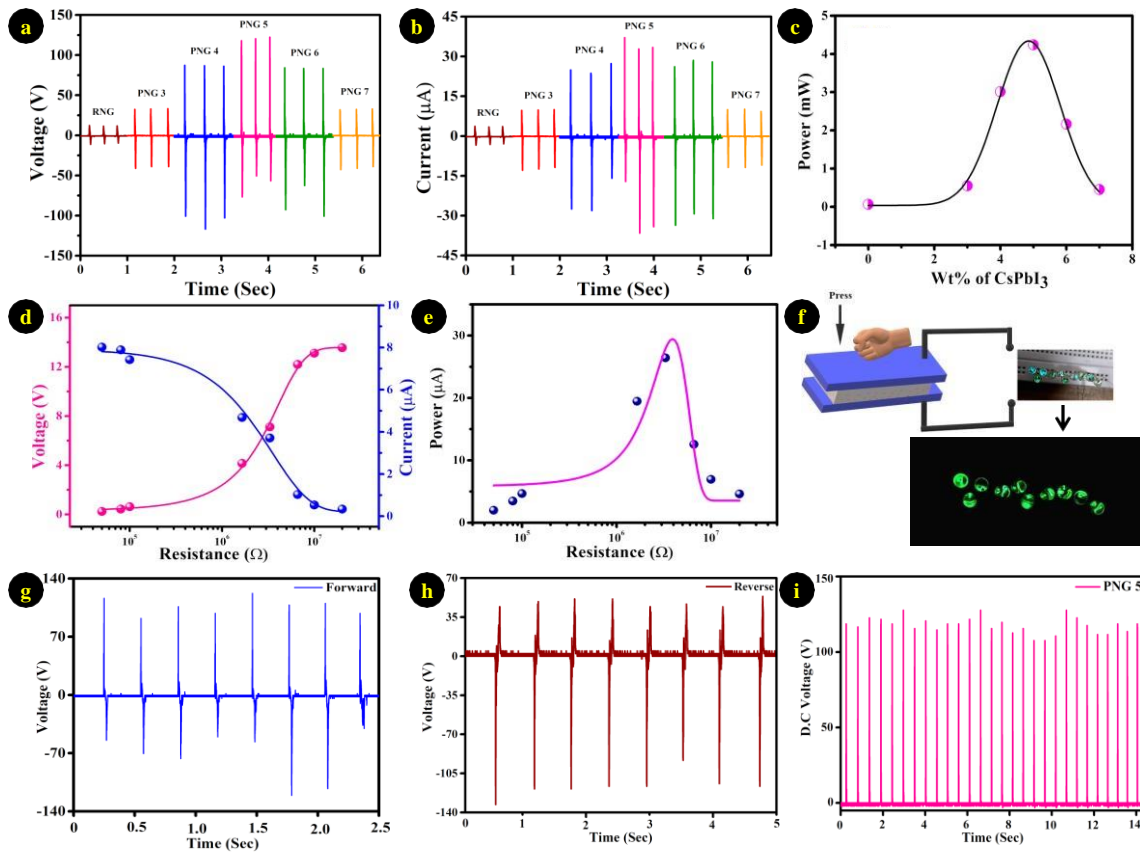
Figure 5.6: *(a) Output voltage (b) current of all the PNGs. (c) output power variation with wt. % CsPbBr3. (d) variation in output voltage and current (e) variation of output power with load resistance for PNG 5 (f) equivalent diagram and glowing of 10 LED bulbs with constant hammering. Output voltage under (g) forward and (h) reverse connection of PNG 5. (i) Rectified DC output voltage of PNG 5.*

voltage of 120 volts and a current of 35 μA. Superior performance delivered by PNG 5 accounted from the maximum percentage electro active phase constitution than others. For such high output characteristics than the other nanogenerators, PNG 5 has been considered as the optimized one and performed further analysis using it. A plausible insight of this phenomenon is the introduction of piezoelectric potential across the surface of film arising out of the deformation in the crystal structure due to mechanical strain. To balance this piezoelectric potential, a charge-induced potential difference between the upper and lower electrodes results which ultimately contributes to effective electrical output. [15] Upon removal

of the external pressure, the piezo-electric potential between the electrodes vanishes, and accumulated charges transport in the direction opposite to the accumulation process thus generating an impulse in a reverse direction. [15] Variation in output power for different wt. % of $CsPbBr_3$ i.e. for different PNGs shown in Figure 5.6c discloses maximum output power with power density of 4 mW/cm^2 at 5 wt. % of $CsPbBr_3$ loading in the composite film (PNG 5). To quantify the instantaneous output power of the nanogenerators, the dependence of output voltage and current on the load resistance (R_L) is studied. R_L is varied from 10 $k\Omega$ to 10 $M\Omega$ while the applied pressure is kept constant (Figure 5.6d). Instantaneous voltage drops (V_L) across the resistances increased gradually with the increment of R_L and gets saturated at high resistance, equivalent to the V_{oc} at a high resistance. In contrast, current (I) is found to decrease with the increase of R_L. Figure 5.6e displays the load resistance vs. power graph. From the graph, the maximum instantaneous power was delivered at a load resistance of 3.5 $M\Omega$ and reached a power of 50 μW. This result suggests that as energy harvesting source PNG 5 is sensitive over a wide range of load resistance. Furthermore, it agrees well with linear circuit theory which measures the internal resistance of PNG 5 of 3.4 $M\Omega$.

To explain the observed piezoelectric performance and account for such noticeable differences among the devices, an understanding of the basic fundamental of non-polarized and piezoelectrically enhanced PVDF is crucial. PVDF, a nonconjugated linear fluorinated hydrocarbon, formed by repeating unit of $-(CH_2-CF_2)-$ carries a vacuum dipole moment of 7×10^{-30} C m pointing roughly from the negative fluorine atom to the positive hydrogen atom. [36] Based on their macromolecular chain conformations of trans and gauge linkage, PVDF generally exhibits four different polymorphs labelled to α, β, γ and δ phase. [36] Both packings of molecules and chain conformations affect the orientation of the dipole. α-phase is a thermodynamically stable polymorph at ambient. Owing to the anti-parallel packing of chains in a unit cell, the dipole moments cancel out, rendering this phase as non-polar one. [37]

Chapter 5

Without any electric poling or mechanical stresses or without a specific temperature PVDF film mostly results in α-phase. Although α phase does not exhibit piezoelectric features, it is usually a precursor of other active piezoelectric phases. [38] In contrast above phase, hydrogen atoms are on one side and fluorine atoms are on the other side of the polymer chain in the β phase. With stronger electron affinity fluorine atoms pull away shared electrons from the hydrogen atoms. Electronegativity differences of these two atoms ensue net dipole moment in a stacked direction inside the β phase. [39] The dipole moment per unit cell is maximum for the β phase as compared to other phases. To obtain the β phase, different strategies have been documented, mainly aiming on inclusion of filler and the development of a suitable processing route. When this stacked polymer chain is subjected to mechanical stress, local dipole distribution changes and an electric field induces in the stack. [40] An induced electric field gathers the charges at top and bottom electrodes, presenting the principle of piezoelectricity. When the electrodes are connected to an external load, the piezo-potential drives electrons to flow through the load. [41] In PVDF, piezoelectricity is mainly governed by volume electrostriction. It is noteworthy to mention here that the presence of fillers in the PVDF matrix might increase the local electric field and can enhance the domain mobility of the localized stress points, thus contributing to improving overall polarization. [40] Here, $CsPbBr_3$ acts as filler. It played a vital role in transferring the non-polar phase of PVDF to a polar one, which helped the hybrid to acquire electroactive features. Increase in perovskite loading up to 5 wt. %, and gradual increment in the β-phase constitution has been occurred. Beyond 5 wt. % loading of the filler, agglomeration of perovskite within PVDF resulted and β-phase concentration decreased. Relying on this, PNG 5 delivered the highest piezo response among all.
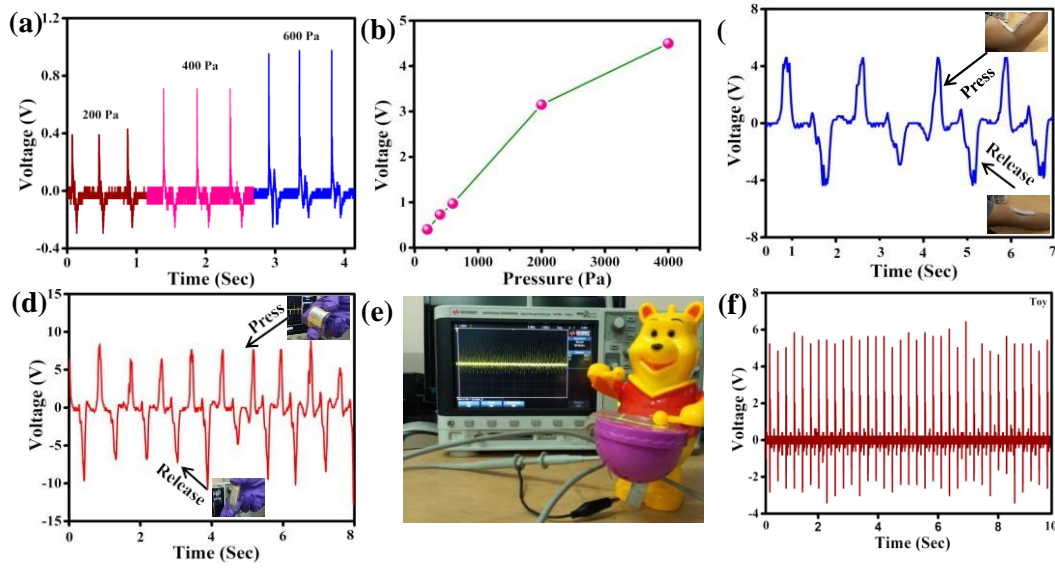
Figure 5.7: *Voltage response of PNG 5 (a) as a function of time for different applied pressures (b) at different applied pressure (c) due to arm bending. (d) Due to finger pressing (e) digital image demonstrates the response of PNG due to the drum beats of a toy. (f) The output voltage of PNG 5 under the impact of drum beats. Inset shows press and release of (c) arm and (d) finger.*

With the increment of electroactive β-phase in the samples dielectric permittivity values also enhanced. Dielectric permittivity of the samples at a particular frequency improved with the filler loading up to 5 wt. % and then it decreases with further perovskite loading. Increase in dielectric constant of $CsPbBr_3$-PVDF composite films due to increase in weight percentage of perovskite ensued an improvement in piezo response since piezoelectric coefficient is directly proportional to the dielectric permittivity of the material. Further, incorporation of $CsPbBr_3$ in PVDF also increased overall crystallinity of the hybrid and the interaction between perovskite and PVDF induced high yield of the β phase. Degree of crystallinity followed the similar kind of behavior as the β-phase content. Piezoelectric coefficient d_{33} of the pristine PVDF and PCS 5 has been calculated. Assessed d_{33} values for PVDF and PCS 5 are found to be 21 and 62 pC/N respectively. This significantly enhanced piezoelectric coefficient also explains the observed enhancement in output response of in composite based devices as compared to PVDF only.

Chapter 5

For the practical usage a PNG 5 was connected to a number of commercially available green light-emitting diodes (LEDs) using a bridge rectifier. Generated power from PNG 5 under periodic compressive and releasing stress is sufficient to turn on 10 LEDs without any storage device, shown in Figure 5.6f. Figure 5.6g and 5.6h shows the output in forward and reverse connection respectively which confirm that the output is due to piezo response. DC outputs signal for PNG 5 presented in Figure 5.6i also suggest a constant output voltage ~120 volts.

To examine the pressure resolved piezo behavior of PNG 5 film, voltage as a function time is monitored under different pressure. PNG with exact pressure sensing ability is desirable for detecting very light touches. To evaluate the sensitivity quantitively, three different pressures, precisely 200, 400 and 600 Pa are applied on PNG 5 film and the electrical responses were monitored. Linear variations of output voltages with different applied pressure is observed (Figure 5.7a) with the applied pressure is 200 Pa, maximum 0.4 V was achieved. Increase in applied pressure to 400 and 600 Pa leads enhancement in output also to 0.8 V and 1.1 V respectively. Almost similar kind of linear relationship is obtained when the applied pressure was increased up to 4 kPa and the output voltage is shown in Figure 5.7b. Several rechargeable electronic gadgets has been charged regularly from the as fabricated device. Replacing energy source for the devices with the energy of PNG is a great alternate. PNG 5 has been fastened in one arm and regularly contracted and expanded the arm. Maximum output ~ 4 V is registered for contraction and expansion of arm (Figure 5.7c). Upon contraction of arm, a pressure is imparted on PNG 5 and it delivered 4 V output voltage. With the release of pressure due to arm expansion, output voltage followed the reverse direction. Such result suggests the usage of PNG 5 as energy source in other human activity like foot striking, jogging etc. Going beyond pressing forces, ability of PNG 5 to detect bending forces was also examined. Voltage vs. time graph presented in Figure 5.7d for slight bending of PNG 5 by finger delivered output voltage of 8 V. Sharp peak was obtained under bending. Upon removal of bending, voltage peaks

appeared in reversed direction. It is necessary to explore the suitability of PNG in real-life applications. To explore the suitability of the PNG 5 in real life applications, The PNG 5 device have been attached upon a drum of a toy (Figure 5.7e). Output voltage was monitored in response to the repeated drum beats of the toy (Figure 5.7f). High output voltage ~5 V generation by PNG 5 under the gentle drum beats opens up its possibility to be used in real life applications.
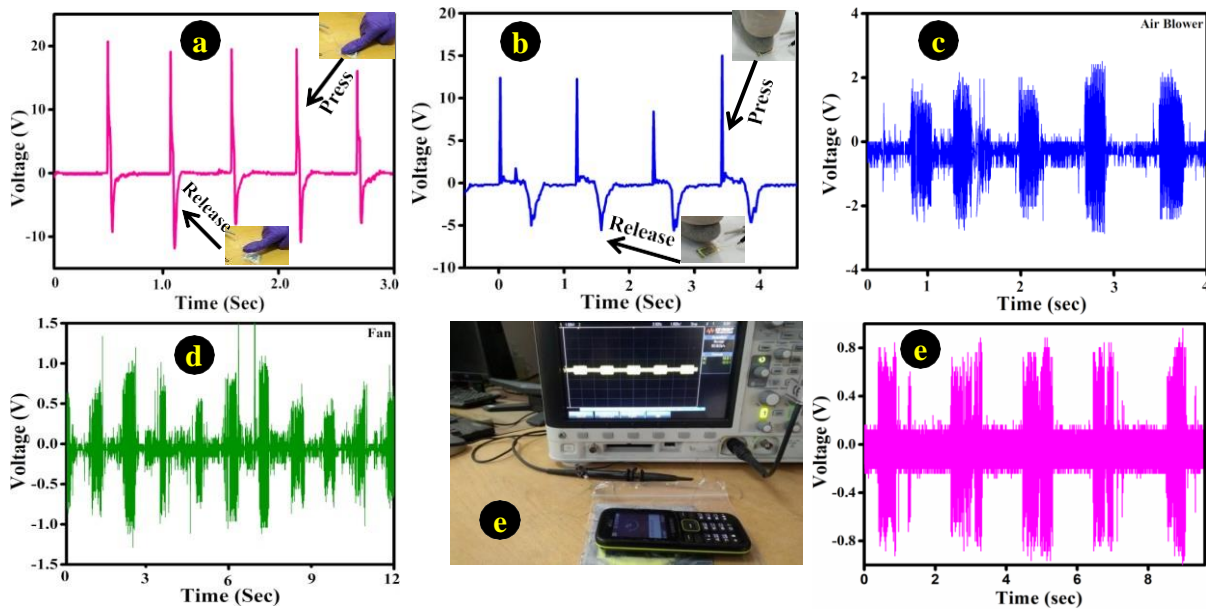
Figure 5.8: *Output voltage of PNG 5 film (a) under the finger tapping (b) under the toe pressing (c) due to air blower pressure (d) due to table fan air pressure (f) due to mobile vibration. (e) Digital image of the piezo-response under mobile vibration.*

Inspired by the above results, the performance of PNG 5 has been tested under several other human movements like tapping by finger and toe. Simple repetitive tapping of index finger on PNG 5 generated 20 V, shown in Figure 5.8a. Almost similar pattern was recorded in reverse direction when the finger tapping was withdrawn. Not only finger tapping, performance of PNG 5 under leg toe impression was also examined. For this experiment, leg toe was pressed repeatedly on the nanogenerator and the corresponding results are presented in Figure 5.8b. A sharp rise of voltage up to 12 V due to the pressure of leg toe indicated the high sensitivity of

PNG 5. Upon removal of toe pressure, voltage gone to reverse direction. Such well-behaved alteration on both sides of the voltage axis (v=0) suggest potential usage of PNG 5 to be attached inside the shoe which will be able to recharge the portable and wearable devices during walking or running. Several countries use wind energy to fulfil their internal energy demand. However, it involves huge wind mill, wind power and other associated machineries which limit their widespread usage. Performance of the PNG 5 was explored under gentle air form commercially available air blower. When an air blower of 800 watt as held 15 cm above PNG 5, output voltage ~ 2 V is registered (Figure 5.8c). This result suggests that PNG 5 can harvest energy from gentle air pressure and it can be used as in air pressure sensor. Figure 5.8d reveals the output voltage about 0.8 V under table fan air pressure. It is interesting to note that voltage responses alter in opposite way due to the vibration caused by table fan air pressure. From the large assortment mechanical energy (energy from wind, acoustics, human movement, etc.) vibrational energy is of utmost valued energy due to its large accessibility at any instant. To check the ability of PNG 5 as vibration sensor, a mobile phone in vibration mode was kept on
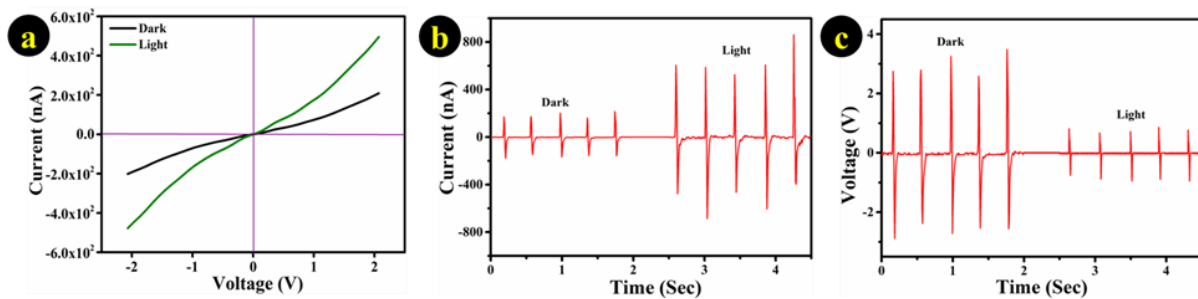
Figure 5.9: *(a) IV characteristics of the detector under dark and light condition (b) change in output current and (c) output voltage under dark and light condition, with same periodic* stress.

it. Output response of the device during mobile calling vibration included periodic alteration of positive and negative voltage peaks (~0.8 V) (Figure 5.8e and 5.8f). When the vibration is in off mode, no response is registered. This result confirmed that PNG can detect mobile vibration and generate electrical response. Not only the air blower but air pressure from regular table fan also generated voltage.

Besides, piezoelectric analysis high optical absorption of PCS 5 as compare to PVDF and perovskite ignites its usage as photodetector. Broad absorption in the visible region for PCS 5 is obvious from the figure which is attributed to the incorporation of $CsPbBr_3$ in PVDF. Absorption in PVDF film solely is forbidden in this region. For the fabrication of photodetector, PCS 5 sample is drop casted over ITO coated PET substrate which serves as one electrode. Conducting carbon tape is pasted on the other side act as another electrode. Further, the entire system is encapsulated with PDMS which ensure flexibility of the device. Prior to all I-V measurement the device is kept under complete darkness which ensures equilibrium conditions attainment. I-V characteristics of PCS 5 presented in Figure 5.9a in both dark and light illumination condition were found to exhibit linear nature which signifies good ohmic character. These curves suggest change in photocurrent under light where photocurrent increases nearly 2 times of its dark value under light.

To use the device for self-powered light detector, piezoelectric energy harvesting under light is examined. Response of the aforesaid device under periodic stress under light and dark condition showed discernible differences in the output characteristics. Output current vs time graph presented in Figure 5.9b suggest an increment in average values of short circuit current under light illumination. On the contrary, under similar kind of stress at regular interval and light decreased the open circuit voltage as compare to dark condition (Figure 5.9c). Such kind of behavior from the device can be explained as follow: under visible light electron-hole pair is generated in $CsPbBr_3$. Photocurrent created from photo generated extra carriers within the sample under light ensues an enhancement in the short circuit current. Furthermore, the photogenerated electron moves within the film and lead to local electromagnetic field enhancement. With such field enhancement orientation of the dipoles in the film interrupts and reduction is open voltage is registered [3, 42].
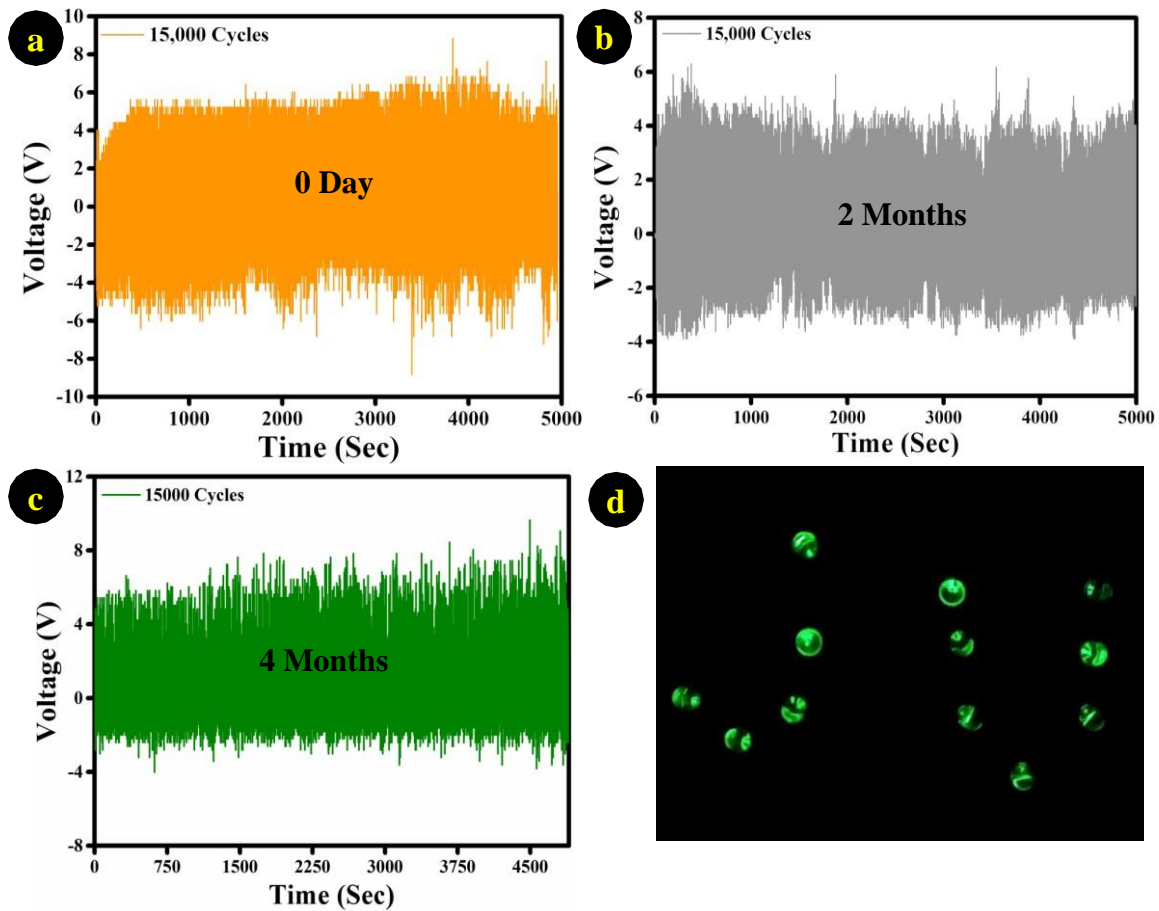
Figure 5.10: *Output voltage recorded over time for continuous 15000 cycles (a) on first day (b) after 2 months (c) after 4 months. (d) Glowing of 12 LEDs designed according to our university name "JU".*

For advance electronic application, a nanogenerator should not only show high output characteristics but also should exhibit long term stability and durability under robust conditions. Cyclic fatigue, an important issue related with nanogenerator was tested via by continuous periodical impacting of PNG 5 for several months by the drum beats of a toy. No discernible diminishment is observed in the output characteristics even after 15,000 cycles (Figure 5.10a). Data were recorded after 2 month (Figure 5.10b) and 4 months (Figure 5.10c). Very nominal change is observed in the output response over the entire period of testing. These results indicate that output performance is not susceptible to the environmental issues like moisture, temperature and etc. Such high stability of PNG 5 with very nominal dip in output characteristics pave a way for developing a robust and effective nanogenerator even in harsh

environmental conditions. Furthermore, to confirm the potential utility of PNG 5 in portable and wearable devices, output behavior of the device was registered under continuous index finger tapping and the output power was used to light up commercially available green LED without any storage devices. A full-wave bridge rectifier was used in the circuit of LEDs to convert the generated power from ac to dc. Generated power from PNG 5 under periodic compression and release of stress was sufficient turn on 12 LEDs designed according to our university name "JU". Result is displayed in Figure 5.10d. Such results established the usage perspective of PNG 5 an energy source for low power wearable electronic devices.

5.4. Conclusions

In conclusion, for the first time, fabrication of piezoelectric nanogenerator using a new class of composited based on simple solution processed all inorganic perovskite $CsPbBr_3$ and PVDF. Concentration of $CsPbBr_3$ is varied in the composite to achieve benchmark level performance. Electroactive phase constitution, degree of crystallinity, optical and energy harvesting features of the samples has been investigated thoroughly. Going beyond regular mechanical stretching and poling techniques, polar phase initiation in PVDF matrix is achieved by $CsPbBr_3$ incorporation. Nucleation of stable electroactive phase in PVDF changes with the subtle variation of $CsPbBr_3$ in the composite and maximum β-phase is obtained for 5 wt% perovskite incorporation. High percentage of β-phase constitution ensures its candidature as an ideal material for piezoelectric energy-harvesting. Besides, electroactive phase induction, PVDF encapsulation improved the stability of the perovskites rod and ensures higher amount of light absorption. Several kinds of external stimulus were applied on the device to check the piezoelectric response. Repeated hammering by hand over PNG 5 produced an output voltage of 120 V. Simple bending of the optimized device by finger generated an open circuit voltage ~10 V. Potential of the device as a vibration sensor was also explored under mobile vibration, air blower and regular table fan. Optimized composite sample-based photodetector delivered

much improved current under light than dark which suggest its promises in light detection. Coupling of the photoactive $CsPbBr_3$ with PVDF ensures visible light detection and leads substantial change in piezoelectric output current 3 times and voltage 2 times. Such results promise the usage of hybrid material for multipurpose applications like piezoelectric energy harvesting, light detection and in hybrid devices and pave the way towards self-powered photodetector.

5.5. References

1. S. H. Lee, C. K. Jeong, G. T. Hwang and K. J. Lee, Nano Energy. 14 (2015) 111−125.

2. S. Li, J. Wang, W. Peng, L. Lin, Y. Zi, S. Wang, G. Zhang and Z. L. Wang, Adv. Energy Mater. 7 (2017) 1602832.

3. A. Sultana, P. Sadhukhan, M. M. Alam, S. Das, T. R. Middya and D. Mandal, ACS appl. Mater. Interfaces 10 (2018) 4121-4130.

4. A. Gaur, S. Tiwari, C. Kumar and P. Maiti, Nanoscale Adv. 1 (2019) 3200-3211

5. T. Paul, B. K. Chatterjee, S. Maiti, S. Sarkar, N. Besra, B. K. Das, K. J. Panigrahi, S. Thakur, U. K. Ghorai and K. K. Chattopadhyay, J. Mater. Chem. C. 6 (2018) 3322-3333.

6. Y. Wang, M. I. Dar, L. K. Ono, T. Zhang, M. Kan, Y. Li, L. Zhang, X. Wang, Y. Yang, X. Gao and Y. Qi, Science 365 (2019) 591-595.

7. A. Pan, Y. Li, Y. Wu, K. Yan, M. J. Jurow, Y. Liu and L. He, Mater. Chem. frontiers 3 (2019) 414-419.

8. Y. C. Chen, H. L. Chou, J. C. Lin, Y. C. Lee, C. W. Pao, J. L. Chen, C. C. Chang, R. Y. Chi, T. R. Kuo, C. W. Lu and D. Y. Wang, J. Phys. Chem. C 123 (2019) 2353-2360.

9. C. T. Huang, J. Song, W. F. Lee, Y. Ding, Z. Gao, Y. Hao, L. J. Chen and Z. L. Wang, J. Am. Chem. Soc. 132 (2010) 4766-4771.

10. K. I. Park, M. Lee, Y. Liu, S. Moon, G. T. Hwang, G. Zhu, J. E. Kim, S. O. Kim, D. K. Kim, Z. L. Wang and K.J. Lee, Adv. Mater. 24 (2012) 2999-3004.

11. L. Li, M. Zhang, M. Rong and W. Ruan, RSC Adv. 4 (2014) 3938-3943.

12. X. Gao, M. Zheng, X. Yan, J. Fu, M. Zhu and Y. Hou, J. Mater. Chem. C 7 (2019) 961-967.

13. S. Jana, S. Garain, S. Sen and D. Mandal, Phys. Chem. Chem. Phys. 17 (2015) 17429-17436.

14. N. L. Meereboer, I. Terzić and K. Loos, Poly. Chem. 10 (2019) 1335-1343.

15. A. Sultana, M. M. Alam, P. Sadhukhan, U. K. Ghorai, S. Das, T. R. Middya, and D. Mandal, Nano Energy 49 (2018) 380-392.

16. R. Ding, H. Liu, X. Zhang, J. Xiao, R. Kishor, H. Sun, B. Zhu, G. Chen, F. Gao, X. Feng and J. Chen, Adv. Funct. Mater. 26 (2016) 7708-7716.

17. T. Paul, B. K. Chatterjee, S. Maiti, N. Besra, S. Thakur, S. Sarkar, K. Chanda, A. Das, P.K. Sarkar, K. Sardar and K. K. Chattopadhyay, AIP Conference Proceedings 1953 (2018) 030085-030089.

18. T. Paul, B. K. Chatterjee, N. Besra, S. Thakur, S. Sarkar and K. K. Chattopadhyay, Materials Today: Proceedings 5 (2018) 2234-2240.

19. T. Paul, S. Maiti, N. Besra, B. K. Chatterjee, B. K. Das, S. Thakur, S. Sarkar, N. S. Das, and K. K. Chattopadhyay, ACS Appl. Nano Mater. 2 (2019) 5942-5951.

20. T. Yang, Y. Zheng, Z. Du, W. Liu, Z. Yang, F. Gao, L. Wang, K.C. Chou, X. Hou and W. Yang, ACS nano 12 (2018) 1611-1617.

21. B. Saravanakumar, S. Soyoon and S.-J. Kim, ACS Appl. Mater. Interfaces 6 (2014) 13716−13723.

22. P. Martins, A. C. Lopes and S. L. Mendez, Prog. Polym. Sci. 39 (2014) 683−706.

23. M. S. Sebastian, A. Larrea, R. Gonçalves, T. Alejo, J. L. Vilas, V. Sebastian, P. Martins and S. Lanceros-Mendez, RSC Adv. 6 (2016) 113007-113015.

Chapter 5

24. A. Peleš, O. Aleksić, V. P. Pavlovi, V. Djoković, R. Dojcilović, Z. Nikolić, F. Marinković, M. Mitrić, V. Blagojević, B. Vlahović and V. B. Pavlović, Phys. Scr. 93 (2018) 105801.

25. T. Paul, D. Das, B. K. Das, S. Sarkar, S. Maiti and K. K. Chattopadhyay, J. Hazard. Mater. 380 (2019) 120855.

26. X. Zhou, C. Shao, S. Yang, X. Li, X. Guo, X. Wang, X. Li and Y. Liu, ACS Sustain. Chem. Eng. 6 (2018) 2316-2323.

27. P. Adhikary, S. Garain and D. Mandal, Phys. Chem. Chem. Phys. 17 (2015) 7275-7281.

28. G. Kresse and J. Hafner, Phys. Rev. B 47 (1993) 558-561.

29. G. Kresse and J. Hafner, Phys. Rev. B 49 (1994) 14251-14269.

30. G. Kresse and J. Hafner, Comput. Mater. Sci. 6 (1996) 15-50.

31. G. Kresse and Furthmüller. J. Phys. Rev. B 54 (1996) 11169-11186.

32. P. E. Blöchl, Phys. Rev. B. 50 (1994) 17953-17979.

33. G. Kresse and D. Joubert, Phys. Rev. B 59 (1999) 1758-1775.

34. J. P. Perdew, K. Burke and M. Ernzerhof, Phys. Rev. Lett. 77 (1996) 3865-3868.

35. S. Grimme, J. comput. chem. 27 (2006) 1787-1799.

36. Z. Yin, B. Tian, Q. Zhu and C. Duan, Polym. 11 (2019) 2033.

37. J. Martín, D. Zhao, T. Lenz, I. Katsouras, D.M. de Leeuw and N. Stingelin, Mater. Horiz. 4 (2017) 408-414.

38. G. Melilli, D. Lairez, D. Gorsea, E. Garcia-Caurel, A. Peinado, O. Cavani, B. Boizot and M.-C. Clochard, Radiat. Phys. Chem. 142 (2018) 54–59.

39. N. Jahan, "Development of the Piezoelectric Properties of Poly(Vinylidene Fluoride) Based Ferroelectrics and Ferroelectrets Using Fillers and Mechanical Stretching." (2018).

40. T. H. Kim and A. C. Arias. "Characterization and applications of piezoelectric polymers." (2015).

41. H. Liu, J. Zhong, C. Lee, S.W. Lee and L. Lin, Appl. Phys. Rev. 5 (2018) 041306.

42. T. K. Sinha, S. K. Ghosh, R. Maiti, S. Jana, B. Adhikari, D. Mandal and S. K. Ray, ACS Appl. Mater. Interfaces 8 (2016) 14986−14993

CHAPTER 6

All-inorganic Halide Perovskite Tuned Robust Mechanical-Energy Harvester: Self driven Posture Monitor and Power Source for Portable Electronics
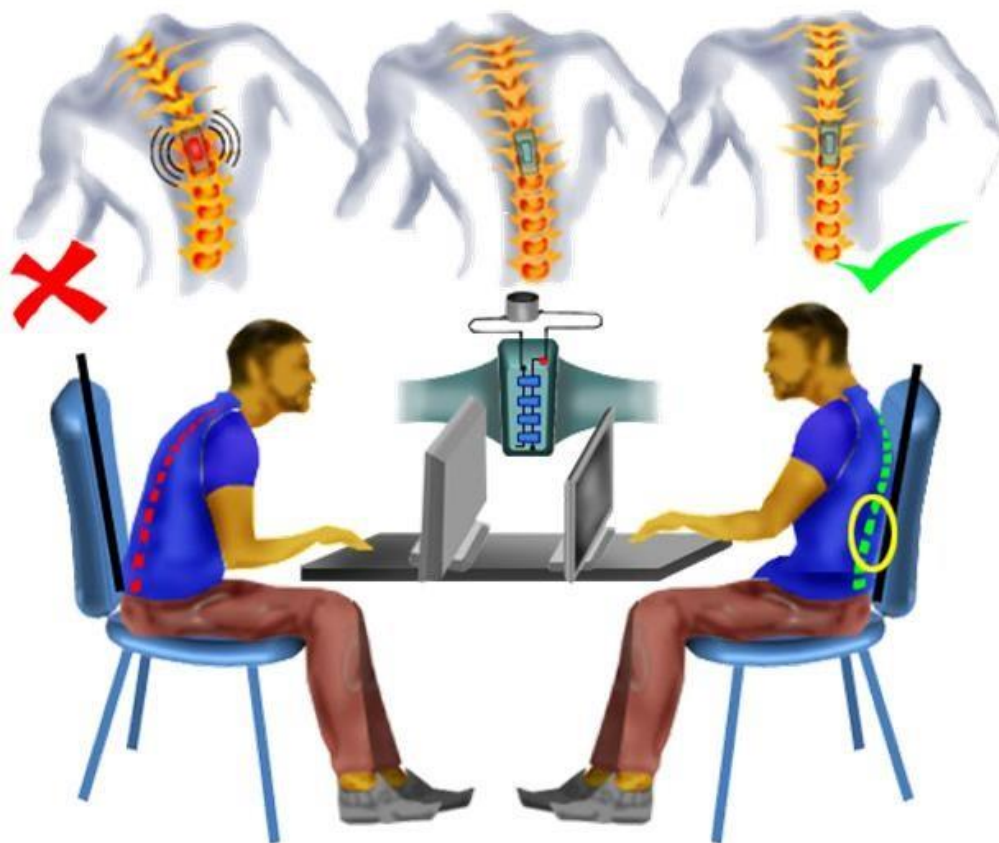
6.1. Introduction

In the 21st century, the world around us is seriously challenged with complicated issues against escalating energy calamity, unremitting environmental disturbances and serious climate change instigated by fast socio-economic progresses, augmented power demands for electronic gadgets, burgeoning dependency over conventional energy resources [1-3]. To cater to this power issue, realization of novel energy harvesters and simple designing techniques for efficient energy generation and storage by exploring sustainable and green energy has become extremely crucial. In particular, optimization of contemporary energy resources management models with the aims of less power consumption from traditional energy resources and building of "battery-free" self-powered, multi-functional electronic systems for environmental monitoring and sensing are two attractive options for this energy movement [4]. Being an environmentally benign and budgetary approach, mechanical energy harvesting is highly appreciated by engineers and scientists where electrical power is generated from ubiquitously available mechanical energy resources around us. Piezoelectric materials are the fittest candidates to exploit this normally wasted mechanical and vibrational energy produced from different sources into electrical signals. The basic mechanism of piezoelectric nanogenerator (PNG) is associated with piezoelectric potential generation in the said materials when they are subjected to dynamic strain under external force, and subsequent transient current flow through the external circuit to balance the potential [5, 6]. Simple structure, relatively small size factor and high durability make these PNGs favourable for use in powering several small power consuming devices, wearable wireless electronics, mobile sensors, and other micro/nano-systems [7]. Output from flexible PNGs is not just limited in energy-harvesting purpose, ability of PNGs to generate different levels of response to mechanical stimuli of variable amplitudes and frequencies with fast response time and high sensitivity vested the realization of self-powered piezoelectric sensors and monitoring system like ambient wind-velocity detection,

vehicle tire pressure monitoring, skin deformation and etc. Over the years, wide variety of PNGs have been documented using several piezoelectric materials like semiconductor (ZnO, CdS, GaN), ceramics (BaTiO$_3$, lead zirconate titanate, sodium niobate), polymer and their copolymer and etc. [8-18] to scavenge energy from biomechanical movement of human body, acoustic/ultrasonic waves, light wind and etc. Despite their high piezoelectric features inorganic semiconductors and ceramics are inherently brittle in nature and generally processed at stringent experimental conditions which restrict their efficacy in modish portable electronic gadgets and in emergent internet-of-things. On the contrary, ferroelectric polymer and its copolymer show processing simplicity, better mechanical flexibility, and notable biocompatibility. However, owing to the low piezoelectric coefficient of pristine polymer and their copolymers, PNGs based on these materials showed low-throughput as compared to those of inorganic PNGs, which is inadequate to run the self-powered system continuously. There has since been a continuous effort in rational construction of high-performance wearable piezo systems with high sensitivity, mechanical flexibility and benchmark power-generation. Among all documented protocols, rational hybridization of high flexibility ferroelectric polymer matrix with the high piezoelectric inorganic fillers to achieve high piezoelectric features with high flexibility and robustness from a single unit is a widely accepted route [19, 20].

From the large assortment of known ferroelectric polymers, poly (vinylidene fluoride) (PVDF) and its copolymer are the most studied piezoelectric materials because of its preeminent physical properties. This semi-crystalline polymer possesses at least four different polymorphs namely α, β, γ, and δ phases among which β phase has highest dipole moment per unit volume and is the most desired phase for energy harvesting application [21-25]. To induce more electroactive β-phase formation as well as to improve the dielectric properties of PVDF, impregnation of the polymer matrix by perovskite is very alluring. Despite the conspicuous progress reported in this regard, most of the systems have adopted high temperature processed

perovskites which possess several limitation and incompatibility issues for self-powering wearable electronics, leaving a vast scope of development in this field by low-temperature, budgetary protocols [26-29]. All-inorganic halide perovskites in well-known ABX_3 chemical formula, (A and B are two different cations and X is halide) generally synthesised at low temperature (<100°C) have already enumerated their sovereignty in diverse application systems due to their unique optical and electronic features [30-33]. These perovskites not only offered optical eminence also presented prominent piezoelectricity because of their piezo- and ferro-electric responses [34-39].

In this experimental out turn, for first time (to the best of the authors' knowledge), the usage of all inorganic chemically processed $CsPbCl_3$ within the PVDF matrix for mechanical energy harvesting has been realized. Prior to this, only two works presented the fabrication of all inorganic lead halide perovskite-PVDF based nanogenerators. However, both works are on $CsPbBr_3$ [30, 40]. Introduction of perovskite filler not only increases the desired electroactive β phase also improves the overall dielectric constant and crystallinity of the hybrid film. Enhancement of these parameters ensures high piezo response from the hybrid as compared to pristine samples as ultimate performance of the device is highly dependent on them. Perovskite concentration in hybrids was also adjusted in subtle manner for device performance optimization. Desired electroactive β phase increased >86% in the optimized hybrid which nearly 2.5-fold of the bare PVDF film. The fabricated PNG based on 3 wt% $CsPbCl_3$ loading generated an output voltage (168 V) and current (2 μA), under simple hand hammering (~100 MPa pressure). Energy harvesting by the PNGs were monitored under different kind of external stimuli. Energy generated from PNG can light an array of commercially available LED without any external bias. Optimized PNG is further utilized to address two important applications namely posture sensor and portable charging system. Currently, assessment and monitoring of human health issues are limited to hospitals and medical clinic as most of the conventional

testing systems are not portable, heavy and depend on bulky power sources. Prolonged sedentary work and bad sitting posture in our workplace for much of the day have several adverse health effects and frequently lead to cardio-metabolic disease, musculoskeletal disorders, coronary artery disease and etc. [41] Most of the office workers who work at the computer in flexed head and neck postures often suffer from severe shoulder pain, back pain and body ache. However, little attention has been devoted to address this serious issue despite the past reports linking it to chronic pain and fatal disorders [7]. Considering its flexibility and high electrical output performance, optimized PNG was further utilized for the fabrication of wearable self-powered posture sensor which could help to rectify the siting and standing posture. Another important issue i.e., the non-availability of electricity for powering our daily used electronic devices in several places was circumvented with help of optimized PNG [42, 43]. Herein, a portable charger has been devised where the energy in the system is stored in expense of the steps took during walking. This device harnessed the voltage generated across the PNG kept within the shoe sole and stored it in a battery which can be exploited further to charge portable devices whenever needed. Flexible and wearable device realized this work will present an opening to evolve our society into a smart world especially in bio-mechanical movement sensing and efficient energy harvesting from PNGs.

6.2. Characterizations and Measurements

The surface morphology of the films was examined using Field Emission Scanning Electron Microscope (FESEM: HITACHI S-4800). X-ray diffraction analysis was performed by employing Bruker D8 diffractometer with Cu-Kα radiation of wavelength 1.5404 Ǻ. FT-IR spectrum was recorded in shimadzu IRprestige-21 spectrometer. Raman spectra were recorded in a WITec ALPHA300 RS confocal Raman spectrometer employing an Nd: YAG laser (532 nm). Dielectric behaviour and impedance spectra were monitored using Agilent 4294A

precision impedance analyser. Electrical polarization hysteresis curves (P-E loop) were obtained from the Precision Premier II ferroelectric tester of Radiant Technologies, Inc. using standard bipolar waveform. To detect output voltage, a digital storage oscilloscope (KEYSIGHT InfiNiiVision DSOX2012A, Digital storage oscilloscope, 100 MHz, 2 GSa/s, input impedance 1 MΩ) was directly connected with the nanogenerator, whereas the piezoelectric current was calculated from the voltage across a known load resistance (R_L) connected in series with nanogenerator.

6.3. Results and Discussion

6.3.1. Structural, Morphological and Compositional Analysis of $CsPbCl_3$

Figure 6.1a shows the XRD profile of the synthesized perovskite. Positioning of all the peaks in this pattern agrees well with literature and signifies the formation of $CsPbCl_3$ in cubic phase (PDF No: 00-018-0366) [47]. XRD data is refined by using Fullprof software and the result is displayed in figure 6.1b. It confirms that $CsPbCl_3$ is a cubic lattice system and belongs to Pm-3m space group. The assessed value of lattice constant is 5.91A°. This refinement confirms the phase purity of the synthesized product. The crystal structure of a unit cell of $CsPbCl_3$ is drawn by VESTA and shown in the inset (figure 6.1b). Figure 1c denotes the array of three-unit cell of $CsPbCl_3$ along X, Y and Z direction, drawn using VESTA software. Morphology of the synthesized product is manifested in figure 6.1d. Cube shaped particles with irregular edges are prominent in this image. Average size of one side of these cubes is ~ 200 nm. This image also suggests large scale morphological uniformity of the product over the scanned area. HRTEM image of the cube presented in figure 6.1e reveals well defined lattice fringes running
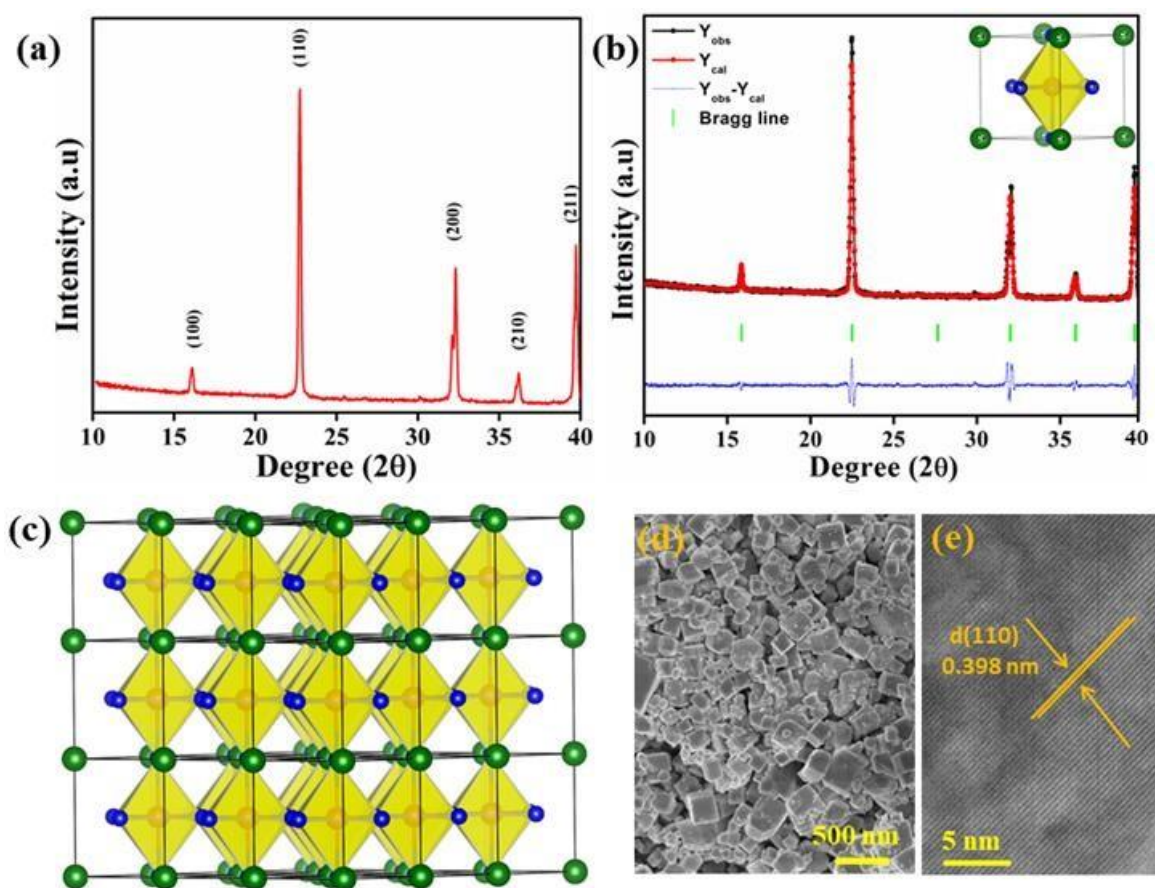
Figure 6.1: *(a) XRD profile (b) rietveld refinement (c) crystal structure (d) FESEM (e) TEM image of CsPbCl₃.*

parallel with a spacing of 0.398 nm corresponding to (110) planes of cubic $CsPbCl_3$. No further peaks are observed related to any impurity element which further authenticates phase purity of $CsPbCl_3$ and corroborates with the aforesaid XRD result. Stoichiometric ratio of the constituent elements as found from the EDS analysis is found to be 19:20:61 which also is in accordance with the previous report [48].

6.3.2. FTIR & Raman Analysis

FTIR spectral investigation of the pristine PVDF and all PVDF-$CsPbCl_3$ hybrid were carried out to explore the crystallinity as well as perovskite induced electroactive phase constitution in the hybrid. For facile understanding, henceforth the hybrid samples are labelled as PPF 1, PPF 2, PPF 3 and PPF 4 where the attached numeric number denotes the concentration of $CsPbCl_3$

in the film and pristine PVDF film is coined as PVDF. Incorporation of perovskite had significant impact on the crystalline phase transformation in PVDF which is obvious from the spectra shown in figure 6.2a. Spectra within the window of 1600-400 cm^{-1} reveal absorption bands at 612, 764, 796, and 976 cm^{-1} correspond to α-phase of PVDF (TGTG configuration) [25, 49]. Electroactive β phase appears at 841 cm^{-1} while the γ-phase of PVDF appears at 811 cm^{-1} [25, 30]. As seen from this figure, pristine PVDF largely crystallized in non-electroactive α phase. Incorporation of perovskite in PVDF matrix resulted in a drastic reduction in α peaks' intensity with a concomitant increment in the peak intensity of β phase. Increasing perovskite content to 3 wt % suppressed the entire α-peaks monotonically and ensured intense β peak. With 3 wt% CsPbCl$_3$ loading, β phase percentage reached >86% which is more than two-folds of the same in pristine PVDF (~ 40%). Further, increments in CsPbCl$_3$ contain up to 4 wt % led in re-emergence of α-phase, perhaps due to the aggregation of the perovskite in PVDF matrix at higher loading. Variation in electroactive phase constitution as function of perovskite loading is presented in figure 6.2b [21-25]. Enhancement of the β phase percentage in PVDF matrix generally results from the interfacial interaction of surface charge of CsPbCl$_3$ and –CH$_2$– and –CF$_2$– dipoles of the PVDF chain. This interaction facilitates favoured ordering of PVDF chains and thereby shifting in chain conformation from α (TGTG) to β (TTTT). As obtained, the vibrational band shifted towards the lower frequency region due to symmetric (v_s) and asymmetric (v_{as}) stretching vibration. As a consequence of such interfacial interaction, effective mass of –CH$_2$– dipole increased. This further resulted in damping in the system and consequently stretching the vibrational frequency (v_s) of –CH$_2$– group of PVDF shifted towards the lower frequency region [23, 24, 39, 50]. To get more insight about the aforesaid interaction, damping constants of all the samples are calculated. Damping frequency (ω), natural frequency (ω$_0$) and damping constant (r$_{dc}$) are related by the following equation [23, 24, 50].
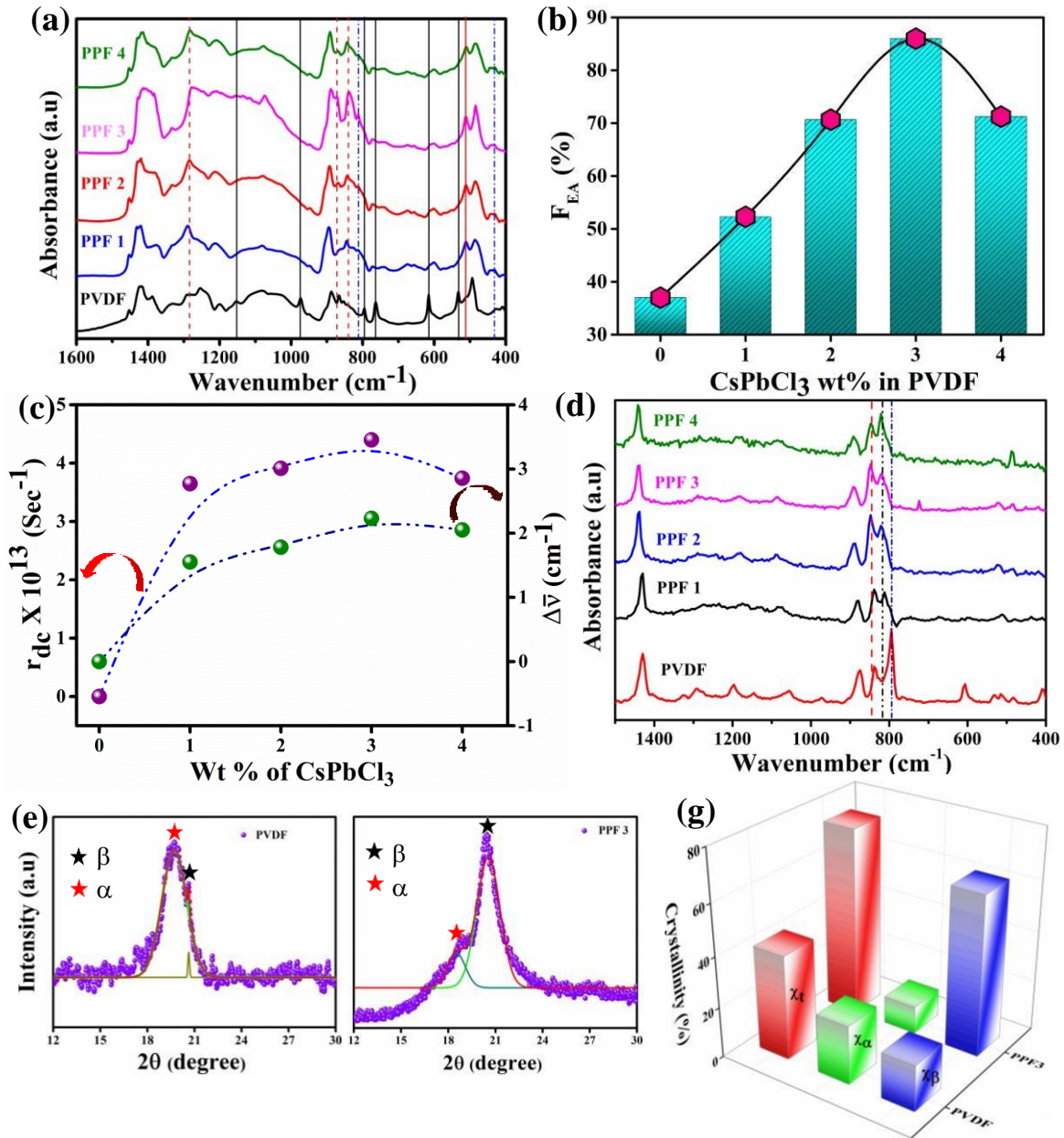
Figure 6.2: *(a) FTIR spectra of all synthesized films, (b) Variation in β phase concentration and (c) r_{dc} and $\overline{v}$ values with different wt. % perovskite loading, (d) Raman spectra of all films; (e) XRD profile of PVDF and PPF 3 within the range 2θ = 16-23˚; (f) crystallinity variation of different phases in PVDF and hybrids.*

$$\omega^2 = \omega_0{}^2 - r_{dc}{}^2 \tag{6.1}$$

In terms of wavenumber, the above equation can be written as,

$$\overline{v} = \left[\overline{v}_0{}^2 - \left(\frac{r_{dc}}{2\pi c}\right)^2\right]^{1/2} \tag{6.2}$$

Where c denotes the velocity of light in a vacuum. Assessed values of r_{dc} and $\overline{\nu}$ for all samples are presented in figure 6.2c. Changes of r_d and $\overline{\nu}$ values for different $CsPbCl_3$ loading are analogous with the electroactive phase content in the sample. This implies direct association between the β phase formation in PVDF due to aforementioned interfacial interaction and $CsPbCl_3$ [39, 30].

Raman spectra of PVDF and all composite films are plotted in figure 6.2d. Intense band-related non-polar α component appeared at 796 cm^{-1} in case of pristine polymer due to $-CH_2-$ rocking. This peak almost disappeared in composite systems and one additional peak associated with γ phase was born at ~812 cm^{-1} due to the out of plane wagging of the $-CH_2-$ dipole. Band at 841 cm^{-1} confirms the presence of electroactive β phase. It also indicates coexistence of $-CH_2-$ rocking, $-CF_2-$ stretching and skeletal C-C stretching [51, 52]. Intensity of this peak gradually enhanced with perovskite. Such a trend in β phase content follows analogous trend as observed in FTIR.

6.3.3. Structural and Morphological Analysis of PVDF/CsPbCl$_3$ Composites

Crystalline structures of PVDF and PPF 3 were further examined using XRD (figure 6.2e-f). Peaks at 18.6° and 20.88° are attributed to nonpolar α-phase and polar β-phase respectively. These profiles also comprise a small peak at 19.3^0 corresponding to the semi-polar γ phase [30, 53, 54]. In PPF 3, intensity of the 18.6^0 diminished by a large amount while the intensity of the peak at 20.88° significantly improved. This result is in accordance with FTIR analysis. Degrees of total, α and β phase crystallinity for all the samples is further calculated from deconvoluted XRD peaks. Crystallinity variation in these samples is shown in figure 6.2f. EDX scan profile of the PPF 3 sample presented in figure 6.3a suggest presence of C, F, Cs, Pb and Cl only. EDX elemental mapping of PPF 3 under FESEM confirms uniform distribution of all the constituent elements, thus successful preparation of CsPbCl$_3$-PVDF hybrid.
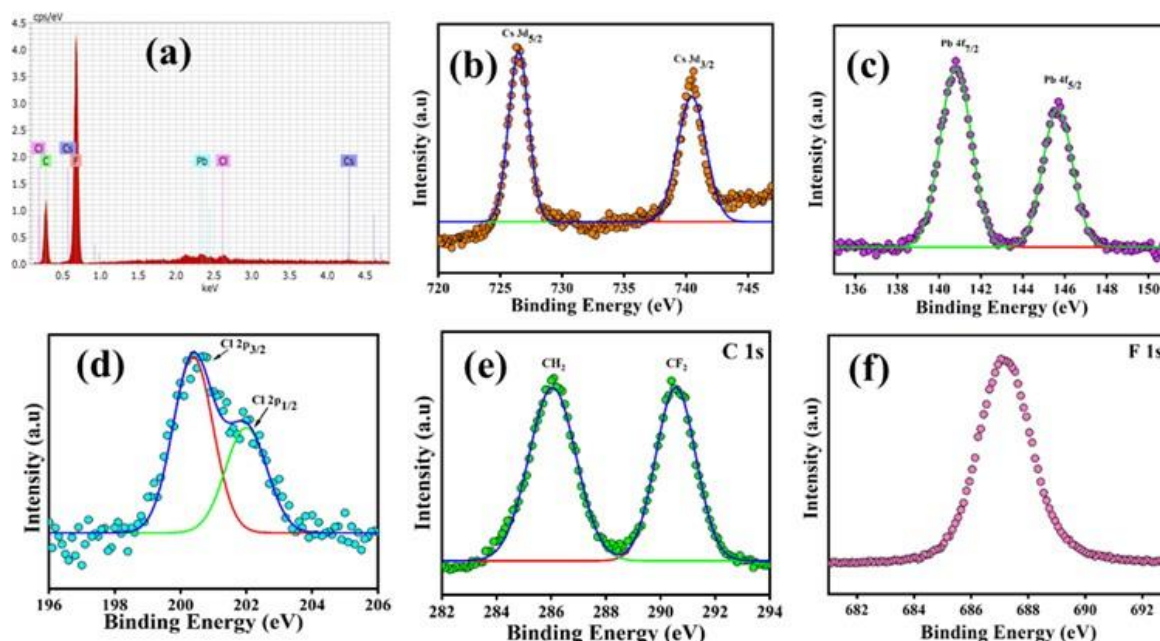
***Figure 6.3:** (a) EDX scan; XPS spectra of (b) Cs 3d (c) Pb 4f (d) Cl 2p (e) C 1s (f) F 1s of PPF 3.*

6.3.4. XPS Analysis

XPS analysis of the same hybrid is further carried out and the results are shown in figure 6.3(b-e). High resolution XPS spectra of Cs and Pb in the figure 6.3b and 6.3c reveal typical doublet features. Peaks appearing at ~740.4 and ~726.3 eV are associated with Cs $3d_{3/2}$ and $3d_{5/2}$ peaks respectively [30]. On the other hand, for Pb, peaks are observed at ~145.4 and ~140.5 eV which are related to $4f_{5/2}$ and $4f_{7/2}$ respectively [30]. Deconvoluted peaks of Cl $2P_{1/2}$ and Cl $2P_{3/2}$ appeared at ~198.8 and~197.2 eV respectively (figure 6.3d). Such positioning of peaks suggests the 1^+, 2^+, 1^- oxidation state of Cs, Pb, Cl respectively [55]. Peak related to C1s showed two components. Peaks at ~286.1 eV and ~290.5 eV can be indexed to CH_2 and CF_2 bond respectively (figure 6.3e). Symmetric peak of F 1s appeared at ~687.2 eV. Such positioning of F 1s is found slightly shifted from the normal PVDF. This shifting may be accredited to electric field generation internally due to the hybrid formation [30]. Finally, no peaks related to any

other impurities are observed in the survey scan. This corroborates with EDX results and signifies the successful preparation of the hybrid.

6.3.5. P-E loop and Dielectric Property of PVDF/CsPbCl$_3$ Composites

Figure 6.4a shows the P-E hysteresis loop of all the samples, monitored by sweeping the electric field (E) in a window of $\pm$ 100 kV/cm at room temperature. The remanant polarization (P$_r$) for PVDF is 0.01 μC/cm^2. This value is increased significantly to 0.17 μC/cm^2 in PPF 3. Under an applied field of 100 kV/cm, the saturation polarisations for PVDF and PPF 3 attained 0.65 and 2.81 μC/cm^2 respectively. Comparison of these loops suggests maximum values of the remanant and saturation polarization for PPF 3. Such increment in remanant polarization and saturation polarization in PPF 3 indicates higher dipole moment per unit volume in PVDF chain (CH$_2$-CF$_2$) present in the hybrid. Much lower remanant polarization for PVDF than the hybrid is due to less dipole-dipole interaction. Pristine PVDF is largely composed of α phase having no dipole moment, while the composite is largely composed of electroactive β phase with higher dipole moment. Addition of perovskite in PVDF eases the dipole alignment in the hybrid system which ensued in the higher values of remanant polarization. Such high remanant polarization is expected to produce higher piezo output. Variation in remanant and saturation polarization of the samples as function of incorporated perovskite concentrations is presented in inset of figure 6.4a. Remanant polarization of the sample is found to increase steadily with increases in the perovskite content. It is found that the energy storage density of the hybrid is much higher than the PVDF under a given electric field. This enhancement may be attributed to dielectric constant increase due to homogeneous distribution of perovskite and interface compatibility enhancement in the polymer matrix [56].

Coupling of perovskites with PVDF also influenced the dielectric behaviour of hybrids. Dielectric constant (ε_r), dielectric loss (tanδ) and AC conductivity (σ) plotted as functions of
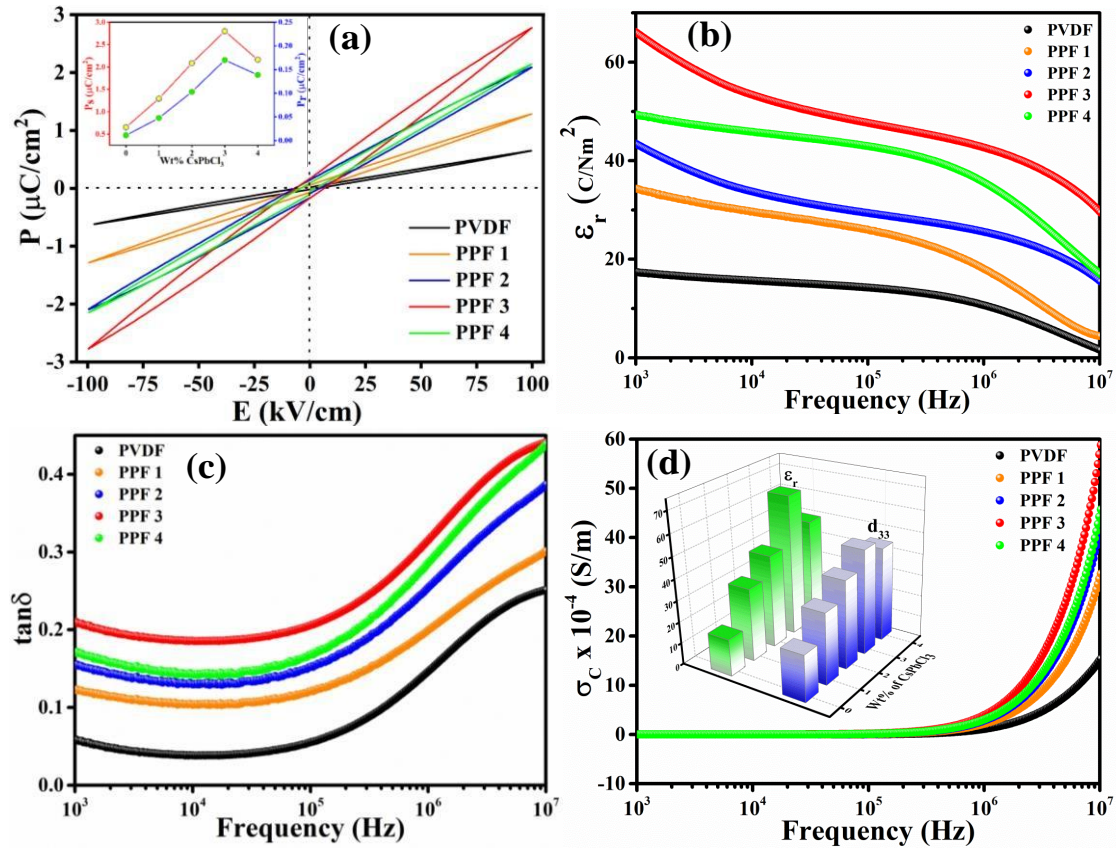
Figure 6.4: *(a) P-E loop of PVDF and all the hybrid films (inset shows variation in remanant and saturation polarisation as a function of perovskite loading) (b) variation of ε_r with frequency (c) variation of dielectric loss with frequency (d) variation in conductivity of PVDF and hybrid films with frequency. Inset shows variation in ε_r and d_{33} values with respect to perovskite loading.*

frequency respectively ranging from 1 kHz to 10 MHz of all samples are manifested in figure 6.4b-c. In comparison to pristine PVDF, ε_r values of the hybrid films increased up to 3 wt % of perovskite incorporation. Afterwards, it decreased for higher $CsPbCl_3$ containing films. Overall increment in ε_r values in hybrids as compared to PVDF indicate the impact of $CsPbCl_3$ amalgamation. Reduction in ε_r value at larger amount of $CsPbCl_3$ incorporation may occur due to the agglomeration [57]. Similar kind of variation in ε_r values as function doping concertation are also observed by several other researchers [4, 58, 59]. This figure also suggests a rapid step down in ε_r values for the hybrid samples with increasing frequency. Perovskite incorporation

in hybrid increases the interfacial space charge which ensures more space charge polarization and subsequently the ε_r value increases. At low frequencies, all kinds of polarisations namely ionic, electronic, interfacial and dipolar lead to significant increment in ε_r with respect to a fixed applied voltage. In contrast, the aforesaid values are reduced at high frequency in the applied frequency window due to weakening of interfacial/space polarization [60]. Figure 6.4c shows the variation of dielectric loss as a function of frequency. Dielectric loss of pristine PVDF is ~ 0.06 at 1 kHz, whereas the hybrid films showed the same that ranged from 0.12 to 0.21. The dielectric loss of all the films increased above 10 kHz due to a relaxation loss of PVDF. Such nominal dielectric loss over this inspected frequency window suggests the figure of merit of hybrid films. AC electrical conductivity of all samples is plotted in figure 6.4d. AC conductivity of the hybrid film is increased due to perovskite incorporation. This conductivity enhancement resulted in enhanced output current from the device. AC conductivity is low at low frequency regime. This may result from a high polarization effect and relatively high relaxation time for dipole orientation in the direction of the field. Then again, values of the same increase at high frequency. Polarization effect becomes insignificant at high frequency. Also, the dipoles take less time to themselves along the applied field [24] Dielectric constant of material is directly related with piezoelectric coefficient. With elevated piezoelectric constant as well as remanent polarization the piezoelectric features of the hybrid films increase. The dielectric constants and piezoelectric coefficient (d_{33}) of PVDF and hybrid films as a function of $CsPbCl_3$ wt % are compared in the inset of figure 6.4d.

6.3.6. Performance of Piezoelectric Nanogenerators

To evaluate the piezo output voltage from the fabricated nanogenerators as a function of different base material and the applied periodic force, films with dimension of 1×1 cm^2 were used for nanogenerator fabrication. We fabricated several nanogenerators using hybrid samples
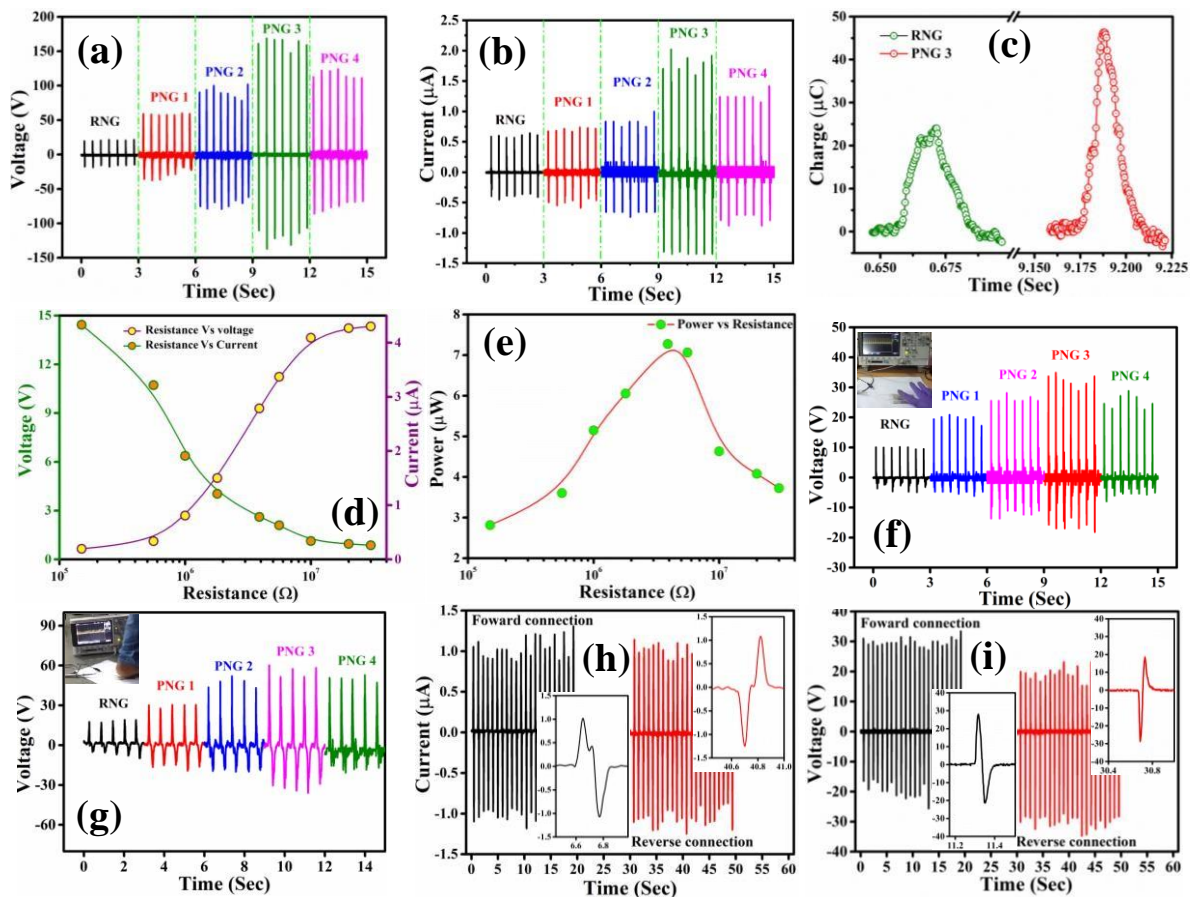
Figure 6.5: *(a) Output voltage (b) current from RNG and PNG due to hand hammering; (c) charging comparison of RNG and PNG 3. (d) Output voltage and current and (e) instantaneous power across load resistance. Output voltage generated from PNGs due to (f) finger tapping (g) leg pressing. (h) Output current in forward and reverse connection and (i) output voltage in forward and reverse connection (inset shows zoom in profile of a single peak).*

as well as with pristine PVDF. Fabricated nanogenerator based on pristine PVDF is considered as reference generator and labelled as RNG. While other nanogenerators prepared with hybrids are coined as PNG 1, PNG 2, PNG 3 and PNG 4 where the attached numeric with PNG represents the wt% of $CsPbCl_3$ in hybrids. Piezoelectric outputs of all devices are examined without any additional electrical poling action. Figure 6.5a and figure 6.5b show the open circuit voltage (V_{oc}) and short circuit current (I_{sc}) of all the devices upon a periodic hammering by hand with constant amplitude ~100 MPa. From both figures, maximum instantaneous output voltage and current ~ 168 V and ~2 µA are observed respectively for PNG 3. Whereas in the

same experimental condition, the output voltage and current registered from RNG are only ~20 V and ~0.60 µA respectively. Calculated output power across PNG 3 is found to be ~336 µW while the same across RNG is 11.6 µW. These figures also suggest elevated output performance from all the PNGs compared to the RNG.

To explain the observed performance differences, from the devices, understanding of the role of $CsPbCl_3$ is crucial. To enhance this electroactive phase content, $CsPbCl_3$ was incorporated as the filler. This incorporation and thereby β phase conversion (self-polling) is not only easy but also quick and cost-effective. The β phase has maximum dipole moment per unit cell as compared to α and γ phases, β phase constitution in the sample increases with the incorporation of filler, confirmed from the FTIR and XRD analysis. Besides β phase enhancement, incorporation of filler also ensures high dielectric constant. Improvement in dielectric constant further ensued enhancement in d_{33} values. Relying on these elevated features, hybrid samples showed better piezoelectric response. Performance supremacy registered from PNG 3 is attributed to its highest percentage of β phase constitution, higher d_{33} coefficient than others. For such output performance supremacy, PNG 3 has been considered as optimized one and executed further studies using it. The calculated value of the transferred charge is 17.48 µC for PNG 3 whereas the same for RNG is 5.21 µC (figure 6.5c). This result indicates that the amount of transferred charge is enhanced after $CsPbCl_3$ incorporation in samples. With the application of external stress on PNG 3, dipoles in the PVDF matrix are aligned. As a result, charge is induced on both the electrodes. Due to this induced charge accumulation, electrical current flows through the external circuit [30]. PNG devices deformed under applied pressure. With maximum deformation, the devices accumulated the highest number of charges within a small interval of time. Upon pressure removal, dipoles get misaligned and the accumulated charge flows in the opposite direction.

Chapter 6

To find the instantaneous output power from the PNG 3, changes in the output voltage and current as a function of load resistance (R_L) under stress of ~100 Pa were examined (Figure 5d). Load resistance was connected in series with the nanogenerator and varied from 150 kΩ to 30 MΩ. This figure demonstrates gradual increment of the output voltage which is nearly saturated at higher resistance. On the contrary, the output current followed the reverse trend which gradually decreased with increasing load resistance. Figure 6.5e shows the variation in output power with load resistance. Resistance corresponding to maximum instantaneous power (P) was calculated using the standard equation: $P = V^2/R_L$. Assessed value of consumed power is maximum (7.3 µW) at the load resistance of 4.4 MΩ. From the maximum power transfer theorem, it can be concluded that internal resistance of the device is 4.4 MΩ. V_{oc} is also estimated using following equation: [17],

$$\frac{1}{V_L} = \frac{R_i}{V_{oc}} \cdot \frac{1}{R_L} + \frac{1}{V_{oc}} \tag{6.3}$$

Here, V_L denotes the voltage developed across the load resistance. Calculated value of V_{oc}, from the plot of $1/V_L$ vs. $1/R_L$ for PNG 3 under periodic finger tapping is ~34 V which is nearly identical to the measured value of V_{oc} ~35 V. Sensitivity is an important criterion of the nanogenerator for its widespread usage. To examine the sensitivity of the PNG 3, very light mechanical stress was applied by placing a cell phone in vibration mode upon it. Output ~0.3 V is registered across PNG 3 due to such vibration (~100 Pa). This result confirmed that PNG 3 can extract mechanical energy from very a small mechanical source and generate electrical response. Figure 6.5f shows the output performance of PNGs under finger tapping (~ 100 kPa). The generated output voltage of PNG 3 is ~35 Volt which is nearly 3-fold than the same delivered by RNG. When heavy stress is applied by toe pressing, the voltage increases to ~ 58.30 Volt (Figure 6.5g) for PNG 3. These results confirm that output of PNG is improved due to the incorporation of $CsPbCl_3$. Observed asymmetric peaks in the output signals in aforesaid

figures can be understood by the difference of strain rate. Pressing is applied by both fingers and toe at higher strain rate. It resulted in high output voltages. Then again, releasing is dominated by the resilience of hybrid film with slower strain rate. This may result in low voltages. Such kind of asymmetry in output signal due the scan rate differences is also observed by other researchers [61-63]. To examine whether the signal in the oscilloscope was genuinely a piezo signal or noise, PNG 3 was connected with the oscilloscope in both forward and reverse bias. Figure 6.5h and 6.5i shows that the current and voltage developed across PNG 3 in forward and reverse connections were nearly the same, thus authenticating nature of the signal as a piezo signal. Zoom in view of a single peak is shown in the respective inset.

To measure the piezo-response of PNG 3 under different bending conditions as well as to examine its mechanical flexibility, their output characteristic was monitored at different bending conditions. Figure 6.6a shows the output of 5.88 and 11.51 V from PNG 3 in half and full bending conditions respectively. Digital images in inset demonstrate two different bending situations. Registered voltage for full bending is found almost double to same of half bending. Further, to attain an idea over its sensitivity towards small extent of bending, output of the device examined at small angles also. Starting with a very nominal bending of 2˚, output performance of PNG 3 examined up to 25˚ and the result is shown in figure 6.6 (b, c). From both the curve, it is obvious that the electrical output of PNG 3 increased with the gradual increase of bending angle, shows its potential for being used in diverse bending gesture recognition. Bending the PNG 3 at angle 2˚, 3˚, 5˚, 10˚, 15˚ 20˚ and 25 ˚generated output voltage of 0.03, 0.09, 0.36, 0.51, 1.04, 1.34 and 1.95 V and the corresponding currents displayed in oscilloscope are 0.02, 0.05, 0.11, 0.21, 0.35, 0.51 and 0.64 μA respectively. As the actions of bending and straightening repeated, both the real-time outputs displayed gradual and periodic
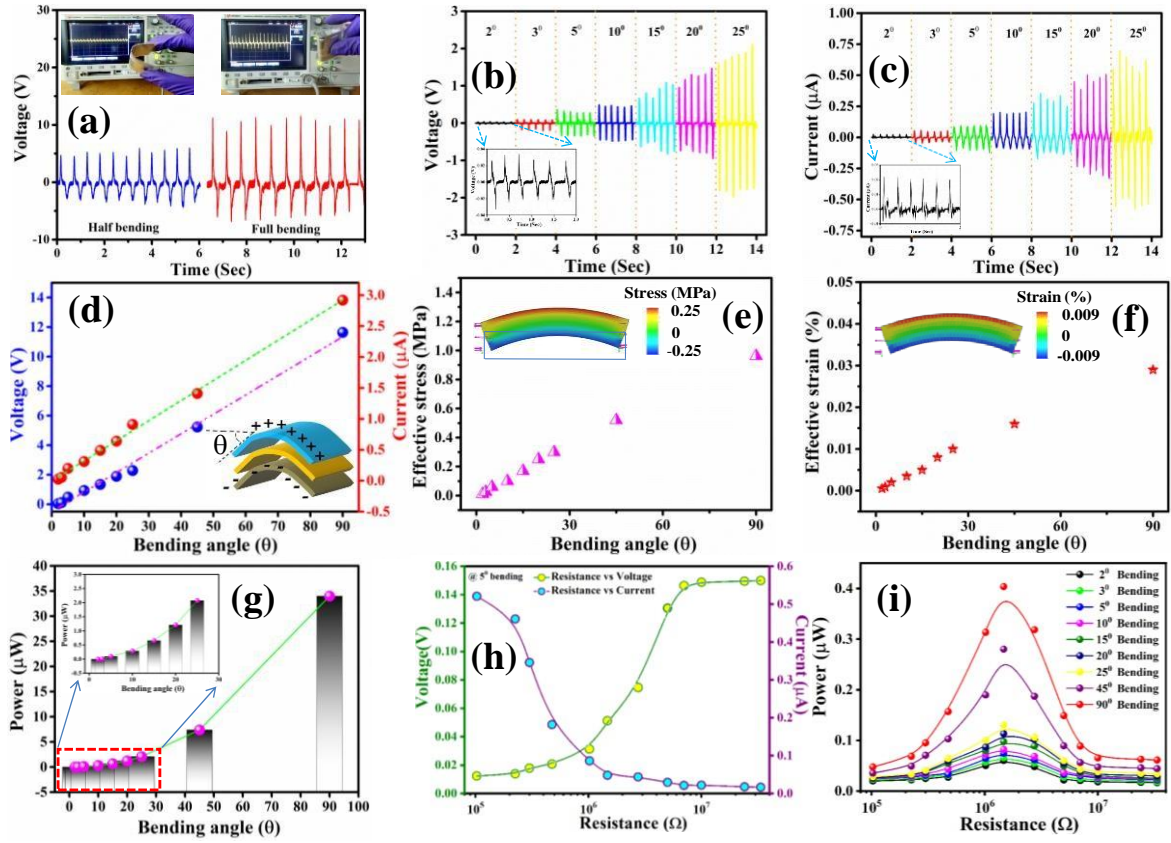
Figure 6.6: *(a) Output voltage due to half banding and complete bending recorded by a digital oscilloscope. (b) Open circuit voltage (c) short circuit current due to bending at a various angle (insets show zoom in view). (d) Output voltage and current (e) effective stress (f) effective strain (g) output power with respect to bending angle. (h) Output voltage and current vs resistance at 5° bending; (i) Resistance vs power variation of PNG 3 at different bending.*

increasing and decreasing, showing a real-time detection ability of sharp angle. For a comparative view, peak values of output voltage and current are compared at different bending angles and the result is plotted in figure 6.6d. Peaks of the measured output increased with the increase of bending angle due to internal piezoelectric potential enhancement by the introduced strain [64]. Upon bending, effective stress and strain are developed in PNG 3. Using a beam bending model, effective stress and strain were calculated [65]. Effective stress on the surface of the device can be expressed as $\sigma_{eff} = M/S$, where M and S denote bending moments and section modulus respectively. Stress at the central region of the device increases gradually with the increment of bending angle, obtaining maximum stress of 1.0 MPa at a bending angle of

90° (figure 6.6e). Upon bending, inhomogeneous bending stress is developed along the thickness of PNG which ensure difference in piezo-potential between its two extreme surfaces. With increase in bending angle, effective stress as well as output voltage increases gradually. The effective stress gradient formation along the thickness of film is further confirmed by COMSOL simulation. Stress variation along the thickness at an angle 20° is shown in figure 6.6e inset. This profiling confirms maximum positive stress generation on the top surface and negative stress in the bottom surface, where the axis of film is considered as neutral. Beside stress, effective strain was also calculated and the result is shown in figure 6.6f. Stress variation along the thickness at an angle 20° is shown in figure 6.6f inset. The effective strains were found to be in the range of 0.001–0.010%. To apply this device in any practical application in bending state, it is necessary to get an optimal output power. Figure 6.6g shows the variation of output power with different bending angles of the PNG 3. The output power profile mimics the similar trend of output voltage and current upon bending angle increment. It delivered maximum power 34 μW at bending angle of 90°. Variation in instantaneous power across different load resistance for PNG 3 under bending condition is also explored. Output voltage and current across the load under small bending at 5^0 showed typical natures where the voltage saturated at higher resistance with the increase in resistance and current followed the reverse trend (figure 6.6h). Difference in output power at different bending angles as a function of load resistance is given in figure 6i. The generated maximum output power comes from PNG 3 for bending angle of 2°, 3°, 5°, 10°, 15°, 20°, 25°, 45° and 90° across the various load is 0.057, 0.060, 0.070, 0.078, 0.094, 0.109, 0.122, 0.250, and 0.375 μW respectively. The output voltage and current of PNG 3 are also tested at frequencies of 0.5, 1, 2, 3, 4, 5 and 6 Hz. Increment in both outputs up to 5 Hz frequency is obvious from the figure. Such increment in outputs at high frequency may be attributing to the faster strain rate of PNG 3 at the said frequency. These results not only suggest mechanical stability and robustness of PNG 3, also ignite its candidature utility
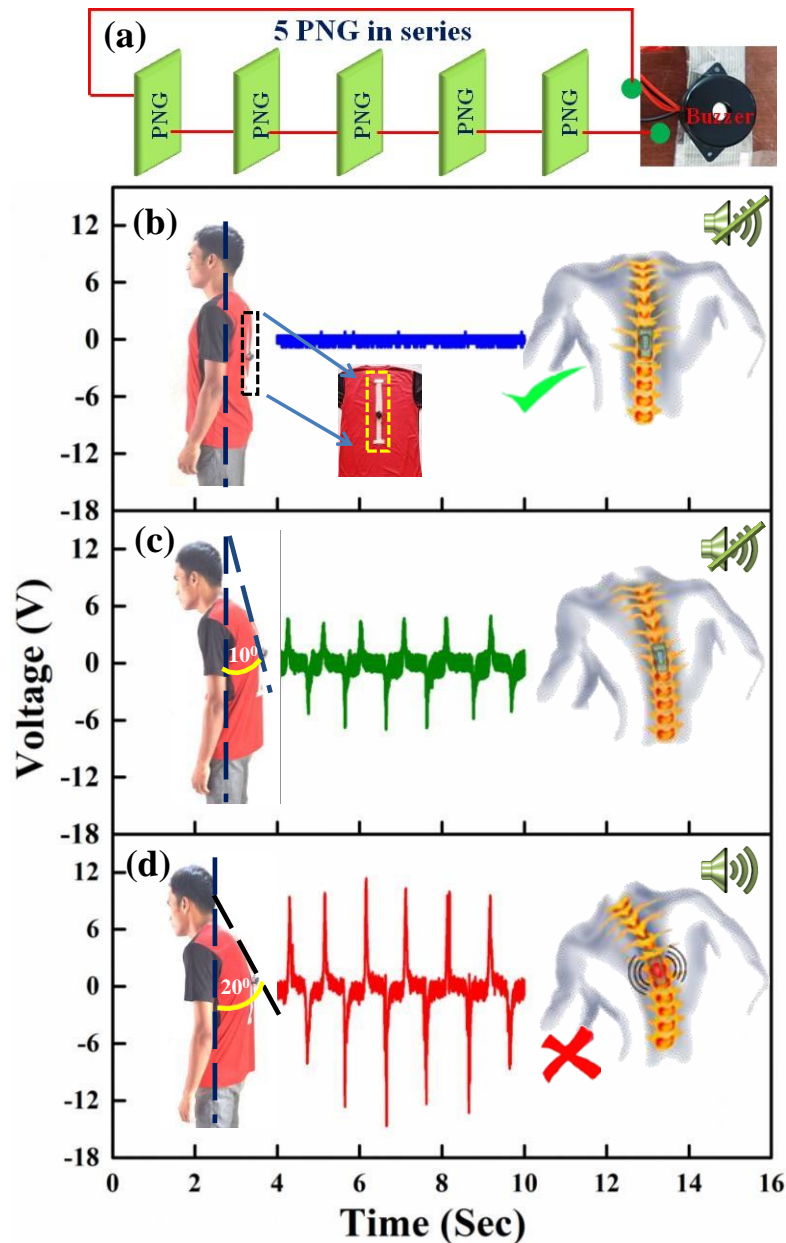
Figure 6.7: Output voltage across the fabricated sensor at different bending posture.

for practical bending sensor system [66]. Due to the output performance dependency over applied strain, PNGs can be employed as active sensors for strain linked mechanical stuffs with current and voltage as sensing parameters. Prolonged sitting at workplace for several hours at a stretch has lots of harmful effects which should be dealt with utmost effort before they become permanent and life threating. Wearable posture correction sensor can help to rectify or improve the sitting or standing posture before it become stressful to the body. Considering its good flexibility and electrical output performance, PNG 3 was utilized for the fabrication of wearable self-powered posture sensor to monitor the bending of our spine. PNGs in the sensor

detect the bending from optimized position and gives an electrical output to the buzzer which gives the user feedback in the form of alarm. Schematic of as the fabricated posture sensor is shown in figure 6.7a. As shown in schematic, five PNG 3 (each device with same size and structure) were integrated into a buzzer system. The buzzer system runs only when the output signal exceeds a threshold voltage of 7.5 V. The entire system is fixed firmly on user's skin with help of an elastic belt which has a very little impact on spine movement. Output performance of fabricated sensor at different angle is shown in figure 6.7. As shown in figure 6.7 b–d, PNG 3 placed on the back can monitor various angles of spine. The PNG 3 was driven by the movement of spine. In normal condition, PNG 3 attached over belt remains in unbended condition. In absence of any bending induced stress, the output across the PNG is significantly low. In such nominal response the buzzer stays in an inactive condition. With more bending, PNG 3 follows same bending curvature of spine due to its high flexibility. For small bending (10˚), PNG 3 delivered an output of voltage and current 0.51 V and 0.2 μA. This output is still lower than the fixed value which ensures the same inactiveness of buzzer. Once the user bends his/her spine more say by >20˚, output exceeds threshold value of buzzer and buzzer starts running. The output signals increased with the bending enlargement. In this way, this PNG 3 based posture sensor can easily distinguish various posture of user's spine. In addition, since high flexible of PNG 3 can be easily driven wherever some bending movement is available due to excellent conformability, it may be used as other self-powered wearable sensor for health monitoring and smart skin system by itself without using any external battery.

Biomechanical energy can be obtained easily from our day to day activitivites without suffering from environmental disparities. Biomechanical motions are considered as sustainable energy sources for wearable self powered portable devices [66]. To expolre the possibility of the PNG 3 in biomechanical energy harvesting, it was subjected to the different human motions.
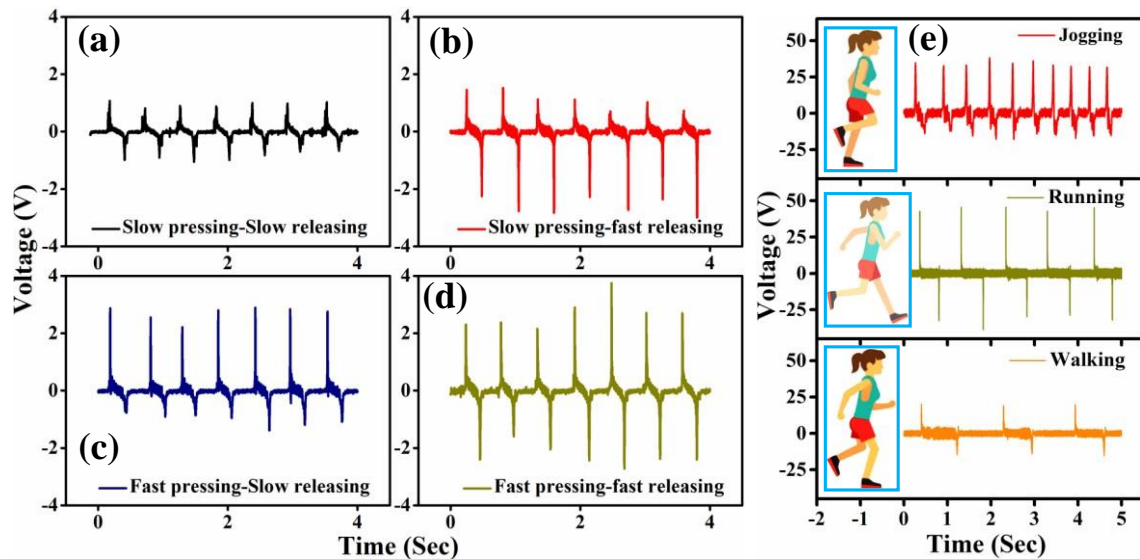
Figure 6.8: *Output voltages for (a) slow pressing-slow releasing (b) slow pressing-fast releasing (c) fast pressing-slow releasing (d) fast pressing-fast releasing. Output voltages due to (e) jogging, running and walking.*

Mechanical force application and relase at different speed resulted difference in the output. As depicted in figure 6.8a-d, both press or release process with fast-moving speed drives the device to deliver relatively high output voltage. More specifically, fast pressing (32 cm/sec; stress~1 kPa) of device with finger resulted higher positive peak value of ac voltage as compared to the same at low speed (12 cm/sec; stress ~1 kPa) finger motion. Then again, as the consequence of finger release at higher speed, peak value of voltage reaches in more negative direction than the slow releasing of finger. Output value reached ~2.90 V due to fast pressing and releasing whereas the same due to slow pressing and releasing is ~1.00 V. These results confirm that PNG 3 can sense slow and fast movement of human motions and it can be utilized in motion sensor fabrication also. Device performance also monitored for different kind of biomechanical force conditions namely like running, walking and jogging (stress in each case ~35 kPa) and the results are shown in figure 6.8e. As can be seen from this figure,
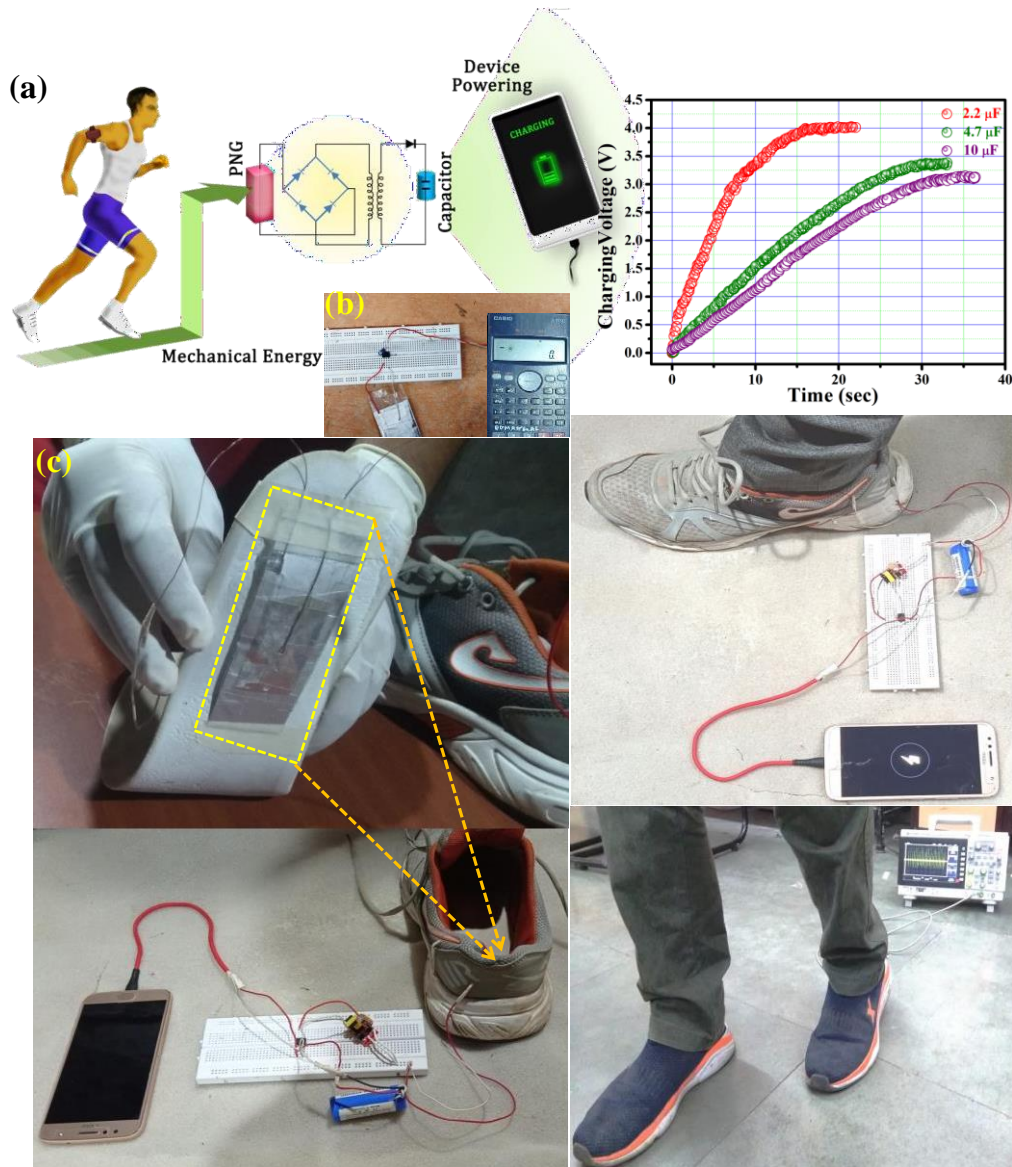
Figure 6.9: *(a) Schematic of the capacitor charging process and different capacitor charging (b) power up a calculator (c) fitting of PNG 3 inside shoe, total circuit connection for mobile charging.*

the output signal generated due to the running is ~44 V. Generated output voltage for jogging and slow walking is 36 and 21 V respectively. It proves that the fabricated device can work as energy harvester to harness all kinds of day-to-day biomechanical motions**.** Such dependency of piezoelectric response on the strain rate is well documented in the literature [62, 63]. With the increase in applied strain rate, charges were transported faster in external circuit to neutralize the piezoelectric response. Such fast transportation of charges ensured a large

piezoelectric output. As the output voltage is the product of the external resistance and output current, the output voltage varies proportionally with the applied strain rate [63].

Along with high instantaneous output, several devices demand fast charging-discharging with a high voltage at small interval of time. In this context, PNG 3 was connected with a capacitor via bridge rectifier and subjected to biomechanical action. Circuit diagram for this capacitor charging is given in figure 6.9a. Capacitor charging as a function of time for different capacitor namely 2.2, 4.7, and 10 µF is shown in figure 6.9a. This figure also demonstrates that 2.2 µF capacitor became fully charged (~ 4 V) due to walking for a very small-time interval ~20 sec. The power stored in capacitor was calculated by following equation, $P_{out} = \dfrac{1}{2t} CV^2$, where P_{out} is power stored, C stands for capacitance of the capacitor. V denotes saturation voltage and t is the time taken to reach that voltage. Assessed value of power stored in capacitor is ~ 0.8 µW. To reveal the feasibility and utility of this capacitor charging more clearly in biomechanical energy harvesting, the device has been used further to run commercial calculator. The harvested energy by capacitor can be used to lighten up of LCD of the calculator screen (figure 6.9b). This result inspired us to charge several other wearable electronic devices by amalgamating few PNGs in series which can increase the overall power. Severe power shortage in the wearable electronic devices due to the limited capacity of Li-ion batteries inside is a huge headache. Building a system for powering these devices by scavenging energy from our biomechanical activities is very promising. In this scenario, a system was designed using PNG 3 to convert low-frequency walking motion energy into reliable and continuous electricity source for small electronic device. The PNG 3 has been stacked in shoe's sole and attached a 5 V battery via bridge rectifier. Digital image of the construction process and working condition is presented in figure 6.9c. High output power of this PNG 3 was able to charge up the 5 V battery which further recharges our mobile battery in any time and any difficult situation. When
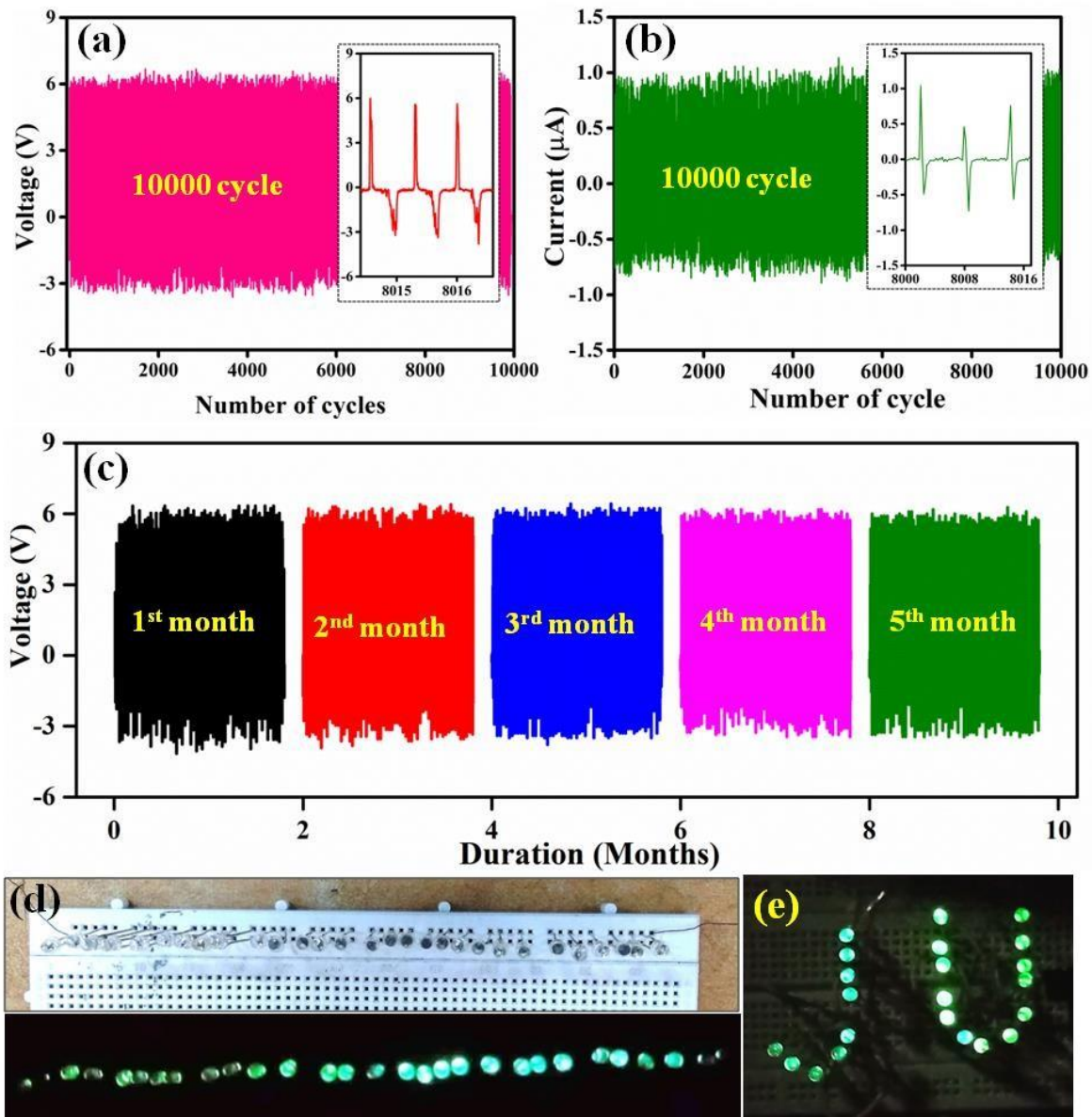
Figure 6.10: *(a) Output voltage and (b) current of PNG 3 for first 10000 cycles (c) fatigue test output voltage for consecutive 5 months. (e) Digital image showing the glowing LED array and university acronym "JU".*

the applied strain in system corresponds to a person (~weighing 55 kg) walking at normal speed of 5-6 km/hr, time taken by 5 V battery to be charged fully was ~10 hours. This fully charged battery can recharged the android phone and other electronic devices of low-power-consumption easily. These results suggest that this kind of system using PNG 3 can has huge potential in illumination and power supplies for the wearable electronic devices of low wattage.

Chapter 6

To examine the endurance of PNG 3 in long term applications, the fatigue test has been performed at frequency of ~3 Hz for five months (50000 cycles, 10000s per month). A 'beat the drum' toy has been placed over PNG 3 for periodic application of mechanical stress. Output voltage and current across PNG 3 in first 10000 cycles is presented in figure 6.10a and 6.10b. No significant attenuation in output voltage and current is observed even such long cycle operation. Output voltage response from PNG 3 over 5 consecutive months is presented in figure 6.10c. Here also, no significant drop in output voltage is observed over the entire period of testing. As suggested by these results, piezo response of PNG 3 is not severely vulnerable against moisture and seasonal temperature change and etc. Careful observation of the FESEM reveals no significant fault, fracture or breakage in the hybrid film even after such long repetitive operations. All these results confirm robust reliability and durability of PNG 3 and thereby it's utility as an effective energy scavenger even in harsh conditions. Futher power up sevaral green LEDs to establish the feasibility of PNG 3. The PNG 3 device was connected with a bridge rectifier, which the convert the alternatng current into direct current output. As seen in figure 6.10d, PNG 3 instantaneously lighted up an array of commercially available 32 green LEDs without any external source, simply by walking when the PNG was placed inside our shoe. Furthermore, the same PNG also instantaneously lit up two letters 'JU' which is the abbreviation of our university under same periodic stress (figure 6.10e). These outstanding results advocate that 3% $CsPbCl_3$-PVDF based PNG is an excellent candidate for its potential utility in high-performance, flexible, wearable mechanical energy harvesting systems.

6.4. Conclusions

In summary, super-flexible PVDF films filled with various mass fractions (wt%) of low temperature processed all inorganic $CsPbCl_3$ were realized to fabricate high performance piezoelectric energy harvesters. Subtle adjustment over the concentration of perovskites in PVDF matrix ensued different electroactive phase nucleation, difference in dielectric features

as well as in remanant polarization in the hybrid samples. Maximum β-phase in the hybrid is obtained for 3 wt. % perovskite loading sample. The blended film was sandwiched between two aluminium electrodes to fabricate PNGs. Recorded values of maximum output voltage and current from PNG 3 were ~ 168 V and 2 μA, whereas those for pristine PVDF film were 20.0 V and 0.58 μA respectively. Benefited with the advantage of high β-phase content, enhanced d_{33} coefficient and dielectric permittivity, PNG 3 showed much improved energy conversion efficiency as compared to pristine samples separately. This output was sufficient to turn on at least 32 commercial green light emitting diodes (LEDs) without any peripheral energy sources simply by walking when the PNG was placed inside our shoe. The highly flexible PNGs shows potential utility as an active posture sensor capable of detecting poor posture during sitting and standing. Furthermore, capacitors have been successfully charged by repetitive finger tap and release signifying the output voltage of PNG 3 can be utilized as self-powered smart electronic devices. Inspired from capacitor charging result, PNG 3 based systems were also designed which can to convert low-frequency walking motion energy and can act as a power source for small electronic device. Mechanical stability and durability were tested by a long 10000 cycle data for consecutive 5 months, which proves its usability as a long-lasting energy supplier. This simple and cost-effective solution-based amalgamation of polymer with all inorganic perovskite in a single unit will provide a promising platform for fabrication of flexible, highly durable energy harvesters and self-powered wearable sensor systems for practical usage at every place where different type's mechanical movement is available.

6.5. References

1. L. Jin, J. Chen, B. Zhang, W. Deng, L. Zhang, H. Zhang, X. Huang, M. Zhu, W. Yang, and Z. L. Wang, ACS nano, 10 (2016) 7874-7881.

2. T. Paul, S. Maiti, U. Mukherjee, S. Mondal, A. Sahoo, and K.K. Chattopadhyay, Materials Letters, 301 (2021) 130264.

3. P. Biswas, N.A. Hoque, P. Thakur, M.M. Saikh, S. Roy, F. Khatun, B. Bagchi and S. Das, ACS Sustainable Chem. En, 7 (2019) 4801−4813.

4. V. Jella, S. Ippili, J.H. Eom, J. Choi, and S.G. Yoon, Nano Energy, 53 (2018) 46–56.

5. S. Lee, R. Hinchet, Y. Lee, Y. Yang, Z.H. Lin, G. Ardila, L. Montès, M. Mouis, and Z.L. Wang, Advanced Functional Materials, 24 (2014) 1163-1168.

6. S. Lee, S. H. Bae, L. Lin, Y. Yang, C. Park, S.W. Kim, S.N. Cha, H. Kim, Y. J. Park, and Z. L. Wang, Adv. Funct. Mater, 23 (2013) 2445–2449.

7. X. Chen, X. Li, J. Shao, N. An, H. Tian, C. Wang, T. Han, L. Wang, and B. Lu, Small, 13 (2017) 1604245.

8. Z.L. Wang, and J. Song, Science, 312 (2006) 242-246.

9. Y.F. Lin, J. Song, Y. Ding, S.Y. Lu, and Z.L. Wang, Z.L., Applied Physics Letters, 92 (2008) 022105.

10. N. Jamond, P. Chrétien, L. Gatilova, E. Galopin, L. Travers, J.C. Harmand, F. Glas, F. Houzé, and N. Gogneau, Nanoscale, 9 (2017) 4610-4619.

11. K.I. Park, J.H. Son, G.T. Hwang, C.K. Jeong, J. Ryu, M. Koo, I. Choi, S.H. Lee, M. Byun, Z.L. Wang, and K.J. Lee, Advanced materials, 26 (2014) 2514-2520.

12. M. Zhang, T. Gao, J. Wang, J. Liao, Y. Qiu, H. Xue, Z. Shi, Z. Xiong, and L. Chen, Nano Energy, 11 (2015) 510-517.

13. M.M. Alam, S.K. Ghosh, A. Sultana, and D. Mandal, Nanotechnology, 26 (2015) 165403.

14. J. Wu, D. Xiao, and J. Zhu, Chemical reviews, 115 (2015) 2559-2595.

15. A. Sultana, M.M. Alam, S. Garain, T.K. Sinha, T.R. Middya, and D. Mandal, ACS applied materials & interfaces, 7 (2015) 19091-19097.

16. S. Garain, S. Jana, T.K. Sinha, and D. Mandal, ACS applied materials & interfaces, 8 (2016) 4532-4540.

17. H. Parangusan, D. Ponnamma, and M. Al-Maadeed, Scientific reports, 8 (2018) 754.

18. M.C. García-Gutiérrez, A. Linares, I. Martín-Fabiani, J.J. Hernández, M. Soccio, D.R. Rueda, T.A. Ezquerra, and M. Reynolds, M., Nanoscale, 5 (2013) 6006-6012.

19. E. Kabir, M. Khatun, L. Nasrin, M.J. Raihan and M. Rahman, Journal of Physics D: Applied Physics, 50 (2017) 163002.

20. S. Bauer, Journal of Applied Physics, 80 (1996) 5531-5558.

21. X. Cai, T. Lei, D. Sun, and L. Lin, RSC Advances, 7 (2017) 15382-15389.

22. N. Soin, P. Zhao, K. Prashanthi, J. Chen, P. Ding, E. Zhou, T. Shah, S.C. Ray, C. Tsonos, T. Thundat, and E. Siores, Nano Energy, 30 (2016) 470-480.

23. D. Mandal, K. Henkel, and D. Schmeißer, Physical Chemistry Chemical Physics, 16 (2014) 10403-10407.

24. S. Jana, S. Garain, S. Sen, and D. Mandal, Physical Chemistry Chemical Physics, 17 (2015) 17429-17436.

25. A. Sultana, M.M. Alam, P. Sadhukhan, U.K. Ghorai, S. Das, T.R. Middya, and D. Mandal, Nano Energy, 49 (2018) 380-392.

26. M. Sahu, S. Hajra, K. Lee, P.L. Deepti, K. Mistewicz, and H.J. Kim, Crystals, 11 (2021) 85.

27. N.R. Alluri, B. Saravanakumar, and S.J. Kim, ACS applied materials & interfaces, 7 (2015), 9831-9840.

28. A. Gaur, S. Tiwari, C. Kumar, and P. Maiti, Energy & Fuels, 34 (2020) 6239-6244.

29. S. Kim, T.M.H. Nguyen, R. He, and C.W. Bark, Nanoscale Research Letters, 16 (2021) 1-7.

30. S. Mondal, T. Paul, S. Maiti, B.K. Das, and K.K. Chattopadhyay, Nano Energy, 74 (2020) 104870.

31. A. Maity, C. Das, A.K. Raychaudhuri, A. Saha, and B. Ghosh, Journal of Physics D: Applied Physics, 54 (2021) 455104.

32. T. Paul, S. Maiti, B.K. Chatterjee, P. Bairi, B.K. Das, S. Thakur, and K.K. Chattopadhyay, The Journal of Physical Chemistry C, 31 (2021) 16892–16902.

33. A. Maity, A.K. Raychaudhuri, and B. Ghosh, The Journal of Physical Chemistry C, 125 (2021) 10646-10652.

34. A. Proto, M. Penhaker, S. Conforto, and M. Schmid, Trends in biotechnology, 35 (2017) 610-624.

35. S.D. Kwon, Applied physics letters, 97 (2010) 164102.

36. N. Zhang, J. Chen, Y. Huang, W. Guo, J. Yang, J. Du, X. Fan, and C. Tao, Advanced Materials, 28 (2016) 263-269.

37. R. Ding, X. Zhang, G. Chen, H. Wang, R. Kishor, J. Xiao, F. Gao, K. Zeng, X. Chen, X.W. Sun, and Y. Zheng, Nano Energy, 37 (2017) 126-135.

38. R. Ding, H. Liu, X. Zhang, J. Xiao, R. Kishor, H. Sun, B. Zhu, G. Chen, F. Gao, X. Feng, and J. Chen, Advanced Functional Materials, 26 (2016) 7708-7716.

39. A. Sultana, P. Sadhukhan, M.M. Alam, S. Das, T.R. Middya, and D. Mandal, ACS applied materials & interfaces, 10 (2018) 4121-4130.

40. H. Chen, L. Zhou, Z. Fang, S. Wang, T. Yang, L. Zhu, X. Hou, H. Wang, and Z.L. Wang, Advanced Functional Materials, 31 (2021) 2011073.

41. R.C. Ailneni, K.R. Syamala, I.S. Kim and J. Hwang, Work, 62 (2019) 27–35.

42. C. Rodrigues, A. Gomes, A. Ghosh, A. Pereira, and J. Ventura, Nano Energy, 62 (2019) 660-666.

43. W. Guo, C. Tan, K. Shi, J. Li, X.X. Wang, B. Sun, X. Huang, Y.Z. Long, and P. Jiang, Nanoscale, 10 (2018) 7751-17760.

44. S. Das, T. Paul, S. Maiti, and K.K. Chattopadhyay, Materials Letters, 267 (2020) 127501.

45. T. Paul, B.K. Chatterjee, S. Maiti, N. Besra, S. Thakur, S. Sarkar, K. Chanda, A. Das, P.K. Sarkar, K. Sardar, and K.K. Chattopadhyay, AIP Conference Proceedings, 1953 (2018) 030085.

46. T. Paul, S. Maiti, N. Besra, B.K. Chatterjee, B.K. Das, S. Thakur, S. Sarkar, N.S. Das, K.K. Chattopadhyay, ACS Appl. Nano Mater. 2 (2019) 5942–5951.

47. N. Pandey, A. Kumar, and S. Chakrabarti, RSC advances, 9 (2019) 29556-29565.

48. T. Paul, B.K. Chatterjee, S. Maiti, S. Sarkar, N. Besra, B.K. Das, K.J. Panigrahi, S. Thakur, U.K. Ghorai, and K.K. Chattopadhyay, Journal of Materials Chemistry C, 6 (2018) 3322-3333.

49. T.K. Sinha, S.K. Ghosh, R. Maiti, S. Jana, B. Adhikari, D. Mandal, and S.K. Ray, ACS Applied Materials & Interfaces, 8 (2016) 14986-14993.

50. S. Sarkar, S. Garain, D. Mandal, and K.K. Chattopadhyay, RSC Advances, 4 (2014) 48220-48227.

51. A. Peleš, O. Aleksić, V.P. Pavlović, V. Djoković, R. Dojčilović, Z. Nikolić, F. Marinković, M. Mitrić, V. Blagojević, B. Vlahović, and V.B. Pavlović, Physica Scripta, 93 (2018) 105801.

52. M.T. Riosbaas, K.J. Loh, G. O'Bryan, B.R. and Loyola, International Society for Optics and Photonics, 9061 (2014) 90610Z.

53. K. Maity, S. Garain, K. Henkel, D. Schmeißer, and D. Mandal, ACS Applied Polymer Materials, 2 (2020) 862-878.

54. V. Jella, S. Ippili, J.H. Eom, J. Choi, and S.G. Yoon, Nano Energy, 53 (2018) 46-56.

55. T. Paul, D. Das, B.K. Das, S. Sarkar, S. Maiti, and K.K. Chattopadhyay, Journal of Hazardous materials, 380 (2019) 120855.

56. S.K. Si, S.K. Karan, S. Paria, A. Maitra, A.K. Das, R. Bera, A. Bera, L. Halder, and B.B. Khatua, Materials Chemistry and Physics, 213 (2018) 525-537.

57. S.K. Pradhan, A. Kumar, P. Kour, R. Pandey, P. Kumar, M. Kar, and A.N. Sinha, Journal of Materials Science: Materials in Electronics, 29 (2018) 16842-16852.

58. P. Adhikary, S. Garain, and D. Mandal, Physical Chemistry Chemical Physics, 17 (2015) 7275-7281.

59. S. Cui, Y. Zheng, T. Zhang, D. Wang, F. Zhou, and W. Liu, Nano Energy, 49 (2018) 31-39.

60. N.P.M.J. Raj, N.R. Alluri, G. Khandelwal, and S.J. Kim, Composites Part B: Engineering, 161 (2019) 608-616.

61. Y. Jiang, Y. Deng, and H. Qi, Polymers, 13 (2021) 3252.

62. C. Chang, V.H. Tran, J. Wang, Y.K. Fuh, and L. Lin, Nano letters, 10 (2010) 726-731.

63. H. Lee, H. Kim, D.Y. Kim, and Y. Seo, ACS omega, 4 (2019) 2610-2617.

64. F. Li, T. Shen, C. Wang, Y. Zhang, J. Qi, and H. Zhang, Nano-Micro Letters, 12 (2020) 1-44.

65. C. Yoon, B. Jeon, and G. Yoon, Sensors and Actuators A: Physical, 318 (2021) 112499.

66. Y. Su, W. Li, L. Yuan, C. Chen, H. Pan, G. Xie, G. Conta, S. Ferrier, X. Zhao, G. Chen, and H. Tai, Nano Energy, 89 (2021) 106321.

CHAPTER 7

Self-Charging Piezo-Supercapacitor: One-Step Mechanical Energy Conversion and Storage
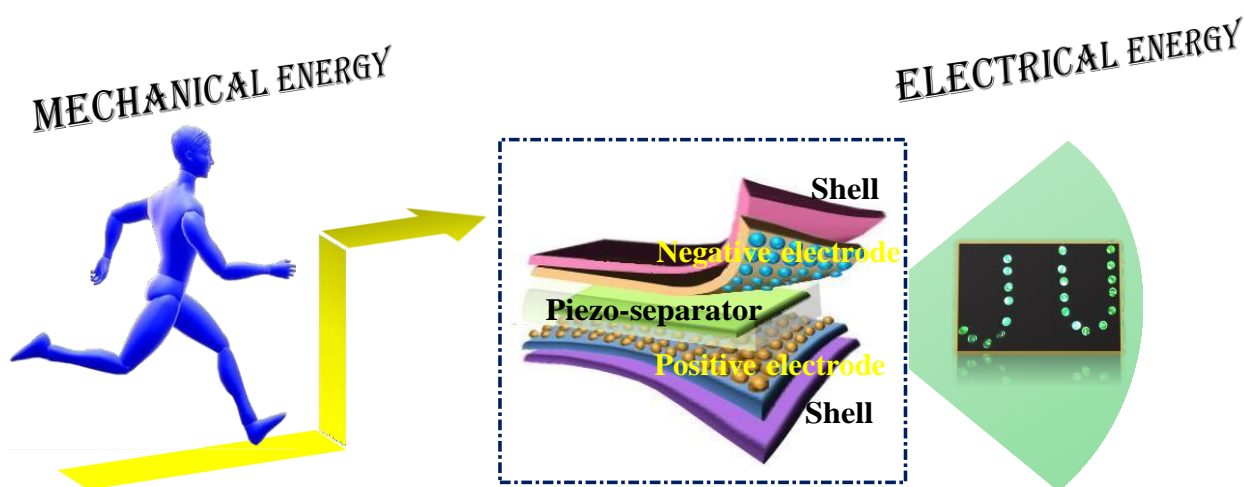
7.1. Introduction

Despite traditional energy sources, the demand for renewable sources increases with the growing population density and industrial revolution throughout the globe, which has accompanied harmful consequences like pollution, global warming, and irreversible environmental degradation. On the other hand, the limited resources are depleting rapidly. Under these circumstances, many scientists and researchers are trying to develop advanced energy harvesting technology to utilize unused and wasted energy that can prevent this energy crisis. With the rapid development of the economy, society, and scientific endeavors, microelectronic devices are playing an increasingly important role in our daily lives. Usually, these devices can be powered using conventional batteries, which require periodic replacement owing to their limited capacities. Moreover, it requires remarkable manpower, financial resources, and time, especially in remote areas. For the power supply, scientists are working on new methods for scavenging clean energy from the surrounding environment. Based on this background, the piezoelectric and triboelectric Nanogenerator were invented by Wang et al. in 2006 and 2012, respectively, which can effectively convert small mechanical energies into electrical energy in the ambient environment, such as wind energy, wave energy, droplet energy, small vibration, human body motion, and other mechanical energies [1, 2]. They are basically the wasted mechanical energy present in our surrounding environment. Nanogenerators can not only scavenge these mechanical energies efficiently, but also include various secondary advantages, e.g., the associated technology and devices are simple, small, light-weight, convenient, low-cost, devoid of auxiliaries, and eco-friendly. They can also be applied to wireless sensors and microelectronic devices [3, 4, 5]. Naturally, research and development of self-powered electronic devices are considered among the hottest topics in sustainable growth, especially in the field of self-charging power textiles for wearable electronics, which has undergone notable expansion. Thus, it is important to investigate self-

charging energy storage devices that can effectively integrate energy harvesting and storage units into one device for powering miniaturized; low-power electronic devices with automated energy supply [6–9].

A lot of materials have been studied for this purpose. Several semiconductors like ZnO, CdS, GaN, ZnS, etc. [10-19] exhibit piezoelectric properties. Numerous ceramic materials like lead zirconate titanate (PZT), various perovskites such as $BaTiO_3$, $ZnSnO_3$, $MAPbX_3$, $FAPbI_3$, etc. [20-28] and polymers (PVDF, PVDF-TrFE, PVDF-HFP, PDMS, etc.) also show a strong piezoelectric effect [29-38]. But most of them are not flexible, but rather brittle and toxic, making them inappropriate for device fabrication. In comparison, piezoelectric polymers are quite attractive due to their high piezoelectric coefficient (d_{33}), flexibility, and diverse genres of applications [39-41]. Among them, PVDF and its copolymers are the most suitable candidates due to their excellent energy storage ability, high piezoelectric coefficient, desirable flexibility, and capability to transform into different elaborate shapes. PVDF exhibits four polymorphs based on different chain conformation *viz.*, α, β, γ, and δ phases. Among these, α and δ phase shows trans-gauche-trans-gauche (TGTG) configuration, and β phase exhibits all-trans (TTTT) configuration and γ phase shows T^3GT^3G configuration. α and δ phases show no spontaneous polarization which makes them non-polar, while due to the parallel dipolar configuration, both of β and γ phases are polar. A monomer unit —(CH_2—CF_2)— is repeated in the PVDF matrix (for β phase) to form a non-conjugated linear fluorinated hydrocarbon with a high vacuum dipole moment (7×10^{-30} C m) [42], pointing roughly from the negatively charged fluorine atom to the positively charged hydrogen atom. However, with larger spontaneous polarization β phase predominantly manifests the piezoelectric effect [43-46]. But in a normal PVDF matrix, β phase content is nominal, so it is needed to enhance the associated β phase fraction. Hence, our primary objective is to enhance the electroactive phase content of the PVDF matrix as much as possible. Different groups have elaborated versatile and novel

approaches to transform the nonpolar phase into an electroactive phase; such as mechanical stretching, electrical polling under high field, thermal annealing, filler incorporation in PVDF matrix, etc. [46-53]. Among these, filler incorporation is a more convenient process for multifunctional applications that hardly affects the flexibility of the film. In previous work, $CsPbBr_3$ has been used as an optically active filler for photo detector construction [46]. Here, a flexible PNG was fabricated and anticipate enhancing the output performance of PNG via blending [54-56].

A rectifier-based circuit is required to store electrical power from a piezoelectric Nanogenerator, which leads to indispensable energy loss in the external circuit. To solve these issues, many efforts have been dedicated to pursuing direct transformation of mechanical energy into electrochemical energy without a rectification circuit. A PNG is an effective tool that can harvest low-frequency mechanical energy from our surroundings by utilizing the piezoelectric properties of some materials. On the other hand, electrochemical capacitors or supercapacitors are considered one of the most momentous next-generation energy storage devices, predominantly for their fast charge-discharge rates, high power density, and long lifetimes compared to conventional chargeable batteries or commercial dielectric capacitors. Several noteworthy efforts have been made to assemble storage units with energy harvesters to develop uninterrupted, small-scale self-charging power systems. Based on two separate mechanisms of self-charging processes (conversion of mechanical energy to electrical energy, that further transforms to electrochemical energy), the mechanical energy is converted into electrical energy and stored at the same time without using a rectifier circuit [57-61].

The rapid advancement of portable electronic devices, such as Bluetooth speakers, mobile phones, and smart watches, has led researchers to look for flexible, low-weight, and energy-saving devices. A piezoelectric self-charging flexible supercapacitor (PSCFS) consists of a flexible piezoelectric separator, flexible positive and negative electrodes, and electrolyte gel.

Chapter 7

These devices are fabricated by sandwiching the piezo separator between two electrodes using gel electrolytes. Conventional supercapacitors using liquid electrolytes have several disadvantages over solid-state supercapacitors with gel-type electrolytes, such as the possibility of electrolyte leakage and short circuit of the electrodes, which makes PSCFSs greatly promising in portable electronics [57-61].

In this work, copper cobalt nickel oxide ($CuCoNiO_4$, abbreviated as CCNO) nanoform has been successfully synthesized. Different proportions of CCNO nanoforms was embedded in PVDF polymer to get the supreme composite for fabricating a high-performance, flexible piezo device and named the composite sample PNCU x, x is the wt. % of CCNO. Here, CCNO filler has been playing a significant role in the conversion of the crystalline electroactive β phase from the nonpolar α phase. The fabricated Nanogenerator using different nanocomposites is named PNG x (where x is the wt. % of CCNO) and checks the output performance of all devices. Besides, a piezoelectric self−charging flexible supercapacitor device (PSCFS) was presented using PNCU 1 film as a piezo separator. The synthesized CCNO samples over carbon cloth substrate (CCNO) act as a positive and negative electrode, and poly (vinyl alcohol) and phosphoric acid (PVA/H_3PO_4) are used as an electrolyte gel. Being a multi-metallic oxide, CCNO demonstrated outstanding super-capacitive performance, as was documented in earlier research.[60] The cyclic stability and high capacitance of this specific material make it stand out and may be useful in the long-cycle investigation. CCNO exhibits an areal capacitance of 15.5 mF cm^{-2} at 0.1 mA cm^{-2} current density within a wide operating potential window of 0–1.2 V, which may suggest it as a promising electrode material for the PSCFS.

7.2. Characterizations and Measurements

Field emission scanning electron microscopy (FESEM) images of synthesized samples were taken using a HITACHI S4800 electron microscope in order to determine their size and

morphology. X-ray diffraction (XRD) patterns are acquired on a Bruker D8 diffractometer using Cu-K radiation of wavelength 1.5404 Å at room temperature in order to confirm the crystallinity of PNCU films. The distinct Raman modes of the synthesized samples were examined using a high-resolution Raman spectrometer (WITECH) that excited a 532 nm laser source. By using an X-ray photoelectron spectrometer (XPS) and a SPECS HSA-3500 hemispherical analyzer with a monochromatic Mg K_α X-ray source, the compositional analysis of CCNO and PVDF-CCNO composite was studied.

Shimadzu IRprestige-21 spectrometer was used to record the FT-IR spectrum. Using a wide range d_{33} meter, the samples' piezoelectric response (d_{33}) was investigated. On an Agilent 4294A precision impedance analyzer with a frequency range of 40 Hz-110 MHz, the dielectric constant, dielectric loss, and conductivity of the produced films were measured. Using a typical bipolar waveform, the P-E loop of synthetic films was measured using a Precision Premier II ferroelectric tester from Radiant Technologies, Inc. The performance of the device was evaluated using a KEYSIGHT InfiNiiVision DSOX2012A, Digital storage oscilloscope (100 MHz, 2 GSa/s, input impedance 1 MΩ). The PGSTAT302N Autolab was used to investigate all electrochemical measurements including cyclic voltammetry (CV) and galvanostatic charge-discharge (GCD).

7.3. Results and Discussion

7.3.1. Structural, Morphological and Compositional Analysis CuCoNiO₄

To study the morphology of the as-synthesized CCNO nanoform, field-emission scanning electron microscopy (FESEM) was conducted and is presented in Figures 7.1a and b, which depicts a typical flowerlike structure. Furthermore, the FESEM image of the CCNO, grown on carbon cloth (CC), is depicted in Figures 7.2a and b in different magnifications. An X-ray diffraction (XRD) profile of the CCNO was carried out to confirm the sample purity and crystal
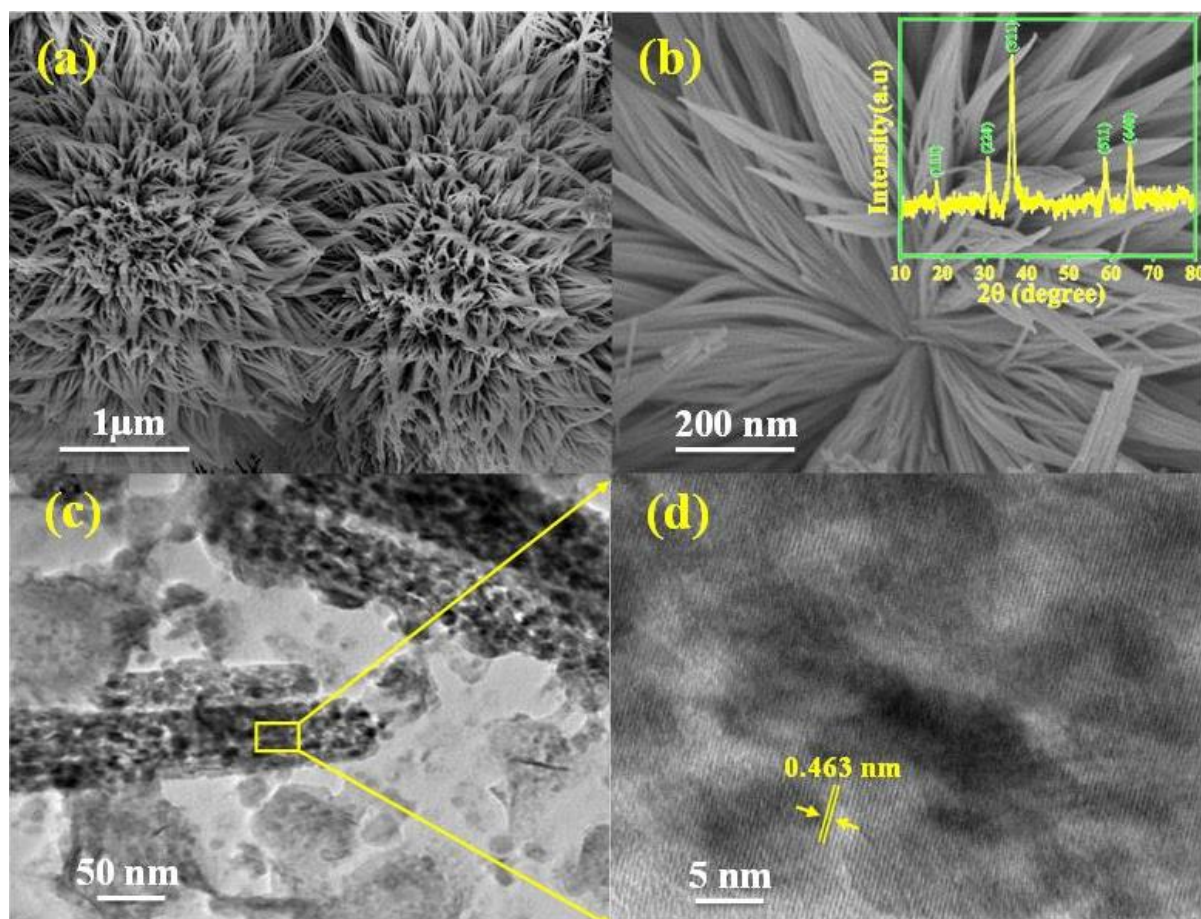
Figure 7.1. *(a, b) FESEM morphology of CCNO (inset: X-ray diffraction pattern of CCNO); (c) TEM and (d) HRTEM images of CCNO nanoforms.*

structure, as presented in Figure 7.1b (inset). All the sharp peaks are indexed and match closely with the literature (JCPDS No. 76-1802). All the other diffraction peaks in both Figures are indicative of the spinel structure phase of the space group *Fd3m*. Careful observation of these peaks suggests a slight shift in position as compared to those of spinel Co_3O_4 (JCPDS card no. 76-1802). Transmission electron microscopy (TEM) is further used to investigate the structural aspects of the CCNO nanostructures. Figure 7.1c shows TEM images of the CCNO nanoform, which reveal porosity in it. From this image, nanowires composed of very small crystallites of different sizes are obvious. The presence of pores is beneficial for electrolyte penetration and quick electron-ion transfer, which increases electrochemical activity. The HRTEM image of the same (Figure 7.1d) shows parallel lines with a spacing of 0.463 nm that corresponds to the (1 1 1) lattice plane of CCNO, suggesting that it is well crystalline.
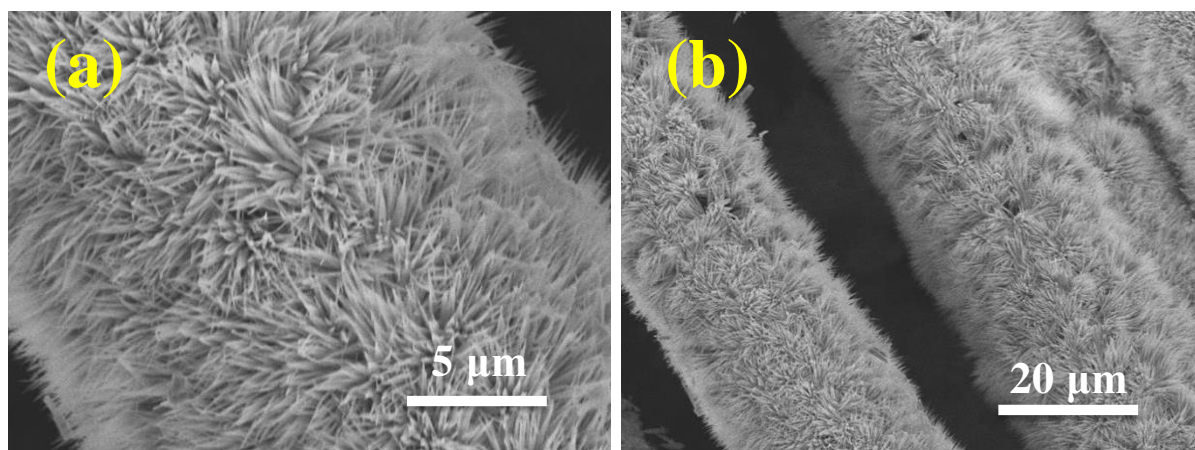
Figure 7.2: *(a)-(b) FESEM image of CCNO grown on CC at different magnifications.*

7.3.2. XPS Analysis

XPS examination was performed in order to determine the precise surface composition and evaluate the oxidation state of the constituent elements of PNCU 1 sample. The results are shown in Figure 7.3. All of the spectra were charge-corrected in consideration of the C 1s peak at 284.6 eV prior to data analysis. High resolution XPS spectra of Cu, Co, and Ni in Figures 7.3a, b and c respectively show characteristic doublet features. Two significant peaks at 952.6 and 933.6 eV that can be attributed to the Cu $2p_{3/2}$ and Cu $2p_{1/2}$, respectively, can be seen in the high-resolution spectra of Cu 2p in Figure 2a. Similarly, for Co, peaks at 780.1 and 795.2 eV are seen that are connected to Co $2p_{3/2}$ and Co $2p_{1/2}$, respectively. The presence of tetrahedral Co^{2+} and octahedral Co^{3+} is indicated by such doublet characteristics of the 2p spectral profile of Co as well as the spin-orbit splitting value over 15 eV. Ni $2p_{3/2}$ and Ni $2p_{1/2}$ are connected to the peaks that emerge at 854 and 868 eV, respectively. A shift in the proportion of covalent to semi-ionic bonds can be seen in the F 1s spectra. In pure PVDF material compared to PNCU 1, semi-ionic bonds are more common (Figure 7.3d, e). The alteration in bond concentration corresponds to the change in crystalline phases. Similar to how semi-ionic bonds are more orientated than covalent ones, β the γ and phases are more oriented than the α phase. The F 1s spectra might then be interpreted as showing a change in bonding in favor of covalent bonds that are less orientated as well as an increase in the concentration of the less oriented phase.
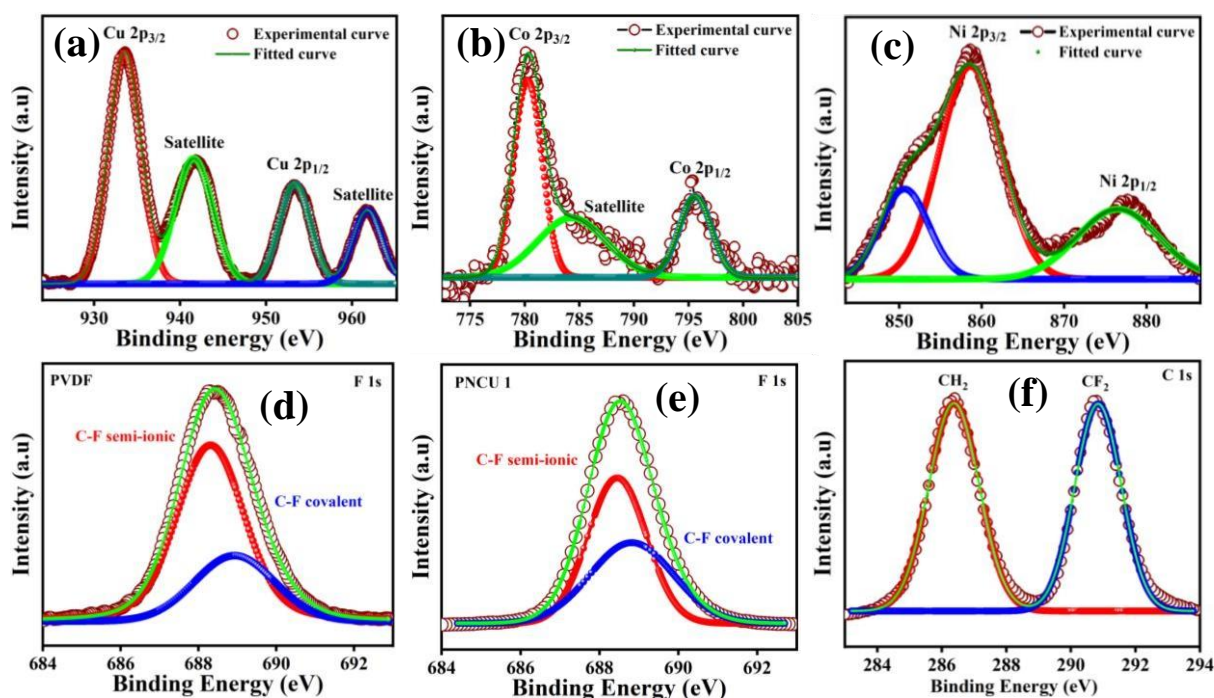
Figure 7.3: *Core level XPS spectra of (a) Cu 2p, (b) Co 2p, (c) Ni 2p, (e) F 1s and (f) C 1s of PNCU 1 and (d) F 1s of PVDF.*

Two components were visible in the peak associated to C 1s. According to Figure 7.3f, the peaks at 286.1 eV and 290.8 eV, respectively, can be indexed to the CH_2 and CF_2 bonds. This shift in peak position compared to pristine PVDF may be attributed to internal electric field generation caused by hybrid formation.

7.3.3. FTIR Analysis

Further analysis of the FTIR spectrum is necessary to confirm the chemical attachment of the CCNO to the host PVDF matrix. Figure 7.4a shows FTIR spectra for all prepared films acquired in absorbance mode at room temperature in the wavenumber range of 400-3200 cm^{-1}. The configuration of the C-C bonds, along with the framework of the carbon chain in the chemical structure of PVDF, characterizes the distinct phases (α, β, γ, δ) of PVDF [43-46]. FTIR spectroscopy confirms the interfacial interaction between the surface charge of CCNO and the dipoles of PVDF polymer, and as a result, PVDF chain orientation is converted from
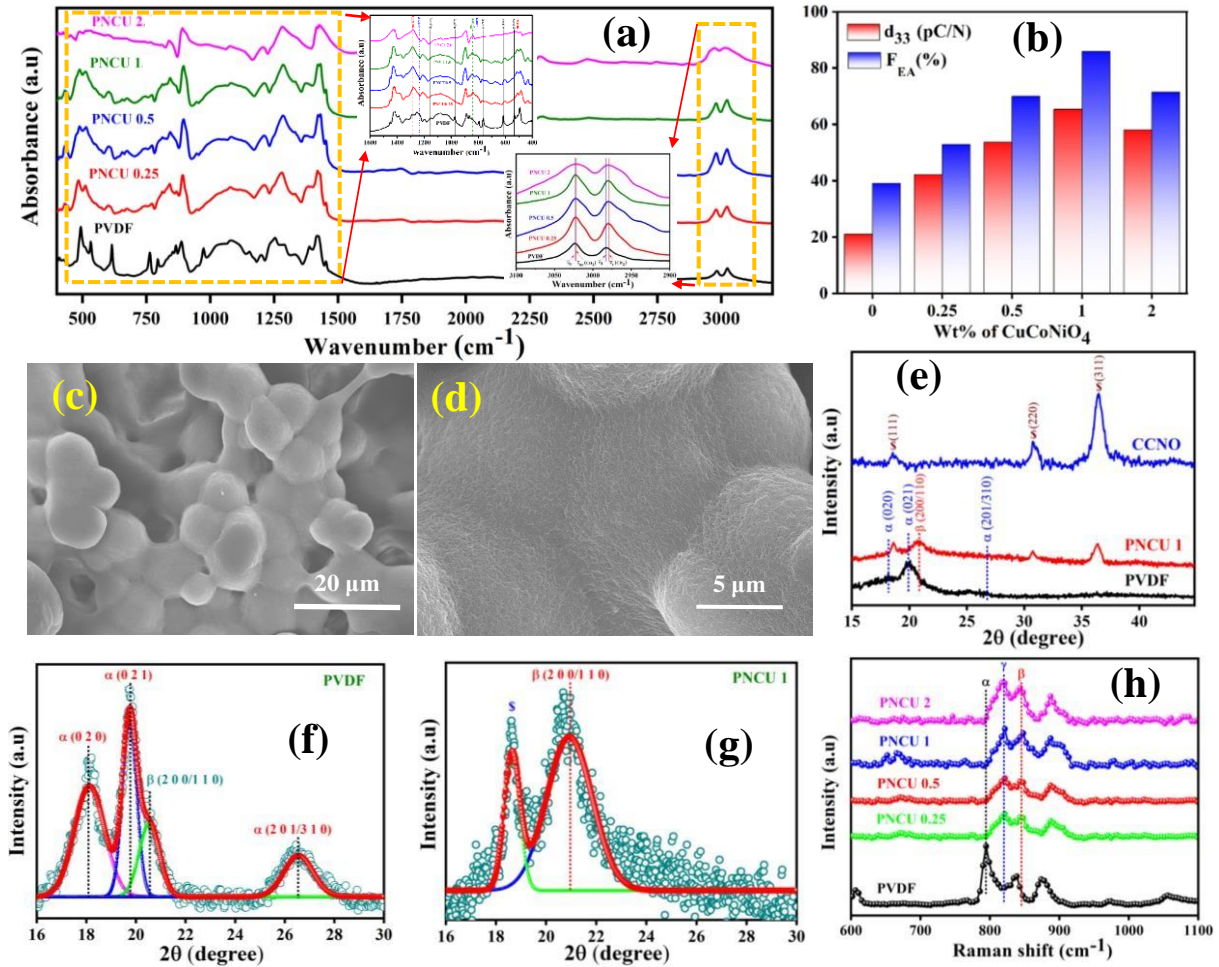
Figure 7.4: *(a) FTIR spectra of all films; (b) Variation of d_{33} and F_{EA} with CCNO content in the sample; (c, d) FESEM image of the PNCU 1 film at two different magnifications; (e) XRD pattern of CCNO, PVDF and PNCU 1 films. Deconvoluted XRD region (16°-30°) of (f) PVDF; and (g) PNCU 1 showing different phase proportions; (h) Raman spectra of all composite films and neat PVDF film.*

TGTG to TTTT and partially to T^3GT^3G [43, 63, 64]. Figure 7.4a (inset) illustrates a zoomed-in image of the same in the 1600-400 cm^{-1} range, with all crystalline phases indexed. Assorted peaks corresponding to the α, β and γ phase can be found in the spectra. The absorption band related to the non-polar α phase appears at wavenumbers 532, 613, 764, 973, and 1155 cm^{-1}, whereas the highly polarized β phase is indicated by the vibrational band peaking at 1279 cm^{-1}, and the semi-polar γ phase is indicated by the vibrational band emerging at 812 cm^{-1} [43-46]. The α phase related peak intensity in bare PVDF is substantially higher than in the other

composite samples. The peak intensity at 1279 cm^{-1} is greatly increased in composite films, whereas the peak attributed to the α phase is significantly reduced. This finding strongly suggests that the highly electroactive β phase is increasing in the composite. As a result, this finding is strong evidence of the highly electroactive β phase's emergence. The peak at 812 cm^{-1} was significantly enhanced in the composite film, indicating that γ phase content increased in hybrid films.

It is obvious that the composite films are mostly made up of electroactive β and γ phases. In composite films, another significant characteristic band appears about 844 cm^{-1}, where β and γ phases are overlapped for the presence of common TTT configuration. It should also be observed that the quantity of β phase fraction is higher than the amount of γ phase [43-46], as evidenced by the absorption band ratio of A_{1275}/A_{1236}. Using the following equation, the electroactive phase percentage for various films may be estimated from Figure 7.4a:

$$F_{EA} = \frac{A_{844}}{\frac{K_{844}}{K_{764}} A_{764} + A_{840}} \times 100\% \qquad (7.1)$$

The absorption coefficients corresponding to the absorption intensity at 764 cm^{-1} (A_α) and 844 cm^{-1} (A_{EA}) peaks, respectively, are K_α (7.7×10^4 cm^2 mol^{-1}) and K_{EA} (6.1×10^4 cm^2 mol^{-1}). The area under the β phase peak and the α phase peak in the same spectrum, which are different for different composites, were compared to determine the β phase percentage in the PVDF matrix. Figure 7.4b shows that the electroactive phase (β and γ) fraction (F_{EA}) reaches a high of 86% for CCNO content 1wt% and then falls. The interfacial interaction between the surface charges of CCNO nanoforms and the molecular dipoles (–CH$_2$– and –CF$_2$–) of PVDF is primarily responsible for the enhancement of the electroactive phase. For low filler concentrations, interfacial interaction in the composite PVDF film is insufficient for optimal α to β phase conversion. Interaction is sufficient for a 1wt% filler concentration, and phase achievement is significant. Furthermore, as the concentration of CCNO inside the PVDF matrix increases, dipoles of the PVDF chain (–CH$_2$– and –CF$_2$–) become stuck by the surface charge or defect

of the CCNO and PVDF interface, resulting in a decrease in dipolar polarization in the composite film. The aggregation of CCNO inside the PVDF matrix due to doping with more than 1wt% CCNO is another reason of polarization loss. Figure 7.4a (inset) illustrates a frequency shift in a vibrational band, and this frequency shift in symmetric (ν_s) and asymmetric (ν_{as}) stretching modes of –CH$_2$– dipoles is evidence of CCNO and PVDF interfacial interaction [46, 64]. Interfacial interaction causes natural vibration to be dampened, lowering the effective mass of PVDF dipoles and shifting certain vibrational frequencies to the lower frequency range. As a result, this damping constant can be used to quantify the interaction. It has the following relation with angular vibrational frequency (ω_{int}) due to damping:

$$\omega_{int}^2 = \omega_0^2 - r_{dc}^2 \tag{7.2}$$

The damping free oscillation's angular vibrational frequency is denoted by ω_0 here. The frequency shift can be deduced using the following equation:

$$\bar{\nu}_{int}^2 = \bar{\nu}_0^2 - \left(\frac{r_{dc}}{2\pi c}\right)^2 \tag{7.3}$$

The velocity of light in free space is given by c. r_{dc} fluctuates depending on the frequency of damped vibration of –CH$_2$– dipoles, with values of 2.79, 2.94, 3.29, and 2.87 s^{-1} for PNCU 0.25, PNCU 0.5, PNCU 1 and PNCU 2 respectively. The damping constant rises until the filler concentration reaches 1 wt. %, then falls.

7.3.4. d$_{33}$ Measurement

The piezoelectric coefficient, represented as d$_{33}$, measures the volume changes that take place when a piezoelectric material is exposed to an electric field or the polarization that develops when a stress is applied. d$_{33}$, which sets a measure of the moment and alignment of dipoles in the PVDF matrix, is a key metric to explain the observed piezo response of the as-fabricated devices. Figure 7.4b depicts the dependence of d$_{33}$ as well as electroactive phase content on

CCNO concentration in the PVDF matrix. The variation of d_{33} and the polar phase fraction follow a similar pattern to the filler loading percentage in the PVDF matrix. This pattern is consistent with the FTIR data, which showed that the maximum β phase amount was found for 1wt% CCNO based hybrid. For the PNCU 1 film, the maximum d_{33} was estimated to be 65.4 pC/N, indicating that the number of oriented dipoles is sufficiently high. PVDF, on the other hand, has the smallest d_{33} value, which represents the minuscule net dipole moment per unit cell.

7.3.5. Structural and Morphological Analysis of CCNO/PVDF Composites

The microstructure of composites and filler distribution inside the polymer matrix are assessed using FESEM. Figure 7.4c, d displays FESEM images of PNCU 1 film at different magnifications, indicating that the CCNO nanoforms are well attached and uniformly distributed in the PVDF matrix in PNCU 1 composites. With the PVDF matrix fully concealed, the underlying CCNO becomes practically undetectable. Further, XRD was also used to identify phases, determine crystallinity, and analyze the phase structures of the bare PVDF and composite films. The CCNO structure, which is also seen in the XRD patterns of PNCU 1, is represented by strong Bragg reflections at 18.6°, 31°, 36.5°, 58.5°, and 64.4° (Figure 7.4e). Figure 7.4e shows broad diffraction peaks in PVDF film at 18.4°, 19.9° and 26.4°, indicating that the pristine PVDF includes primarily α crystalline phase [29, 64]. The α crystalline peaks in XRD patterns vanish completely as the filler is gradually introduced into the PVDF matrix, while a new peak at 20.8° appears, which is actually due to the highly polar β crystalline phase. PNCU 1 has the highest peak intensity at 20.8º and the other peaks are almost diminished. These findings support prior findings that the incorporation of the can significantly boost the electroactive-phase content. The crystallinity of all phases of bare PVDF and PNCU 1 films was determined from the deconvoluted XRD peaks, which were well-fitted using a Gaussian

function. The nonpolar α phase is represented by the deconvoluted peak at 18.4°, whereas the polar β phase is represented by the peak at 20.8°, as seen in Figure 7.4f, g [29, 64]. When comparing PNCU 1 to PVDF, the peak intensity at 20.8° is larger, whereas the peak at 18.4° is completely diminished.

7.3.6. Raman Analysis

Figure 7.4h shows the Raman spectra of all synthesized samples, with the corresponding crystalline phases labeled accordingly. The peak at 796 cm^{-1} in the bare PVDF is attributed to the –CH$_2$– rocking vibrations of the non-polar α phase, whereas the characteristic band at 840 cm^{-1} corresponds to the highly polar β phase involving –CH$_2$– rocking, –CH$_2$– stretching and skeletal C–C stretching. Another prominent peak appears at 812 cm^{-1}, which corresponds to the semi-polar γ phase. The peak intensity of pristine PVDF at 840 cm^{-1} and 812 cm^{-1} is relatively low, but it is significantly higher for CCNO-incorporated PVDF film, indicating that the β phase is boosted due to blending [65, 66].

7.3.7. PFM Analysis

The local polarization state and dynamic domain switching behavior of the PNCU 1 were investigated using PFM measurements. Because of the direct tip-surface interaction, PFM has high spatial resolution and sensitivity to local polarization [30, 67, 68], making it an ideal tool for studying the ferroelectric domain at the nanoscale. The amplitude picture of PFM reveals a nearly regular spontaneous domain (Figure 7.5a, b). Domains with opposite polarization orientations can be identified by the image contrast in Figure 7.5a, b. Domain polarization is signified by the bright yellow and dark brown regions, which are oriented downward and upward, respectively. By applying a voltage across the thickness of the PNCU 1 film through a conducting tip, the characteristic butterfly-shaped amplitude and phase hysteresis loop were
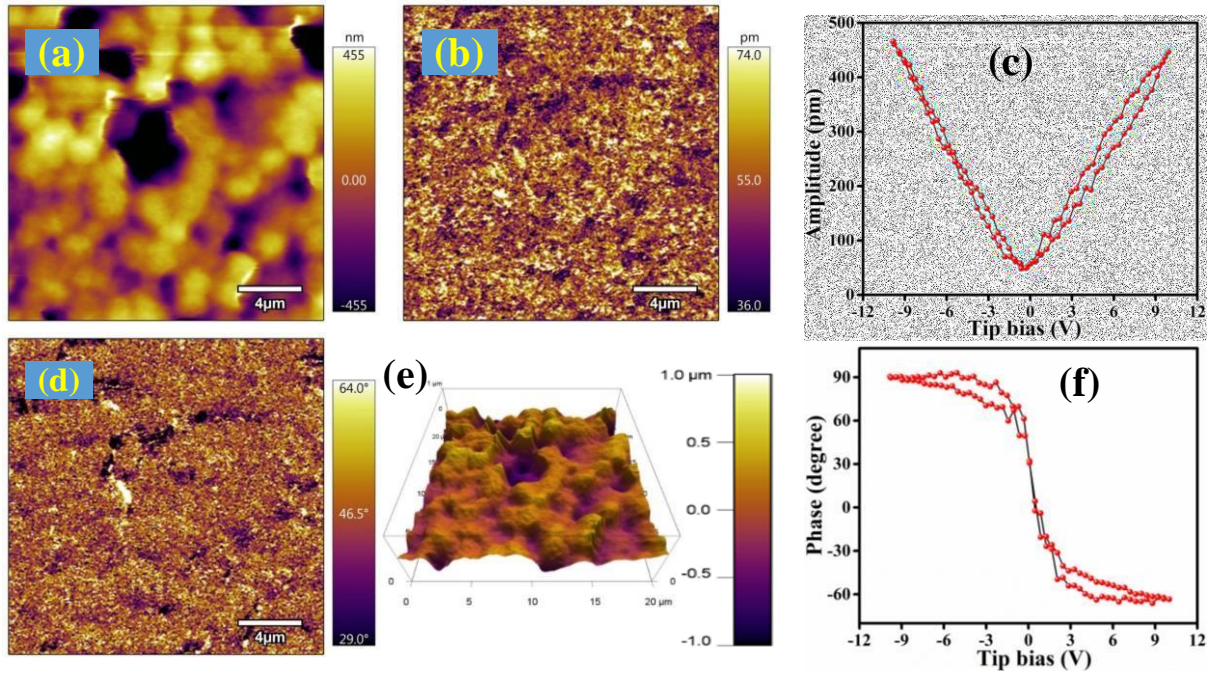
Figure 7.5: *Local piezoelectric behavior PNCU 1 material. (a, b) Topography image of the film (c) PFM amplitude (butterfly loop) (d) PFM phase image (e) 3D surface morphology (f) phase hysteresis loop of PNCU 1.*

also recorded. The cantilever of the PFM tip picked up the strain produced in the film as the voltage was applied across the thickness of the film to explore the ferroelectricity and local piezo-response of the PNCU 1. The asymmetry of the amplitude loop shown in Figure 7.5c could be attributed to domain movement and a built-in piezoelectric field under the tip region. In the measurement configuration, a very non-uniform electric field could develop under the conducting tip, causing an in-plane driving force to bend or move the non-180° domains. It is obvious from this result that the dipoles can easily alternate in the presence of an external electric field. The z-axis amplitude and phase were mapped, as shown in Figures 7.5a, b, and d, because the tip deflection is caused by out-of-plane deformation in the PNCU 1 film. When the tip biasing voltage was swept from +10V to -10V, the as-obtained classical butterfly loop is illustrated in Figure 7.5c for composite PVDF film. Figure 7.5e depicts 3D pictures of surfaces representing the calculated amplitude of the sample deformation. The piezoelectric phase hysteresis loop for the PNCU 1 is illustrated in Figure 7.5f.
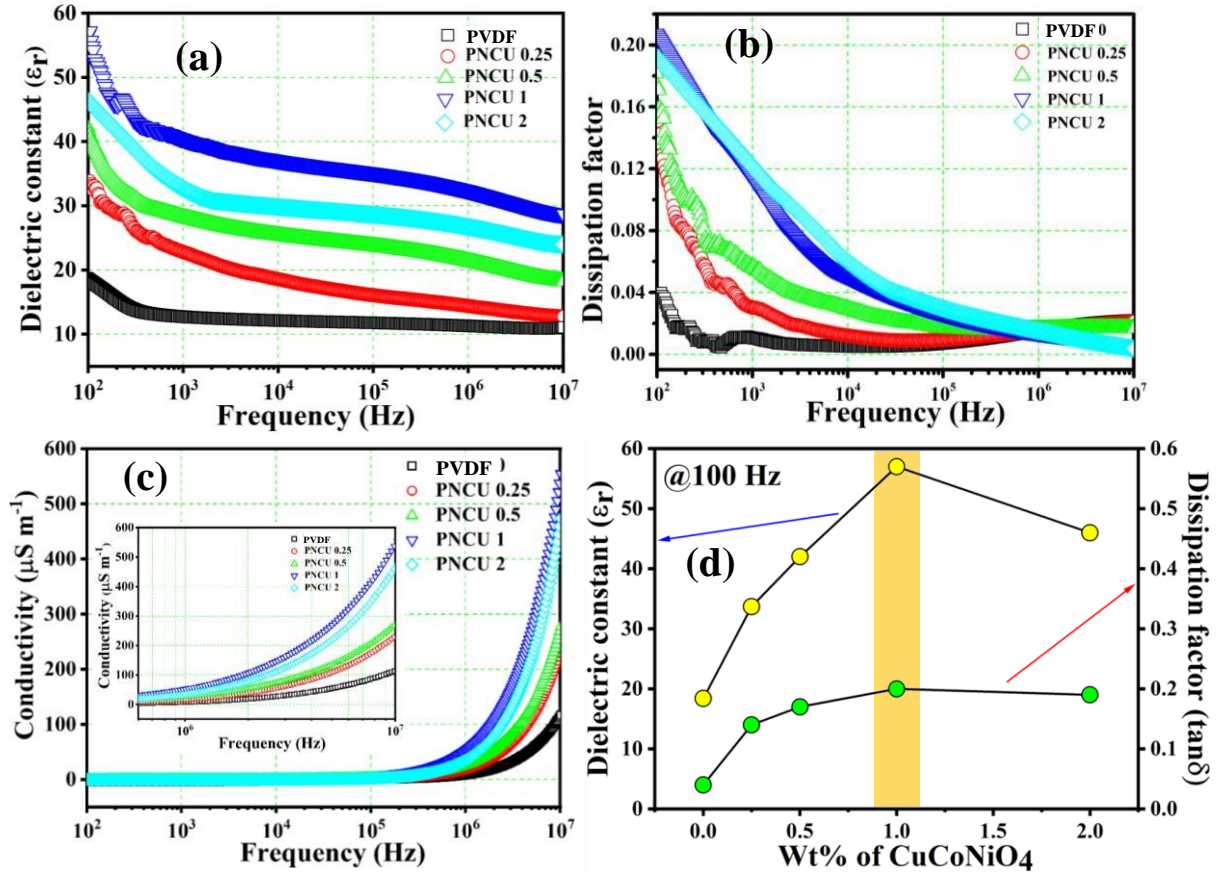
7.3.8. Dielectric Measurement

Figure 7.6: *Dispersions within the frequency range 100 Hz to 10 MHz of (a) dielectric constant; (b) dielectric loss tangent and (c) ac conductivity (inset: magnified view of conductivity variation for the range 0.6-10 MHz) of all synthesized composite films along with neat PVDF film; (d) comparison of dielectric constant and dielectric loss with CCNO loading in the PVDF matrix at 100 Hz.*

At room temperature, the dispersion of relative dielectric permittivity (ε_r), dielectric loss or dissipation factor (tan δ), and ac conductivity (σ_{ac}) as a function of the frequency of the input ac signal was investigated for the different amount of filler wt. % in the samples. Figure 7.6a, b, and c show dispersions of PVDF, PNCU 0.25, PNCU 0.5, PNCU 1, and PNCU 2 films in the frequency range 100 Hz to 10 MHz. The dielectric constant and loss factor of pristine PVDF and all composites decreased with increasing frequency of the external ac field for all films. We can't ignore the effect of space charge in the lower frequency region. A higher filler

concentration resulted in more space charge, which improved both ε_r and tan δ [69, 70]. Restricting the mobility of PVDF dipoles lowers the Maxwell Wagner Sillars interfacial polarization (MWSIP) and dielectric constant as the frequency rises [69]. The mobility of the molecular dipoles in PVDF can follow the external ac field in the low-frequency zone. However, they categorically fail to chase the external alternating field in the high-frequency zone. As a result, the mobility of dipoles is confined in this region and lags behind the electric field [69, 70]. At higher frequencies, the dielectric constant and dielectric loss are lowered as a result of this. The insertion of CCNO in the PVDF matrix resulted in an increase in the dielectric constant and tangent loss up to a certain amount (1wt %) of CCNO content in the polymer matrix, followed by a reduction. At 100 Hz, the maximum dielectric constant of ~57 corresponds to the PNCU 1 with a small dissipation factor of ~0.2, whereas pristine PVDF has a dielectric constant of ~18.4 and a dielectric loss of ~0.04. The introduction of CCNO into the PVDF matrix caused the polymer chain to re-form and convert to an all-trans configuration, resulting in the nucleation of a highly polar phase and an increase in the composite film's interfacial polarization, which was greatest in the PNCU 1 sample. In addition, the MWSIP effect helps improve the dielectric properties of composites. However, excess filler material loading causes agglomeration, which affects interfacial polarization and results in a decrease in dielectric constant [69, 70]. Figure 7.6d depicts the dielectric constant and dissipation factor/dielectric loss as a function of filler concentration at 100 Hz. The frequency dispersive ac conductivity was calculated from the equation below,

$$\sigma_{ac}(\omega) = 2\pi f \, \varepsilon_0 \, \varepsilon_r \tan \delta \qquad (7.4)$$

Figure 7.6c shows that conductivity increases with frequency, peaking at 550 μS m^{-1} for PNCU 1 at 10 MHz (whereas unblended film conductivity is only 110 μS m^{-1}).
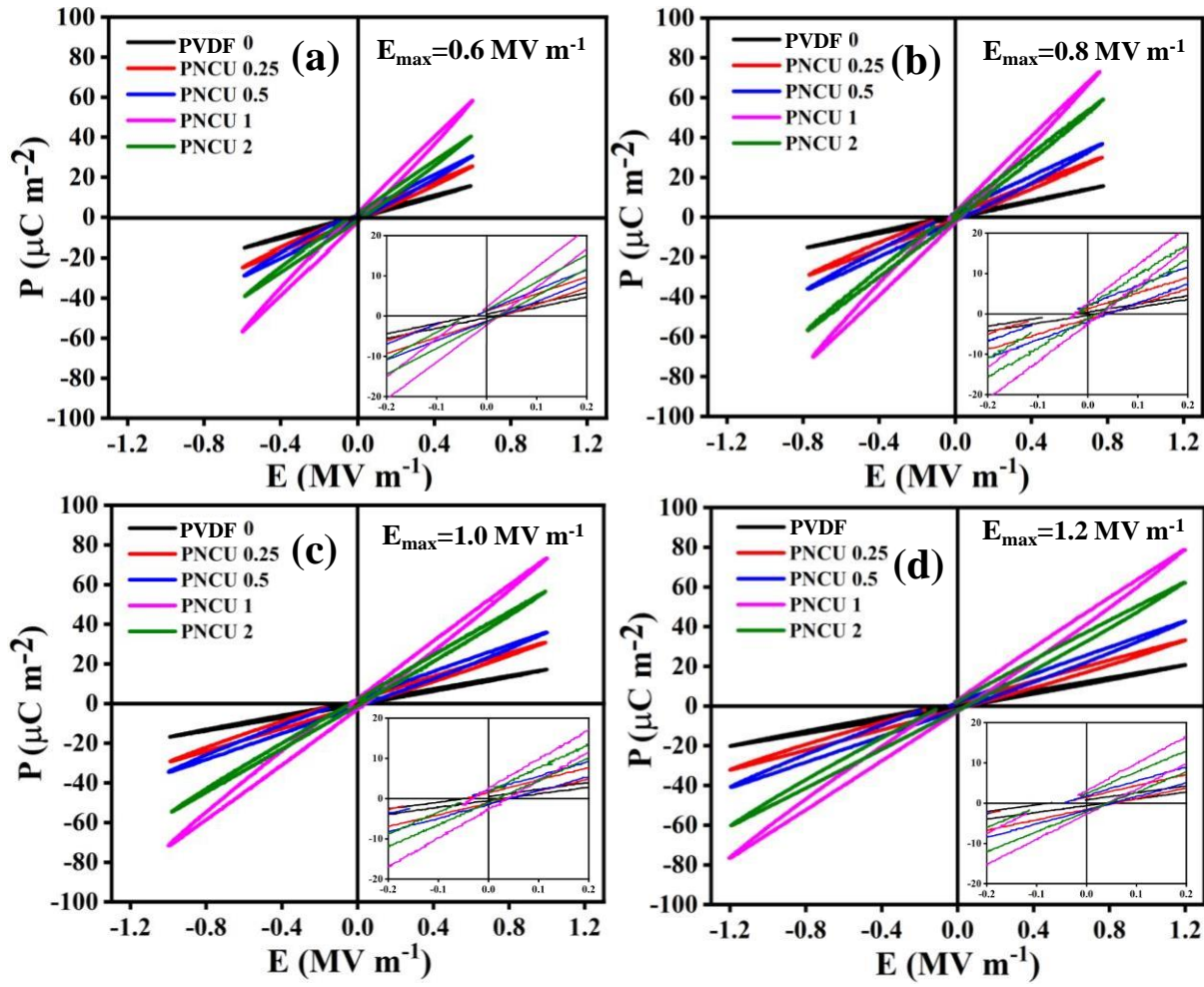
7.3.9. P-E loop Measurement

Figure 7.7: *P-E curves for all synthesized films under a maximum applied field of (a) 0.6 MV m^{-1}; (b) 0.8 MV m^{-1}; (c) 1.0 MV m^{-1}; and (d) 1.2 MV m^{-1} (enlarged view is presented in the inset).*

Polarization (P)-electric field (E) hysteresis loops are critical for determining the ferroelectric behavior and charge-storing capacity of films at room temperature. The P-E loops are thus recorded for films with different CCNO content at room temperature and at a frequency of 1 Hz, as shown in Figure 7.7a-d. PNCU 1 film was found to possess maximum saturation polarization ($P_{S,max}$) ~80 μC m^{-2}, and coercive field ($E_{c,max}$) ~0.066 MV m^{-1} against the highest field of 1.2 MV m^{-1}. While, PVDF film only attains the values of $P_{S,max}$ ~20.8 μC m^{-2} and $E_{c,max}$ ~0.034 MV m^{-1} under identical conditions, which is quite lower than PNCU 1 film. Figure 7.8a depicts the change in saturation polarization for all films as a function of applied voltage. Increased filler concentration up to a certain level transforms the polymer chain from
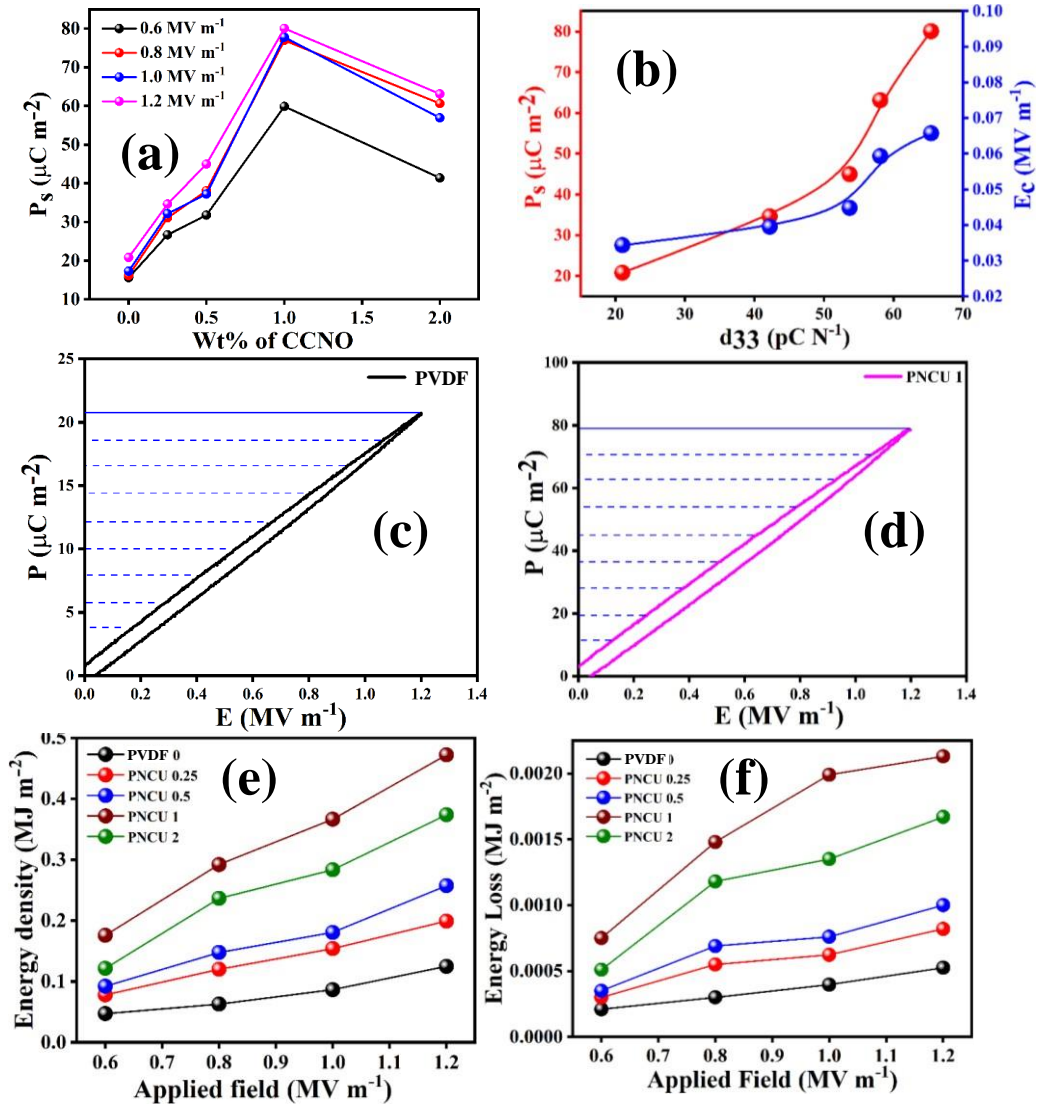
Figure 7.8: *(a) Variation of saturation polarisation of the composite films at different applied fields. (b) Change of saturation polarization and coercive field as a function of the piezoelectric coefficient (d_{33}). Electric polarisation vs Electric field hysteresis loop (P-E Loop) of (c) PVDF and (d) PNCU 1 at electric field 1.2 MV m^{-1}. (e) Energy density and (f) energy loss as function of applied field for different samples.*

TGTG zig-zag to ferroelectric TTTT configuration with proper dipolar alignment along the c axis in the polymer chain [46, 56], where switching dipoles, interface effect, and filler-

inducedcharge trapping are most likely involved. As the filler content rises, molecular dipoles shift in a certain direction (c-axis) that is most prominent in the PNCU 1 sample.

In addition, Figure 7.8b shows the fluctuation of saturation polarization and coercive field as a function of the piezoelectric coefficient (d_{33}). Furthermore, low CCNO percentage means fewer mobile charge carriers and smaller loop regions, whereas a greater CCNO fraction produces more charge-carrying nanoform. It results in increased energy dissipation and an enhanced loop area. The energy density was calculated from the shaded area (A) of Figure 7.8c, d and the loop area, which describes the energy loss [71]. Figure 7.8e and f show the energy density and energy loss of different composite films under different applied fields. As the CCNO percent rises, the energy dissipation rises with it, as seen in Figure 7.8f.

7.3.10. Performance of Piezoelectric Nanogenerators

To investigate the device's output performance, initially five nanogenerators with different samples has been fabricated, namely PVDF, PNCU 0.25, PNCU 0.5, PNCU 1, and PNCU 2, and labeled them RNG (reference nanogenerator), PNG 0.25, PNG 0.5, PNG 1, and PNG 2, respectively. The effective area of each PNG device is 3×2 cm^2. Additionally, they are laminated to minimize the triboelectric effect. When mechanical strain is applied to the PNGs, a deformation in the PVDF matrix occurs, causing the $-CH_2-/-CF_2-$ dipole to align. As a result, a potential is developed along the vertical direction of the film. An electrical potential develops between two electrodes and a current flow through the external circuit to balance this dipole-induced potential. When the pressure is withdrawn, the dipole-induced potential disappears, and the current flow in a reversed direction [46, 56]. As a result, for the entire press-release action, an alternate pulse-type signal is generated. Periodic hammering (~100 kPa) is applied at a frequency of 5 Hz to investigate the performance of all manufactured PNGs, and the as-generated output performance is recorded in a digital oscilloscope, as shown in Figures 7.9a
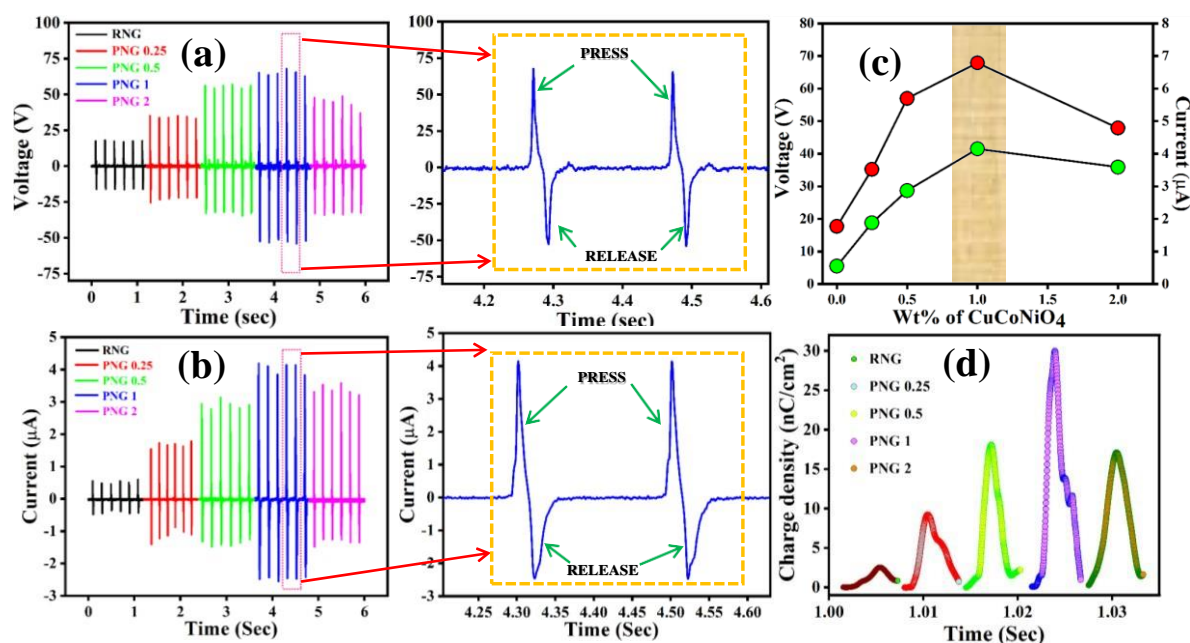
Figure 7.9: *(a) Open-circuit voltage with the enlarged view of voltage (right side); and (b) short circuit current with the enlarged view in the right side for different nanogenerators (RNG, PNG 0.25, PNG 0.5, PNG 1 and PNG 2); (c) Variation of maximum open-circuit voltage and short circuit current as a function of filler loading in PVDF matrix; (d) Charge transfer with time for all nanogenerators under hammering.*

and b. The best output performance is found for PNG 1, among all the fabricated devices, since its constituent film has the highest piezoelectric coefficient of all the PNGs. Positive and negative amplitudes of the produced open circuit voltage and short circuit ensure the complete cycle of press and release on the piezoelectric energy harvesting device by human hand hammering. Because the signal strength depends on the strain rate when pressing and releasing, the first half of the generated signal has a larger amplitude than the second half [72]. Figure 6a and b indicate that PNG 1's output voltage and current have reached their maximum values of 67.9 V and 4.15 µA, respectively, which is sufficient to power several portable smart electronic gadgets. Under hammering in identical conditions, RNG produces output voltages of 17.7 V and currents of 0.55 µA, which are pretty small when compared to PNG 1. Figure 7.9c displays the variation in the output voltage and current for different devices. Figure 7.9d depicts the charge generated by all PNGs when subjected to periodic hammering. The transferred charge

density for PNG 1 is around 30 nC/cm^2, which is quite high when compared to the RNG (2.52 nC/cm^2). The PNG 1 is connected to a load because in practice the devices do not operate in open circuit conditions. To assess the internal resistance (R_i) of the device and maximum output power (P_{max}) generated from the piezo-device, it is needful to cultivate the instantaneous open-circuit voltage and short-circuit current across various load resistance (R_L) ranging from 10 kΩ to 30 MΩ against periodic force (~100 kPa). From Figure 7.10a it is shown that, the voltage drop (V_L) across load resistance (R_L) gradually increases with increased load resistance and saturates after a certain high value of resistance (30 MΩ). And the short-circuit current gradually decreases with the increasing load, which agrees with the theoretical expectation ($I = \frac{P}{V}$). Figure 7.10b shows the instantaneous power as a function of load resistance, from which the internal resistance of the PNG can be determined. The maximum power (P_{max}) delivered from the PNG 1 is 205.1 μW corresponding to the resistance (~10 MΩ). Hence, from the linear circuit theorem, it is accurately conclude that, the same is the internal impedance of PNG 1. In energy harvesting applications, the output performance of the PNG 1 substantiates the usefulness of the device over a broad range of load resistance. To check the authenticity of piezoelectric output, it is necessary to connect the piezo-device in both forward and reverse directions [46]. Figure 7.10c and f shows the result of the polarity switching test, which confirms the output signal is piezo-signal; and not noise. Figure 7.10c and f, demonstrate that, the amplitude of the generated pulses is almost the same but oppositely directed compared to the forward connection, and the inset shows the COMSOL simulation of piezo-signal in a different connection. Some applications demand a high-power DC source along with instantaneous ac output voltage. PNG 1 is connected via a bridge rectifier for this, and the rectified output is recorded in the oscilloscope, as shown in Figure 7.10d. The rectified output voltage under periodic hammering shows a maximum value of 67.9 V. The enlarged view of the rectified voltage is demonstrated in Figure 7.10e, where DC voltages for both halves of the ac signal are
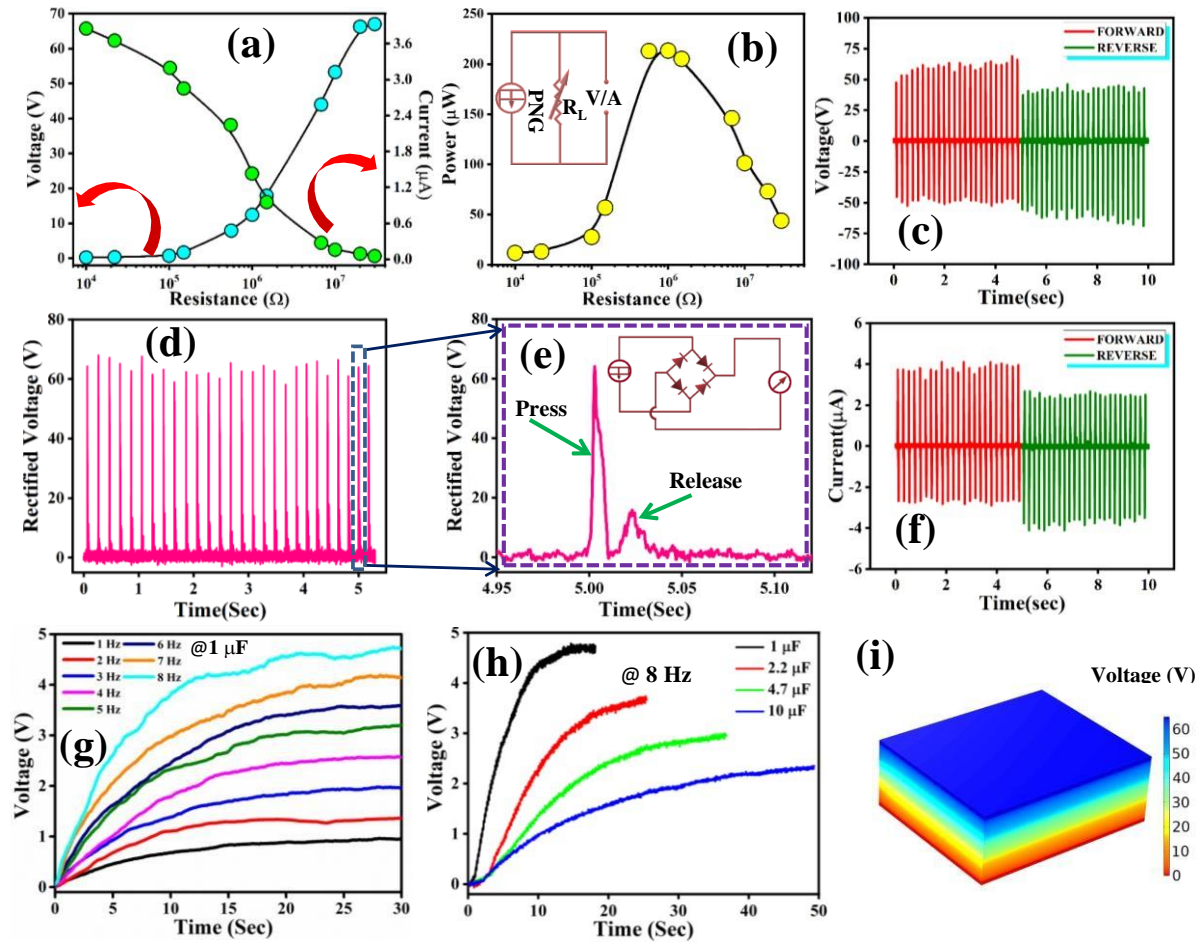
Figure 7.10: *(a) Variation of the voltage, current and (b) power with the load resistance (R_L) and the inset shows the schematic circuit diagram; (c) Output voltage and (f) current measured in forward and reverse connection; (d) Rectified DC output voltage and (e) zoom view of rectified DC voltage of PNG 1; (g) Charging performance of 1 µF capacitor with different imparting frequency from 1-8 Hz; (h) The measured output voltage across the various commercial capacitors of 1, 2.2, 4.7, and 10 µF as charged by PNG 1 at 8 Hz; (i) Simulation results of PNG 1 using the COMSOL Multiphysics programming software.*

shown with the necessary circuit diagram (see the inset). Several applications of the PNG 1 has been demonstrated to self-powered electronics. In order to test the energy harvesting capability of the PNGs and to provide continuous electrical energy to electric appliances, electrical power has been stored from PNG 1 through several capacitors as a temporary charge storage system via a bridge rectifier circuit. The charging performance of a capacitor (1µF) was recorded under

different agitation frequencies, see Figure 7.10g. The storage curve shows that a higher frequency yielded higher voltage along with a faster charging rate. The charging voltage of the capacitor reaches 4.7 V at an imparting frequency of 8 Hz, whereas the voltage of the capacitor at 1 Hz reaches 0.94 V. A further study was executed with four different capacitors with capacitances of 1 to 10 μF under the same tapping frequency (8 Hz). A wide range of capacitors charged up successfully, which can be further used to drive various low-powered devices. The energy stored in a capacitor of capacitance C under a saturation voltage V, is given by:

$$E_{out} = \frac{1}{2} CV^2 \qquad (7.5)$$

Figure 7.10h shows the charging curve. The capacitor charging voltage of 1, 2.2, 4.7, and 10 μF capacitors reaches the maximum steady-state value of 4.7, 3.7, 2.9, and 2.3 V respectively. The output power of the PNG 1 is measured from capacitor charging processes by the relation below:

$$P_{out} = \frac{E_{out}}{Time\ required\ to\ reach\ satuaration\ voltage\ (T)} \qquad (7.6)$$

The calculated output power of the four respective capacitors is 0.62, 0.59, 0.54, and 0.52 μW for small time intervals. This result permits the PNG 1 as an alternative energy harvesting power source for smart portable electronic devices. For a better understanding of the energy-generating mechanism in PNG 1, the open-circuit voltage is simulated in the COMSOL software as shown in Figure 7.10i.

As the mechanical pressure temporarily alters the PVDF crystal structure, the imparting pressure is vital in the production of output voltage. Figure 7.11a shows the electrical reaction to placing various lightweight objects on PNG 1 to show how sensitive it is to pressure. Under applied mechanical pressures of 0.50, 0.65, 0.81, 1.10, 1.50, and 2.20 kPa, respectively, the open-circuit voltages were determined to be 0.42, 0.86, 1.08, 1.79, 1.97, and 2.42 V. Figure 7.11b shows that the voltage increases almost linearly with the applied pressure, with a high
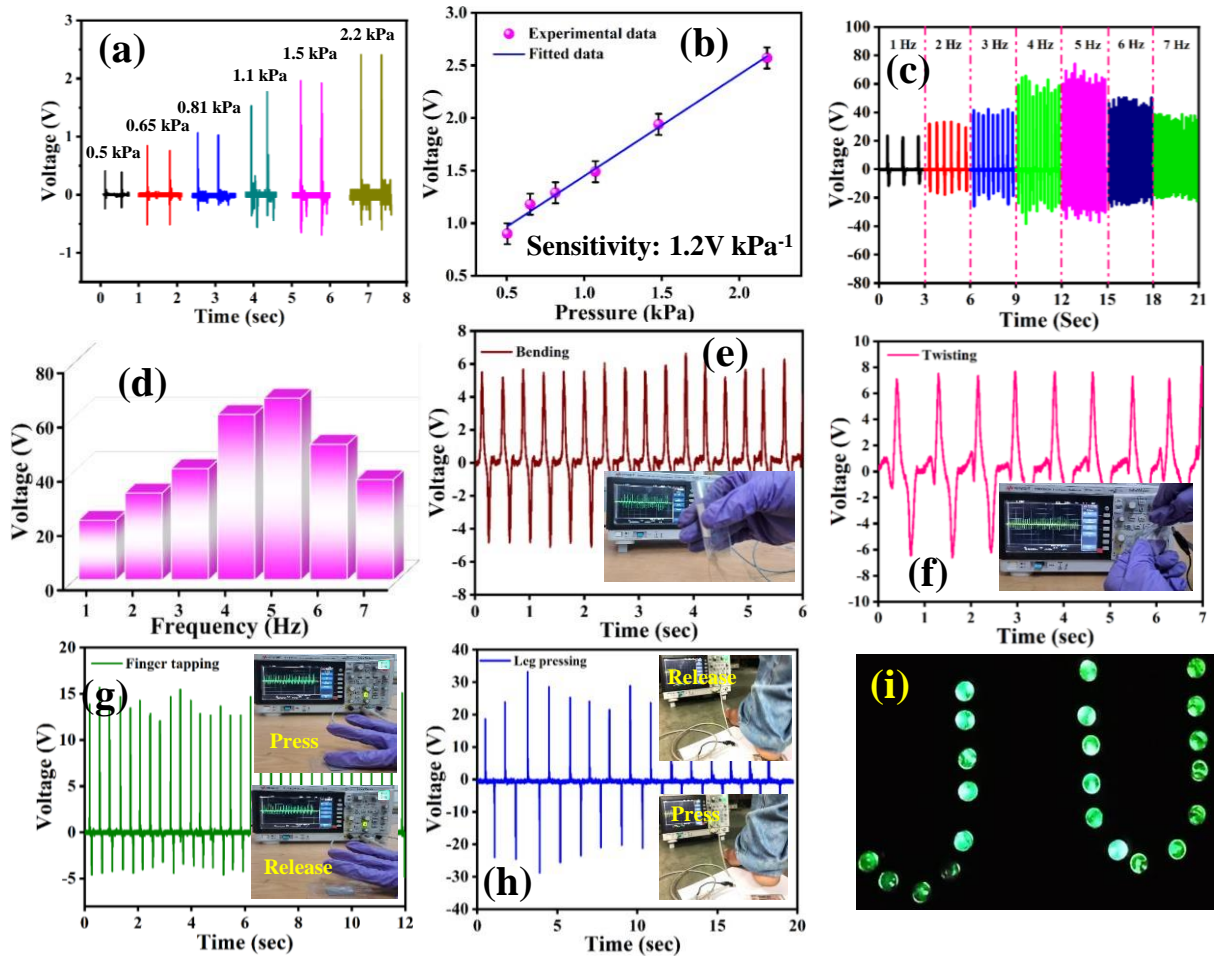
Figure 7.11: *(a) Measured output voltage of PNG 1 under different pressure; (b) Sensitivity of fabricated PNG 1 in pressure range 0-2.2 kPa; (c) Output voltage under different pressing frequency form 1-7 Hz; (d) variation of output voltage as a function of tapping frequency. The open-circuit voltage generated under (e) bending; (f) twisting by the finger; (g) finger tapping; and (h) leg pressing on PNG 1 (insets show corresponding captured images); (i) Captured image in the dark of commercial LEDs glowing in a 'JU' pattern.*

sensitivity of 1.2 V/kPa, where the dimension of PNG 1 is 3×2 cm^2. The performance of PNG 1 was further assessed under different frequencies but constant amplitude impulses (~100 kPa) and is presented in Figure 7.11c. Figure 7.11d explains the frequency-dependent fluctuation of the PNG 1's output voltage under uniform periodic pressing and release. The output voltage appears to rise with the frequency of the continuous periodic force and peak at a frequency of 5 Hz (~ 67.9V). Piezo voltage then starts to drop with more frequent occurrences. When the
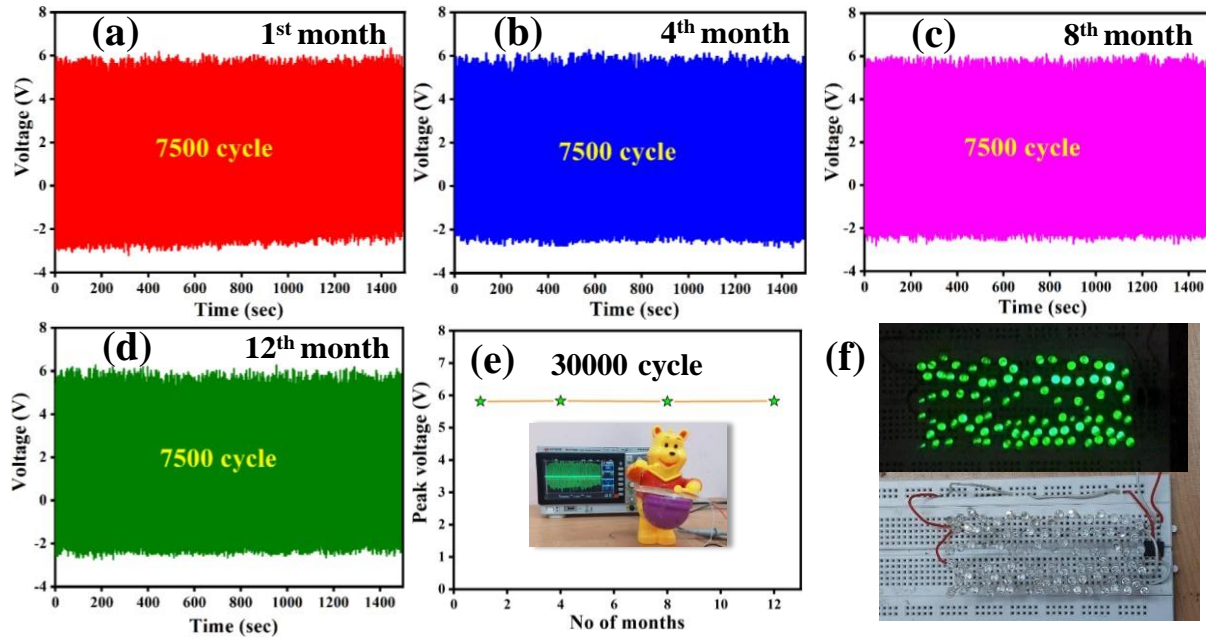
Figure 7.12: *(a-d) Long cycle stability test of PNG 1 over 12 months (30,000 cycles) with an enlarged view in the inset; (e) consistency of peak voltage at different times under long cycle tests; (f) digital photograph showing the ability of PNG 1 to drive 89 LEDs.*

applied frequency is low, the PNG 1 has time to return to its initial shape, but at high frequency (> 5 Hz), it hardly ever has enough time to do so before the next impact, which causes the open-circuit voltage to fall [72]. Durability and flexibility make the PNGs more effective as well as enhance the span of applications. The bending performance of the nanogenerator was investigated for PNG 1 by a human finger, and output performance (up to ~6.55 V) was recorded as shown in Figure 7.11e. Further, testing of the mechanical flexibility was confirmed by twisting the PNG 1. The voltage generated due to twisting by the human hand is ~7.67 V, see Figure 7.11f. Next, the piezoelectric output voltage of PNG 1 was tested under repetitive finger tapping with a pressure of ~10 kPa and a frequency of 2 Hz. Figure 7.11g demonstrates that PNG 1 delivers an open-circuit voltage of about ~15.5V.

Using our piezo devices, mechanical energy can extract from various human activities like walking, arms bending, hand movement, etc. While walking, a voltage of ~28.8 V was generated due to the force applied on PNG 1 via footsteps, as shown in Figure 7.11h. By using

capacitors, we can charge up our mobile batteries anywhere, which is an essential part of our daily life. Moreover, PNG 1 can be used as a replacement for bulky batteries used in common electronic gadgets used in everyday life. The LED glowing in the 'JU' pattern by the power generated in PNG 1 is shown in Figure 7.11i.

Using a "beat the drum" toy over the course of a year (30,000 cycles), the mechanical stability and durability of PNG 1 are further demonstrated. The results are shown in Figure 7.12a–d. It is noted that the output signal is stable for an extended period of time. In order to assure the constancy of applied force and PNG 1's long-term use, the "beat the drum toy" was employed to test the electric power-generating capacity of PNG 1. Figure 7.12e, which depicts the absence of any appreciable voltage drop over time, clearly illustrates the stability performance of PNG 1. A number of the commercial LEDs illustrated in Figure 7.12f can glow with the device's instantaneous output power. Due to the device's exceptional stability, it can be used for extended periods of time in energy harvesting applications that are motivated by sporadic disputes in our neighborhoods.

7.3.10. Electrochemical Performance of PSCFS Device

The intriguing charge storage mechanism within the ultra-small space of the fabricated PSCFS was further investigated by cyclic voltammetry (CV) and galvanostatic charge-discharge (GCD) measurements with an operating voltage of 1.2 V. The ideal capacitive properties of the PSCFS electrode are indicated by the quasi-rectangular forms of the CV curves in Figure 7.13a under the stable potential window of 1.2V. Figure S7b displays the GCD performance in an operating potential window of 1.2 V at several current densities from 0.1 to 0.2 mA cm^{-2}. GCD curves of the electrode exhibit symmetric behavior, which is indicative of fast charge-discharge properties and capacitive response [57-61]. The device possesses a maximum areal capacitance of 15.5 mF cm^{-2} at a current density of 0.1 mA cm^{-2}, and even at a current density of 0.2 mA
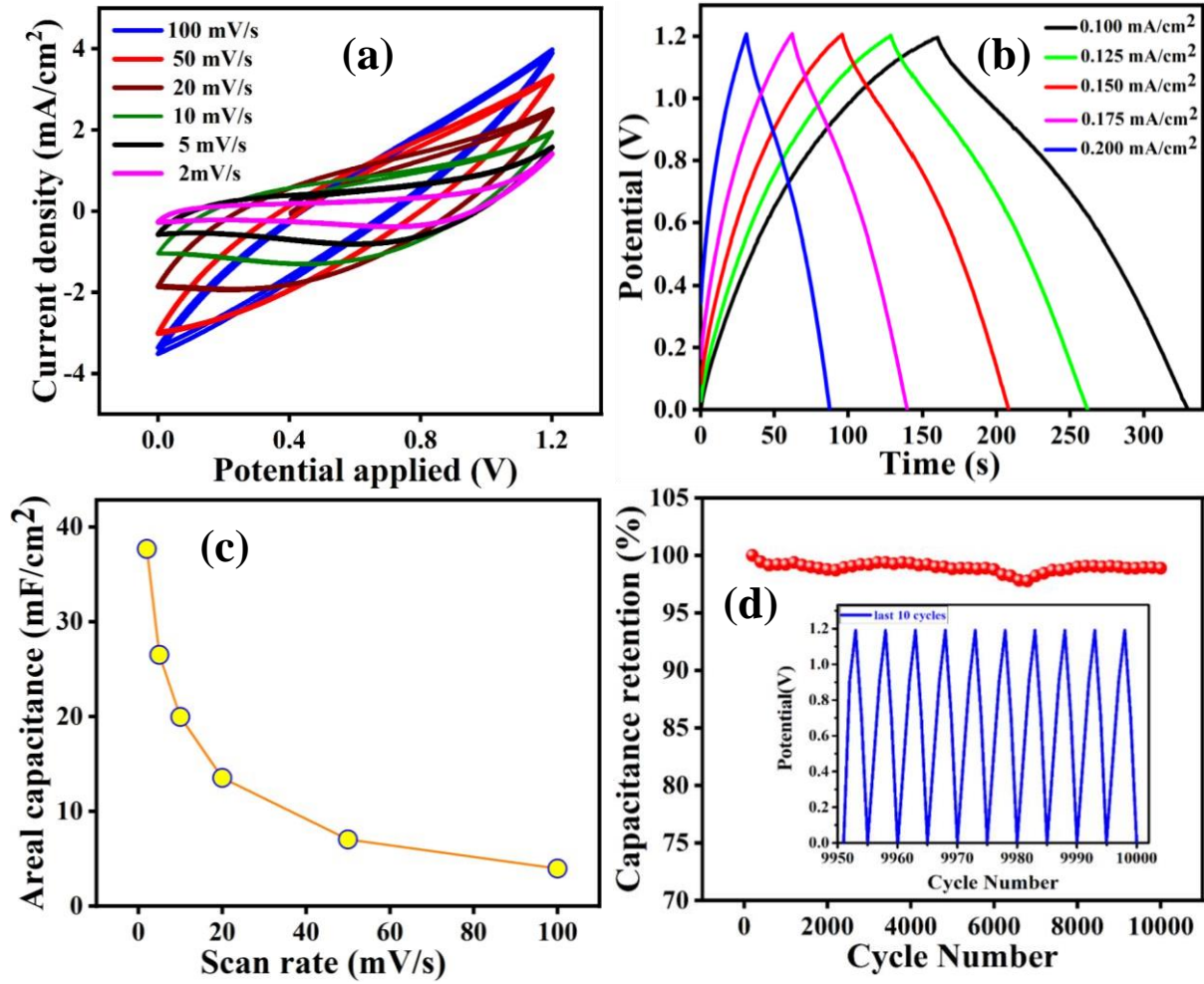
Figure 7.13: *(a) CV profile at different scan rate; (b) GCD profiles at different applied current range; (c) specific device capacitance at different scan rate. (d) Capacitance retention performance after 10,000 cycles (inset: last 10 charging-discharging cycles) of the CCNO electrodes.*

cm^{-2}, the areal capacitance of the device is maintained at a considerable value of 9.7 mF cm^{-2}. The variation of areal device capacitance with applied scan rates is presented in Figure 7.13c, which shows that the PSCFS device exhibits an areal device capacitance of 37.6 mF cm^{-2} at an applied scan rate of 2 mV s^{-1}. It is inferred from this Figure that the areal device capacitance decreases with an increasing applied scan rate. Moreover, the PSCFS exhibits an areal device capacitance of about 3.9 mF cm^{-2} as the scan rate is raised by 50 times (100 mV s^{-1}). The device's capacitance is monitored during 10,000 cycles of charging and discharging at a current density of 0.2 mA cm^{-2} to investigate the device's cyclic stability (Figure 7.13d). The fact that

the capacitance retention remained at 98 percent of its initial value after 10,000 cycles implies

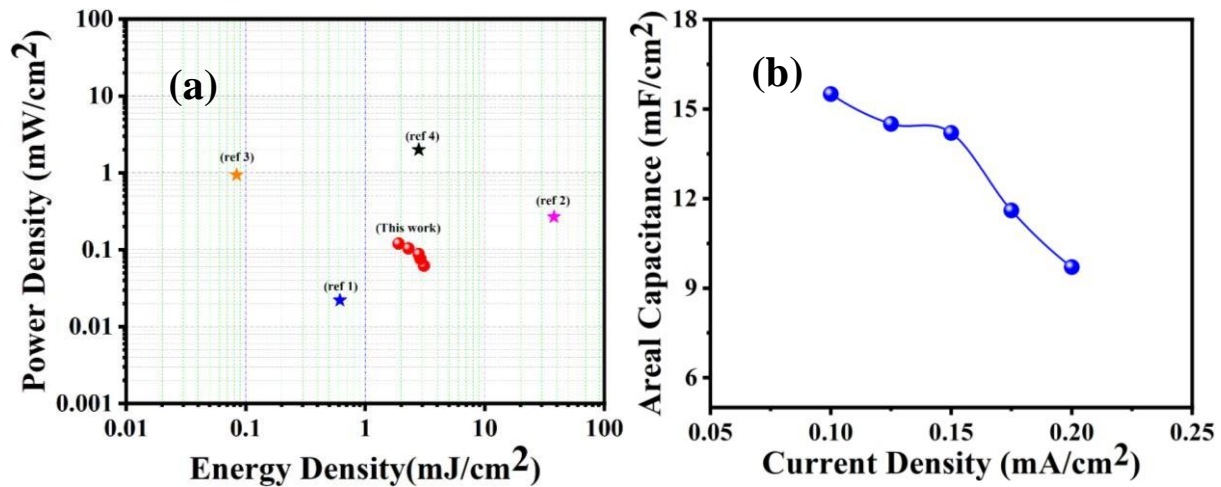that the CCNO is a promising electrode material for the supercapacitor. The fluctuation of the

Figure 7.14: *(a) Variation calculated power density with energy density (Ragone plot) of the*

fabricated device. (b) The specific areal capacitances vs current density plot.

last 10 cycles of the capacitance retention studies is shown in the inset of Figure 7.13d, and it

shows that there have been no appreciable variations in potential with the cycle.

For supercapacitor applications, the usefulness of this PSCFS device was further established

by investigating its energy and power densities. The capacitance can be estimated in F g^{-1} from

$C_m = \frac{\int I dv}{vm\Delta V}$ and $C_m = \frac{I \times \Delta t}{m \times \Delta V}$, respectively for CV and GCD curves at different current densities,

where $\int I dv$ is the integral area (S) under the CV curve, v symbolizes the scan rate (mV s^{-1}),

m is the mass of the electroactive material in g, ΔV indicates the potential window in volts, Δt

is the discharge time in seconds, and I is the constant discharging current in A. From the

measured capacitance (C_m), the areal capacitance (F cm^{-2}) of the single electrode in the two-

electrode cell can be determined from the equation, $G = 4C_m$. The energy, $E = \frac{C_m(\Delta V)^2}{7.2}$ in mW

h cm^{-2} and power density, $P = \frac{E \times 3600}{\Delta t}$ in mW cm^{-2} are further estimated from the

charge/discharge curves [63]. For the fabricated PSCFS, Figure 7.14a depicts the relationship

between computed energy density and power density. The CV curves collected at a constant

discharge current density of 0.1 mA cm^{-2} are used to estimate that the energy density reached 1.9 mW h cm^{-2}, which corresponds to a power density of 0.12 mW cm^{-2}. Furthermore, the PSCFS device still holds an energy density of 3.1 mW h cm^{-2} at a power density of 0.062 mW cm^{-2} even when the constant discharge current density doubles from its original value (0.2 mA
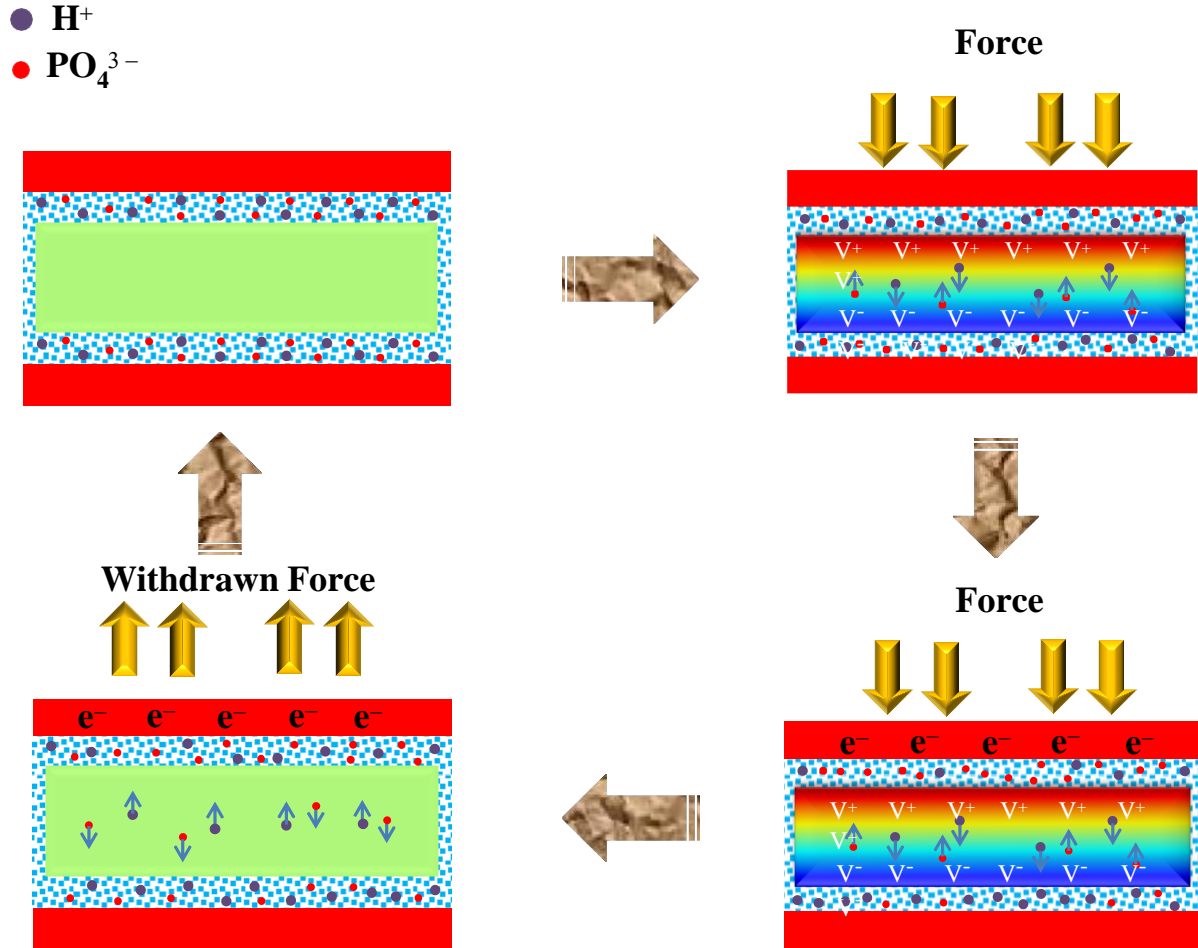
Figure 7.15: Schematic of the self-charging process of PSCFS device.

cm^{-2}). From the CD curves, the evaluated areal capacitances were 15.5, 14.5, 14.2, 11.6, and 9.7 μF cm^{-2}, corresponding to the current density of 0.1, 0.125, 0.15, 0.175, and 0.2 mA cm^{-2}, as shown in Figure 7.14b.

7.3.11. The Working Mechanism of PSCFS

The PSCFS device has been fabricated with a piezo-separator (PNCU 1) between positive and negative electrodes (CCNO) and an electrolyte (PVA/H$_3$PO$_4$) which is uniformly distributed

through the whole surface of the piezo-separator and the electrodes. Figure 7.16a shows a schematic of the PSCFS device, which can transform mechanical energy into electrical energy [57–61]. A schematic of the self-charging process of the PSCFS device is also given in Figure 7.15.

7.3.12. Self-Charging Performance of the As-designed PSCFS
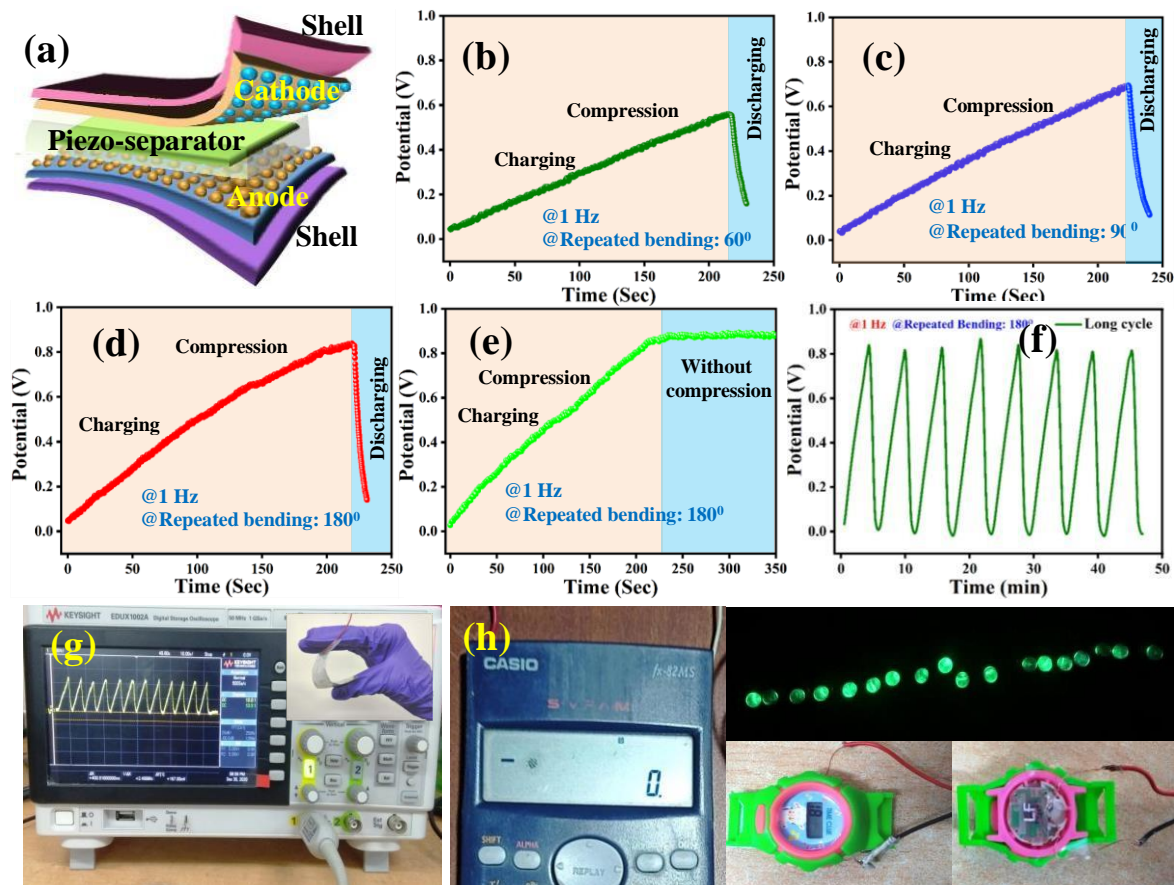
Figure 7.16: *(a) Schematic diagram of the PSCFS device; (b–d) Self-charging performance of PSCFS under different bending states viz., ~60°, ~90°, ~180° and discharging through external load; (e) Self-charging test and charge retention capability of the as-fabricated PSCFS device; (f) Repetitive charging-discharging cycles; (g) Digital image of the self-charging experiment using oscilloscope; (h) Digital photographs of portable electronic gadgets (calculator, wristwatch and green LEDs, respectively) driven by PSCFS device.*

The self-charging behavior of the PSCFS was investigated under varied periodic bends in order to demonstrate applicability for self-powered devices, as shown in Figures 7.16b–d. As shown in Figure 7.16d, when the PSCFS device was periodically bent at an angle of ~180° at 1 Hz frequency, the device charged from 35 to 845 mV (810 mV charging) in 220 seconds. A small voltage first appears in the device, which is probably caused by the PSCFS's minor intrinsic capacitance, which is produced by the separator's piezo-remanent polarization [60, 61]. Additionally, the device's functionality was tested at bending angles of ~60° and ~90° at the same frequency, for which the voltage increased by 535 mV and 666 mV, respectively (Figure 7.16b, c). The larger bending angle improves the self-charging capability of the PSCFS device as the piezoelectric output voltage rises with increasing strain. Furthermore, at a steady current of 10 mA, it discharged back to its initial value for all bending angles in less than 15 seconds. Under frequent bending, the fabricated PSCFS was able to store 810 mV on its electrodes in just 220 seconds. Even after stopping the bending, it maintained a steady value (Figure 7.16e). This result demonstrates that the created charge is stored in the PSCFS device. The charging-discharging cycle is also tested, and the result is displayed in Figure 7.16f. An image of the charging-discharging cycle as captured is presented in Figure 7.16g. Figure 7.16h, which displays the PSCFS device's capacity to power a variety of wearable gadgets like calculators, wristwatches, and LEDs, illustrates the practical applications of the device.

7.4. Conclusions

In conclusion, a novel strategy has been demonstrated for building a multipurpose, high-performance energy harvesting device. A composite films was developed by hydrothermally synthesizing CCNO and adding various concentrations of CCNO to the PVDF matrix. The electroactive phase fraction in the PVDF matrix attained an optimum value ($> 86\%$) in PNCU 1 film. the value of ε_r of all the synthesized films was measured and found that PNCU 1 had the highest value (~57). Furthermore, it was discovered that the d_{33} of PNCU 1 was 65.4 pC N$^-$

[1] as opposed to 21 pC N^{-1} for pristine PVDF film. In addition, PNCU 1 films have the highest saturation polarization ($\sim$ 80 μC m^{-2}) at 1.2 MV m^{-1}, indicating increased piezoelectric nature. The fabricated PNG employing this film delivered the highest piezoresponse (V_{oc} $\sim$67.9 V, I_{sc} $\sim$4.15 μA) compared to the other constructed devices. PNG responds to a variety of mechanical forces, including finger tapping, leg imparting, bending, and twisting, with a very high sensitivity of 1.2 V kPa^{-1}. It is capable of quickly charging a number of capacitors. With 30,000 cycles run over a year, it also displays good operating stability. Fabricated piezoelectric driven self-charging supercapacitor, which is the first report on a CCNO-based system, was produced using PNCU 1 as a piezoelectric material, cum separator, poly (vinyl alcohol)-phosphoric acid as a gel electrolyte, and CCNO on CC as positive and negative electrodes. It showed high theoretical areal capacitance ($\sim$15.5 mF cm^{-2}) and shows 98% capacitance retention even after 10,000 cycles. With the construction of the next generation of self-powered, sustainable power sources for wearable and flexible electronic devices, this research opens up a new, promising direction in the field of supercapacitors.

7.5. References

1. C. Yoon, S. Ippili, V. Jella, A. M. Thomas, J. S. Jung, Y. Han, T. Y Yang, S. G Yoon, and G. Yoon, 2022. Nano Energy, 91, 106691.

2. M. A. Mahmud, P. Adhikary, A. Zolfagharian, S. Adams, A. Kaynak, and A. Z. Kouzani, 2022. Electronic Materials Letters, 1-16.

3. N. P. M. J. Raj, K. S. Abisegapriyan, G. Khandelwal, and S. J. Kim, 2022. Sustainable Energy & Fuels, 6(3), 674-681.

4. S. M. A. Z. Shawon, Z. D. Carballo, V. S. Vega, C. Lin, M. S. Rafaqut, A. X. Sun, J. J. Li, and M. J. Uddin, 2022. Nano Energy, 92, 106653.

5. H. Li, T. Chang, Y. Gai, K. Jiao, Y. Li, D. X. Jiang, Y. Wang, X. Huang, H. Wu, and Y. Liu, 2022. Nano Energy, 92, 106786.

6. X. Gao, Y. Zhang, Y. Zhao, S. Yin, J. Gui, C. Sun, and S. Guo, 2022. Nano Energy, 91, 106701.

7. S. Yu, Y. Ling, S. Sun, Y. Wang, Yu, Z., Zheng, J., Liu, G., Chen, D., Fu, Y., Liu, Y. and Zhou, H., 2022. Nano Energy, 94, 106911.

8. X. Xue, S. Wang, W. Guo, Y. Zhang, and Z. L. Wang, 2012 Nano letters, 12(9), 5048-5054.

9. J. Kim, J. H. Lee, J. Lee, Y. Yamauchi, C. H. Choi, and J. H. Kim, 2017. APL Materials, 5(7), 073804.

10. S. Stassi, V. Cauda, C. Ottone, A. Chiodoni, C.F. Pirri, and G. Canavese, 2015 Nano Energy, 13, 474-481.

11. Y. Xi, J. Song, S. Xu, R. Yang, Z. Gao, C. Hu, and Z. L. Wang, 2009. Journal of materials chemistry, 19(48), 9260-9264.

12. S. Mondal, S. Das, S. Maiti, N. Besra, T. Paul, and K.K. Chattopadhyay, 2021. International Journal of Nanotechnology, 18(5-8), pp.669-678.

13. Y.F. Lin, J. Song, Y. Ding, S. Y. Lu, and Z. L. Wang, 2008. Applied Physics Letters, 92(2), 022105.

14. Y. F. Lin, J. Song, Y. Ding, S. Y. Lu, and Z. L. Wang, 2008. Advanced Materials, 20(16), 3127-3130.

15. M. A. Johar, M. A. Hassan, A. Waseem, J. S. Ha, J. K. Lee, and S. W. Ryu, 2018. Nanomaterials, 8(6), 437.

16. J. H. Kang, D. K. Jeong, and S. W. Ryu, 2017. ACS applied materials & interfaces, 9(12), 10637-10642.

17. M. Y. LuSong, Lu. J, M. P. C.Y. Lee, L.J. Chen, and Z.L. Wang, 2009. ACS nano, 3(2), 357-362.

18. J. M. Wu, and C. C. Kao, 2014. RSC Advances, 4(27), 13882-13887.

19. A. Sultana, M. M. Alam, A. Biswas, T. R. Middya, and D. Mandal, 2016. Translational Materials Research, 3(4), 045001.

20. J. Yan, and Y. G. Jeong, 2016. ACS applied materials & interfaces, 8(24), 15700-15709.

21. H. Su, X. Wang, C. Li, Z. Wang, Y. Wu, J. Zhang, Y. Zhang, C. Zhao, J. Wu, and H. Zheng, 2021. Nano Energy, 83, 105809.

22. K. Y. Lee, D. Kim, J. H. Lee, T. Y. Kim, M. K. Gupta, and S.W. Kim, 2014. Advanced Functional Materials, 24(1), 37-43.

23. S. M. A. Z. Shawon, , Z. D. CarballoVega, V. S. Lin, C. Rafaqut, M. S. Sun, A. X. Li, J. J. and M. J. Uddin, 2022. Nano Energy, 92, 106653.

24. V. Jella, S. Ippili, and S. G. Yoon, 2020. ACS Applied Electronic Materials, 2(8), 2579-2590.

25. V. Jella, S. Ippili, J. H. S. V. N. Pammi, J. S. Jung, V. D. Tran, V. H. Nguyen, A. Kirakosyan, S. Yun, D. Kim, and M. R. Sihn, 2019. Nano Energy, 57, 74-93.

26. S. Liang, M. Zhang, G. M. Biesold, W. Choi, Y. He, Z. Li, D. Shen, and Z. Lin, 2021 Advanced Materials, 33(50), 2005888.

27. S. Ippili, V. Jella, A.M. Thomas and S.G. Yoon2021. Nanoenergy Advances, 1(1), 3-31.

28. T. Paul, S. Maiti, U. Mukherjee, S. Mondal, A. Sahoo and K. K. Chattopadhyay, 2021. Materials Letters, 301, 130264.

29. M. Faraz, H. H. Singh, and N. Khare, 2022. Journal of Alloys and Compounds, 890, 161840.

30. S. Liang, M. Zhang, G. M. Biesold, W. Choi, Y. He, Z. Li, D. Shen, and Z. Lin, 2021. Advanced Materials, 33(50), 2005888.

31. S. Liang, M. Zhang, G. M. Biesold, W. Choi, Y. He, Z. Li, D. Shen, and Z. Lin, 2021. Advanced Materials, 33(50), 2005888.

32. H. Su, X. Wang, C. Li, Z. Wang, Y. Wu, J. Zhang, Y. Zhang, C. Zhao, J. Wu, and H. Zheng, 2021. Nano Energy, 83, 105809.

33. K. Batra, N. Sinha, and B. Kumar, 2021. Vacuum, 191, 110385.

34. Z. Zhou, X. Du, Z. Zhang, J. Luo, S. Niu, D. Shen, Y. Wang, H. Yang, Q. Zhang, and S. Dong, 2021. Nano Energy, 82, 105709.

35. K. Shi, B. Chai, H. Zou, P. Shen, B. Sun, P. Jiang, Z. Shi, and X. Huang, 2021 Nano Energy, 80, 105515.

36. S. Wang, H.Q. Shao, Y. Liu, C.Y. Tang, X. Zhao, K. Ke, R.Y. Bao, M.B. Yang, and W. Yang, 2021. Composites Science and Technology, 202, 108600.

37. D. Mandal, K. Henkel, and D. Schmeißer, 2014. Physical Chemistry Chemical Physics, 16(22), 10403-10407.

38. H. Parangusan, D. Ponnamma, and M. A. A. Al-Maadeed, 2018. Scientific reports, 8(1), 1-11.

39. M. Fortunato, A.Tamburrano, M. P. Bracciale, M. L. Santarelli, and M. S. Sarto, 2021. Beilstein Archives, 2021(1), 55.

40. Y. Shen, Y. Guan, Y. Hu, Y. Lei, Y. Song, Y. Lin, and C. W. Nan, 2013. Applied Physics Letters, 103(7), 072906.

41. D. Sengupta, Y. Pei, and A. G. P. Kottapalli, 2019. ACS applied materials & interfaces, 11(38), 35201-35211.

42. Z. Yin, B. Tian, Q. Zhu, and C. Duan, 2019. Polymers, 11(12), 2033.

43. S. Mondal, S. Maiti, T. Paul, A. Sahoo, S. Bhattacharjee, N. S. Das, and K. K. Chattopadhyay, 2022. Applied Materials Today, 26, 101385.

44. X. Cai, T. Lei, D. Sunand, L. Lin, 2017. RSC advances, 7(25), 15382-15389.

45. F. Guo, J. Zhao, F. Li, D. Kong, H. Guo, X. Wang, H. Hu, L. Zong and J. Xu, 2020. CrystEngComm, 22(37), 6207-6215.

46. S. Mondal, T. Paul, S. Maiti, B.K. Das, and K. K. Chattopadhyay, 2020. Nano Energy, 74, 104870.

47. H. Lei, A. Pizzi, and G. Du, 2008. Journal of applied polymer science, 107(1), 203-209.

48. H. J. Ye, L. Yang, W. Z. Shao, S.B. Sun, and L. Zhen, 2013, RSC Advances, 3(45), 23730-23736.

49. R. M. Wolfe, A. K. Menon, T. R. Fletcher, S. R. Marder, J. R. Reynolds, and S. K. Yee, 2018. Advanced Functional Materials, 28(37), 1803275.

50. D. Chen, and J. X. Zhang, 2015. Applied Physics Letters, 106(19), 193901.

51. M. N. Almadhoun, M. A Khan, K Rajab, J. H. Park, J. M. Buriak and H. N. Alshareef, 2019. Advanced Electronic Materials, 5(1), 1800363.

52. H. Zhou, H. Wang, Z. Liu, H. Yang, C. Yuan, and Y. Wang, 2021. Polymer, 220, 123564.

53. S. Bhattacharjee, S. Mondal, A. Banerjee, and K. K. Chattopadhyay, 2020. Materials Research Express, 7(4), 044001.

54. J. Nie, L. Zhu, W. Zhai, A. Berbille, L. Li, and , Z. L. Wang, 2021. ACS Applied Electronic Materials, 3(5), 2136-2144.

55. M. Faraz, H. H. Singh, and N. Khare, 2022. Journal of Alloys and Compounds, 890, 161840.

56. A. Sultana, M. M. Alam, P. Sadhukhan, U. K. Ghorai, S. Das, T. R. Middya, and D. Mandal, 2018. Nano Energy, 49, 380-392.

57. Y. Lu, Y. Jiang, Z. Lou, R. Shi, D. Chen, and G. Shen, 2020. Progress in Natural Science: Materials International, 30(2), 174-179.

58. H. He, Y. Fu, T. Zhao, X. Gao, L. Xing, Y. Zhang and X. Xue, 2017. Nano Energy, 39, 590-600.

59. S. Sahoo, K. Krishnamoorthy, P. Pazhamalai, V. K. Mariappan, S. Manoharan, and S. J. Kim, 2019. Journal of Materials Chemistry A, 7(38), 21693-21703.

60. A. Rasheed, W. He, Y. Qian, H. Park, and D.J. Kang, 2020. ACS applied materials & interfaces, 12(18), 20891-20900.

61. A. Ramadoss, B. Saravanakumar, S. W. Lee, Y. S. Kim, S. J. Kim, and Z. L. Wang, 2015. ACS Nano, 9(4), 4337-4345.

62. S. Thakur, S. Maiti, K. Sardar, N. Besra, P. Bairi, K. Panigrahi, K. Chanda, T. Paul, and K. K. Chattopadhyay, 2021. Journal of Energy Storage, 35, 102249.

63. J. E. Lee, Y. Eom, Y. E Shin, S. H. Hwang, H. H. Ko, and H. G. Chae, 2019. ACS applied materials & interfaces, 11(14), 13665-13675.

64. S. Sarkar, S. Garain, D. Mandal, and K. K. Chattopadhyay, 2014. RSC Advances, 4(89), 48220-48227.

65. D. Chipara, V. Kuncser, K. Lozano, M. Alcoutlabi, E. Ibrahim, and M. Chipara, 2020. Journal of Applied Polymer Science, 137(30), 48907.

66. M.H. Ghajar, M. M. Mashhadi, M. Irannejad, M. Yavuz, and E. Abdel-Rahman, 2018. Bulletin of Materials Science, 41(2), 1-7.

67. Z. Hanani, I. Izanzar, S. Merselmiz, T. El Assimi, D. Mezzane, H. Uršič, U. Prah, J. Ghanbaja, I. Saadoune, M. Lahcini, and M. Spreitzer, 2022. Sustainable Energy & Fuels, 6(8), 1983-1991.

68. N. P. M. J. Raj, K. S. Abisegapriyan, G. Khandelwal, and S. J. Kim, 2022. Sustainable Energy & Fuels, 6(3), 674-681.

69. C. Behera, R. N. P. Choudhary, and P.R. Das, 2017. Journal of Polymer Research, 24(4), 1-13.

70. G. Chen, X. Wang, J. Lin, W. Yang, H. Li, Y. Wen, L. Li, Z. Jiang, and Q. Lei, 2016. Journal of Materials Chemistry C, 4(34), 8070-8076.

71. P. Singh, H. Borkar, B. P. Singh, V. N. Singh, and A. Kumar, 2014, AIP advances, 4(8), 087117..

72. H. Lee, H. Kim, D. Y. Kim, and Y. Seo, 2019. ACS omega, 4(2), 2610-2617

CHAPTER 8

Hybrid Piezoelectric Nanogenerator Based on PVDF And Vertically Alligned Zno Nanorods for Energy Harvesting Application
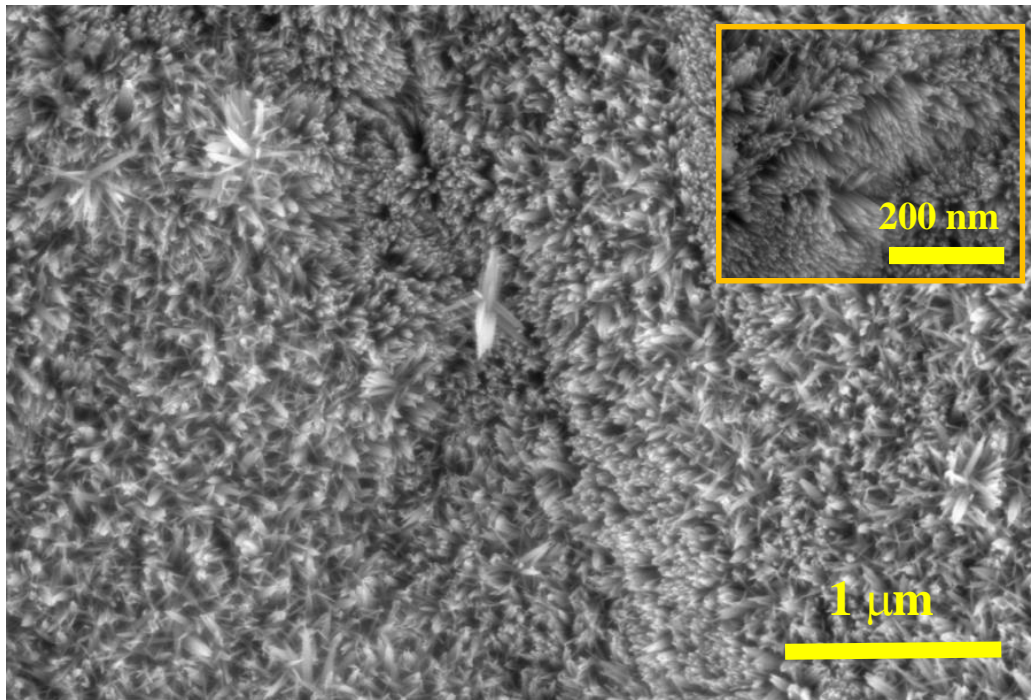
8.1.   Introduction

D ue to the prevailing energy crisis, tremendous efforts are being made to harvest renewable energy from the environment. Mechanical energy harvesting is the one of the best way to prevent energy deficiency which is easily available in our environmental surrounding. It comes from various sources like human body movement, cycling, running, walking, human's heart beat and several other natural vibrations. Mechanical energy converts into electrical energy by using smart portable devices based on piezoelectric materials [1, 2]. When a mechanical stress is applied on a piezoelectric material, charge accumulation takes place and a potential difference is generated between two electrodes [3, 4]. Various organic and inorganic piezoelectric materials are used in piezoelectric Nanogenarator (PENG) among them some are semiconductors like ZnO, CdS, ZnS, GaN, etc [4-6], some ceramic materials like PZT, BaTiO$_3$ [7] and some polymers like PVDF, PMMA, PDMS, PVDF-TrFE, PVDF-TFE, PVDF-HFP etc [3, 6, 8], behave as piezoelectric materials. In comparison to all of these organic, inorganic and polymer materials, PVDF is the most attractive polymer which has some interesting properties like flexibility, transparency, lightweight and biocompatibility [9]. PVDF has four phases with different properties α, β, γ and δ. Of them β phase is the most important phase as well as working worthy due to its electroactive properties. α and δ phases are non-polar and γ phase is also polar one with a very small dipole moment [10, 11]. The β phase is the most useful one in energy harvesting due to its intense polar character. This phase is responsible for high piezoelectric, pyroelectric and ferroelectric properties of PVDF.

This work mainly concerned about the enhancement of the performance of a PENG, made of PVDF and ZnO hybrid structure. PVDF film is deposited upon a layer of vertical ZnO nanorods grown on Zn foil. The piezoelectric voltages at different pressures are measured.

8.2.   Characterisations

Chapter 8

X-ray diffraction (XRD) patterns are recorded on a Bruker D8 diffractometer with Cu-Kα radiation of wavelength 1.5404 Ǻ at room temperature. Field emission scanning electron microscope (FESEM) images were taken by a HITACHI S 4800 electron microscope. Fourier transform infrared spectroscopy (FTIR) measurement was performed using Shimadzu FTIR spectrometer, IR prestige. All-time vs voltage measured by KEYSIGHT InfiNiiVision DSOX2012A digital storage oscilloscope.

8.3. Results and Discussion

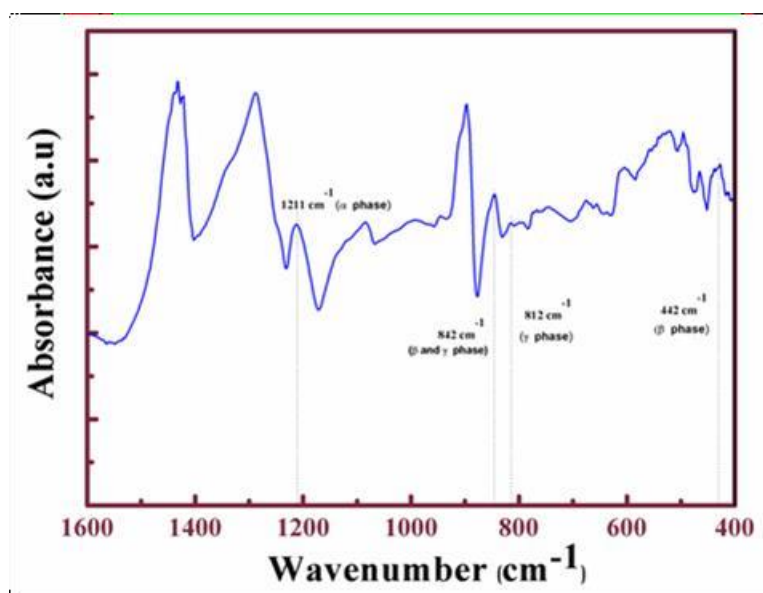### 8.3.1. Structural and Morphological Analysis

Figure 8.1: *FTIR spectra of PVDF in wavenumber range1600-400 cm^{-1} to study enhancement of electroactive β phase.*

FTIR (Fourier transformed infrared spectroscopy) spectrum of PVDF film is shown in Figure 8.1 Where peaks arising out from all the crystalline phases of PVDF are labelled. The presence of non-polar α phase (TGTG) [2, 12] in the PVDF-HFP film shows strong vibrational band at 533, 612, 764, 796, 856, 976, 1150, 1212 cm^{-1}. Some peaks arise due to superposed of β (TTTT) and γ (T^{3}GT^{3}G) [2, 12] phases at 510, 841, 1176 cm^{-1} [2, 12]. Whereas absorbance band arise at 431, 841, 1234 cm^{-1} [2, 11, 12] indicates presence of electro active β (TTTT) phase.

The relative electro-active phase fraction (F_{EA}) is calculated by the following equation

$$F_{EA} = \frac{A_{841}}{\frac{K_{841}}{K_{763}}A_{763}+A_{841}} \times 100\% \qquad (8)$$

Where A_{841}, A_{764} are the intensity of absorption peaks at 841, 764 cm^{-1} respectively and K_{841} (7.7 x 10^4 cm^2 mol^{-1}) and K_{764} (6.1 x 10^4 cm^2 mol^{-1}) are absorption coefficient of corresponding wavenumber. In our experiment, the electro active β phase achieved upto 55%.

It is already stated that, out of four crystalline phases β phase has piezoelectric and ferroelectric properties due to its structure of chain conformation [1, 12, 14]. So it is usable in nanogenerator for energy harvesting application. In this experiment, PVDF is used with ZnO which is a popular piezoelectric material to increase the output performance of nanogenerator [9]. FESEM images of ZnO nanorods, deposited on zinc substrate at room temperature are shown in Figure 8.2a and 8.2b. It is seen from these figures that the nanorods have length ~1 µm and diameter ~20 nm.
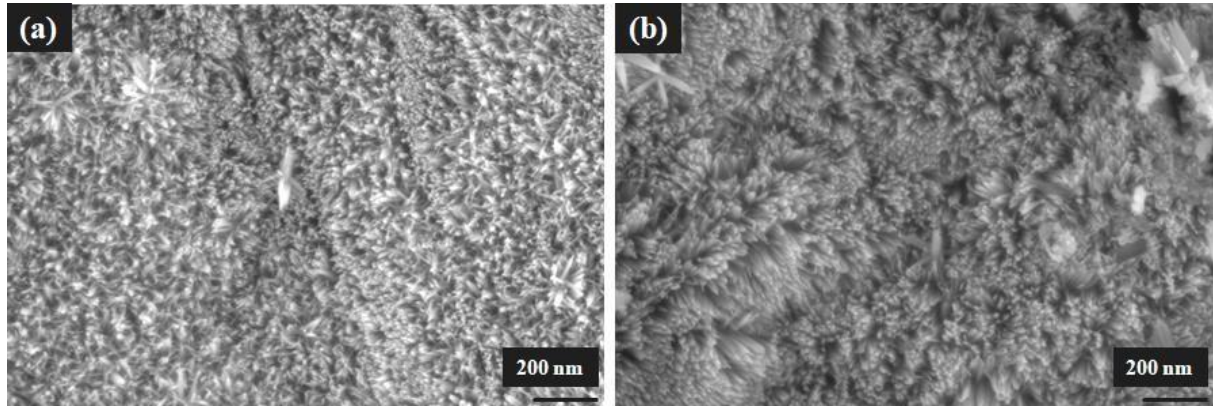

Figure 8.2: (a) and (b) FESEM image of ZnO Nanorods.

8.3.2. Working Principle and Electrical Measurement of PENG

Individually ZnO and PVDF both have piezoelectric properties, so ZnO-PVDF hybrid structure enhances the piezoelectric effect as well as the output performance. In normal condition dipoles of PVDF are not well aligned but applying mechanical pressure dipoles may align properly. Under the mechanical trace, bending of ZnO nanorods generates a voltage which is developed

at the two ends of the nanorod [3]. This potential helps to align dipole through stress induced polarisation of PVDF film**.** The polarisation upgrades the performance of nanocomposite and output voltage of PENG. Output voltage is directly dependent on thickness of PVDF film, if thickness of PVDF film increases then charge generation decreases dramatically. Also it influences to decrease the output voltage of the device [4]. So thickness of PVDF film is one of the key factors of nanogenerator performance. Figure 8.3a-c describes the working principle of fabricated device.
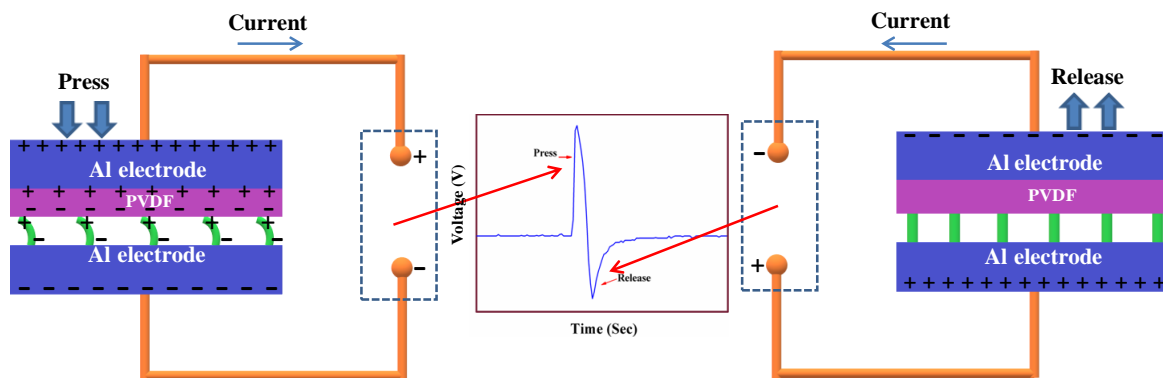

Figure 8.3: *Schematic diagram of PENG during pressing and releasing condition.*

In order to established sensitivity of the fabricated device, the device has been tested under different applied pressure. It is shows that the PENG device exhibits different output voltage changes significantly by varying applied external pressure. Figure 8.4 demonstrated that the output voltage increases with increasing pressure. If the applied force is 1 MPa then maximum generated voltage is 4.4 V and current is 1.25 µA and the generated power is 5.5 µW and when applied pressure are 1.52 MPa, 3.4 MPa and 4.5 MPa then generated output voltage are 8 V, 17.5 V, 21.5 V respectively and corresponding current 2.2 µA, 4 µA, 6.3 µA respectively also power generated 17.6 µW, 70 µW, 135.45 µW respectively which shown in Figure 8.4a-h. This power is able to glow small voltage LED light (shown in Figure 8.5c).
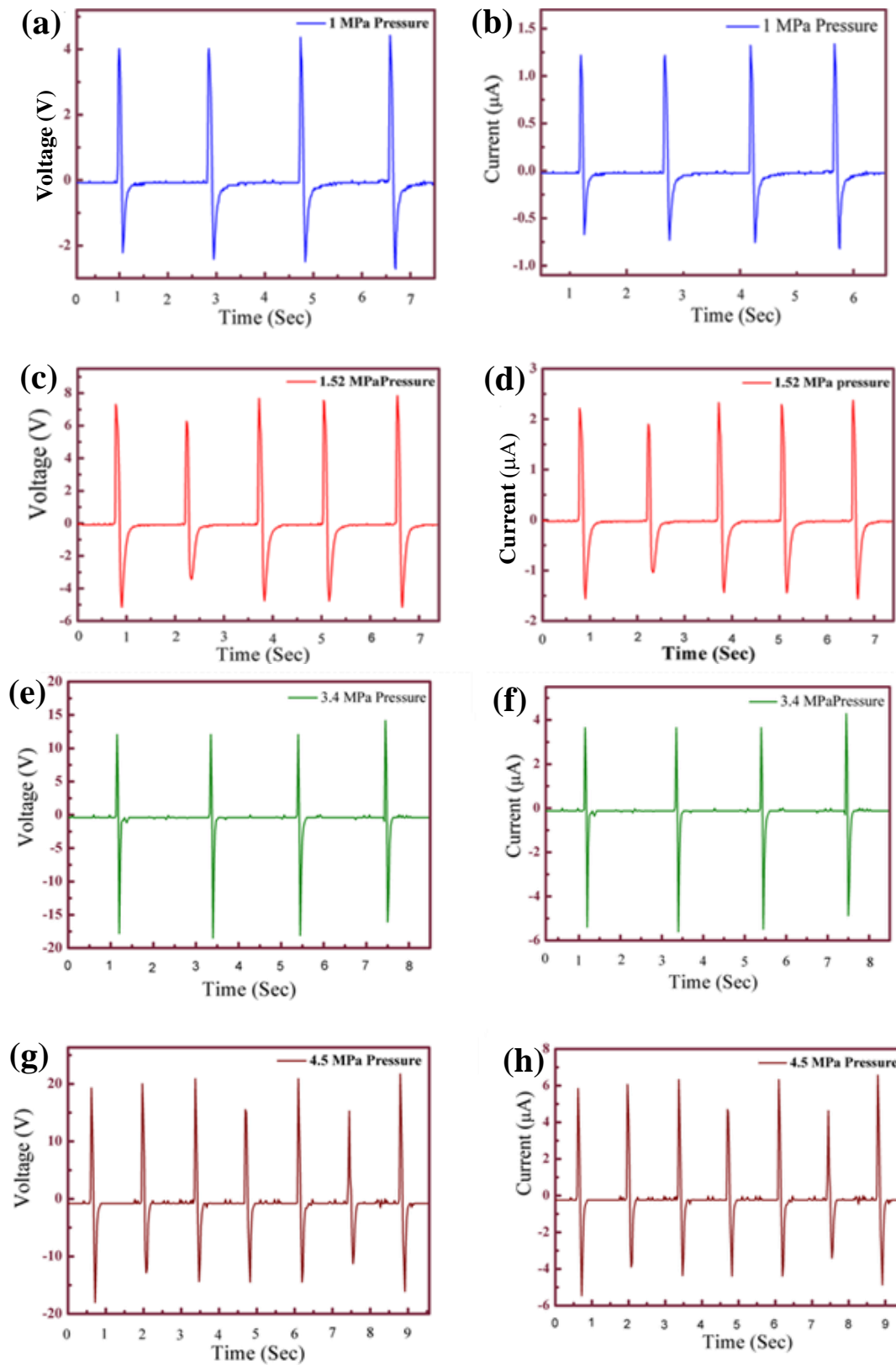
Figure 8.4: *(a), (c), (e), (g) are shows voltage generation under pressure 1 MPa, 1.52 MPa, 3.4 MPa, 4.5 MPa respectively and (b), (d), (f), (h) are shows current under pressure 1 MPa, 1.52 MPa, 3.4 MPa, 4.5 MPa respectively.*
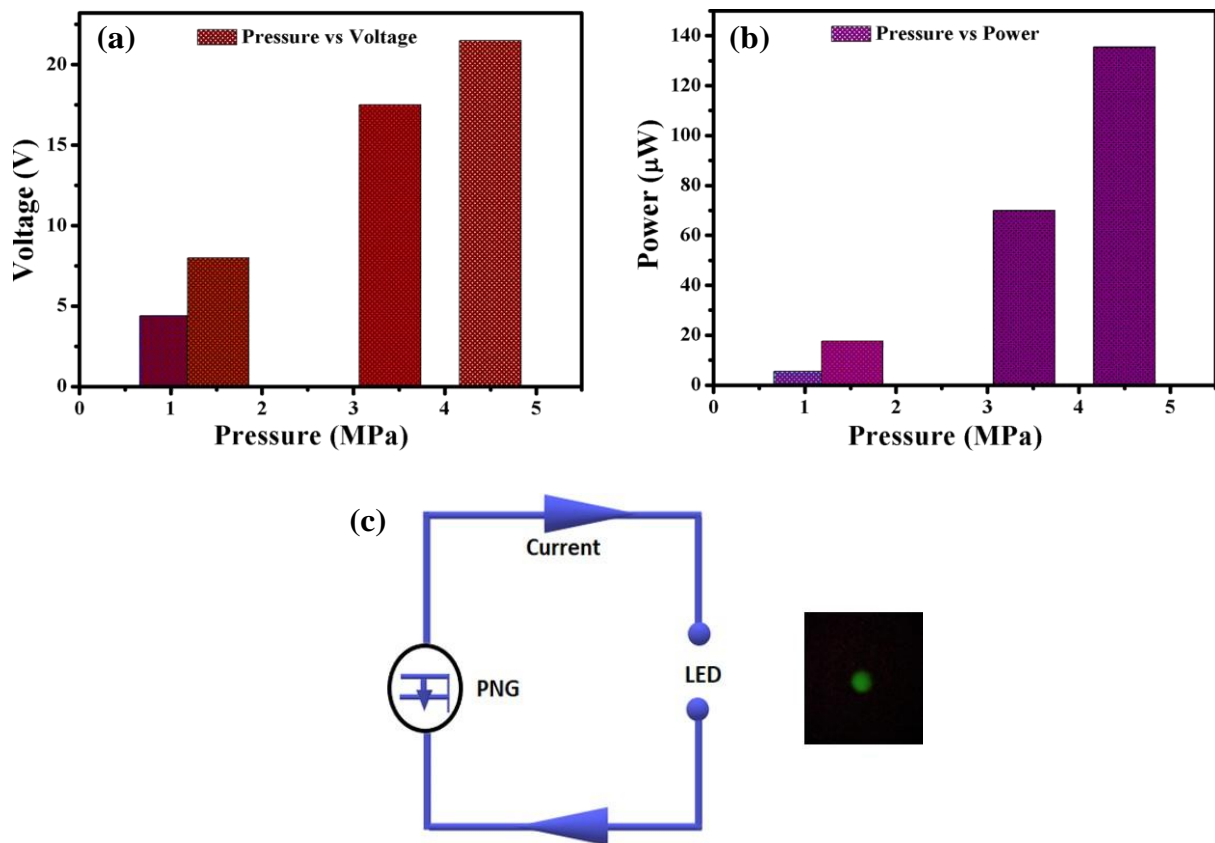
Figure 8.5: (a) Change of voltage with pressure. (b) Change of power with pressure. (c) Schematic circuit diagram of LED lighting using PENG.

8.4. Conclusions

In summary, ZnO nanorods were successfully grown on (1 cm×1 cm) Zn foil via normal aqueous solution route. It was found that energy harvesting mechanical energy to electrical energy was dramatically improved by using PVDF thin film due to electro-active properties of PVDF, which play significant role to increase the output performance of Nanogenarator. Applying a stress on the ZnO-PVDF sandwiched structure, charge accumulation and a voltage difference is appeared between two electrodes and a current is flowing through the external circuit. This current is dependent on stress applied on composite and gets 137.4 µW and 6 µW under pressure 4.5 MPa and 1 MPa respectively. PNG is useful to act as a component of self-power, portable electronic device that harvest mechanical energy from environments and convert electrical energy.

8.4. References

[1] M. M. Alam, S. K. Ghosh, A. Sultana, and D. Mandal, Nanotechnology, 2015, 26(16), 165403.

[2] A. Sultana, M. M. Alam, P. Sadhukhan, U. K. Ghorai, S. Das, T. R. Middya, and D. Mandal, Nano Energy 2018, 49, 380-392.

[3] Z. L. Wang, and J. Song, Science, 2006, 312(5771), 242-246.

[4] C. T. Huang, J. Song, W. F. Lee, Y. Ding, Z. Gao, Y. Hao, L. J. Chen and Z. L. Wang, Journal of the American Chemical Society, 2010, 132(13), 4766-4771.

[5] A. Sultana, M. M. Alam, S. Garain, T. K. Sinha, T. R. Middya and D. Mandal, ACS applied materials & interfaces, 2015, 7(34), 19091-19097.

[6] H. Paik, Y. Y. Choi, S. Hong and K. No, Scientific reports, 2015, 5, 13209.

[7] T. K. Sinha, S. K. Ghosh, R. Maiti, S. Jana, B. Adhikari, D. Mandal, and S. K. Ray, ACS applied materials & interfaces, 2016, 8(24), 14986-14993.

[8] J. Yan, and Y. G. Jeong, ACS applied materials & interfaces, 2016, 8(24), 15700-15709.

[9] M. Kim, Y. Wu, E. Kan and J. Fan, Polymers, 2018, 10(7), 745.

[10] X. Ren, H. Fan, Y. Zhao, and Z. Liu, ACS applied materials & interfaces, 2016, 8(39), 26190-26197.

[11] S. Cha, S. M. Kim, H. Kim, J. Ku, J. I. Sohn, Y. J. Park, B. G. Song, M. H. Jung, Lee, E. K., Choi, B. L. and J. J. Park, Nano letters, 2011, 11(12), 5142-5147.

[12] D. Mandal, K. Henkel, and D. Schmeißer, Physical Chemistry Chemical Physics, 2014, 16(22), 10403-10407.

[13] J. Chang, M. Dommer, C. Chang, and L. Lin, Nano energy, 2012, 1(3), 356-371.

[14] S. Garain, T. K. Sinha, P. Adhikary, K. Henkel, S. Sen, S. Ram, C. Sinha, D. Schmeißer, and D. Mandal, ACS applied materials & interfaces, 2015, 7(2), 1298-130.

CHAPTER 9

Grand Conclusion & Future Outlook

9.1. Grand Conclusion

Composites composed of piezoelectric nanomaterials dispersed in a flexible polymer have emerged as promising materials for highly durable and flexible energy harvesters and sensors. Although piezoelectric materials in their bulk form have a high electromechanical coupling coefficient and can efficiently convert mechanical energy to electrical energy, the ceramic form has low fracture toughness and thus they are limited in certain applications due to difficulty in machining and conforming to curved surfaces. A piezoelectric nanogenerator is a device that converts low-frequency mechanical vibration into electrical energy through piezoelectric, pyroelectric and triboelectric effects. Most of the researchers are using PVDF as a piezoelectric material in Piezoelectric nanogenerators. PVDF and its copolymers are the most suitable candidates due to their excellent energy storage ability, high piezoelectric coefficient, desirable flexibility, and capability to transform into different elaborate shapes. Generally, PVDF exhibits five polymorphs based on different chain conformations *viz.*, α, β, γ, δ, and ε phases. Among these, α and δ phase shows trans-gauche-trans-gauche (TGTG) configuration, and β phase exhibits all-trans (TTTT) configuration and γ phase shows T^3GT^3G configuration. α and δ phases show no spontaneous polarization which makes them non-polar, while due to the parallel dipolar configuration, both of β and γ phases are polar. A monomer unit —(CH_2—CF_2)— is repeated in the PVDF matrix (for β phase) to form a non-conjugated linear fluorinated hydrocarbon with a high vacuum dipole moment (7×10^{-30} C m), pointing roughly from the negatively charged fluorine atom to the positively charged hydrogen atom. However, with larger spontaneous polarization β phase predominantly manifests the piezoelectric effect. But in a normal PVDF matrix, β phase content is nominal, so it is needed to enhance the associated β phase fraction. Hence, our primary objective is to enhance the electroactive phase content of the PVDF matrix as much as possible. Different groups have elaborated versatile and novel approaches to transform the nonpolar phase into an electroactive phase; such as

Chapter 9

mechanical stretching, electrical polling under high field, thermal annealing, filler incorporation in PVDF matrix, etc. Among these, filler incorporation is a more convenient process for multifunctional applications that hardly affects the flexibility of the film.

The research described in this Ph.D. thesis explains how to synthesize PVDF composite materials and how to use them in multipurpose piezoelectric nanogenerators. The thesis begins with an overview of PVDF composites (chapter 1) that provides a brief description of their structure, numerous physical characteristics, and several optoelectronic factors that significantly influence their uses. The literature overview of PVDF-based piezoelectric nanogenerators and their applications, as well as several ground-breaking reports, are discussed in chapter 2. Chapter 3 describes the precise synthesis processes for the PVDF composite and the precise device construction process. Chapter 4 discusses the fundamental operating principles and a broad overview of the crucial characterization tools that are utilised during the entire course of the study.

Chapter 5 also provides an introduction to a novel piezoelectric sensor fabricated by a composite with room temperature processed all-inorganic cesium lead bromide ($CsPbBr_3$) perovskite rod and polyvinylidene fluoride (PVDF) nanofiber. $CsPbBr_3$ enables nucleation of the electroactive β phase in PVDF >90% and makes it suitable for piezoelectric energy harvesting. Piezoelectric energy generation from the devices has been investigated under several simple human movements like hammering by hand, finger touch, toe pressing, bending by arm and so on. Optimized composite (5 wt. % $CsPbBr_3$ containing PVDF film) based PNG delivered an output power of 4 mW with a high open-circuit voltage of 120 V and short-circuit current of 35 μA. In addition, the photosensitivity of the composite is demonstrated under light, which promises its potential as a photodetector. Considering the photoresponse and electroactive features, a new class of self-powered photoactive piezoelectric energy harvesters has also been fabricated.

Chapter 6 introduces cesium lead chloride ($CsPbCl_3$)-embedded β-phase comprising polyvinylidene fluoride (PVDF) hybrid films turn into a suitable functional material for piezoelectric-based mechanical energy harvesters. Incorporation of $CsPbCl_3$ in the PVDF matrix enables high crystallinity and nucleation of electroactive β-phase ~86% in the PVDF with piezoelectric coefficient d_{33} of 49 pm/V, much higher as compared to pristine PVDF. The fabricated PNG delivered an instantaneous output voltage of 168 V and a peak-to-peak output current of 2 μA. The high sensitivity of the flexible PNGs enables us to measure even a slight deformation due to bending by 2˚. Considering its good flexibility and high electrical output performance, optimized PNG was utilized for the fabrication of a wearable self-powered posture sensor to monitor the regular movement of our spine. Walking-based wearable PNGs are also devised for powering up normal android mobile phone batteries.

Chapter 7 introduces a self-charging flexible supercapacitor is successfully realized that can harvest sporadic mechanical energy, convert it to electrical energy, and simultaneously store power. Initially, chemically processed multi-metallic oxide, namely copper cobalt nickel oxide ($CuCoNiO_4$) is amalgamated within the PVDF framework in different wt. % to realize high-performance PNGs. The combination of $CuCoNiO_4$ as filler creates a notable electroactive phase inside the PVDF matrix, and the composite realized by combining 1wt% $CuCoNiO_4$ with PVDF exhibits the highest electroactive phase (>86%). Under periodic hammering (~100 kPa), PNGs fabricated with this optimized composite film deliver an instantaneous voltage of ~67.9 V and a current of ~4.15 μA. Furthermore, PNG is ingeniously integrated into a supercapacitor to construct PSCFS, using PNCU as a separator and $CuCoNiO_4$ nanowires on carbon cloth as the positive and negative electrodes. The self-charging behavior of the rectifier-free storage device was established under bending deformation. This work offers a high-performance, self-powered device that can be used to replace bulky batteries in everyday electronic devices by

harnessing mechanical energy and converting mechanical energy from its environment into electrical energy.

Energy harvesting from mechanical strain using piezoelectric materials has attracted considerable attention from researchers for their direct utilization in cutting-edge smart devices. In chapter 8, a piezoelectric nanogenerator based on polyvinylidene fluoride (PVDF) and aligned zinc oxide (ZnO) nanorods is fabricated for mechanical energy harvesting. ZnO nanorods array over zinc foil was realized via facile wet chemical method at ambient conditions. ZnO- PVDF hybrid structure was prepared by stacking PVDF on ZnO nanorods. The synergistic piezoelectric effect of PVDF and ZnO nanorods delivered high output characteristics under applied pressure. As fabricated device showed an open-circuit voltage of ~21.5 V and an instantaneous power of ~135.45 µW at an applied pressure of 4.5 MPa. Generated output power was more than sufficient to glow commercial green LEDs.

9.2. Future Outlook

The capacity of active materials to work with intelligent soft robotic and mechanical systems that use triboelectric and piezoelectric-based devices, or a mix of both, will be extremely helpful in a number of expanding study areas. Despite the fact that a lot has been accomplished in the last five years, there are still issues with soft robotic systems that need to be resolved. There are many opportunities for the development of triboelectric and piezoelectric-based soft actuators and effectors, especially for applications like soft manipulators, grippers, and microfluidic systems. Much of the work done in the field so far has focused on stretchable and flexible sensors and e-skins.

The integration of e-skin and power supply for soft actuation are additional difficulties and potential for TENG and PENG in soft robotic systems. For sensing and actuation, soft robotic systems need fluid flow tubes or electricity lines, which creates new difficulties for the creation

of wearable tech and self-powered, untethered robots. Through their distinctive energy harvesting methods and the simplicity of detecting small voltages and currents, TENG and PENG devices offer chances to develop self-powered sensing and systems. The increased energy requirements that may exceed the power levels that PENG and TENG may provide make self-powered actuation more difficult. Therefore, combining nanogenerators with low-power actuation techniques is useful. There are chances to speed up the prototyping and production of the devices thanks to advanced manufacturing technologies like 3D printing, which can incorporate soft materials, TENG or/and PENG, and electronics into the soft actuator and robotic systems. The development of effective methods and techniques for the modelling and control of TENG or/and PENG-based soft robotic systems are necessary to support the problems posed by the complicated nonlinear behaviour of soft bodies and to speed up the development and optimization of these systems. Modern, cutting-edge modelling approaches are primarily concerned with the creation and development of materials.

Combining TENG and PENG is anticipated to maximise their advantages and eliminate any potential disadvantages for soft robotic systems and wearable technology. For applications, more effective energy harvesting and sensing may be achieved by connecting TENGs with PENGs. Understanding the factors that can significantly boost actuation force and bandwidth will become increasingly important as TENG-based actuators develop. In the literature, a few PENG- or TENG-based microscale soft robots and gadgets have also been reported. There has also been evidence of the advantages of combining TENG and PENG devices with additional materials to achieve multi-functionalities, such as optical properties, antibacterial properties, or self-healing properties.